UNIVERSITY COLLEGE LONDON

Faculty of Mathematics and Physical Sciences

Department of Physics and Astronomy

Influence of solar wind on the Jovian thermosphere.

Thesis submitted for the Degree of Doctor of Philosophy

at University College London

by

Japheth Nesta Yates

Supervisors:

Dr. Nicholas Achilleos

Prof. Alan Aylward

Examiners:

Prof. Emma Bunce

Prof. Steve Miller

August 21, 2013

TLC and Family

I, Japheth Nesta Yates, confirm that the work presented in this thesis is my own. Where information has been derived from other sources, I confirm that this has been indicated in the thesis.

I would also like to declare that the work presented in this thesis has been or is in the process of being published in peer reviewed Journals, resulting in:

Yates, J., Achilleos, N., Guio, P., 2012. Influence of upstream solar wind on thermospheric flows at jupiter. Planetary and Space Science 61 (1), 15 – 31, surfaces, atmospheres and magnetospheres of the outer planets and their satellites and ring systems: Part VII.

Yates, J., Achilleos, N., Guio, P., 2013. Response of the Jovian thermosphere to a transient 'pulse' in solar wind pressure. Planetary and Space Science, under review.

Abstract

We aim to explain the reason why Jupiter's upper atmosphere is hotter than initial theories predicted by employing a coupled magnetosphere, ionosphere and thermosphere model. We use this coupled model to study how changes in upstream solar wind dynamic pressure affect Jupiter's thermospheric dynamics, energy balance, aurora and magnetosphere-ionosphere coupling currents. The variation in solar wind pressure is investigated on long ($\geq$ 50 Jovian days) and short ($\leq$ 3 hours) time scales, which we respectively refer to as steady state and transient state. We vary the solar wind pressure by changing the size of the magnetosphere, as these two parameters are inversely correlated.

In steady state, three different configurations are used: compressed, average and expanded magnetospheres. We find that the power dissipated by Joule heating and ion drag increases by $\sim$ 190 % from a compressed to expanded magnetosphere. For transient modelling, the magnetosphere is compressed and expanded in a period of $\leq$ 3 hours. Compressions cause a reversal in momentum transfer between the thermosphere and magnetosphere. Compressions and expansions lead to at least a factor-of-two increase in ion drag and Joule heating, resulting in a $\sim$ 2000 TW increase in total power dissipated in the thermosphere and local temperature variations $\geq$ 25 K. Compressions also cause a $\sim$ 450 % increase in auroral UV emission whilst expansions increase UV emission modestly by $\sim$ 37 %.

While these analyses do not provide a definitive answer to the elevated Jovian thermospheric temperature, they show that, in moving from a steady-state to a time-dependent paradigm, the thermospheric response to magnetospheric reconfiguration is characterised

by dramatically different distributions of temperature and wind. In particular, magnetospheric compressions produce extensive cells of equatorward flow emanating from the auroral zone, suggesting that a Jovian-like magnetosphere subject to adequately frequent, repeated episodes of contraction/expansion may possess elevated thermospheric temperatures, perhaps even at the level of those observed.

Acknowledgements

Firstly I would like to thank my supervisors Nick, Alan and Patrick for their unwavering support. I would not have finished this PhD were it not for you. I would also like to thank Chris for creating JASMIN; Caitriona for showing me the ropes and Licia for the useful discussions. Thanks are also due for numerous people from MSSL, Leicester and JAXA-ISAS.

Special thanks to the many friends I made here in Group A. In particular, Ingo and Stephen for always cracking me up, Fotini for trying to keep me sane and the members of the 'g18 list' for the vast number of memorable, and some hopefully forgettable, experiences.

I would like to thank my family and friends for their support, companionship and belief throughout my studies. Special thanks are due to Mum and Dad for their constant belief and to Tracey, Naphtali, Sarah and Jeshua for their perpetual reminders that I am indeed a geek.

I acknowledge support of the STFC funded Miracle Consortium (part of the DiRAC facility) in providing access to computational resources.

You need to set up the right atmosphere for a woman...
Atmosphere? As in clouds and stuff?

Higurashi and Inuyasha (Inuyasha)

Contents

This page was intentionally left blank

List of Figures

This page was intentionally left blank

List of Tables

This page was intentionally left blank

Chapter 1

Introduction

All truths are easy to understand once they are discovered; the point is to discover them.

Galileo Galilei

Theoretical Planetology is a multidisciplinary field aiming to solve questions on the origin, dynamics and energy balance of planets and their space environments. Solving these questions lays the foundation for other, age-old questions such as 'Are there other worlds out there capable of harbouring life?'. Amongst the eight planets in our solar system, Jupiter rules supreme. Jupiter, being the largest planet in the solar system, has intrigued mankind since we first gazed up at the stars. Despite numerous centuries of observations, the 'king of planets' still holds many secrets.

One such secret lies in Jupiter's upper atmospheric temperature. The upper atmospheres (thermosphere) of the Gas Giant planets are poorly understood. Since the dawn of the Space Age, only eight spacecraft have taken in situ measurements at the gas giants Jupiter and Saturn. Even fewer missions have visited the ice giants Uranus and Neptune. Measurements were typically acquired outside the thermosphere, in the magnetosphere. There are, however, two sets of in situ observations of planetary atmospheres beyond Mars: i) the Galileo probe - observations of the physical conditions in Jupiter's atmosphere (Seiff et al. 1996, 1998; Niemann et al. 1996, 1998) and ii) the Huygens probe - analogous measurements of the Kronian moon Titan's atmosphere (Lebreton et al. 2005; Niemann et al.

2005; Tomasko et al. 2005) . All other observations of gas giant atmospheres are remote i.e. acquired via ground- or space-based telescopes.

This thesis is concerned solely with the Jovian system, but the concepts and results discussed herein may be applicable to Saturn and the other gas giants. One of the main issues which scientists (over the past four decades) have studied the gas giants for is that of the so-called 'energy crisis'. The upper atmosphere of Jupiter and the other gas giants is considerably hotter than what is expected from the action of solar Extreme Ultra Violet (EUV) heating alone. Past studies have tried to account for the extra energy input required in the Jovian thermosphere by adding heat sources below and above the thermosphere (Nishida and Watanabe 1981; Waite et al. 1983; Young et al. 1997; Miller et al. 2000). More recently, models have started to investigate how variations in solar wind dynamic pressure affect energy sources and sinks in the Jovian thermosphere (e.g. Cowley et al. (2007); Yates et al. (2012)). This is the main purpose of this thesis - to investigate how the thermosphere couples to the solar wind, and whether this process may solve the 'energy crisis' problem. This coupling is complex, and also involves the ionosphere and magnetosphere of the planet.

We also investigate the influence of solar wind dynamic pressure on the other aspects of the Jovian system, such as the efficiency of magnetosphere-ionosphere (M-I) coupling, the velocity of thermospheric flows and the morphology of auroral emissions. These investigations demonstrate the usefulness of theoretical models in developing observational diagnostics of the M-I coupling process.

1.1 Jovian upper atmosphere

1.1.1 Observations

As mentioned above the Jovian upper atmospheric temperature is higher than expected. Strobel and Smith (1973) modelled the importance of solar EUV radiation on the energy balance of the Jovian thermosphere. They assumed that solar EUV was the sole source of heating in the Jovian thermosphere. This resulted in an average temperature difference between the mesopause (assumed to have a temperature of 140 K) and the exosphere of ∼15 K; rising to a maximum of ∼60 K if the redistribution of energy in the thermosphere

was negligible and solar conditions were at maximum (factor-of-two increase in incident solar flux). Their theoretical study produced results comparable to others such as Gross and Rasool (1964); McGovern and Burk (1972); Shimizu (1971). However, stellar occultations by Hubbard et al. (1972) suggest Jovian thermospheric temperatures ∼300 K, considerably larger than those predicted by solar heating alone. This was one of the first suggestions that the Jovian thermosphere was much hotter than expected.

The Voyager 1 and 2 flybys of Jupiter allowed for the first set of occultations to be observed. The Ultraviolet Spectrometer (UVS) on Voyager 1 was used to carry out solar occultations from which Atreya et al. (1979) found the Jovian thermosphere to have a neutral temperature of 1100 ± 100 K (at a pressure level of $\sim 10^{-2}$ nbar). The UVS instrument on Voyager 2 observed stellar occultations of Jupiter's atmosphere (Festou et al. 1981). These works found two different neutral temperatures of 200 ± 30 K and 425 ± 25 K at pressure levels of $\sim 1.0^{+1.0}_{-0.5}$ μbar and $\sim 3 \times 10^{-4}$ μbar respectively.

The next set of measurements of the Jovian thermospheric temperature came from H_3^+ emission in Jupiter's auroral regions, discovered in Infrared (IR) auroral observations by Drossart et al. (1989); Trafton et al. (1989); Miller et al. (1990). The H_3^+ ro-vibrational temperature is obtained by assuming quasi-thermal equilibrium (QTE) and calculating the line intensity ratio of two different vibrational manifolds (see Fig. 1.1 showing vibrational temperature as a function of the line intensity ratio for observations by Stallard et al. (2002)). Drossart et al. (1989) used H_3^+ to determine the thermospheric temperature of the Southern auroral region, ∼1100 K. Using H_3^+ emission at 4.0 μm, Miller et al. (1990); Maillard et al. (1990) found the auroral ionosphere to have a ro-vibrational temperature of ∼1100 K whilst Oka and Geballe (1990) found the temperature to be ∼650 K. The IR observations summarised so far are located in the auroral regions of the Jovian thermosphere/ionosphere. Marten et al. (1994) observed H_3^+ emission near the Northern equator (∼10 ° latitude) and found its rotational temperature to be $\sim 800 \pm 100$ K. These temperatures are all larger than initially predicted by early modelling (Strobel and Smith 1973) but they still show a variation of 450 K. It was uncertain whether these variations depended on local time or some time-dependent phenomena.

It was thus necessary to obtain a global map of Jupiter's H_3^+ emission to establish

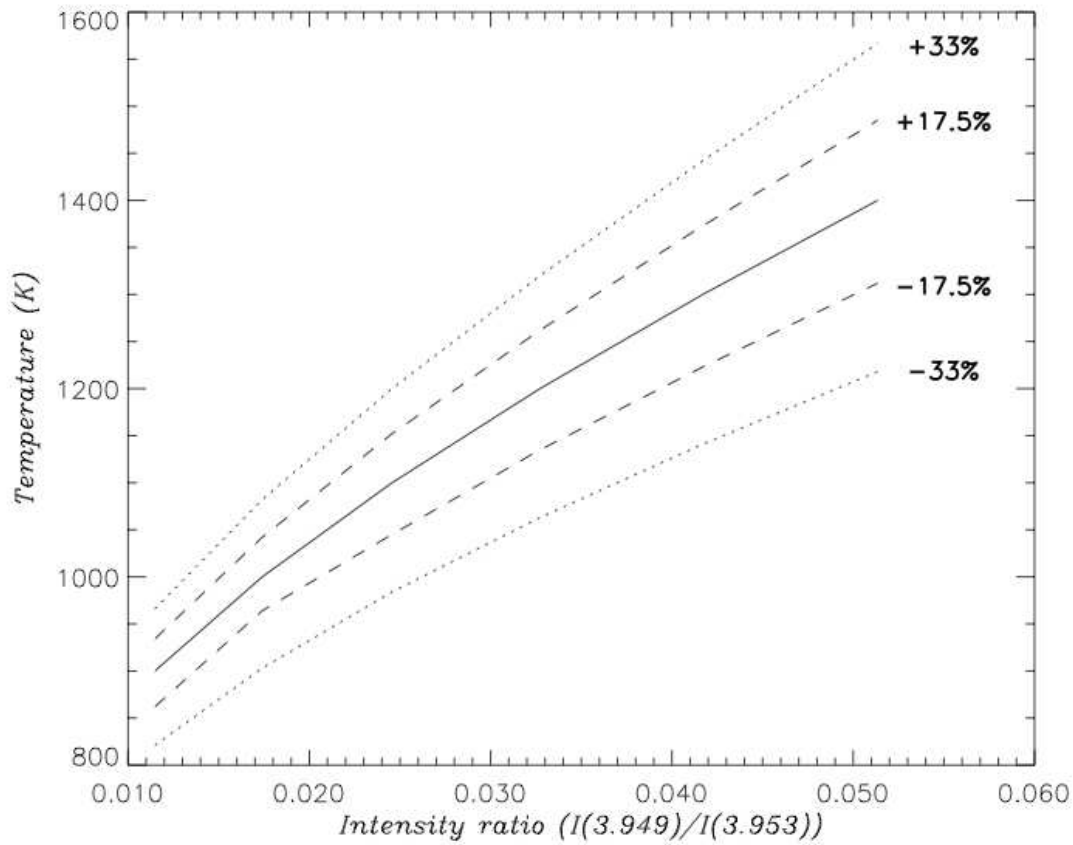

Figure 1.1. Showing H_3^+ vibrational temperature as a function of the hotband (3.949 μm) and fundamental (3.953 μm) intensity ratios (solid line). The dashed and dotted lines respectively show the 17.5 % and 33 % error limits. These observations were obtained across Jupiter's Northern auroral region and presented in Stallard et al. (2002).

whether the large variation in thermospheric temperature was due to spatial- or time-dependent phenomena. Two techniques were devised to obtain global H_3^+ maps (Yelle and Miller 2004):

i) Direct imaging using circular variable filters or custom narrowband filters (Kim et al. 1991; Baron et al. 1991). This technique led to the re-location of the Jovian main auroral oval (Baron et al. 1991), the discovery of a separate (from the main oval) Io footprint (Connerney et al. 1993) and auroral features in the polar region (Satoh et al. 1996; Satoh and Connerney 1999) as shown in Fig. 1.2.

ii) Spectral imaging (Lam et al. 1997; Miller et al. 1997). Lam et al. (1997) were able to use this technique to obtain global distributions for H_3^+ temperature and column density,

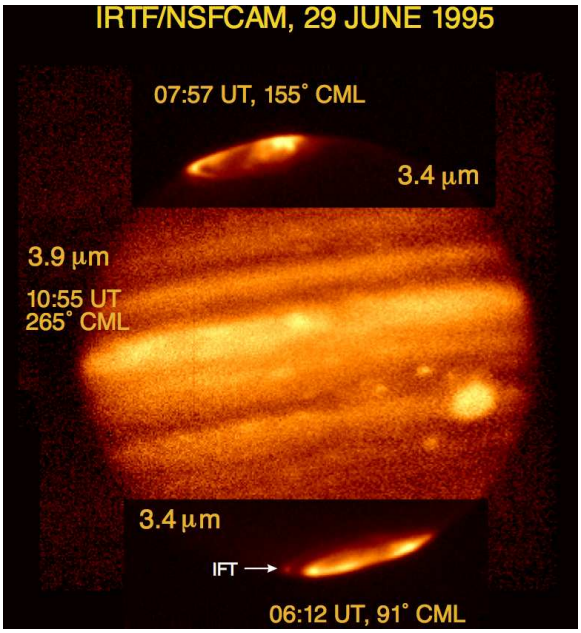

Figure 1.2. Showing 3.42 μm auroral emission of both Jupiter's North and South poles. Equatorial latitudes are shown in 3.9 μm. IFT indicates the Io footprint. Image from Satoh and Connerney (1999).

shown in Fig. 1.3. Lam et al. found that the H_3^+ temperature was largest at the polar and equatorial regions ($750 - 1050$ K) whilst mid-latitudes were cool ($700 - 800$ K) in comparison (see top plot in Fig. 1.3). The column density distribution (bottom plot in Fig. 1.3) also indicated significantly larger densities in the polar regions of the thermosphere.

More recently, H_3^+ emission spectra were used to identify four different regions of the polar/auroral ionosphere (Stallard et al. 2001): a Rising Auroral Oval (ROA); a Dark Polar Region (DPR); a Bright Polar Region (BPR); and a Setting Auroral Oval (SAO). Work by Stallard et al. (2002) used ratios between the intensities of H_3^+ 'hotband' and 'fundamental' lines to obtain the ro-vibrational temperatures across the Jovian Northern auroral ionosphere. The difference in emission between these auroral regions was found to correspond to temperature differences of $\sim 900 - 1250$ K (Stallard et al. 2002). These studies were used to support the theory of Hill (1979), discussing the corotation (with the deep planet), and subsequent breakdown thereof, of plasma in the magnetosphere (see section 1.2 for more detail).

We have summarised a small amount of evidence indicating that the Jovian thermo-

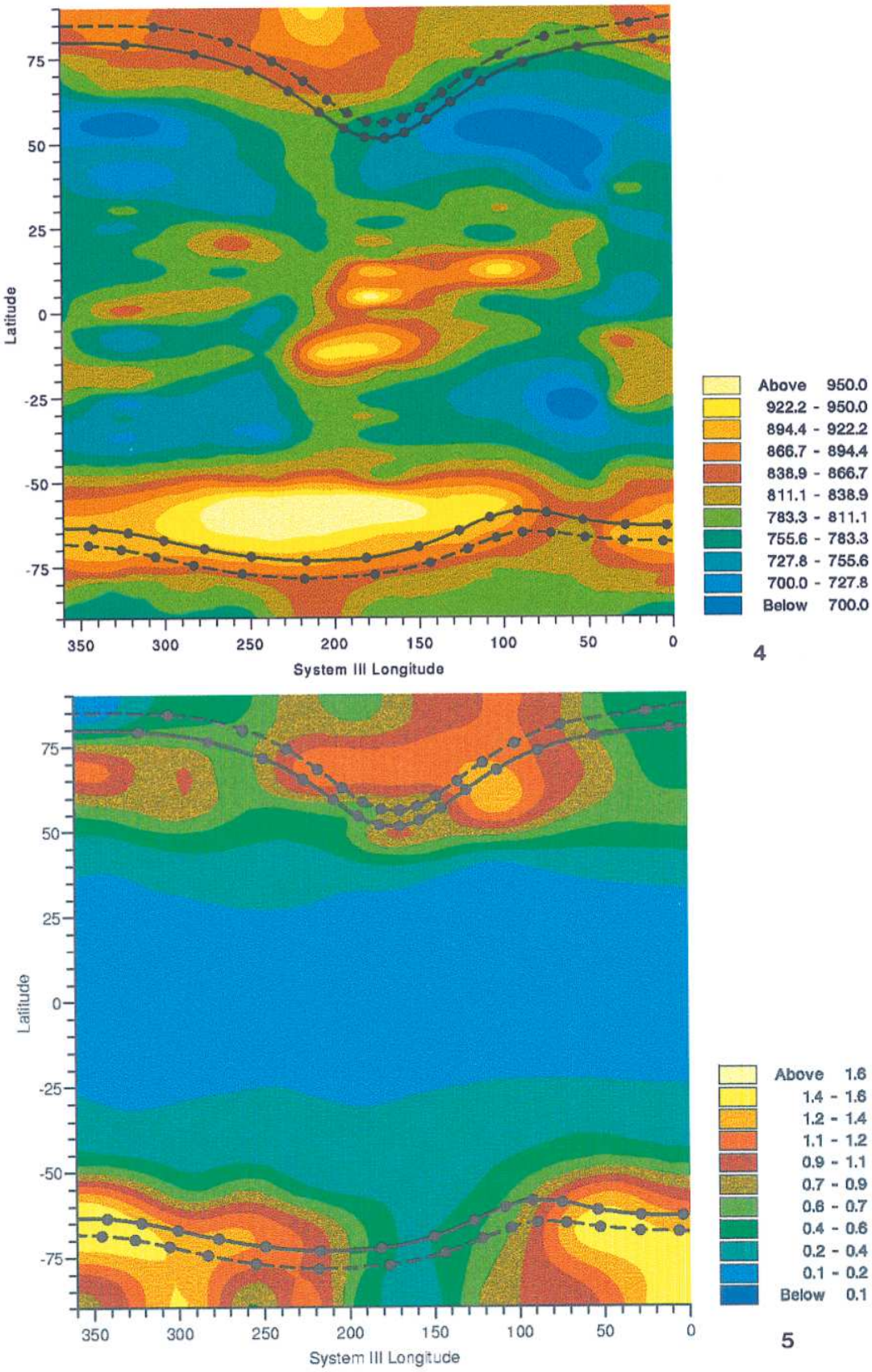

Figure 1.3. H_3^+ temperature (a) and column density (b) maps from spectral imaging of Jupiter. Column density is in units of $10^{16}\,m^{-2}$. The dashed lines indicate the location of the main oval and the solid lines represent the location of the Io footprint (Connerney 1993). From Lam et al. (1997); Miller et al. (1997); Yelle and Miller (2004).

spheric temperature is up to 700 K (Yelle and Miller 2004) higher than that predicted by solar heating alone (Strobel and Smith 1973). The reader is referred to the comprehensive discussions in Yelle and Miller (2004) for further detail on observations of the Jovian thermosphere and ionosphere. In light of all the evidence we ask the question: If the Jovian thermosphere is so hot, and solar heating does not provide the required energy for this, then where does the extra energy come from? This leads us to the next section, where we discuss the recent, and not so recent, modelling efforts made to try solve the 'energy crisis'.

1.1.2 Modelling

A number of different theories have been put forward to explain the high Jovian upper atmospheric temperature. These range from auroral particle precipitation (Waite et al. 1983; Eviatar and Barbosa 1984; Grodent et al. 2001) to gravity waves (Young et al. 1997), Joule heating (Nishida and Watanabe 1981) and ion drag (Miller et al. 2000; Smith et al. 2005; Millward et al. 2005).

Particle precipitation

Initial modelling for heating rates resulting from auroral particle precipitation at Jupiter was conducted by Waite et al. (1983) for electrons and Eviatar and Barbosa (1984) for ions. Waite et al. (1983) modelled the heat deposited in the thermosphere by solar EUV, 1 keV and 10 keV auroral electron beams. The electrons were assumed to possess an energy flux of 10 mW m^{-2}, and this was found to be sufficient to reproduce the Voyager UVS observations and provide $\sim$5 mW m^{-2} of heat (two orders of magnitude larger than produced by solar radiation alone). This heating resulted in neutral thermospheric temperatures of 260 K for solar heating alone, 1900 K when using 10 keV electrons and 3000 K when using 1 keV. The fact that the 10 keV electron beam resulted in cooler temperatures than the 1 keV beam was determined to be a consequence of the 10 keV beam depositing heat at lower altitudes near (or in) the IR cooling region. Whilst Waite et al. (1983) do acknowledge that these thermospheric temperatures are indeed higher than observations suggest, and are thus unlikely to be accurate, they do stress that the heating rates they obtain are likely to be lower limits in the auroral regions. Joule heating is not included in their model; if it were included, the auroral heating rates would be very large creating strong thermospheric winds that would supposedly redistribute the energy to lower latitudes.

Eviatar and Barbosa (1984) proposed that the intense Jovian UV aurora was created by the precipitation of heavy ions from Io, which could provide ∼40 TW of power to the auroral region.

Gravity waves

Gravity waves transfer momentum from the lower atmosphere to the upper atmosphere. They have long been thought to play an important role in the energy balance of the Jovian thermosphere (French and Gierasch 1974; Sagan et al. 1974; Yelle et al. 1996). The Jovian thermal profile obtained using the Atmospheric Structure Instrument on board the Galileo probe (see Fig. 2.11 (Seiff et al. 1998)) showed wave-like fluctuations which Young et al. (1997) interpreted to be caused by gravity waves capable of depositing the required heat in the thermosphere. However, the heating due to gravity waves in the Jovian (and other Gas Giant) thermosphere is a controversial topic. Studies have suggested that the calculations of Young et al. (1997) are incorrect and that gravity waves are not energetic enough (Matcheva and Strobel 1999) and others have suggested that these waves might in fact cool the thermosphere (Hickey et al. 2000). Nonetheless, gravity waves do not feature in this thesis and will not be discussed further.

Joule heating and Ion drag

Joule heating is thermal energy caused by the collisions between ionospheric ions and neutrals in the thermosphere. It is strongly dependent on the difference in angular velocities between the neutral thermosphere and magnetospheric plasma. Nishida and Watanabe (1981) modelled the interaction between the Jovian ionosphere and magnetosphere to estimate the thermal heating (Joule heating) created by corotation enforcement currents. These currents accelerate the outflowing plasma from the Io torus towards corotation with the planet. They found that Joule heating in the high-latitude regions could account for more than 10 $\mathrm{mW\,m^{-2}}$ of heating, approximately three orders of magnitude larger than that caused by solar EUV heating, ∼3.7x10^{-2} $\mathrm{mW\,m^{-2}}$ (Yelle and Miller 2004).

Melin et al. (2006) analysed data from an auroral heating event (on September 8-11 1998) observed in IR emissions by Stallard et al. (2001, 2002) and found that particle precipitation alone cannot account for the observed temperature increase (940−1065 K). Joule

heating and ion drag[1] inputs increased from 67 mW m^{-2} (on September 8) to 277 mW m^{-2} (on September 11) corresponding to a doubling of the ionospheric electric field; this additional increase in heating was able to account for the observations. Cooling terms (hydrocarbon and H_3^+ emission) also increased during the event but only to ∼20 % of the total increase in heating and thus, were unable to fully compensate the increase in thermospheric heating. More detailed analysis showed that local cooling terms would be unable to return the thermosphere to its initial temperature before the likely onset of subsequent heating events. Melin et al. (2006) thus concluded that the temperature increases must lead to an increase in velocity of equatorward winds, which may then transport energy to lower latitudes (Waite et al. 1983).

Joule heating and ion drag are directly related to the coupling of the magnetosphere and ionosphere. For reliable representations of these mechanisms and how they affect the thermospheric energy budget, a coupled magnetosphere-thermosphere-ionosphere model is required (discussed in section 1.2 and Chapter 3); Joule heating and ion drag are a significant part of our investigations. However, to date, none of the aforementioned studies and their corresponding mechanisms have been able to fully account for the high thermospheric temperatures observed.

1.2 Jovian magnetosphere-ionosphere coupling

In addition to being the largest planet in the solar system, Jupiter also possesses the largest magnetic moment and magnetosphere. The Jovian magnetosphere interacts with both the solar wind and the ionised conducting layer (ionosphere), in the planet's upper atmosphere. Its dynamics are strongly influenced by its internal source of plasma (Io's volcanism (Bagenal and Sullivan 1981)) and Jupiter's rapid rotation rate. These interactions can be quite complex, however, we may use models with some simplifying assumptions (e.g. axial symmetry) to gain insight into the dynamics of the magnetosphere and upper atmosphere, and their physical interactions with the solar wind.

Prior to the arrival of the Voyager spacecraft at Jupiter it was assumed that the plasma contained in the Jovian magnetosphere corotated perfectly with the planet (Kennel and

[1]Ion drag is the change in kinetic energy resulting from ion-neutral collisions.

Coroniti 1977). McNutt et al. (1979) analysed the first *in situ* plasma data in the Jovian system and found that the plasma corotated at a fraction of planetary rotation for radial distances $> 10\,\mathrm{R_J}$ (Jovian radii; $1\,R_J$=71492 km). Hill (1979) modelled the departure from corotation of the magnetospheric plasma by balancing torques between the inertial drag of magnetospheric plasma (created by the production and radial diffusion from Io) and the viscous torque resulting from ion-neutral collisions in the ionosphere. This torque was transmitted from planet to magnetosphere via field-aligned currents. Hill found that the magnetospheric plasma should sub-corotate by $\sim$50 % at a critical radial distance ($64\,\mathrm{R_J}$ in his calculations).

After the initial theoretical M-I coupling study by Hill (1979), the magnetospheric plasma (located in the middle magnetosphere / magnetodisc) was shown to possess a wide range of angular velocities ($\sim$50 % at $\sim 20\,\mathrm{R_J}$ compared to $\sim 64\,\mathrm{R_J}$ predicted in Hill (1979)) as it diffuses radially outwards in the magnetosphere (Hill et al. 1983; Pontius 1997; Vasyliunas 1983). Details regarding the Jovian magnetosphere such as Io's volcanism and its current systems are described in section 2.1.4. Here we discuss recent M-I coupling models and their results as related to the coupling currents and thermospheric dynamics and energy balance (where applicable).

1.2.1 Steady state modelling

Several studies have made substantial progress in modelling Jovian steady-state M-I coupling (Hill 1979; Pontius 1997; Cowley and Bunce 2001; Hill 2001; Cowley and Bunce 2003a,b; Nichols and Cowley 2004, 2005; Cowley et al. 2005, 2007; Ray et al. 2010, 2012). The models of Cowley and Bunce (2001, 2003a,b); Nichols and Cowley (2004) were primarily used to study the interaction of the inner and middle magnetosphere and how these regions couple with the Jovian ionosphere; Cowley et al. (2005) and Cowley et al. (2007) expanded on the former studies by incorporating simplified models for the outer magnetosphere and polar cap region, and thus coupling the 'entire' magnetosphere to the ionosphere. Nichols and Cowley (2005); Ray et al. (2010, 2012) self-consistently included the effect of field-aligned potentials in their M-I coupling models. Another set of models investigated how the magnetosphere affected Jovian thermospheric dynamics and heating by including a Global Circulation Model (GCM) in their modelling, essentially making a

coupled magnetosphere-thermosphere-ionosphere model (Achilleos et al. 1998, 2001; Millward et al. 2002, 2005; Bougher et al. 2005; Majeed et al. 2009; Smith and Aylward 2009; Tao et al. 2009).

Cowley and Bunce (2001); Southwood and Kivelson (2001) carried out theoretical studies investigating how changes in solar wind dynamic pressure (leading to changes in magnetospheric size[2]) would affect the M-I coupling currents and aurora. They proposed that magnetospheric compressions (caused by an increase in solar wind pressure) would increase plasma angular velocity towards corotation and consequently decrease the magnitude of the coupling currents and auroral emission. Magnetospheric expansions would lead to the opposite effect – an increase in auroral emission and in the magnitude of M-I currents. Steady state modelling in Cowley and Bunce (2003b); Cowley et al. (2005) and Cowley et al. (2007) subsequently found that the magnitude of M-I coupling currents and auroral emission at Jupiter was anti-correlated with solar wind dynamic pressure, as suggested by Cowley and Bunce (2001); Southwood and Kivelson (2001).

An important component of an M-I system is the ability for the thermosphere-ionosphere to conduct a current - represented through the height-integrated Pedersen conductance Σ_P. This property is expected to be enhanced, above background, by upward-directed field-aligned current (FAC). Prior to Nichols and Cowley (2004) M-I coupling modellers usually assumed that the Jovian thermosphere possessed a constant conductance throughout the region magnetically mapped to the middle magnetosphere. Nichols and Cowley (2004) used modelling results from Millward et al. (2002) to formulate an empirical model for the enhancement of Pedersen conductance due to FAC density (see Fig. 1.4). They found that their total radial current and plasma angular velocity profiles (in the magnetodisc) were consistent with observations by Galileo (Khurana 2001) (see Fig. 1.5a and b respectively). The agreement between model and observations was improved, compared to the case of modelling using a constant Pedersen conductance. The Nichols and Cowley (2004) model is used in our studies and is described in detail in section 3.3.1.

[2]By magnetospheric size we mean the size of the dayside magnetopause, which is the boundary between the planetary magnetic field and the solar wind.

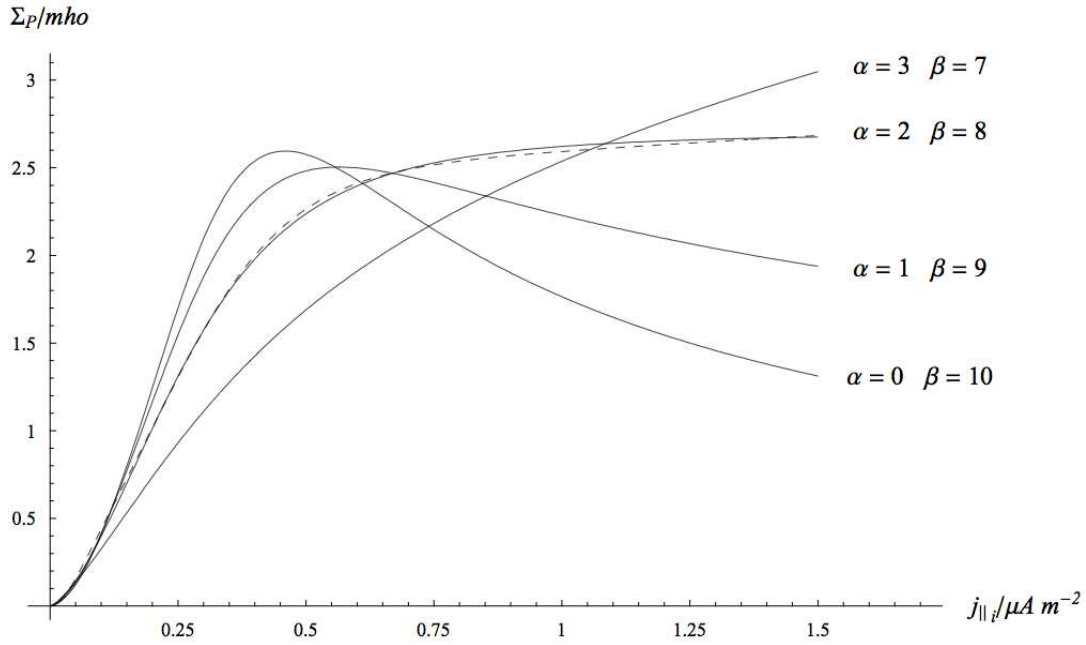

Figure 1.4. Height-integrated Pedersen conductance as a function of FAC density. The solid lines differentiate between four different auroral electron distributions functions based on modelling by Millward et al. (2002). The analytical formulation derived in Nichols and Cowley (2004) is indicated by the dashed line. Figure from Nichols and Cowley (2004).

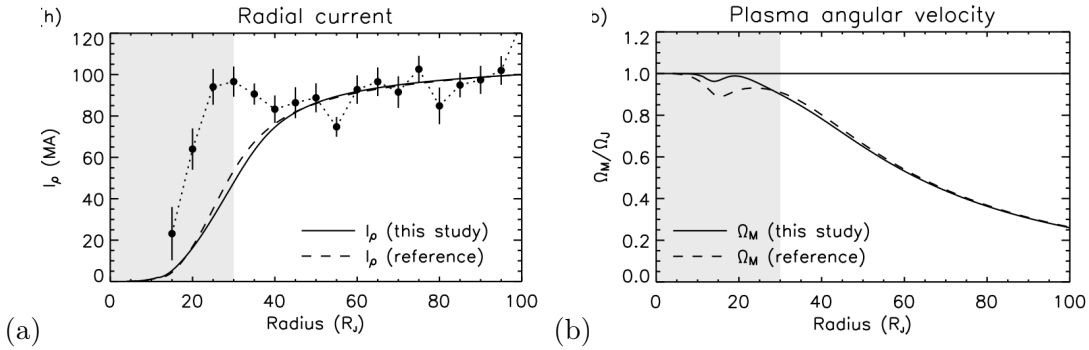

Figure 1.5. (a) Radial current as a function of equatorial distance from Jupiter. (b) Plasma angular velocity as a function of radial distance. Solid line Smith and Aylward (2009), dashed line (Nichols and Cowley 2004) and dots show Galileo magnetometer measurements (Khurana 2001). Plots from Smith and Aylward (2009).

Magnetosphere-ionosphere-thermosphere modelling

The thermospheric angular velocity at Jupiter partly controls the magnitude of the ionospheric Pedersen currents and thus the dynamics of the magnetosphere. We do not, however, have any direct measurements of these thermospheric velocities. Studies such as Huang and Hill (1989) and Pontius (1995) have attempted to model these velocities by coupling the magnetosphere, ionosphere and thermosphere, with the assumption that angular momentum was transported from the deep planetary atmosphere through the thermosphere solely by vertical viscous transport. These studies yielded two main conclusions: (i) the relationship between thermospheric and magnetospheric angular velocities was a linear one and (ii) thermospheric dynamics could be parameterised using an 'effective' ionospheric conductivity, which represented the effects of the difference ('slippage') between the angular velocity of the thermosphere and that of the deep atmosphere (i.e. planetary value). This resulted in a 'slippage' parameter K. The aforementioned studies took account of the thermosphere by using the effective Pedersen conductivity $\Sigma_P^* = (1-K)\Sigma_P$, with $K = 0.5$.

The only way to fully account for the thermosphere dynamics was to create a GCM for the Jovian system. Achilleos et al. (1998) created the first three-dimensional model of the Jovian ionosphere and thermosphere JIM (Jovian Ionosphere Model). JIM investigated the influence of solar radiation and auroral electron precipitation on the Jovian ionosphere and found that ions created in the auroral regions are transported outside the auroral region via strong winds ($\sim$600 ms^{-1}) caused by pressure gradients. These winds also transport heat both poleward and equatorward of the auroral regions. The JIM model was later used by Millward et al. (2002) to investigate the dependence of ionospheric conductivity on the flux of precipitating electrons and their initial energy flux. The relation between these parameters was not linear but the modelling showed that electrons with an energy of 60 keV were most efficient at ionising the thermosphere and that the dominant source of ionospheric conductivity was the H_3^+ ion. Work by Millward et al. (2005) resulted in a 'slippage' parameter profile that varied with altitude with a maximum of ~ 0.8 compared to the 0.5 used in the other M-I coupling studies discussed above.

Smith and Aylward (2009) expanded further on the current body of M-I models by combining the advanced middle magnetosphere model of Nichols and Cowley (2004) with

the axisymmetric model of the entire magnetosphere presented in Cowley et al. (2005). These magnetospheric inputs were then coupled to a global two-dimensional circulation model of the Jovian thermosphere. The auroral region in this coupled model is represented by the one-dimensional auroral thermosphere and ionosphere model by Grodent et al. (2001). This auroral profile is linearly scaled at each time step according to the global pattern of auroral conductance (see section 3.2 for more details). Their approach allowed for the self-consistent calculation of the Jovian thermospheric angular velocity, in a two-dimensional (axisymmetric) coupled M-I system which had reached a steady state. The study by Smith and Aylward (2009) produced some notable results:

i) Angular momentum transfer: meridional advection of momentum rather than vertical viscous transfer is the main process by which angular momentum is distributed to the high-latitude thermosphere. This is depicted schematically for Saturn in Fig. 1.6 but the same also applies for Jupiter.

ii) Thermospheric super-corotation: the thermosphere super-corotates (Ω_T=1.05 Ω_J) throughout those latitudes ($\sim$65$-$73 °) where it magnetically maps to radial distances of $\sim$6$-$25 R_J in the equatorial magnetosphere. In this region ion drag forces, that promote sub-corotation, are insignificant compared to Coriolis forces, that promote corotation. As ion drag tends to zero, neutral gas upwells, expanding and cooling adiabatically. This leads to a pressure gradient which drives poleward flows at altitudes less than 600 km (pressures higher than $\sim$ 0.04 μbar). Coriolis forces, unopposed by ion drag, can accelerate the gas to super-corotation. A force sketch showing the force balance for poleward flow (a), equatorward flow (b) and super-corotational (c) flow is shown in Fig. 1.7.

iii) Transport of heat: the simulated thermospheric winds show that two main cells of meridional flow develop (Achilleos et al. 2001), which cool lower latitudes ($\lesssim$75 °) whilst heating the polar regions ($\gtrsim$80 °) resulting in a polar 'hotspot'. These cells are: (i) A low-altitude ($<$ 600 km), poleward flow, and (ii) A high-altitude ($>$ 600 km) flow which is equatorward, joining with return flow (poleward) at lower altitudes. This means that all energy deposited at low altitude, where the Pedersen conducting layer is present, will be transported polewards. Smith et al. (2007) named this phenomena the 'ion drag fridge', and a sketch of this is shown in Fig. 1.8.

Tao et al. (2009) developed a coupled axisymmetric model of the Jovian thermosphere,

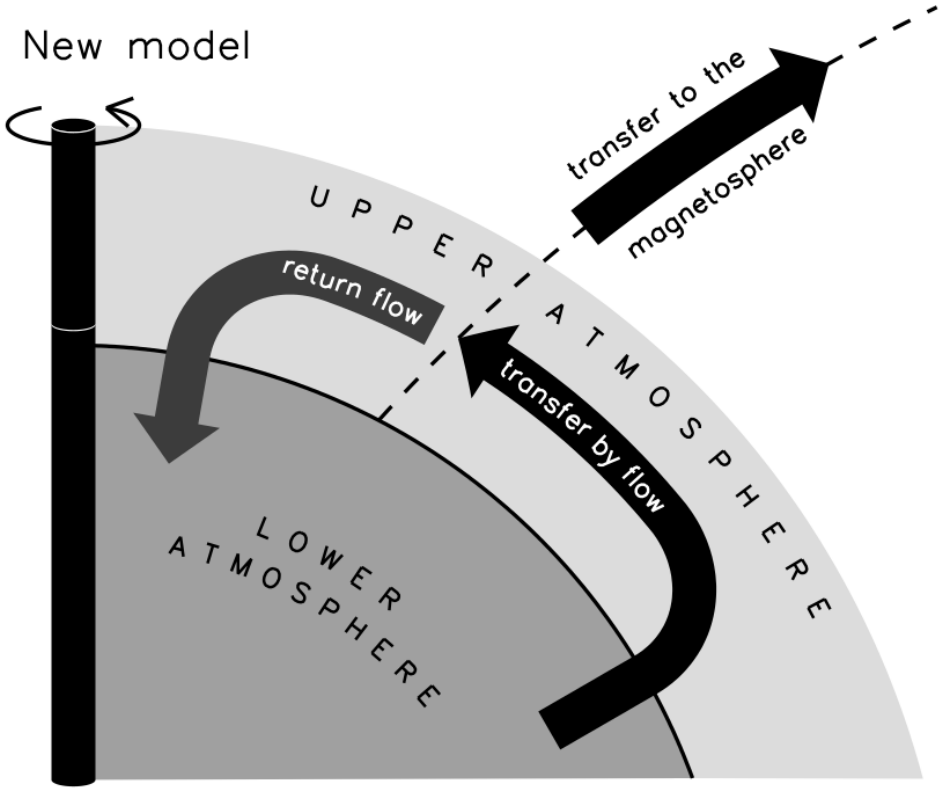

Figure 1.6. Schematic of angular momentum transport from the lower atmosphere to the thermosphere. Neutrals upwell at mid-latitudes and are transported polewards via meridional winds. They then transfer angular momentum to the magnetosphere via ion-neutral collisions before down-welling at the poles. Plot from Smith and Aylward (2008).

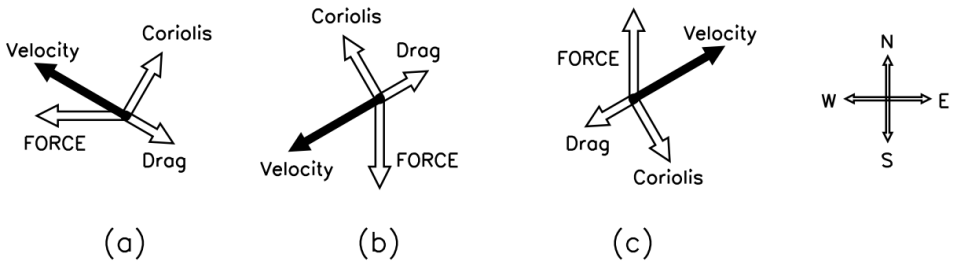

Figure 1.7. Schematic diagrams for possible force balance scenarios in the thermosphere. (a)-(c) show respectively sub-corotaional poleward flow, sub-corotaional equatorward flow and super-corotaional poleward flow. The FORCE arrow could represent ion drag in (a) and equatorwards and polewards pressure gradients respectively in (b) and (c). Plots from Smith (2006).

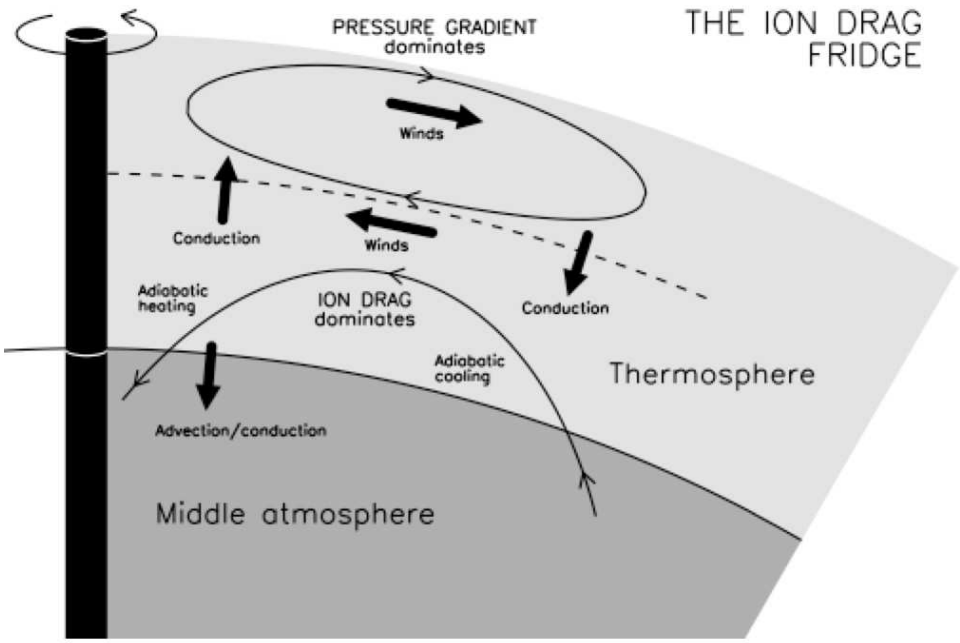

Figure 1.8. Schematic of the 'ion drag fridge'. Thin lines with arrows indicate neutral gas motion whilst the thick black arrows indicate flows of energy. The dashed line separates the high and low altitude regions of the thermosphere. Energy is deposited at low altitudes via Joule heating and this is transported polewards effectively cooling low/equatorial latitudes. Plot from Smith et al. (2007).

magnetosphere (Nichols and Cowley 2004) and auroral ionosphere. Qualitatively their results show similarities with the modelling of Smith and Aylward (2009). However, their M-I coupling currents have magnitudes which are at least a factor of two smaller than those in Smith and Aylward (2009); the total radial current being four times smaller than that measured in Khurana (2001). Fig. 1.9 shows Tao et al's neutral temperature distribution as a function of altitude and latitude. The black arrows indicate the direction of meridional flow. The temperature distribution is comparable to observations (discussed above) and significantly ($\sim 200-500\,\mathrm{K}$) larger than Smith and Aylward (2009) at lower latitudes. These differences in temperature can be attributed to their use of more heating and cooling terms such as sonic wave heating at low latitudes (Bougher et al. 2005) and IR cooling, as well as their use of an initially hot thermospheric temperature profile (see their Fig. 1a).

Yates et al. (2012) used the Smith and Aylward (2009) model to study the influence of solar wind pressure on the steady-state thermospheric flows of Jupiter. They found that ionospheric and magnetospheric currents, thermospheric powers, temperature and auroral

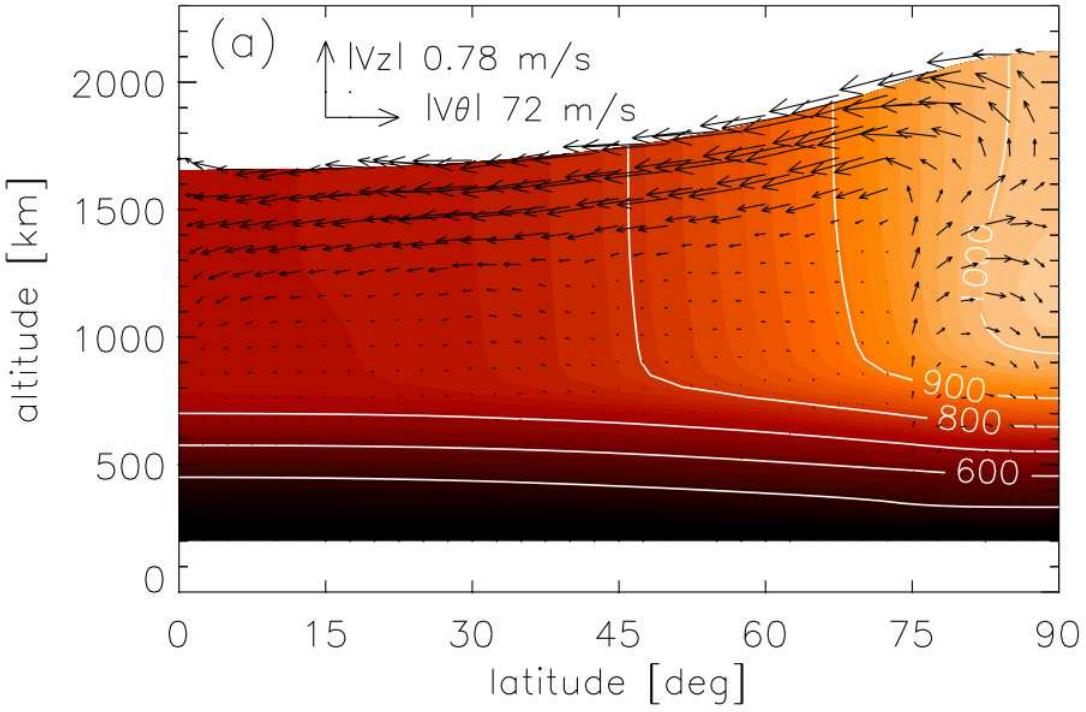

Figure 1.9. Latitude-altitude distribution of thermospheric temperature (magnitude indicated by white contours). The black arrows indicate the direction of meridional flow. Figure from Tao et al. (2009).

emission (a proxy for FAC) all showed an increase with decreasing solar wind dynamic pressure (from 0.213 nPa to 0.021 nPa (Joy et al. 2002) corresponding to a change in magnetodisc radius from 45 R_J to 85 R_J). In particular, ion drag (changes kinetic energy) and Joule heating (changes thermal energy) were shown to increase by $\lesssim$200 % (integrated power per hemisphere), which led to a corresponding $\sim$135 K increase in auroral thermospheric temperature. This work is discussed in Chapter 4 and concluded in section 7.1.

1.2.2 Transient modelling

Southwood and Kivelson (2001) predicted that, after a magnetospheric compression, there would be an increase in the degree of magnetospheric plasma corotation (i.e. the quantity $(\Omega_J - \Omega_M)$ would decrease), and this would consequently lead to a sizeable decrease in M-I coupling currents and auroral emission. They also argued that the reverse would be true for a magnetospheric expansion. Modelling by Cowley and Bunce (2003b); Cowley et al. (2007) and Yates et al. (2012) confirmed these predictions, provided the system is given enough time to achieve steady-state. On the other hand, the studies of Cowley and

Bunce (2003a,b); Cowley et al. (2007) simulated the short-term response of the system to very rapid ($\lesssim$3 hours) magnetospheric compressions and expansions. This short-term behaviour was found to exhibit very different properties to that of the steady state. For rapid compressions, the conservation of plasma angular momentum causes the magnetosphere to super-corotate compared to the planet and thermosphere. The flow shear between the thermosphere and magnetosphere, represented by $(\Omega_T - \Omega_M)$, is now negative and leads to current reversals at co-latitudes that are magnetically mapped to the middle and outer magnetospheres ($\sim$10$-$17 °). Negative flow shear also causes energy to be transferred from the magnetosphere to thermosphere; in contrast to the steady-state, where energy is transferred from the thermosphere to the magnetosphere, in order to accelerate magnetospheric plasma towards corotation. For transient expansions, Cowley et al. (2007) showed that Ω_M decreases but the flow shear increases, leading to a $\sim$500 % increase in the intensity of M-I currents (for an expansion from a dayside magnetopause radius of 45 R_J to 85 R_J).

Cowley et al. (2007) also modelled the auroral response to transient compression and expansion events. Cowley et al. (2007) found that the precipitating electron energy flux ($\sim$10 % of which is used to produce ultraviolet (UV) aurora) increases by two orders of magnitude at the open-closed field line boundary and decreases by $\sim$50 % at the 'main auroral oval' during an event where the magnetopause moves inward from 85 to 45 R_J. Essentially the opposite occurs for an expansion event: main oval emission increases by a factor of 30 whilst emission at the open-closed boundary is reduced to $\sim$2 % of its steady-state value.

M-I coupling models by Achilleos et al. (1998); Smith and Aylward (2009); Tao et al. (2009); Yates et al. (2012) have all discussed steady-state heating and cooling terms in the Jovian thermosphere. Cowley et al. (2007) discussed 'transient' heating in terms of power dissipated into the thermosphere via Joule heating and ion drag, as well as, power used to accelerate magnetospheric plasma. They found for compressions (40 R_J displacement of the Jovian model magnetopause), a net transfer of power from magnetosphere to planet of $\sim$325 TW due to the super-corotation of magnetospheric plasma. For expansions, they found that the power dissipated in the thermosphere and used to accelerate magnetospheric plasma increased by a factor of $\sim$2.5 , resulting from the large increase in flow shear between the magnetosphere and thermosphere.

Millward et al. (2005) used JIM to investigate M-I coupling by varying the equatorial voltage V_E in the auroral region from 0 to 3 MV (corresponding to electric fields of 0 to 0.6 V m^{-1}). They ran JIM from the same starting configuration but with different values of V_E and noted the difference in temperature, and ion and neutral velocities between the two runs. Their results for the Northern hemisphere are shown in Fig. 1.10, which shows (a) ion velocities for $V_E = 3$ MV and (b-d), neutral velocities and the temperature difference between $V_E = 3$ MV and $V_E = 0$ at times of 27 , 53 and 160 minutes respectively. They conclude that ion velocities respond instantaneously to changes in the electric field, whilst the response of neutral velocities and temperature (via Joule heating) is slower. The neutral zonal velocities are estimated to fully respond to the electric field changes in ∼45 minutes (Millward et al. 2005). It can also be seen that as the simulation evolves with time the temperature in the polar region increases. This increase results from the poleward transport of heat by neutral winds.

1.3 Jovian aurora

The aurora is the light emitted when precipitating energetic particles collide with a planet's atmosphere. All magnetised planets with significant atmospheres will have aurora. Jupiter's UV aurora was first detected with the UVS instrument onboard Voyagers 1 and 2 (Broadfoot et al. 1979; Sandel et al. 1979) and is emitted by H_2 and H (e.g. Clarke et al. (1980)). An example of the Jovian UV aurora is shown in Fig. 1.11, which shows the three different types of features: i) polar emission, ii) main oval and iii) emission from moon interactions. Jovian IR aurora also exists and is emitted by H_3^+ (Drossart et al. (1989); discussed in section 1.1.1). There are numerous published studies on the Jovian aurora. As this thesis is primarily concerned with thermospheric modelling, we will only summarise some of the latest auroral observational studies. For a more comprehensive discussion on the Jovian aurora the reader is referred to Clarke et al. (2004).

HST-STIS observations of Jupiter presented in Grodent et al. (2003a) resulted in the definition of new auroral reference ovals (the spatial loci of the main rings of emission). They also noted that the morphology of the oval is fixed in System-III longitude and persistent in time (at least ∼5 years). Large-scale changes in auroral morphology were detected (e.g. Bonfond et al. (2012)); the main oval was seen to contract by $2 \pm 0.8\,^\circ$ whilst its

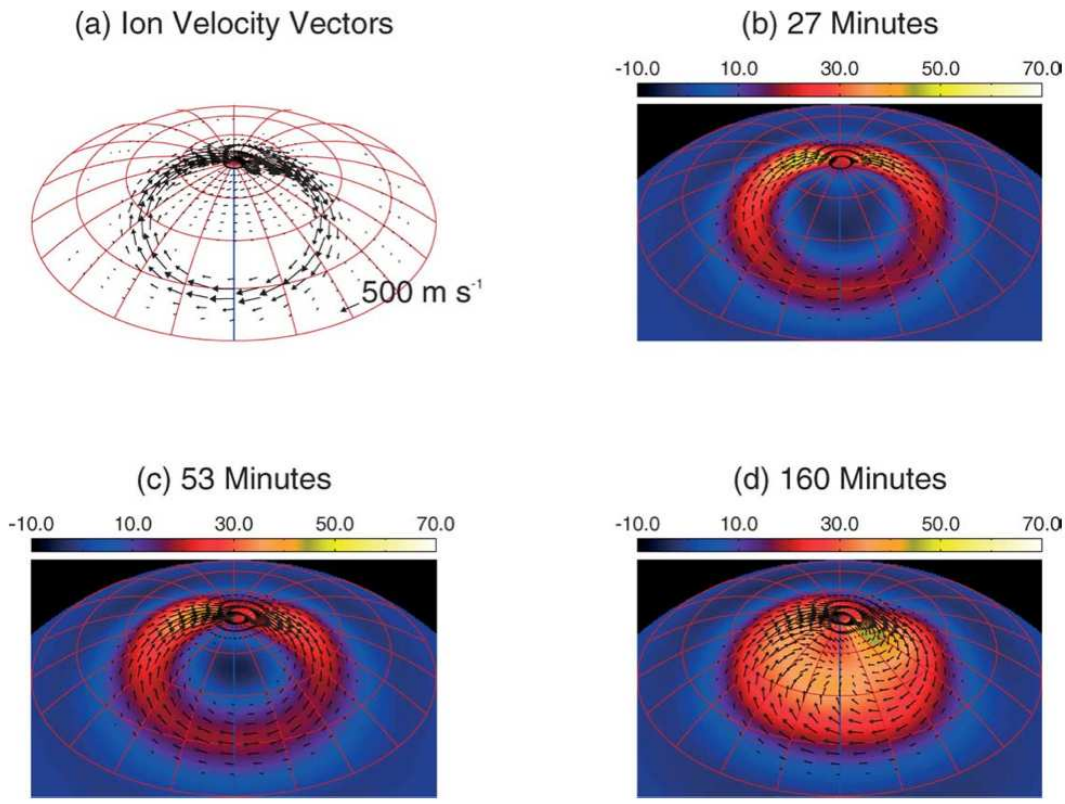

Figure 1.10. Shows the latitude-longitude distribution of the change in thermospheric temperature (magnitude indicated by colour bar) between the case where the trans-auroral voltage $V_E = 0$ and 3 MV at times indicated. (a) Ion velocity vectors for V_E =3 MV; (b) temperature difference at 27 minutes with neutral wind vectors; (c) same as (b) but at 53 minutes; (d) at 160 minutes. Figure from Millward et al. (2005).

brightness increased by a factor-of-two to 1 MR. The Cassini spacecraft detected a coincident increase in solar wind density from $\leq$0.2 cm^{-3} to $\sim$1 cm^{-3} but it was not possible to determine whether the increase in emission and oval constriction was caused by a rapid magnetospheric compression or expansion as long-term monitoring of the size of the Jovian magnetosphere was not available. The same HST images were subsequently analysed in Grodent et al. (2003b); Nichols et al. (2007). Nichols et al. (2007) confirmed that the event was caused by a modest compression, although they concluded that the main oval's location remained essentially unchanged (within the errors). They also note that the observations suggest that rapid compressions cause a significant increase in auroral emission, contradictory to previous theory and modelling (Southwood and Kivelson 2001; Cowley and Bunce 2001, 2003a,b). However, this conclusion assumes that the entire event can be thought of as a single compression and not as a series of more transient events ($\leq$ 2 hours).

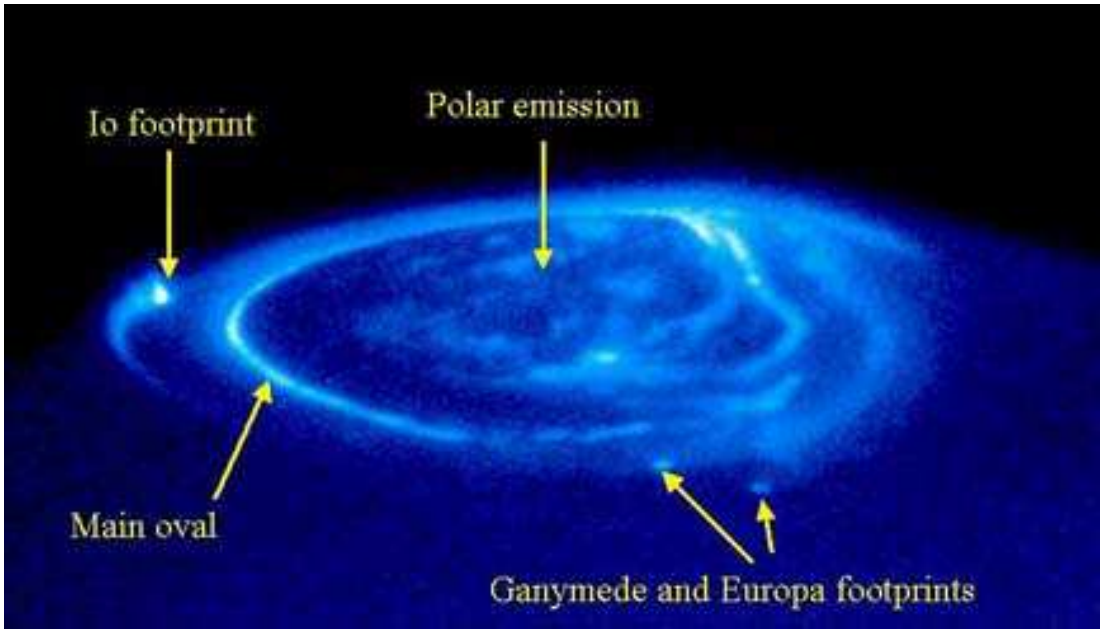

Figure 1.11. Jupiter's Northern UV aurora showing polar emission, the main oval and moon footprints. Image courtesy of J. Clarke and NASA.

From the above discussions it can clearly be seen that simultaneous solar wind data and images of Jupiter's aurora are needed in order to accurately infer the solar wind's influence on the aurora, as was done during the observational campaign by Clarke et al. (2009). Observations of the aurora were obtained using the HST and solar wind data were propagated to Jupiter (and Saturn) from 1 AU and also measured in situ at Jupiter using the New Horizons spacecraft. Clarke et al. (2009) show a factor-of-two increase in total UV auroral power, near the arrival of a solar wind compression region, typically corresponding to an increase in solar wind dynamic pressure of $\sim 0.01-0.3$ nPa. Furthermore, Nichols et al. (2009) showed, using the same HST images, that this increase in auroral emission consists of approximately equal contributions from the so-called main oval and the high-latitude polar emission. Nichols et al. (2009) also demonstrated that the location of the main oval shifted polewards by $\sim 1^\circ$ in response to solar wind pressure increase of an order of magnitude. For a rarefaction region in the upstream solar wind, comprising an order-of-magnitude decrease in solar wind pressure, Clarke et al. (2009) observed little, if any, change in auroral emission. The seemingly indifferent response of the Jovian aurora to solar wind rarefactions is not expected from past theoretical and modelling studies (e.g. Southwood and Kivelson (2001); Cowley et al. (2007)) but could be accounted for

by the long time scale of these rarefactions compared to the shocked regions of solar wind (order-of-magnitude decrease in solar wind pressure occurring over several days instead of 'instantly' like the shocks). The magnetospheric reconfiguration being less dramatic would allow more time for quasi steady-state dynamics to be established and a correspondingly weaker auroral response. The authors also note that, whilst solar wind did influence some Jovian auroral processes, there are others, such as auroral dawn storms, that showed no correlation to solar wind and must thus have some other driving source.

Auroral emission models were developed to understand the auroral ionosphere and its influence on the Jovian thermosphere. Two such models have been presented in Grodent et al. (2001) (for Jupiter) and in Tao et al. (2011) (for Jupiter and Saturn). The Grodent et al. (2001) model is one-dimensional and uses two streams of auroral electrons to investigate the correlation between auroral heating and the vertical temperature profile of Jupiter's thermosphere. They use two electron streams (energy distributions) to reproduce the discrete and diffuse aurora. They find that their model needs a non-particle heating source to balance the hydrocarbon cooling below the homopause ($\sim$2 μbar). The Grodent et al. (2001) auroral model forms one portion of the coupled model used in this thesis and is discussed in more detail in section 3.2. A more recent auroral emission model, developed by Tao et al. (2011), simulated the dependence of UV and IR auroral emission on precipitating auroral electrons. They find that UV auroral intensity is proportional to the incident electron energy flux, whilst IR auroral intensity is proportional to the square root of the electron energy flux. The UV emission is found to increase with electron energy whilst IR emission increases with energy up to 10 keV where it then decreases with increasing energy.

1.4 Time scales of the Jovian system

Variations in magnetic field, plasma angular velocity and thermospheric flow patterns due to changes in solar wind dynamic pressure present challenges for modelling the Jovian system. Various time-scales, such as those associated with M-I coupling, compression or expansion of the magnetosphere and thermospheric response, need to be considered. The studies by Nishida and Watanabe (1981); Watanabe and Nishida (1982); Cowley and Bunce (2003a,b) and Cowley et al. (2007) are among the few to have addressed these issues, using

the simplifying approximations discussed hereafter.

i) Compression (and expansion) of the magnetosphere: Large changes in magnetopause (R_{MP}) size ($\sim$40 R_J) can occur when the Jovian magnetosphere encounters a sudden change in solar wind dynamic pressure (typically an order of magnitude e.g. from 0.01 − 0.1 nPa), such as would be caused by a Coronal Mass Ejection (CME) or a Corotating Interaction Region (CIR). Cowley and Bunce (2003a) and Cowley et al. (2007) considered compressions (and expansions) occurring over $\sim$2−3 hours. This time scale τ_{MP}, was computed using an assumed solar wind velocity of $v_{sw} = 500\,\mathrm{km\,s^{-1}}$ and an assumed change in solar wind dynamic pressure from $p_{swi} = 0.06$ nPa to $p_{swf} = 0.6$ nPa. Using these values and the following equations (Huddleston et al. 1998; Cowley and Bunce 2003a):

$$R_{MP} \approx \frac{35.5}{p_{sw}^{0.22}(nPa)} R_J, \tag{1.1}$$

$$\tau_{MP} \approx \frac{\Delta R_{MP}}{\alpha v_{sw}}, \tag{1.2}$$

where $\alpha = \left(1 - (p_{swi}/p_{swf})^{1/2}\right)$, it can be shown that τ_{MP} is $\sim$ 2.2 hours.

ii) M-I coupling time scale: Ion-neutral collisions in the neutral atmosphere transfers angular momentum to the magnetosphere by means of electric currents which flow along magnetic field lines. These currents flow radially in the equatorial plasmasheet, and accelerate the radially outflowing magnetospheric plasma towards planetary corotation. The time-scale on which this angular momentum is transferred has been estimated by Cowley and Bunce (2003a) to generally be $\sim$5−20 hours. This result applies to the so-called middle magnetosphere region (radial distances $\sim 10 - 50\,R_J$). Similar results have been obtained by Vasyliunas (1994). The conservation of plasma angular momentum can be assumed provided this M-I coupling time scale is long compared to the compression/expansion time scale discussed in *i)*.

iii) Thermospheric response time: The thermosphere and magnetosphere are coupled together via ion-neutral collisions in the ionosphere. A change in plasma angular velocity in the magnetosphere would cause a corresponding change in the thermosphere's effective angular velocity. Recent studies investigating the thermospheric response are generally

divided into two scenarios: (i) A system where the thermosphere responds promptly, on the order of a few tens of minutes (Millward et al. 2005), and (ii) a system where the thermosphere responds on the order of two days and, as such, is essentially unresponsive to transient events (Gong 2005). As in Millward et al. (2005), we make no a priori assumption about the thermospheric response. We simply allow the GCM which we employ to react to the imposed changes in plasma angular velocity assumed for the transient compressions and expansions. Our approach differs slightly from that in Millward et al. (2005); they impose changes in the ionospheric equatorward electric field whilst we change the size of the magnetosphere, and self-consistently compute the corresponding changes in auroral current and the ionospheric electric field.

Cowley and Bunce (2003a); Cowley et al. (2007) discuss other time scales of interest, such as (a) the communication time between the magnetosphere and ionosphere (mediated by the Alfvén waves), (b) the re-establishment of steady state conditions and (c) the radial diffusion of magnetodisc plasma. The latter two are of the same order, and Cowley and Bunce (2003a) estimate them to be $\sim 1-2$ days. The communication time between the magnetosphere and ionosphere is dependent on the Alfvén speed. Watanabe and Nishida (1982) estimate this communication time to be $\sim$ 6 minutes compared to 26 s (at 20 R_J) and 18 minutes (at 80 R_J) determined by Cowley and Bunce (2003a). The Alfvén wave travel time suggests that the magnetosphere and ionosphere remain in full communication throughout the magnetospheric compression/expansion events which occur on the $\sim 2-3$ hour times discussed above (and supported by the modelling of Millward et al. (2005)); implying that the Pedersen current would rapidly respond to the imposed magnetospheric reconfigurations. This conclusion follows since the Alfvén travel time is also the time scale at which M-I coupling currents are established.

1.5 Aim of the thesis

The Jovian system is an interesting and complex one. As discussed above there is one particular issue regarding its thermosphere that has perplexed planetary scientists for almost two generations: the 'energy crisis'. The auroral thermosphere is $\sim$ 700 K hotter than predicted if solar radiation were the sole source of energy to the system. This crisis is not restricted to the Jovian system but common to all the Gas Giants (Saturn, Uranus and

Neptune). In this introduction we have discussed numerous observations supporting high Jovian thermospheric temperatures and various mechanisms proposed as solutions to the issue. Unfortunately, none to this day have definitively solved the 'energy crisis'.

In this thesis we set out to, as many have before, address this issue. We employ a simplified model of the Jovian magnetosphere (Nichols and Cowley 2004; Cowley et al. 2005) and auroral ionosphere (Grodent et al. 2001) coupled to a two-dimensional general circulation model representing the Jovian thermosphere (Smith and Aylward 2009). We proceed to investigate how the solar wind influences Jovian thermospheric dynamics and heating by modelling the response of the thermosphere to assumed changes in solar wind parameters. We firstly consider the different steady states of the system for several different solar wind pressures. Following this initial study, we then examine the time-dependent response of the thermosphere and aurorae to "pulses" of solar wind pressure, designed to simulate changes in this parameter on $\sim 2-3$ hour time scale.

The scientific background necessary to our studies is discussed in Chapter 2 whilst our coupled magnetosphere-ionosphere-thermosphere model is presented in Chapter 3. We present our steady state modelling in Chapter 4, transient state thermospheric dynamics in Chapter 5 and transient thermospheric heating in Chapter 6. We conclude and suggest potential future studies in Chapter 7.

This page was intentionally left blank

Chapter 2

Scientific Background

We can't solve problems by using the same kind of thinking we used when we created them.

Albert Einstein

In this chapter we present and discuss some of the scientific background required for the the studies in Chapters 4 - 6.

2.1 Magnetospheres and plasmas

Magnetospheres can be thought of as magnetic 'shields' that protect magnetised planets from extra-planetary radiation, such as particles from the solar wind or cosmic rays. The magnetic field within the magnetosphere is due to two sources: i) The dipole-like internal field of the planet, generated in the deep interior; ii) External sources of currents, such as planetary ring currents and magnetopause currents. In reality, magnetospheric fields are rarely purely dipolar as they are usually deformed by the solar wind flow and by plasma sources which may exist within the magnetosphere itself. Plasma can enter the magnetosphere either from the solar wind, planetary ionosphere or an internal plasma source such as a volcanic moon (e.g. Io, in the case of Jupiter). Fig. 2.1 shows a schematic of Jupiter's magnetosphere; black solid lines represent magnetic field lines, thick black dashed lines show currents and thin black dashed lines outline the magnetodisc region. The moon Io is also shown. This Figure shows how the Jovian magnetic field lines are stretched out, into

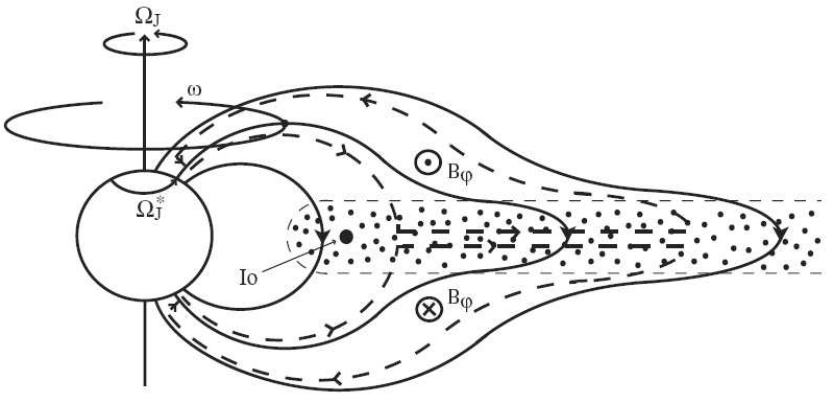

Figure 2.1. Schematic of Jupiter's magnetosphere showing the magnetic field lines (solid lines) and the currents (dashed lines). The magnetodisc is also shown and enclosed by the thin dashed lines. From Cowley and Bunce (2001).

a disc-like structure beyond Io's orbit, resulting from the large amount of erupted material from Io which is subsequently ionised. The Jovian magnetosphere is discussed further in section 2.1.4.

This thesis is mainly concerned with upper atmospheric phenomena related to magnetospheric reconfigurations and thus uses relatively simple analytical models for the structure of the Jovian magnetosphere. As such, we will give a brief overview regarding the magnetospheric and plasma physics which are important for formulating these model inputs.

2.1.1 Basic plasma properties

Plasma motion

The majority of planets in our solar system are magnetised. It is thus useful to consider how charged particles behave within electromagnetic fields. These particles, having generally non-zero temperatures, also undergo thermal motions. In the presence of magnetic and/or electric fields, they are influenced by the Lorentz force $\boldsymbol{F}$, given by

$$\boldsymbol{F} = q\,(\boldsymbol{E} + \boldsymbol{u} \times \boldsymbol{B}), \tag{2.1}$$

where q is the particle's charge, $\boldsymbol{u}$ is the velocity, $\boldsymbol{E}$ and $\boldsymbol{B}$ are the electric and magnetic fields respectively. If we let $\boldsymbol{E}$=0 and assume that $\boldsymbol{B}$ is uniform and directed along $\hat{\boldsymbol{z}}$,

Eq. (2.1) shows that the motion of the charged particle (ion or electron) will be circular in the x-y plane with a characteristic cyclotron or Larmor frequency Ω_c:

$$\Omega_c = \frac{|q|B}{m}, \tag{2.2}$$

where m is the mass of the ion or electron. The radius of this circle is:

$$\rho_c = \frac{v_\perp}{\Omega_c} = \frac{mv_\perp}{|q|B}, \tag{2.3}$$

where ρ_c is known as the cyclotron or Larmor radius and $v_\perp$ is the velocity perpendicular to the magnetic field. If the velocity component parallel to $\boldsymbol{B}$, $v_\parallel$, is non-zero then the particle will move along the magnetic field lines in a helical trajectory (see Fig. 2.2a); in a left-hand (LH) sense for positively charged particles and a right-hand (RH) sense for negatively charged ones (see Fig. 2.2b). As the magnetic force is always perpendicular to particle motion, it does no work on the particle, whose speed thus remains constant.

Plasma motion can also be influenced by other forces, such as gravity and the electrostatic force. Suppose that a uniform external force $\boldsymbol{F}$ is added to the uniform magnetic field discussed above. Now, let us only consider the motion perpendicular to $\boldsymbol{B}$, described by the perpendicular velocity $\boldsymbol{v}_\perp$. This velocity can be thought of as a combination of a 'cyclic' velocity (due to $\boldsymbol{B}$) and of a constant drift velocity $\boldsymbol{v_F}$ arising from the presence of $\boldsymbol{F}$.

$$\boldsymbol{v_F} = \frac{\boldsymbol{F} \times \boldsymbol{B}}{qB^2}. \tag{2.4}$$

This drift velocity describes the motion of the 'guiding centre' of the particle. The force $\boldsymbol{F}$ will increase the natural Larmor radius for half of a circular particle orbit, and decrease it for the other half. This results in a small perpendicular drift described by $\boldsymbol{v_F}$ which can, in some cases, cause currents to flow.

Let us now consider the effect of adding a uniform electric field to the uniform magnetic

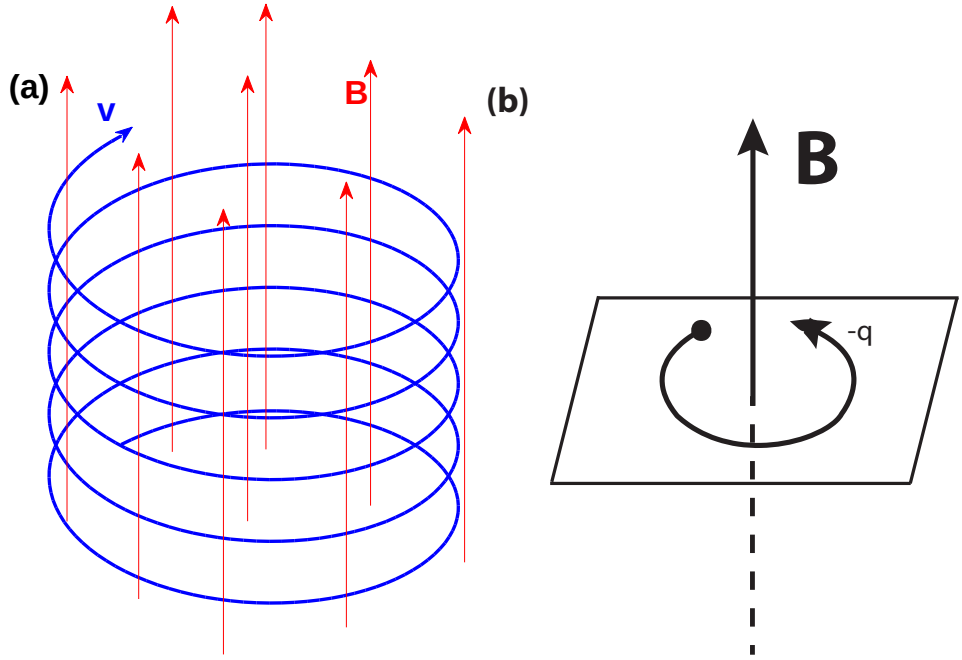

Figure 2.2. The motion of a charged particle in a uniform magnetic field. (a) for a positively charged particle with both perpendicular and parallel velocity components. (b) for a negatively charged particle with only a perpendicular component of velocity (Image credit: Jeshua Yates).

field discussed above. The formalism is essentially the same as that of motion under a general force $\boldsymbol{F}$ discussed above. However, the electric field creates an equivalent electrostatic force $\boldsymbol{F_E}$ given by

$$\boldsymbol{F_E} = q\boldsymbol{E}. \tag{2.5}$$

Placing $\boldsymbol{F_E}$ in Eq. (2.4) gives

$$\boldsymbol{v_E} = \frac{\boldsymbol{E} \times \boldsymbol{B}}{B^2}. \tag{2.6}$$

where $\boldsymbol{v_E}$ is the drift velocity due to an electric field with a component perpendicular to the magnetic field. Note that $\boldsymbol{v_E}$ is independent of charge and mass, meaning no drift currents are created as both positive and negative charges drift at the same velocity $\boldsymbol{v_E}$. Fig. 2.3 shows the motion of a positively charged ion in a uniform electric and magnetic field where the effect of $\boldsymbol{v_E}$ can clearly be seen.

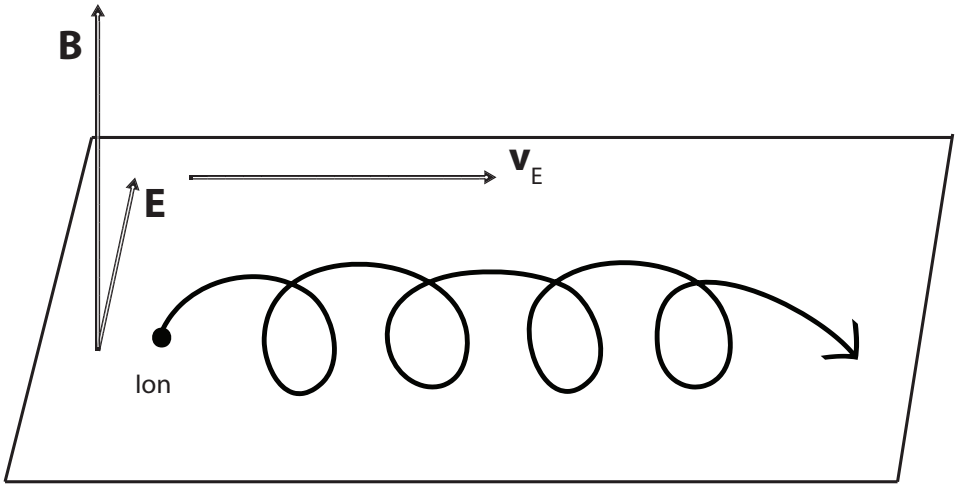

Figure 2.3. The motion of a positively charged ion in a uniform electric field. Image credit: Jeshua Yates.

2.1.2 Magnetohydrodynamics

As space plasma is essentially a quasi-neutral, ionised gas, its macroscopic properties and motion can be described through a combination of hydrodynamic and electromagnetic theory. This creates the field of Magnetohydrodynamics (MHD). MHD is an approximation valid only under the following conditions: i) length scales of plasma pressure and electromagnetic field gradients are large compared to characteristic microscopic scales (i.e. particle gyration, Debye length), ii) time scales of the processes being modelled are long compared to characteristic plasma oscillations and periods (e.g. gyroperiod, plasma frequency).

MHD combines the hydrodynamic equations of momentum, energy and mass continuity with the governing equations of electromagnetism known as Maxwell's equations. The Maxwell equations are shown below in their differential form:

$$\boldsymbol{\nabla} \cdot \boldsymbol{E} = \frac{\rho_q}{\epsilon_0}, \tag{2.7}$$

$$\frac{\partial \boldsymbol{B}}{\partial t} = -\boldsymbol{\nabla} \times \boldsymbol{E}, \tag{2.8}$$

$$\boldsymbol{\nabla} \times \boldsymbol{B} = \mu_0 \left(\boldsymbol{j} + \epsilon_0 \frac{\partial \boldsymbol{E}}{\partial t} \right), \tag{2.9}$$

$$\boldsymbol{\nabla} \cdot \boldsymbol{B} = 0, \tag{2.10}$$

$$\frac{\partial \rho_q}{\partial t} + \boldsymbol{\nabla} \cdot \boldsymbol{j} = 0. \tag{2.11}$$

ρ_q is the charge density, ϵ_0 is the permittivity of free space, μ_0 is the permeability of free space and $\boldsymbol{j}$ is the current density. Eq. (2.7) is the Poisson equation representing Gauss' Law, Eq. (2.8) is the Faraday's law relating time-varying magnetic fields with spatially varying electric fields, Eq. (2.9) is Ampère's Law which relates the magnetic field with the current density and Eq. (2.10) is the requirement of the magnetic field - to be divergence-less. Eq. (2.11) is a statement on current continuity - which means that the total charge in a system must be conserved in the absence of sources and sinks (e.g. chemical reactions).

Once the above approximations are taken into account, one can show that terms involving the charge density or derivatives (temporal or spatial) of the electric field are negligibly small and can generally be removed from the Maxwell equations in the MHD regime. Below is a list of the Maxwell equations appropriate for the 'MHD regime'. Note that Eqs. (2.8 and 2.10) remain unchanged and Eq. (2.7) is removed as both terms are very small.

$$\frac{\partial \boldsymbol{B}}{\partial t} = -\boldsymbol{\nabla} \times \boldsymbol{E},$$

$$\boldsymbol{\nabla} \times \boldsymbol{B} = \mu_0 \boldsymbol{j}, \tag{2.12}$$

$$\boldsymbol{\nabla} \cdot \boldsymbol{B} = 0,$$

$$\boldsymbol{\nabla} \cdot \boldsymbol{j} = 0. \tag{2.13}$$

One of the main results of the MHD modifications is that represented by Eq. (2.13). This equation implies that in an MHD approximation all currents must close. Another important component of MHD theory is the generalised version of Ohm's Law which gives the required current density in terms of the electric and magnetic fields:

$$\boldsymbol{j} = \sigma\,(\boldsymbol{E} + \boldsymbol{u} \times \boldsymbol{B}), \tag{2.14}$$

where σ is the conductivity of the MHD plasma and $\boldsymbol{u}$ is the bulk velocity of the plasma. If σ is large enough, as can be assumed when the plasma is (near-) collisionless, the above form of Ohm's Law can be expressed as

$$\boldsymbol{E} + \boldsymbol{u} \times \boldsymbol{B} = 0. \tag{2.15}$$

This leads to Alfvén's theory of frozen-in flux, which states that *the magnetic flux through a closed loop, co-moving with an infinitely conducting fluid, remains constant with time* (Alfvén 1956). This closed loop and the constant flux it contains can be thought of as the cross section of a 'bundle' of field lines known as a flux tube.

2.1.3 The solar wind

The solar wind is a stream of charged particles, originating from the Sun. They possess sufficiently high kinetic energy allowing them to escape the Sun's gravity at supersonic speeds. Pressure associated with the solar wind stream is balanced by the pressure of the Local InterStellar Medium (LISM) at distances of $100{-}150\,\mathrm{AU}$[1] from the Sun, forming the Heliosphere.

Solar wind variation occurs on all time scales including that of the solar cycle, which is an 11-year cycle of activity where the Sun goes from a period of high activity (Solar maximum) to low activity (Solar minimum). Solar activity is usually represented by the sunspot number as depicted in Fig. 2.4. The solar wind is found to possess two 'streams'; a 'fast' ($\sim 750\,\mathrm{km\,s^{-1}}$) stream and a 'slow' ($\sim 400\,\mathrm{km\,s^{-1}}$) stream. The fast solar wind originates from open field regions and coronal holes (generally at high/polar heliospheric latitudes) whilst the slow solar wind originates from the closed field regions in the equator and is denser than the fast solar wind. The amount of fast and slow solar wind is partly dependent on the solar cycle; at solar minimum there are coronal holes which extend even

[1] 1 AU = 149.6x10^6 km and is the mean distance from the Sun to the Earth.

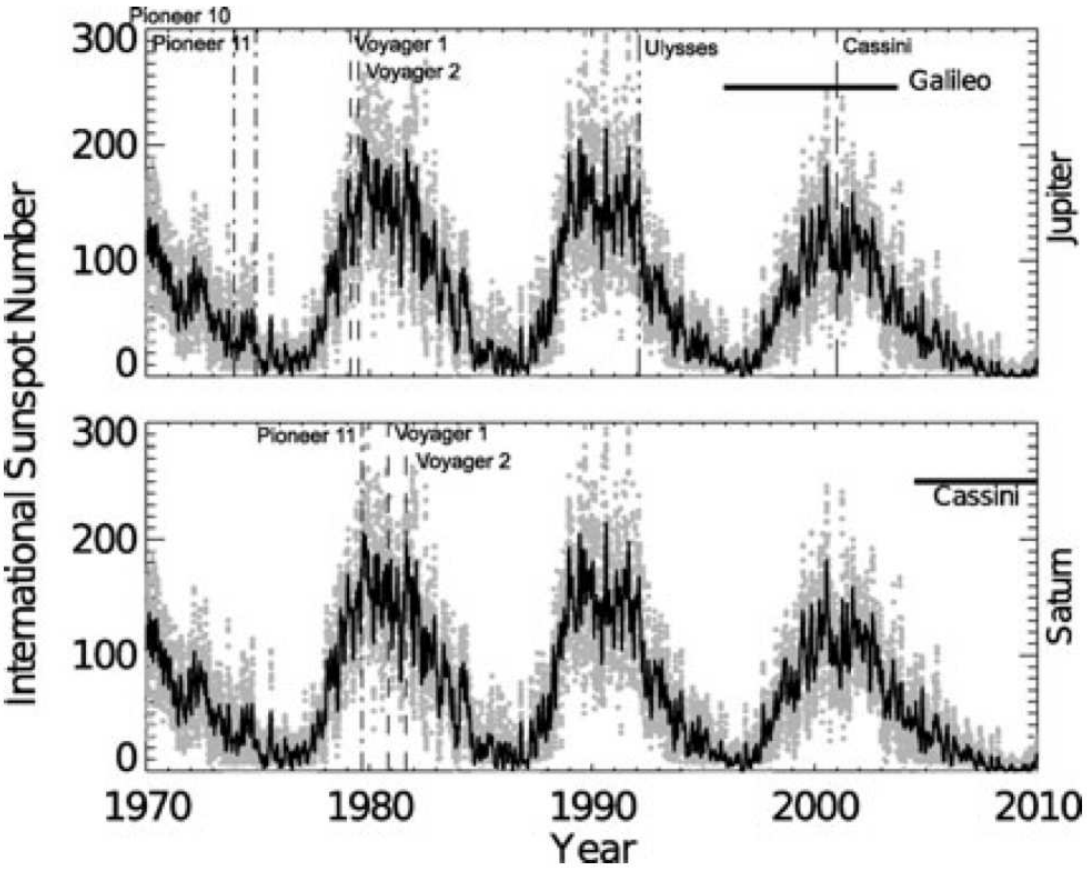

Figure 2.4. Figure showing sunspot number from 1970 – 2010. The grey dots show sunspot numbers from the Solar Influences Data Analysis Centre (SIDC) whilst the black lines show the average values over a solar rotation. The top panel indicates sunspot number as well as the closest approach times of various spacecraft visiting the Jovian system whilst the bottom panel shows the same as the top but for the Kronian system. This figure was obtained from Jackman and Arridge (2011).

to low latitudes along with the closed field regions of the equator (Kunow 2000).

Fast and slow solar wind inevitably interact with each other creating shock/compression regions where the fast stream catches up to the leading slow stream and rarefaction regions following the compressed regions where the fast stream is leading the subsequent slow stream. This interaction forms Corotating Interaction Regions (CIRs), which are spirals of compressed solar wind aligned with the Parker spiral (Parker 1958) between 2 – 3 and 20 AU and rotating with the Sun[2]. A schematic of the creation of CIRs can be seen in Fig. 2.5. During periods near (declining phase of solar cycle) and at Solar minimum

[2]The Sun's equatorial rotation rate is 25.38 days.

CIRs are the dominant structures in the heliosphere (Kunow 2000). As these high pressure (compressed) regions propagate throughout the solar system they will encounter the magnetic fields of magnetised planets like Jupiter; planetary magnetospheres will react to this increase in solar wind dynamic pressure by shrinking in size (being compressed) with the arrival of the solar wind compressed region or with the arrival of a rarefaction region, the magnetosphere will expand (the pressure balance which determines the size of planetary magnetospheres is discussed in section 2.1.4).

Other types of shocks exist in the solar wind, one such is called a Coronal Mass Ejection (CME). CMEs consist of a large release of electromagnetic energy and mass from the solar corona. Their speed can range from $10 - 2000\,\mathrm{km\,s^{-1}}$ with an average of $400\,\mathrm{km\,s^{-1}}$ (Low 2000). Shocks in the solar wind can develop in a similar way to CIRs; fast CMEs compress the slow solar wind in front of them or vice versa where slow CMEs are compressed from behind by the faster solar wind. Such shock may result in reconfigurations of planetary magnetospheres but at the distance of Jupiter, the influence of CIRs is far more dominant. The occurrence frequency of CMEs is correlated to the solar cycle: at solar minimum there is one CME every few days whilst at solar maximum there are about three per day.

2.1.4 The Jovian magnetosphere

The Jovian magnetosphere differs significantly from that of the Earth. Jupiter has the largest magnetic moment of all the magnetised planets in the solar system (20000 times that of the Earth). Consequently, the Jovian magnetosphere is the largest object in the solar system - quite befitting the king of planets. Unlike the Earth's magnetosphere, the Jovian one is mainly driven by internal processes and not by the solar wind. These internal processes consist of *i)* its rapid planetary rotation rate and *ii)* the major source of plasma from the moon Io's volcanism (e.g. Bagenal and Sullivan (1981)).

Inner and Middle Magnetosphere

The inner magnetosphere spans up to $\sim 10\,\mathrm{R_J}$ from Jupiter and encompasses Io's orbit. Io ejects large amounts of sulphur dioxide gas into its local environment (an orbit of $\sim 6\,\mathrm{R_J}$ from Jupiter). The ejected neutral gas forms a torus in the equatorial plane of the inner magnetosphere. Around 500–$1000\,\mathrm{kg\,s^{-1}}$ (Kivelson et al. 2004) of this gas is ionised,

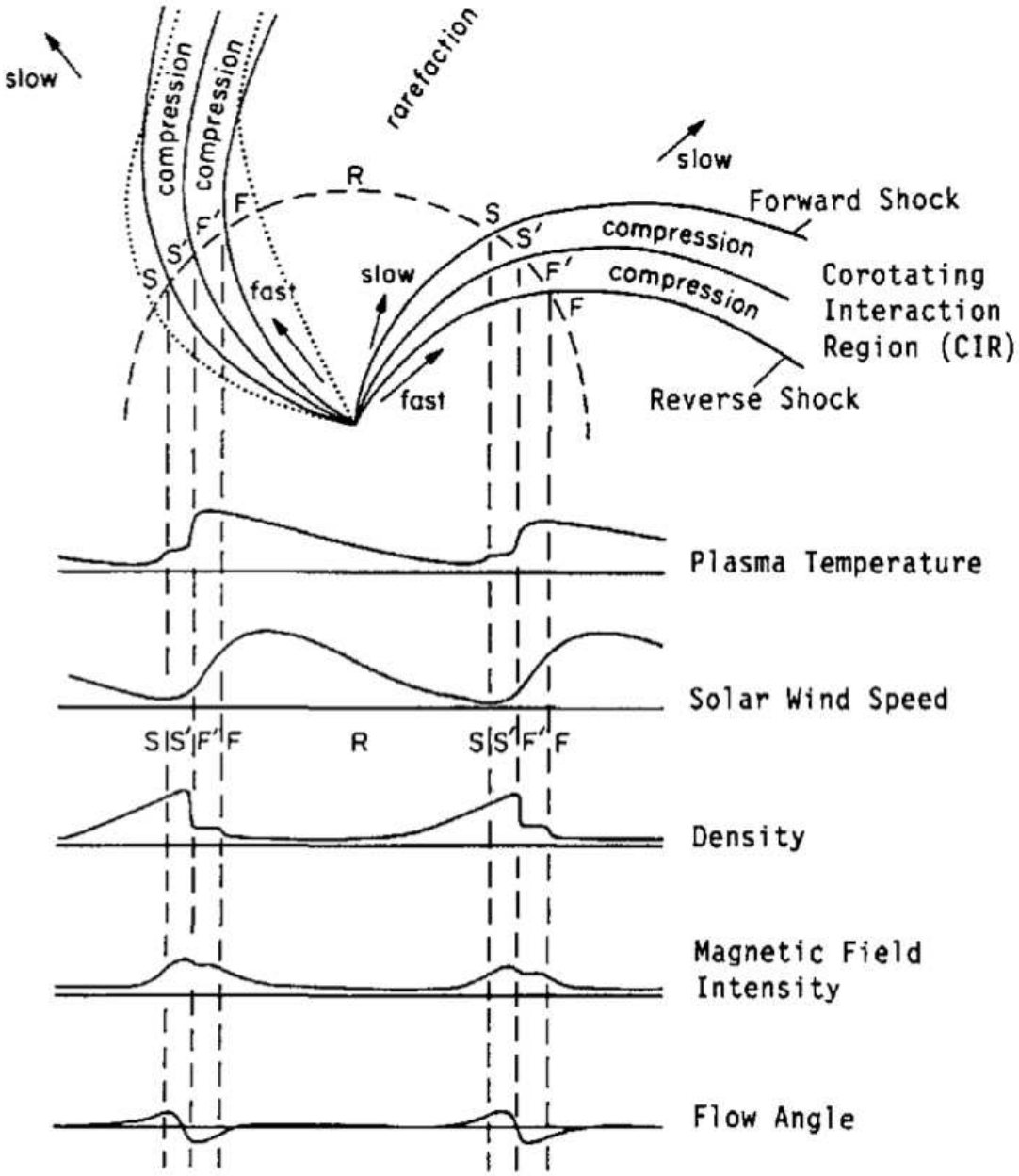

Figure 2.5. Schematic showing two CIRs corotating with the Sun along with plasma and magnetic field parameters associated with different regions in the CIRs. This figure was obtained from Kunow (2000).

acted upon by the Lorentz[3] force, and accelerated towards corotation with the planet. Jupiter's rapid rotation possesses a great amount of angular momentum and energy which is transferred, via ion-neutral collisions in the ionosphere, along field-aligned currents connecting to the magnetospheric plasma. This newly accelerated plasma eventually moves outward and exhibits a wide range of angular velocities, corresponding to a small departure from rigid corotation with the planet at distances near Io (6–10 R_J) out to regions beyond ~20 R_J, which rotate at ~50 % of the planetary rate (McNutt et al. 1979; Hill 1979; Hill et al. 1983; Pontius 1997; Vasyliunas 1983). This lag in corotation results from the finitely conducting ionosphere being unable to supply the necessary angular momentum to the radially diffusing plasma (previous references and Siscoe and Summers (1981)). The previously described internal processes result in the creation of a disc-like structure, called the 'magnetodisc', located in the equatorial plane beyond Io's orbit and throughout the middle magnetosphere region (~10 R_J to several tens of R_J). The structure of the Jovian magnetosphere thus differs from that of the Earth which is shaped primarily by solar wind, and not subject to significant centrifugal stresses associated with planetary rotation. A schematic of the Jovian magnetosphere is shown in Fig. 2.6; the magnetic field lines (black lines with arrows) and solar wind flow (red lines with arrows) are shown. The bow shock, magnetosheath, magnetopause, current sheet (magnetodisc), magnetotail and Io torus are also indicated. One can clearly see the stretched magnetic field lines in the current sheet region (dark lilac shading with yellow disc) resulting from the magnetodisc.

In steady state, the angular velocity of magnetospheric plasma Ω_M is less than that of the thermosphere Ω_T and planet Ω_J, following the general relation

$$\Omega_M < \Omega_T < \Omega_J. \tag{2.16}$$

This ensures that energy and angular momentum flows from the planet to the magnetosphere as discussed above. This relation is not, however, strictly true at all locations in the thermosphere and/or magnetosphere due to transport of angular momentum by meridional flows in the thermosphere and radial flows in the magnetosphere (Smith 2006). In addition, the above relationship is invalid when investigating short time scale (≤5 hours)

[3]These newly created ions start to "E×B"-drift in response to the convective electric field of the ambient plasma.

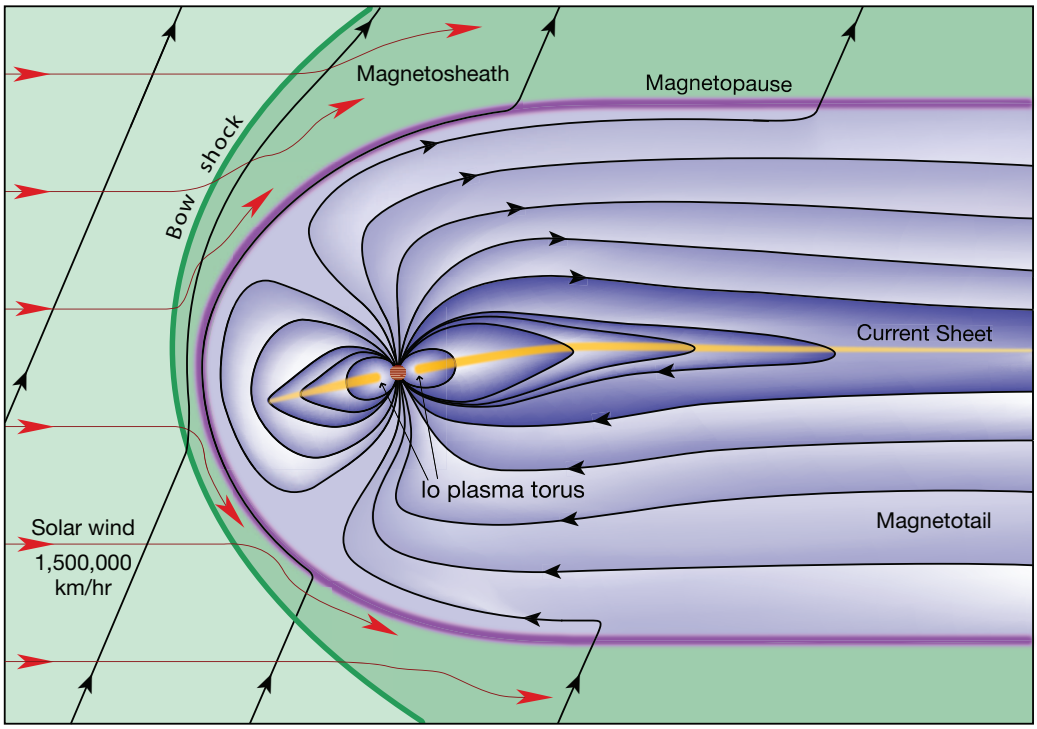

Figure 2.6. Schematic showing a side view of a vertical slice through Jupiter's magnetosphere. Magnetic field lines are shown in black and solar wind flows are shown in red. The Jovian bow shock, magnetosheath, magnetopause, current sheet (magnetodisc), magnetotail and Io torus are also indicated in the Figure. Image credit: Fran Bagenal and Steve Bartlett.

magnetospheric reconfigurations in the Jovian system (see Cowley et al. (2007) and Chapters 5 and 6).

The radial variation in magnetospheric plasma angular velocity has profound effects on the Jovian system, particularly on ionospheric and magnetospheric currents. The rest frame electric field (see section 2.3) in Jupiter's neutral atmosphere depends on the difference in angular velocity between the thermosphere and the magnetically conjugate magnetodisc, and drives a flow of equatorially directed Pedersen currents. Due to current continuity, FAC in the steady-state must flow both upwards and downwards along the magnetic field lines connecting the ionosphere and magnetodisc (see arrows on dashed lines in Fig. 2.6). Downward FACs flow from the outermost magnetosphere to the ionosphere. The upward directed FACs are carried by downward precipitating electrons from the magnetosphere (Cowley and Bunce 2001; Hill 2001; Khurana 2001; Southwood and Kivelson 2001). These electrons excite emissions in the upper atmosphere and produce the

main auroral oval at ∼15 ° magnetic co-latitude (Satoh et al. 1996; Clarke et al. 1998, 2004; Prangé et al. 1998; Vasavada et al. 1999; Pallier and Prangé 2001; Grodent et al. 2003a). Currents flow radially outward in the equatorial plane of the magnetosphere and, via the $\boldsymbol{J}\times\boldsymbol{B}$ force, accelerate the plasma towards corotation. The Pedersen, radial and FACs thus represent a complete current 'circuit' coupling the magnetosphere and ionosphere. In steady state, these current systems close, in accordance with Eq. (2.13).

Outer Magnetosphere

The outer magnetosphere's role in M-I coupling is poorly constrained and as such it plays a small role in the coupling of our model. This is not to say that the outer magnetosphere is unimportant in the Jovian system; it plays a vital role in the redistribution and recycling of magnetic flux and plasma as well as, in determining the overall size of the magnetosphere. We proceed with a basic discussion on the Jovian outer magnetosphere and its role in the Jovian system. The size of the Jovian magnetosphere was initially determined by the pressure balance between the solar wind dynamic pressure p_{sw} and the magnetic pressure p_B; respectively given by:

$$p_{sw} = \rho_{sw} v_{sw}^2, \tag{2.17}$$

$$p_B = \frac{B^2}{2\mu_0}. \tag{2.18}$$

ρ_{sw} is the mass density of the solar wind, v_{sw} is the solar wind velocity, B is the magnetic field strength and μ_0 is the permeability of free space. If one assumes that the Jovian magnetosphere can be represented by a dipole field then this pressure balance gives a sub-solar magnetopause size/radius $R_{MPdip} \sim 40\,\mathrm{R_J}$. However spacecraft observations, and statistical studies based on such observations (e.g. Joy et al. (2002)), find that the Jovian sub-solar magnetopause boundary R_{MP} on average lies at $\sim 75\,\mathrm{R_J}$ with a bimodal distribution between $\sim 63\,\mathrm{R_J}$ and $\sim 92\,\mathrm{R_J}$. The observations show that Jupiter's magnetosphere is predominantly $> 1.5\,\mathrm{x\,R_{MPdip}}$. This comes from the fact that Jupiter has a large internal plasma source (the moon Io) and a rapid planetary rotation rate, as discussed above. The large amount of plasma in Jupiter's magnetosphere gets centrifugally confined into a magnetodisc; this disc and the plasma therein, possesses a plasma pressure which in simple terms gets added to the magnetic pressure enlarging the magnetosphere. Magnetospheres

containing substantial plasma densities are thus larger than those with no (or minimal) plasma densities. A more appropriate pressure balance equation for Jupiter would thus be of the form:

$$p_{sw} = p_B + p_p, \tag{2.19}$$

where p_p is the plasma pressure in the magnetosphere. Plasma pressures are however, not well constrained and may vary on temporal and spatial scales. The solar wind dynamic pressure is also a variable quantity and can increase or decrease quite suddenly with the arrival of shocks and rarefaction regions (CIRs and/or CMEs) as discussed in section 2.1.3. Such spatial and temporal variation in different pressure terms make it difficult to form an accurate pressure balance equation for planets with an internal plasma source.

It is generally accepted that there are two large scale dynamical processes acting in the outer magnetosphere: i) the Vasyliunas cycle and ii) the Dungey cycle.

i) The Vasyliunas cycle (Vasyliunas 1983) involves flux tubes which are mass-loaded with Iogenic plasma in the inner magnetosphere. This plasma then diffuses radially outwards. Once the diffusing plasma reaches the edge of the magnetodisc, it will behave differently depending on whether its flux tube is on the day or night side of the magnetosphere. If the tube is in the dayside, it will be influenced by the oncoming solar wind pressure and confined to a pseudo-dipolar state. As this flux tube drifts into the nightside magnetosphere, it stretches the magnetic field lines tailward and eventually 'pinches off' a plasmoid which drifts tailward. The newly closed and depleted magnetic field line then returns to a "dipolar" state and flows to the dayside where the process is repeated (see Fig. 2.7).

ii) The Dungey cycle was first proposed by Dungey (1961) with regards to Earth's magnetosphere and describes the large scale magnetospheric flows due to interactions between the solar wind and magnetosphere. In the Dungey cycle, closed magnetic field lines at the magnetopause reconnect with the interplanetary magnetic field and are pushed tailward by the solar wind flow. Once in the tail, these open field lines reconnect and the flux is

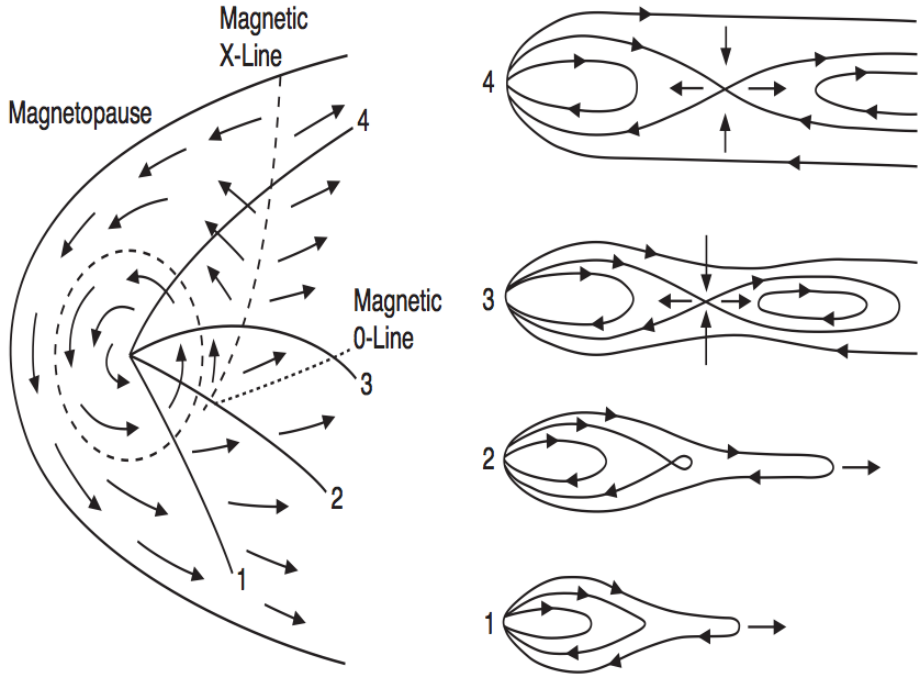

Figure 2.7. Schematic of Vasyliunas cycle in Jupiter's magnetosphere. The left plot shows plasma flows in the equatorial plane of the magnetosphere as seen from above the northern pole. The right plot shows a vertical slice through the magnetosphere, viewed from dusk. The solid lines represent the magnetic field. The Sun for both plots is off to the left. From Russell (2000).

returned towards the planet (Cowley et al. 2003). A schematic of this mechanism is shown in Fig. 2.8.

These Vasyliunas and Dungey flows discussed above will result in different flows on the high latitude ionosphere which is magnetically mapped to the discussed magnetospheric regions. Resulting ionospheric flows are shown schematically in Fig. 2.9, where solid black lines with arrows indicate the direction of ionospheric flows, the circled dots indicate regions of upward-directed FACs and the circled crosses indicated downward FACs. Relevant regions are labelled in the figure and separated by the dashed lines. At 70 ° latitude (edge of figure) flows are assumed to be corotating with the deep atmosphere; this region is followed by the sub-corotating (up to $0.5\,\Omega_J$) 'Hill region' where upward FACs located around $\sim 75\,^\circ$ create the main auroral oval. Polewards of the Hill region, there are sub-corotating flows associated the Vasyliunas cycle where flux tubes are expected to be depleted after plasmoid release down the magnetospheric tail. The Vasyliunas-cycle flows are particularly prominent on the dusk side of the ionosphere. On the dawn side, regions of downward FAC

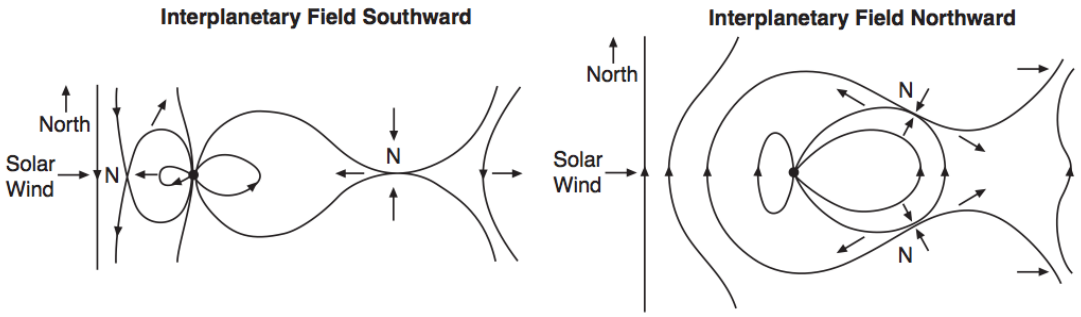

Figure 2.8. Schematic of Dungey cycle in Earth's magnetosphere. The black lines represent the magnetic field lines. From Russell (2000).

exist and ionospheric flows arise from both Vasyliunas and Dungey cycles. Those associated with the Dungey cycle and open field lines are deemed to be 'stagnant' as they rotate at approximately $0.1\,\Omega_J$ (Isbell et al. 1984). The polar flows and FACs discussed briefly here support observations by Stallard et al. (2001, 2002) who show that the dusk side of Jupiter's pole has sub-corotating flows, bright diffuse aurora and is named the Bright Polar Region (BPR) whilst the dawn side has significantly sub-corotating plasma flows, no significant aurora and is thus called the Dark Polar Region (DPR). A detailed description of Jovian ionospheric flows may be found in Cowley et al. (2003).

Some controversy exists as to which of these processes, Vasyliunas or Dungey is dominant. The reader is referred to the study by Badman and Cowley (2007) for a comprehensive discussion on outer magnetospheric dynamics in the gas giants. Badman and Cowley (2007) investigated the importance of the solar wind-driven Dungey cycle in the Jovian and Kronian system. They found that traditional estimates of the flux transported by the Dungey cycle consists of only $\sim$1 % of the total flux, and is thus expected to be suppressed compared to other rotational-driven transport mechanisms (i.e. Vasyliunas cycle). However, by taking account of the location of the transport mechanisms (most rotational transport taking place within the innermost magnetosphere), they were able to increase the flux transported by the Dungey cycle to $\sim$10 % (most noticeably during compressed magnetospheric configurations). They therefore conclude that the Dungey cycle does (under appropriate solar wind conditions) play a significant role in flux transport at the Gas Giants (Jupiter and Saturn).

The dynamics of the Jovian and Kronian outer magnetospheres i.e. reconnection and

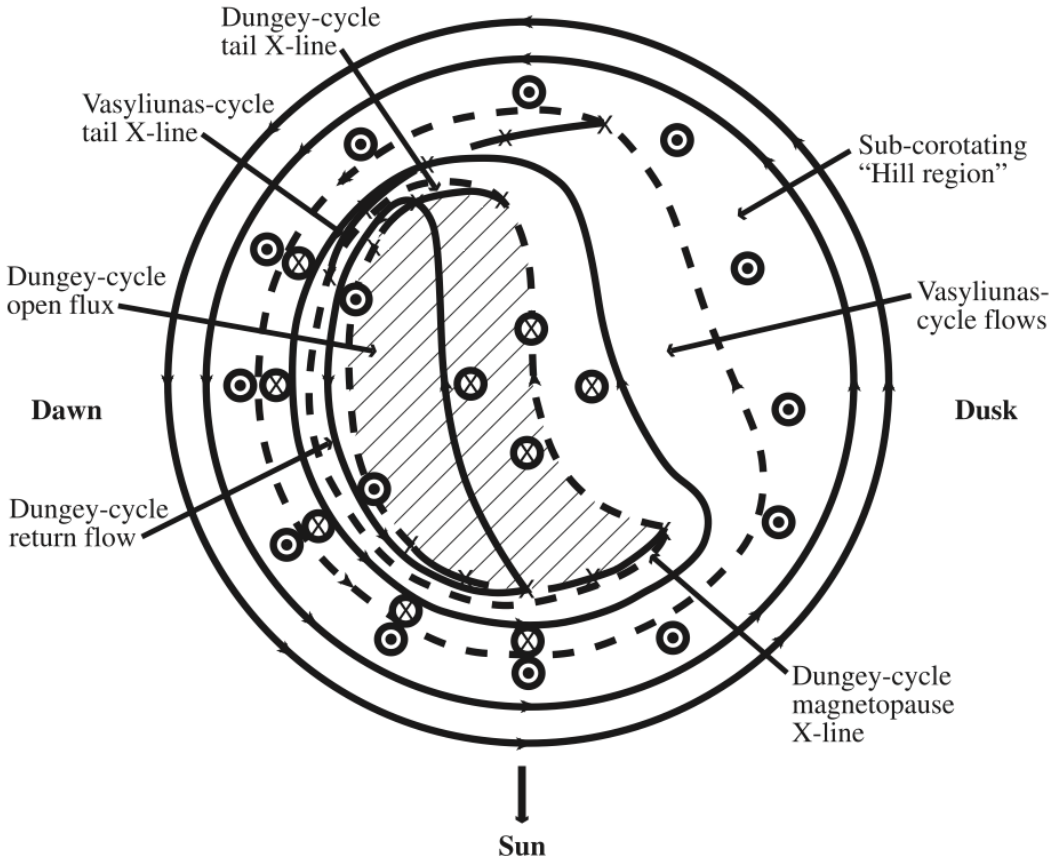

Figure 2.9. Schematic of Jupiter's ionospheric flows looking down on the North pole from Cowley et al. (2003). The Sun is to the bottom of the figure with dusk and dawn respectively to the right and left. The shown region encompasses ionospheric latitudes $\geq 70\,^{\circ}$. Circled dots indicate upward FACs and circled crosses represent downward FACs. The solid black lines with arrows represent ionospheric flows whilst the dashed lines show magnetospheric region boundaries. The x's indicate reconnection x-lines as labelled. The hatched region in the pole indicates open magnetic flux.

transport of magnetic flux are of considerable interest at present. The reader is referred to studies by Kronberg et al. (2005); Vogt et al. (2010) for Jupiter and Jackman et al. (2007, 2008) for Saturn.

2.2 Physics of the upper atmosphere

2.2.1 Basic atmospheric physics

The modelling in this thesis is primarily concerned with the Jovian upper atmosphere i.e. the neutral thermosphere and ionosphere. In this section, basic atmospheric physics

pertaining to these regions is discussed.

Hydrostatic equilibrium

Planetary atmospheres are subject to the planet's gravitational field, and so their vertical structure depends primarily on the balance between gravitational and pressure forces. This balance is known as 'hydrostatic equilibrium'. Let p represent the pressure at altitude z (vertically upward from a reference surface, such as the $p = 1\,\mathrm{bar(B)}$ pressure level). When moving upward through an increment dz in altitude, the corresponding change in pressure dp must be balanced by the gravitational force acting on the corresponding increment in mass. Thus:

$$dp = -\rho g dz, \tag{2.20}$$

where ρ is the density of the gas and g is the acceleration due to gravity. g can be assumed to be constant because the vertical extent of the atmosphere is generally small compared to the planet's radius. We can further assume that the atmospheric gas behaves like an ideal gas, obeying the relation:

$$p = \frac{\rho R T}{\mu}, \tag{2.21}$$

where T is temperature, R ($=8.31\,\mathrm{J\,K^{-1}mol^{-1}}$) is the molar gas constant and μ is the mean molar mass. Combining Eqs. (2.20 - 2.21) gives

$$\frac{dp}{dz} = -\frac{p}{H}, \tag{2.22}$$

where H is the scale height, defined as the *increase in altitude necessary to reduce the pressure by a factor of* e, and is given by:

$$H = \frac{RT}{\mu g}. \tag{2.23}$$

Integrating Eq. (2.22) gives a relation for pressure as a function of altitude for an atmosphere with constant H:

$$p(z) = p_0 \exp\left(-\frac{(z - z_0)}{H}\right), \tag{2.24}$$

where p_0 is the pressure at an arbitrary altitude z_0. For a more general atmosphere where H varies with altitude z, the pressure is given by:

$$p(z) = p_0 \exp\left(-\int_{z_o}^{z} \frac{dz\prime}{H(z\prime)}\right). \tag{2.25}$$

Adiabatic lapse rate

The vertical motion and temperature variation of a gas 'parcel' in a simple atmosphere (transparent to radiation and in hydrostatic equilibrium (Houghton 1986)) can be described using the *dry adiabatic lapse rate* Γ_d

$$\Gamma_d = -\frac{dT}{dz} = \frac{g}{c_p}, \tag{2.26}$$

where c_p is the specific heat capacity at constant pressure. We have used Eqs. (2.20 and 2.21) along with the *first law of thermodynamics* $dq = c_v dT + pdV$, to obtain Γ_d (q is the heat content, c_v is the specific heat capacity at constant volume and V is volume). This term describes whether an atmosphere has a stable vertical structure. If, as a parcel rises adiabatically, the atmospheric temperature decreases slower than the adiabatic lapse rate, then the parcel will fall back down to its initial altitude. The atmosphere is stable in this case. If, however, the parcel rises and the atmospheric temperature decreases more quickly than the adiabatic lapse rate, the parcel will continue to rise; the atmosphere is, in this case, unstable to convective motions.

2.2.2 Diffusive processes

Diffusion is a microscopic transport process which results in atmospheric mixing. The diffusive processes discussed in this section can all be divided into molecular and eddy 'parts', resulting, respectively, from random molecular motions and small scale turbulence

in the atmospheric bulk flow. The studies in Chapters 4 - 6 investigate the variation of the Jovian thermospheric structure and dynamics with solar wind dynamic pressure. This variation can essentially be related to magnetospheric reconfigurations on long or short time scales. Due to this dependence on the magnetosphere, the affected atmospheric momentum and heating sources will mainly be related to ion drag and Joule heating. As such, we do not expect diffusive processes to play a large role in the studies presented herein. Nevertheless we will briefly describe diffusive processes. For a more detailed description the reader is referred to Achilleos et al. (1998) and/or Smith (2006) (section 2.5) and the references therein. Note that the diffusive coefficients discussed in the following sections are calculated as in Achilleos et al. (1998) unless stated otherwise.

Molecular and eddy diffusion

Molecular diffusion is the process in which random molecular (thermal) motion leads to the eventual mixing of the atmosphere. This is parameterised by a a molecular diffusion coefficient K_D (in SI units of $\mathrm{m^2\,s^{-1}}$). In general molecular diffusion is a fairly slow process for gases[4] ($K_D \sim 1000\,\mathrm{m^2\,s^{-1}}$ for methane in the Jovian thermosphere (Moses et al. 2005), giving a timescale of $\sim$8.5 days). Eddy diffusion, on the other hand, is a process where turbulent eddies cause atmospheric mixing. These eddies are created by the random motion of the fluid, which in our case is the Jovian upper atmosphere, and are parameterised by the eddy diffusion coefficient K_τ (in SI units of $\mathrm{m^2\,s^{-1}}$). K_τ is a complex parameter to quantify as it is heavily dependent on the turbulent properties of the system under investigation. K_τ in our model has a value of $1.4 \times 10^2\,\mathrm{m^2\,s^{-1}}$ in accordance with Atreya (1982).

An atmosphere can be divided into two regions: i) the homosphere and ii) the heterosphere. In the homosphere, eddy diffusion is the dominant mixing process and this ensures that atmospheric composition is kept fairly uniform with altitude. In the heterosphere however, molecular diffusion is the dominant process and this leads to the individual/molecular species in the gas being separated according to their respective scale heights (dependent on molecular mass). The boundary between these two regions is called the homopause. It can be defined as the surface where molecular and eddy diffusion velocities are equal. In the Jovian atmosphere the homopause is taken to lie at an altitude where eddy and molecular diffusion timescales are equal for methane (Smith 2006).

[4]For liquids the time taken is much longer due to the smaller mean free path.

Thermal conduction

Thermal conduction is the process by which heat is transferred between colliding molecules in a medium (Jacobson 2005). In the thermosphere model used herein, both molecular and eddy[5] thermal conduction processes are characterised by the following equation

$$F_x = -\kappa_x \frac{\partial T}{\partial z}, \tag{2.27}$$

where F_x is the upwards heat flux, κ_x is thermal conductivity and the x subscript indicates whether the conduction is via molecular (m) or eddy (τ) processes.

Viscosity

Viscosity quantifies a fluid's ability to transport momentum and energy in directions orthogonal to the bulk flow. Viscosity is parameterised with a viscosity coefficient η, which consists of both molecular and eddy (turbulent) terms. If a body of gas has a vertical velocity gradient $\partial u/\partial z$, shear stresses σ will be created and exerted on the molecules in the gas.

$$\sigma = \eta \frac{\partial u}{\partial z}, \tag{2.28}$$

where u is the flow velocity. By finding the gradient of Eq. (2.28), we can obtain an expression for the viscous force per unit volume F_η

$$F_\eta = \frac{\partial \sigma}{\partial z} = \frac{\partial}{\partial z}\left(\eta \frac{\partial u}{\partial z}\right). \tag{2.29}$$

The presence of a viscous force implies that this force accelerates some of the local medium[6], doing work in the process. The total work done by viscosity Q_η, to first-order, is given by

[5] Eddy thermal conduction also has a term proportional to $\kappa_\tau \Gamma_d$ but for simplicity and to ensure that the second law of thermodynamics is not violated it is not included in this thermosphere model. For more details please refer to section 2.5.2 in Smith (2006).

[6] An atmosphere in our case.

$$Q_\eta = u\frac{\partial \sigma}{\partial z} + \sigma\frac{\partial u}{\partial z} = \frac{\partial\left(u\sigma\right)}{\partial z}. \tag{2.30}$$

This equation contains two terms; the first representing the change in kinetic energy caused by F_η and the second term, representing viscous heating (Smith 2006).

2.2.3 Ionospheric physics

The ionosphere is the portion of the neutral atmosphere that is ionised by a combination of photoionisation (by energetic photons) and impact ionisation (precipitation of energetic particles). The ionosphere, similarly to the neutral atmosphere, is affected by gravitational and pressure forces; however, it is also influenced by electromagnetic forces. Below, the different mechanisms of ionisation will be discussed briefly.

Photoionisation

In nature, the dominant source of ionisation in planetary atmospheres is, often, solar radiation. This has been found to be primarily due to photons in the extreme Ultraviolet (EUV) to ultraviolet (UV) range of the spectrum. In the gas giants, the primary constituents of the upper atmospheres are H_2, H and He, having ionisation potentials corresponding to the EUV to UV wavelength range ($10-100\,nm$) (Strobel and Atreya 1983).

The (optical) depth τ to which the ionising incident radiation penetrates the atmosphere depends upon the neutral atmospheric density $n(z)$. At high altitudes, with low neutral densities, incident photons will be able to penetrate, with little or no attenuation, the neutral atmosphere and significantly ionise it. At low altitudes, with high densities, the opposite occurs - incident photons are almost entirely attenuated by the atmosphere over short distances and the ionisation rate falls to zero. Let the photon flux be represented by F and F_∞ (initial) and let these photons have energy E and E_0 (initial). Assuming that the atmosphere is isothermal with a uniform scale height H, the ionisation rate $q(z)$ can be given by:

$$q(z) = \frac{dF(z)}{dz} = n(z)\sigma F(z), \tag{2.31}$$

where

$$n(z) = n_0 exp\,(-(z - z_0)/H), \tag{2.32}$$

$$F(z) = F_\infty exp\,(-\tau), \tag{2.33}$$

$$\tau(z) = \sigma H n(z), \tag{2.34}$$

n_0 is the density at altitude z=z_0 and σ is the absorption cross-section units of m^2. Eq. (2.31) is known as the *Chapman function* which describes ion production as a function of density. Taking the natural logarithm and differentiating Eq. (2.31) shows that the maximum ionisation rate occurs at density $n(z) = 1/(\sigma H)$.

Impact ionisation

The precipitation of energetic charged particles from the magnetosphere and/or solar wind can cause significant ionisation. This ionisation process is particularly important at high latitudes for planets with dipolar-like magnetic fields; in the night-side ionosphere; and in moons with atmospheres embedded in planetary magnetospheres (Luhmann 1995). Similarly to photoionisation (see section 2.2.3), the precipitating particle energy flux is attenuated with increasing atmospheric density. As the particles collide with the atmospheric neutrals they lose kinetic energy. If this lost energy exceeds the ionisation potential of the neutral, the neutral is ionised. Thus, a particle's kinetic energy will gradually decrease due to inelastic collisions with a number of atmospheric neutrals. In reality, these initial ion-neutral interactions may lead to: i) secondary electrons being ejected, which themselves can ionise neutrals or ii) cause significant changes in the precipitating particle's acceleration causing it to radiate *bremsstrahlung* (usually in the X-ray region of the spectrum) which can cause further photoionisation.

If we consider making similar calculations as in section 2.2.3, where F_∞ represents the initial particle number flux, σ now represents the collisional cross-section and the initial and subsequent particle energies are E_∞ and E respectively, the particle ionisation rate $q_p(z)$ can be approximated by:

$$q_p(z) = \frac{F_\infty}{E_{th}} \frac{dE}{dz} = \sigma n(z) F_\infty, \tag{2.35}$$

where

$$E(z) = E_\infty - \sigma H n(z) E_{th} \tag{2.36}$$

and E_{th} is the energy lost in each collision with an atmospheric neutral. The maximum ionisation rate due to precipitating particles occurs at an altitude where the particles kinetic energy reaches zero. Rearranging Eq. (2.36), the ionisation peaks at a density of $n(z) = E_\infty/(\sigma H E_{th})$.

Charge neutrality and ambipolar diffusion

Ions and electrons in a planetary atmosphere will generally have different temperatures (T_i for ions and T_e for electrons) and consequently different thermal velocities (v_i for ions and v_e for electrons). As such, one would expect the distance between electrons and ions to increase with time. However, as the mean separation distance between them increases, electric fields are created which act to minimise this charge separation. Using Gauss' law, one can show that these distances are very small (on the order of an atomic radius $\sim 1 \times 10^{-10}$ m) meaning that, locally, charge neutrality must be conserved.

Ambipolar diffusion is intrinsically linked to the concept of charge neutrality discussed above. It results from the combination of gravitational and electromagnetic forces. Ions and electrons have different mass; when acted upon by gravity in an atmosphere they will attempt to settle at different altitudes dependent on their scale heights. The scale height of ions is generally smaller than that of electrons due to the large difference in mass. Ions will thus seem to be transported downwards due to gravity compared to electrons. As the distance between them increases, electric fields will be generated as discussed above. This will decrease the separation between the ions and electrons by moving the electrons downward and moving the ions upwards. Essentially, the electrons and ions, under the influence of gravity and their electrostatic interactions, will act equivalently to a neutral gas with half the ion mass (Ratcliffe 1972). Ratcliffe (1972) also considered that, if ion

and electron temperatures were equal the 'plasma scale height' H_p would be twice that of a neutral gas with mass equal to the ion mass.

2.2.4 Atmospheric structure

Neutral atmospheres of different planets may have different compositions but their vertical structure remains fairly common. On Earth, for example, the primary atmospheric constituents are Nitrogen ($\sim 79\,\%$) and Oxygen ($\sim 21\,\%$) whilst Jupiter and Saturn consist mostly of Hydrogen and Helium. A vertical temperature profile of Earth's neutral atmosphere is shown in Fig. 2.10 (Smith 2006). Different regions spanning the whole vertical atmosphere are labelled. Starting from the surface and moving upwards lies the troposphere; here heat is transferred from the surface to the surrounding atmosphere. Turbulent mixing is important and the negative temperature gradient can be described reasonably well by the adiabatic lapse rate. A temperature inversion occurs at the tropopause which is where the stratosphere begins. This region has a positive temperature gradient meaning that it is dynamically stable i.e. there is no significant convection or turbulence. Its increase in temperature is primarily due to the absorption of solar radiation by ozone. The end of the stratosphere, the stratopause is indicated by a temperature maximum which then leads on to the mesosphere. This is the middle layer of the atmosphere and has a negative temperature gradient resulting from the increase in radiative cooling (by Carbon Dioxide) and a decrease in solar heating. Note that atmospheric gravity waves become unstable and deposit energy in this region of Earth's atmosphere.

The thermosphere lies above the mesosphere[7]. In this region the temperature increases to very large values (1000+ K) due to absorption of solar EUV radiation and low cooling rates. The thermosphere is also heated by particle precipitation and plays host to the ionosphere and aurora. In the terrestrial atmosphere, the homopause[8] boundary lies in the thermosphere; therefore, below this boundary (in the heterosphere) all atmospheric constituents are evenly mixed due to the turbulent processes but above this boundary (in the homosphere) constituents are separated by their scale height (or molecular mass). The thermosphere and ionosphere are the main regions of concern in the modelling herein and these regions for the case of Jupiter are discussed in the next section. Above the

[7] The mesosphere terminates at the mesopause.
[8] Another name for the homopause is the turbopause.

thermosphere lies the final region of a planetary atmosphere: the exosphere. Here the temperature is fairly constant and the density is so low that molecules seldom collide and therefore must be treated as individual particles with ballistic trajectories. The boundary between the thermosphere and exosphere, known as the exobase, is considered to lie at an altitude where the mean free path is equal to the pressure scale height. The upper boundary of the exosphere is often found to be indistinguishable from outer space.

2.2.5 Jupiter's atmosphere and ionosphere

Most of our knowledge of the Jovian thermosphere and ionosphere comes from remote observations (be they space-based or ground-based). The Galileo Probe is the only instance where *in situ* measurements of the Jovian upper atmosphere have been made. In this section we briefly discuss a few simple properties of the Jovian thermosphere and ionosphere. The reader is referred to a comprehensive discussion by Yelle and Miller (2004) (and the references therein) for further details.

The Jovian thermosphere, like other planetary thermospheres, is a relatively hot region of the atmosphere that lies between the mesosphere and exosphere (almost indistinguishable from outer space). Thermospheric molecules are ionised by incident solar extreme ultraviolet (EUV) radiation and energetic charged particles from the magnetosphere (Yelle and Miller 2004). The Jovian upper atmosphere is composed primarily of molecular hydrogen along with a small amount of helium (approximately a 10:1 ratio). Atreya et al. (2003) detected the presence of numerous minor constituents in the Jovian atmosphere such as water, ammonia, methane and various other hydrocarbon species. These are however, predominantly located at lower altitudes (below the homopause) and will not constitute a significant part of the neutral thermosphere modelled in this thesis. Complex hydrocarbon chemistry can thus be ignored in our modelling.

The temperature profile of Jupiter's neutral atmosphere is shown in Fig. 2.11. This profile was obtained using data from the Galileo probe presented by Seiff et al. (1998). Zero altitude corresponds to the 1 bar pressure level. The thermosphere model used in this thesis has a lower boundary at an altitude of 300 km corresponding to an atmospheric pressure of 2 μbar (just above the homopause).

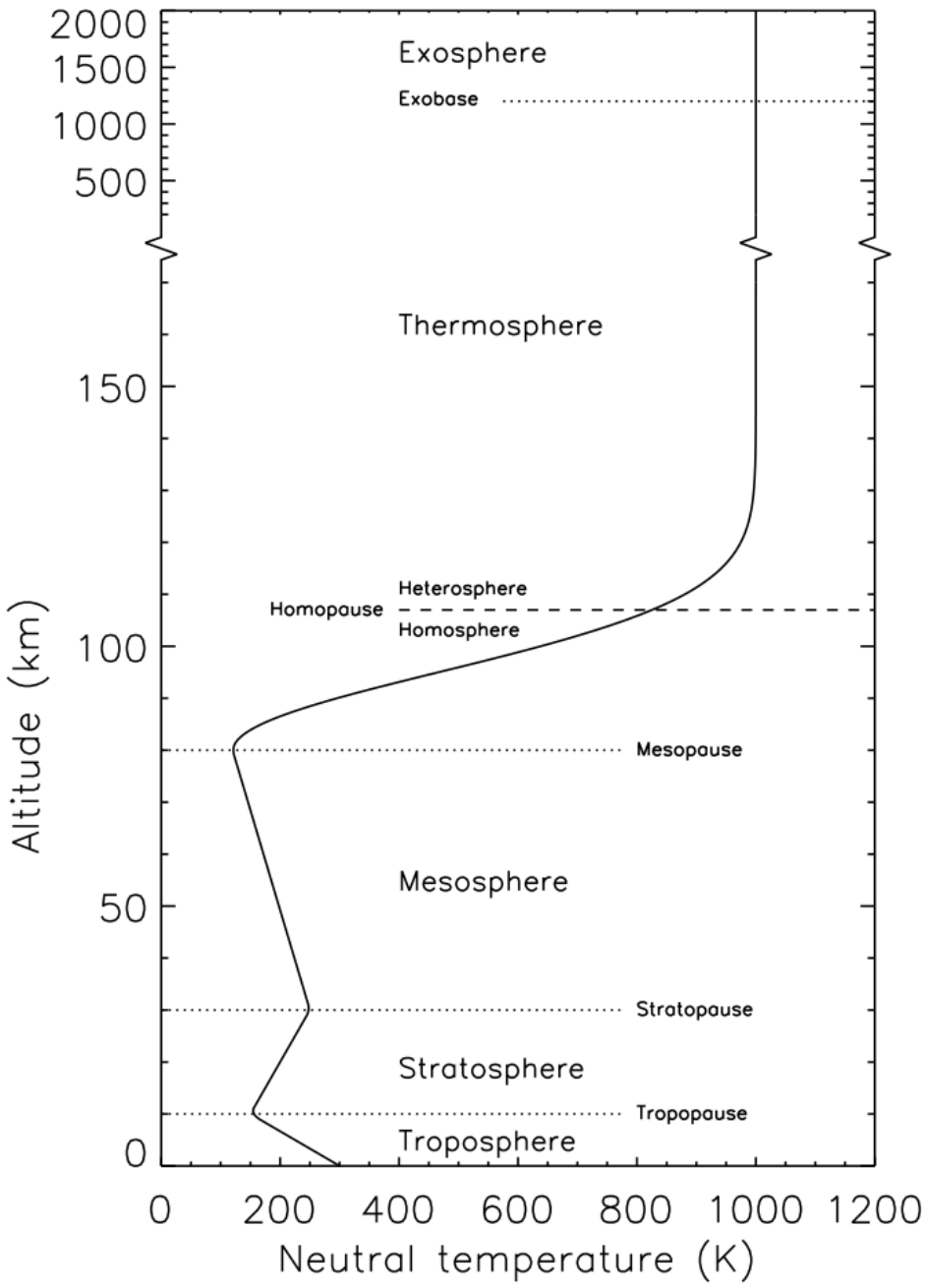

Figure 2.10. Vertical temperature profile of Earth's atmosphere with labels showing the different regions. This Figure was obtained from Smith (2006).

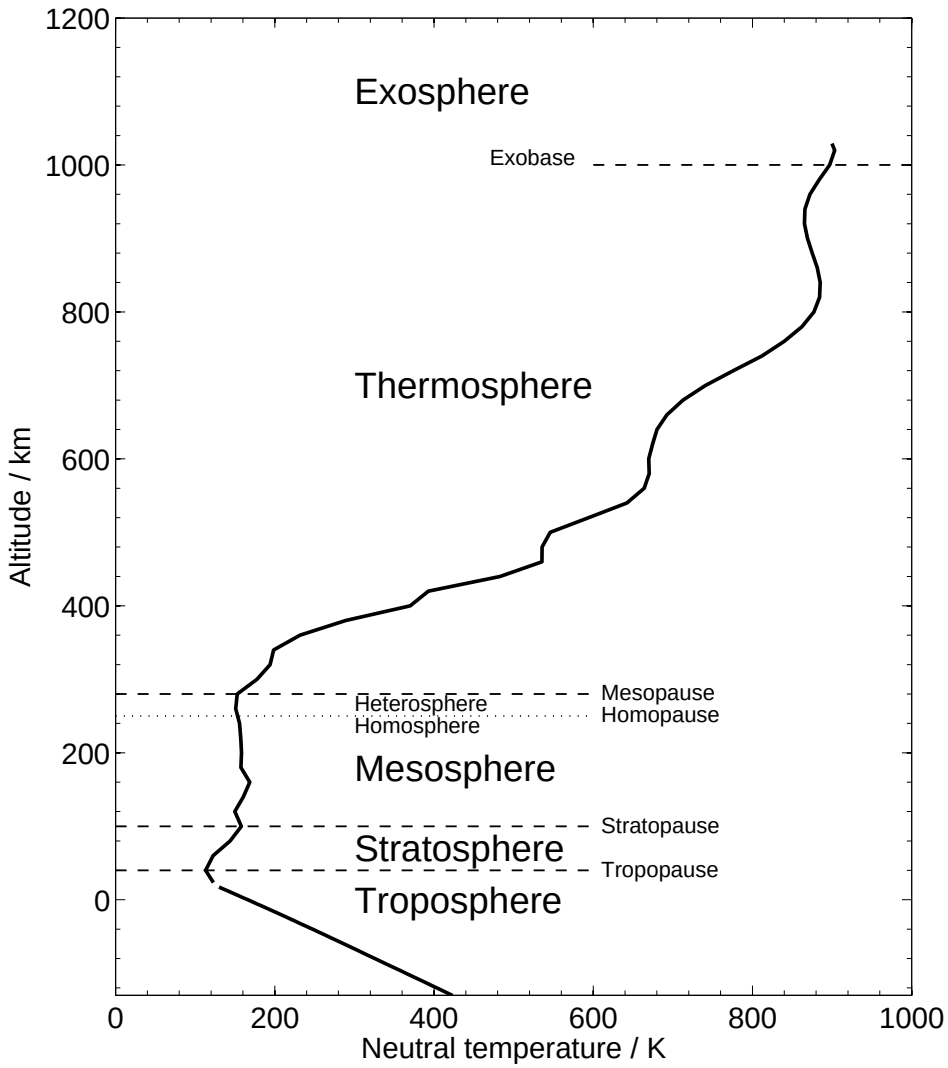

Figure 2.11. Vertical temperature profile of Jupiter's thermosphere. This profile was plotted using measurements from the Galileo probe (Seiff et al. 1998).

In Chapter 1 we discussed that the Jovian thermospheric temperature was initially predicted to be $\sim 150-200\,\mathrm{K}$ (Strobel and Smith 1973); based on the assumption that the sole source of heating came from solar EUV radiation. As can clearly be seen from Fig. 2.11, showing Galileo probe measurements (Seiff et al. 1998), the thermospheric temperature of Jupiter is $\sim 700\,\mathrm{K}$ larger than predicted in initial studies (Strobel and Smith 1973). This inevitably leads to the questions: Why is the Jovian thermosphere so hot? Where does the energy required to heat the thermosphere come from, if not from solar radiation? These questions have been discussed in Chapter 1 so for brevity we merely state that the problem, known as the Gas Giant 'energy crisis', still remains unresolved.

The Jovian ionosphere is similar to that of the other gas giants; it mainly consists of ionised hydrogen and helium species. These are ionised by photoionisation and impact ionisation (see section 2.2.3) (Sanchez-Lavega 2010)

$$H + h\nu \rightarrow H^+ + e^- \tag{2.37}$$

$$H_2 + h\nu \rightarrow H + H^+ + e^- \tag{2.38}$$

$$H_2 + h\nu \rightarrow H_2^+ + e^- \tag{2.39}$$

$$H_2(\nu \geq 4) + H^+ \rightarrow H_2^+ + H \tag{2.40}$$

H_2^+ quickly reacts with H_2 to form H_3^+ via the reaction

$$H_2^+ + H_2 \rightarrow H_3^+ + H \tag{2.41}$$

As H_2^+ is very short lived, the main constituents of the Jovian ionosphere are H_3^+ and H^+. Note that He^+ is also created in the Jovian ionosphere but as its neutral concentration is so low compared with the hydrogen species, it is of negligible consequence in our modelling. Both ionospheric ions eventually recombine with electrons forming neutral Hydrogenic species. The lifetime of H^+ is considerably longer than that of H_3^+ as the recombination of H_3^+ is more energetically favorable[9]. H_3^+ can therefore only be abundant on the dayside and auroral regions of Jupiter, as it needs a constant source of ionisation. H^+ on the other hand is abundant uniformly across the planet.

2.3 Magnetosphere-Ionosphere coupling at Jupiter

The coupling of the magnetosphere, ionosphere and neutral thermosphere is a major focus of this work. Energy and angular momentum are transferred between the thermosphere and magnetosphere via ion-neutral collisions resulting in currents aligned with the magnetic field. We begin this section by discussing ion-neutral collisions and then proceed to discuss the larger, macroscopic effects of these collisions.

[9]See Achilleos et al. (1998) for a detailed summary of their respective lifetimes and favorable reactions.

2.3.1 Ion-neutral collisions

Recall that a charged particle in an electromagnetic field feels the influence of the Lorentz force shown in Eq. (2.1). We can divide this equation into components perpendicular and parallel to the magnetic field. The parallel component of the equation of motion for a positive ion depends on the parallel electric field $\boldsymbol{E}_{\parallel}$ as

$$m_i \dot{\boldsymbol{v}}_{\parallel \boldsymbol{i}} = e\boldsymbol{E}_{\parallel}, \tag{2.42}$$

where m_i is the ion mass, $\dot{\boldsymbol{v}}_{\parallel \boldsymbol{i}}$ is the ion acceleration in the parallel direction and $\boldsymbol{v}_{\parallel \boldsymbol{i}}$ is the parallel ion velocity. As discussed above, charged particles in the Jovian ionosphere can be approximated to being in a quasi-neutral state. As such, any parallel motion creating magnetic field aligned charge separation would quickly be halted by the creation of an opposing electric field. We therefore only consider electric fields that are purely perpendicular to the magnetic field. The perpendicular equation of motion for an ionospheric ion in the inertial frame S is

$$m_i \dot{\boldsymbol{v}}_{\boldsymbol{i}} = e\left(\boldsymbol{E} + \boldsymbol{v}_{\boldsymbol{i}} \times \boldsymbol{B}\right). \tag{2.43}$$

Let us now define a reference frame S' which is moving at the plasma drift velocity $\boldsymbol{v}_{\boldsymbol{E}}$ given by Eq. (2.6). In this frame, the electric field $\boldsymbol{E'}$ is given by

$$\boldsymbol{E'} = \boldsymbol{E} + \boldsymbol{v}_{\boldsymbol{E}} \times \boldsymbol{B} = 0, \tag{2.44}$$

which must be equal to zero as the plasma (ions and electrons) are at rest in a quasi-neutral state. The equation of motion in frame S' is similar to that in Eq. (2.43) but has no electric field component.

$$\dot{\boldsymbol{v}}'_{\boldsymbol{i}} = \Omega_c \boldsymbol{v}'_{\boldsymbol{i}} \times \hat{\boldsymbol{b}}, \tag{2.45}$$

where Ω_c is the Larmor frequency, $\boldsymbol{v}'_{\boldsymbol{i}} = \boldsymbol{v}_{\boldsymbol{i}} - \boldsymbol{v}_{\boldsymbol{E}}$ and is the ion velocity in frame S';

Eq. (2.2) and the unit vector along the field $\hat{\boldsymbol{b}} = \boldsymbol{B}/|B|$ were used to attain this simplified equation of motion. This equation results in circular motion about the magnetic field superposed on the drift perpendicular to the field. As described in section 2.1.1, this ion motion, along with a corresponding electron motion, does not create currents.

The above description of ionospheric plasma motion has not yet included the effects of collisions between ions and the atmospheric neutrals. To incorporate this, it is necessary to add an extra term dependent on the *collision frequency for momentum transfer* ν_{in}, to Eq. (2.45) (Ratcliffe 1972). This new equation of motion is given by

$$\dot{\boldsymbol{v}}_{\boldsymbol{i}}' = \Omega_c \boldsymbol{v}_{\boldsymbol{i}}' \times \hat{\boldsymbol{b}} + \nu_{in} \left(\boldsymbol{u}' - \boldsymbol{v}_{\boldsymbol{i}}' \right), \tag{2.46}$$

where $\boldsymbol{u}' = \boldsymbol{u} - \boldsymbol{v}_{\boldsymbol{E}}$ is the neutral bulk velocity in frame S' and $\boldsymbol{u}$ is the neutral bulk velocity in frame S. This term can be thought of as drag force exerted by the neutrals on the ions.

Let us consider the ion motion over time periods that are long compared to the inverse of the Larmor and collisional frequencies. In this case, we can assume steady-state so that $\dot{\boldsymbol{v}}_{\boldsymbol{i}}' = 0$. Rearranging for $\boldsymbol{v}_{\boldsymbol{i}}'$ and noting that $\boldsymbol{v}_{\boldsymbol{i}}' = -(\boldsymbol{v}_{\boldsymbol{i}}' \times \hat{\boldsymbol{b}}) \times \hat{\boldsymbol{b}}$, Eq. (2.46) becomes

$$\boldsymbol{v}_{\boldsymbol{i}}' = \frac{1}{r_i + r_i^{-1}} \boldsymbol{u}' \times \hat{\boldsymbol{b}} + \frac{r_i}{r_i + r_i^{-1}} \boldsymbol{u}', \tag{2.47}$$

where $r_i = \nu_{in}/\Omega_c$. We can simplify this further by defining another function

$$f(r_i) = \frac{1}{r_i + r_i^{-1}}, \tag{2.48}$$

and substituting this in Eq. (2.47) making

$$\boldsymbol{v}_{\boldsymbol{i}}' = f(r_i) \boldsymbol{u}' \times \hat{\boldsymbol{b}} + r_i f(r_i) \boldsymbol{u}'. \tag{2.49}$$

If we assume that electron-neutral collisions are negligible compared to the ion-neutral collisions, the electron motion can still be described by $\boldsymbol{v_E}$. However, the collisional term in Eq. (2.49) means that an 'ionic' current will flow in the ionosphere as the ions have velocity $\boldsymbol{v_i'}$ relative to the electrons. The resulting current density $\boldsymbol{j}$ is

$$\boldsymbol{j} = |e| n_i \boldsymbol{v_i'}. \tag{2.50}$$

Note that the charge $|e|$ is for a single-charged positive ion. An ionosphere with multiple charged species would require a sum over all species to calculate $\boldsymbol{j}$.

Let us now switch to yet another reference frame - the neutral rest frame S^*. In this frame, the plasma drifts with velocity $-\boldsymbol{u'}$ and the electric field $\boldsymbol{E^*}$ can be obtained by solving for and replacing $\boldsymbol{E}$ in Eq. (2.44) with $\boldsymbol{E^*}$ with the new plasma drift velocity $-\boldsymbol{u'}$. This gives the current $\boldsymbol{j}$ in terms of the electric field in frame S^*

$$\boldsymbol{j} = \frac{e n_i}{|B|} \Big(f(r_i) \boldsymbol{E^*} + r_i f(r_i) \boldsymbol{E^*} \times \hat{\boldsymbol{b}} \Big). \tag{2.51}$$

The above current can be divided into two components: i) The Pedersen current which flows parallel to $\boldsymbol{E^*}$, and ii) The Hall current flowing perpendicular to $\boldsymbol{E^*} \times \hat{\boldsymbol{b}}$. We can now introduce the Pedersen and Hall conductivities represented by σ_P and σ_H respectively:

$$\sigma_P = \frac{e n_i}{|B|} f(r_i), \tag{2.52}$$

$$\sigma_H = r_i \sigma_P. \tag{2.53}$$

Now that we have relations for ionospheric conductivities, we can infer some of their properties using Eq. (2.48). Pedersen conductivity is proportional to $f(r_i)$; at high altitude the neutral and ion densities are low so collisions between them will approach zero; at low altitudes collisions are very common and will approach infinity. These both lead to $f(r_i) \to 0$ and very small Pedersen conductivities. The Pedersen conductivity layer can thus be found at an altitude where $f(r_i{=}1) = 0.5$. Hall conductivity is proportional to

$r_i f(r_i)$, which approaches 0 at high altitudes and 1 at low altitudes. Therefore, we expect the conductivity peaks for Pedersen currents to lie at a higher altitude than that of Hall currents.

For M-I coupling, σ_P and σ_H are often expressed through height-integrated conductances, Σ_P and Σ_H respectively. This simply involves integrating conductivities over all altitudes using

$$\Sigma_P = \int_{bottom}^{top} \sigma_P \, \mathrm{d}z, \tag{2.54}$$

$$\Sigma_H = \int_{bottom}^{top} \sigma_H \, \mathrm{d}z. \tag{2.55}$$

2.3.2 Macroscopic Magnetosphere-Ionosphere coupling

In this and the following sections, we describe how the microscopic effects of ion-neutral collisions discussed above manifest themselves in macroscopic terms. We begin by introducing a term used to quantify the frictional drag on the neutral atmosphere as a result of the magnetosphere. This term, known as the 'slippage parameter' K was first introduced by Huang and Hill (1989) and we represent it as

$$(\Omega_T - \Omega_J) = -K(\Omega_J - \Omega_M), \tag{2.56}$$

or equivalently

$$(\Omega_T - \Omega_M) = (1 - K)\,(\Omega_J - \Omega_M). \tag{2.57}$$

Here Ω_M, Ω_J are the angular velocities of the magnetosphere and Jupiter itself (deep planetary angular velocity) respectively. Ω_T is the effective rotation angular velocity of the thermosphere. K thus represents the 'slippage' of the neutrals from rigid corotation.

Smith and Aylward (2009) define Ω_T as a weighted average of the effective rotation angular velocity throughout the thermosphere-ionosphere. Smith and Aylward (2008) showed

that the equatorward current density (see Eq. (2.51)) in the ionosphere consists of two contributions: (1) Pedersen current associated with the azimuthal thermospheric velocity u_ϕ and (2) Hall current associated with the meridional thermospheric velocity u_θ. u_ϕ and u_θ (defined in the frame corotating with the planet) will, in general, vary with altitude z in the thermosphere. As such, we define a local effective angular velocity ω_T at each altitude z as follows (Smith and Aylward 2008, 2009):

$$\rho_i \omega_T = \rho_i \Omega_J + u_\phi + \frac{\sigma_H}{\sigma_P} u_\theta. \tag{2.58}$$

where ρ_i is the cylindrical radial distance of the ionosphere ($\rho_i \approx R_J \sin\theta_i$). Integrating over the height of the thermosphere-ionosphere and comparing with the Pedersen current in Eq. (2.61) (section 2.3.3), we find that Ω_T can be defined as

$$\Sigma_P \Omega_T = \int \sigma_P \, \omega_T dz, \tag{2.59}$$

where Σ_P is defined in Eq. (2.54). In these expressions Ω_T is a weighted average of the effective neutral angular velocity ω_T throughout the thermosphere-ionosphere, which also contains contributions from meridional winds. Thus, by using the weighted average of ω_T we can leave behind the assumption of a thin sheet ionosphere.

2.3.3 Coupling currents

The coupling of the magnetosphere and ionosphere induces an ionospheric electric field within the thermosphere's rest frame which then causes ionospheric currents to flow. This electric field, at co-latitude θ_i, is E_θ and can be written as:

$$E_\theta = B_i \rho_i \, (\Omega_T - \Omega_M), \tag{2.60}$$

where B_i=2B_J and is the assumed radial ionospheric magnetic field, B_J is the equatorial magnetic field strength at the planet's surface, ρ_i=$R_i \sin\theta_i$ and is the perpendicular distance to the planet's magnetic / rotation axis and R_i is the ionospheric radius. We adopt B_J=426400 nT as Jupiter's dipole equatorial field (Connerney et al. 1998), and

R_i=67350 km as the radius of the polar Pedersen layer (radius of the ionosphere) (Cowley et al. 2007). Note that the auroral ionosphere is at high latitudes, where the planet's radius is ∼66854 km at the 1 bar surface. The resulting, equatorially directed ionospheric height-integrated Pedersen current density, i_P, and the total, azimuthally integrated form of this current, $I_P(\theta_i)$, are (Cowley et al. 2007; Smith and Aylward 2009):

$$i_P = \rho_i \Sigma_P \left(\Omega_T - \Omega_M\right) B_i, \tag{2.61}$$

and

$$I_P(\theta_i) = 2\pi \rho_i^2 \Sigma_P \left(\Omega_T - \Omega_M\right) B_i, \tag{2.62}$$

where, as discussed in section 2.3.1, Σ_P is the height-integrated Pedersen conductance.

Current continuity requires that there also exists a radial current density in the magnetodisc, i_ρ, which can also be azimuthally integrated, represented as I_ρ (Nichols and Cowley 2004; Smith and Aylward 2009). We write

$$\rho_e i_\rho = 2\rho_i i_P, \tag{2.63}$$

$$I_\rho = 8\pi \Sigma_P F_e \left(\Omega_T - \Omega_M\right), \tag{2.64}$$

where the flux function $F_e(\rho_e) = F_i(\theta_i) = B_J \rho_i^2$ on a magnetic flux shell which intersects the ionosphere at co-latitude θ_i. ρ_e is the equatorial distance from the planet centre to the field lines lying in this shell. F_e and F_i are the equatorial and ionospheric flux functions respectively (discussed further in section 3.3). The mapping between θ_i and ρ_e is represented by the equality $F_e(\rho_e) = F_i(\theta_i)$.

Another result of current continuity with regard to the variation of the Pedersen current with latitude is the creation of FACs which flow from the ionosphere to the magnetosphere. The density of these currents (at the ionospheric footpoint of the relevant field line) is

$$j_{||i}(\theta_i) = -\frac{1}{2\pi R_i^2 \sin\theta_i}\frac{dI_P}{d\theta_i}, \tag{2.65}$$

where $j_{||i}(\theta_i)$ is the FAC density and the sign (positive for radially outward current) corresponds to the northern hemisphere where the magnetic field points outward from the planet (Cowley et al. 2007).

2.3.4 Coupling momentum and energy

In section 2.3.1 we calculated the acceleration of an ion under the influence of electromagnetic and collisional forces (see Eq. (2.46)). In steady-state, there is no acceleration and the electromagnetic term is equal to the collisional term. To calculate the total force per unit volume exerted by the electromagnetic term on the neutrals, we simply multiply the first term of Eq. (2.46) by the ion mass and density, giving

$$\boldsymbol{F_D} = en_i|B|\boldsymbol{v_i'} \times \hat{\boldsymbol{b}} = \boldsymbol{j} \times \boldsymbol{B}. \tag{2.66}$$

$\boldsymbol{F_D}$ is the *ion drag* force; thought of as a drag force exerted by the ions in the ionosphere and imposed on the thermospheric neutrals, which causes the neutrals to partially follow the ionospheric plasma motion (Ratcliffe 1972).

There are two main energy sources arising from M-I coupling and the underlying ion-neutral collisions. These are i) ion drag energy - the kinetic energy exchanged by the collisions and ii) Joule heating - a thermal energy resulting from the ion-neutral collisions. The total work done[10] in the inertial frame S is Q_{tot} and given by

$$Q_{tot} = en_i\boldsymbol{v_i} \cdot \boldsymbol{E}. \tag{2.67}$$

By using $\boldsymbol{v_i'} = \boldsymbol{v_i} - \boldsymbol{v_E}$, changing to frame S^* and Eq. (2.44), we can expand Eq. (2.67) giving

[10]This work done is not actually measured in Joules but rather Joules per unit time per unit volume or for brevity, it is a volume power density.

$$Q_{tot} = \boldsymbol{j} \cdot \boldsymbol{E}^* + \boldsymbol{u} \cdot (\boldsymbol{j} \times \boldsymbol{B}). \tag{2.68}$$

The first term in Eq. (2.68) represents the Joule heating. There are two different interpretations on what Joule heating actually is: i) a form of 'ohmic heating' (due to electrical resistance) - is the generally more accepted interpretation, and ii) a 'frictional heating' between the ion and neutrals (Vasyliūnas and Song 2005). In this work, either interpretation maybe be used with the same results but we use interpretation i) - *ohmic heating*. The second term in Eq. (2.68) is merely the rate of change of kinetic energy associated with the ion drag or $\boldsymbol{j} \times \boldsymbol{B}$ force in frame S.

The above discussions described the energy change per unit volume resulting from the ion-neutral collisions associated with M-I coupling. As mentioned in section 2.3.1, for M-I coupling it is useful to calculate height-integrated quantities. The following discussion on energy/power will consider these. We mentioned in section 2.1.4 that angular momentum and energy are transferred from Jupiter to the ionosphere/thermosphere and then to the magnetosphere. We now introduce the macroscopic equations that describe the energy transfer from the planetary rotation to: (i) magnetospheric rotation, and (ii) heating of the neutral atmosphere. According to Hill (2001), the total power per unit area of the ionosphere extracted from planetary rotation, P is given by

$$P = \Omega_J \tau, \tag{2.69}$$

$$\tau = \rho_i i_P B_i, \tag{2.70}$$

where τ is the torque per unit area of the ionosphere exerted by the $\boldsymbol{j} \times \boldsymbol{B}$ force. P is then subdivided into the two components mentioned above, the smaller (in steady state) of which is the magnetospheric power P_M, used to accelerate the magnetospheric plasma

$$P_M = \Omega_M \tau. \tag{2.71}$$

The remainder of this power is dissipated in the upper atmosphere as heat and mechanical

work

$$P_A = (\Omega_J - \Omega_M)\tau. \tag{2.72}$$

Smith et al. (2005) found that the atmospheric power P_A consists of two components; namely, Joule heating P_J, and ion drag power P_D - dependent on the sub-corotation of the neutral atmosphere. These are given by

$$P_J = (\Omega_T - \Omega_M)\tau, \tag{2.73}$$

and

$$P_D = (\Omega_J - \Omega_T)\tau. \tag{2.74}$$

These expressions are usually expressed in units of $W\,m^{-2}$. We can integrate them over the appropriate region of the ionosphere to obtain total (global hemispheric) powers.

2.3.5 Precipitating electron flux

The Jovian UV aurora is created by downward precipitating electrons colliding with atmospheric hydrogen species. These downward electrons are carried along the magnetic field lines from the equatorial magnetodisc to the Jovian atmosphere by FACs. If we assume that the electrons in the magnetodisc form an isotropic Maxwellian distribution, and that they precipitate with a full downward loss cone (such that all electrons reach the atmosphere), then the maximum FAC that can flow without the presence of field-aligned potential drops[11] is $j_{||i0}$ and given by

$$j_{||i0} = eN\left(\frac{W_{th}}{2\pi m_e}\right)^{1/2}, \tag{2.75}$$

where e is magnitude of the electron charge, N is the electron number density, $W_{th} = k_B T$

[11] These potential drops accelerate the electrons along the field lines towards the planet.

is the thermal energy and k_B is the Boltzmann constant. The matching unaccelerated electron precipitating energy flux E_{f0} is

$$E_{f0} = 2NW_{th}\left(\frac{W_{th}}{2\pi m_e}\right)^{1/2}. \tag{2.76}$$

The work of Knight (1973) implies that if $j_{||i0}$ is smaller than $j_{||i}$ (Eq. (2.65)), field-aligned voltages are required in order to accelerate the current-carrying electrons, ensuring that they reach the atmosphere. The minimum potential difference needed for the acceleration is $\Phi_{||min}$

$$\Phi_{||min} = \frac{W_{th}}{e}\left(\left(\frac{j_{||i}}{j_{||i0}}\right) - 1\right), \tag{2.77}$$

where the above expression is only applicable if the top of the potential drop is located above a minimum radial distance r_{min} (Cowley et al. 2005, 2007)

$$\frac{r_{min}}{R_i} = \left(\frac{j_{||i}}{j_{||i0}}\right)^{1/3}, \tag{2.78}$$

where R_i is the radius of the Jovian ionosphere. By taking only upward (positive) FAC densities (obtained using Eq. (2.65)) we can then apply the method described in Lundin and Sandahl (1978) to calculate the enhanced precipitating electron energy flux E_f

$$E_f = \frac{E_{f0}}{2}\left(\left(\frac{j_{||i}}{j_{||i0}}\right)^2 + 1\right). \tag{2.79}$$

To allow for comparisons with similar, earlier studies, we use electron population parameters equal to those described in Cowley et al. (2005, 2007). These are obtained from Voyager electron data in Scudder et al. (1981) and Ulysses thermal electron data in Phillips et al. (1993a,b). These parameters are presented in Table 2.1.

Eq. (2.79) is a linear approximation to the theory of Knight (1973). We employ this method as it allows for comparison with previous studies (e.g. Cowley et al. (2007)). One

Table 2.1. Magnetospheric electron source parameters. This table is adapted from Table 1, Cowley et al. (2007). N represents the electron density, W_{th} the electron thermal energy, $j_{||i0}$ the unaccelerated current density and E_{f0} the unaccelerated energy flux.

Parameter	Open field lines	Outer magnetosphere	Middle magnetosphere
N / cm^{-3}	0.5	0.02	0.01
W_{th} / keV	0.05	0.25	2.5
$j_{\|\|i0}$ / μA m^{-2}	0.095	0.0085	0.013
E_{f0} / mW m^{-2}	0.0095	0.0042	0.067

limitation with the modelling carried out in this thesis and in the studies mentioned above is that they do not account for field-aligned potentials. This means that once these potentials have increased to values which result in a full downward loss cone, the FAC density is still allowed to increase, whereas in reality it should be saturated (Ray et al. 2010). The M-I coupling modelling by Ray et al. (2010) self-consistently incorporates field-aligned potentials which have interesting effects such as changing the electric field mapping between the ionosphere and magnetosphere (see section 3.3).

Modifications are currently being made to our model (Chapter 3) which include the field-aligned potentials described in Ray et al. (2010). For further information about accounting for these potentials the reader is referred to Ray et al. (2009, 2010, 2012).

The above sections describe the underlying science used in the field of magnetosphere-ionosphere-thermosphere coupling. In the following chapter we describe our coupled model. We begin by describing the thermospheric GCM that we employ, detailing all assumptions, boundary conditions and the governing equations of continuity, motion and energy. Descriptions of the ionosphere and magnetosphere models used is then presented along with the modifications required in order to obtain the work presented in Chapters 3-6.

Chapter 3

Jovian Model

All sorts of computer errors are now turning up. You'd be surprised to know the number of doctors who claim they are treating pregnant men.

Isaac Asimov

This chapter describes the main features of the model used in Chapters 4 - 6. We discuss the concepts developed in Chapters 1 and 2 and how they are applied in our coupled magnetosphere-ionosphere-thermosphere model.

3.1 Thermosphere model

The thermosphere model used herein is based on a model developed for the Earth over three decades ago by Fuller-Rowell (1981). Over the years this model has undergone many changes including the coupling of the ionosphere and plasmasphere (CTIM and CTIP)(Fuller-Rowell et al. 1996; Millward et al. 1996). Achilleos et al. (1998) was the first study to implement a three-dimensional Jovian Ionosphere Model (JIM) using components from CTIM and CTIP. JIM led to the investigation of various areas of the Jovian thermosphere-ionosphere (e.g. Millward et al. (2005)) but due to its computational complexity, runtimes were very long. The next step in adapting Fuller-Rowell (1981)'s thermosphere model came when CTIM and CTIP were modified to model Titan's thermosphere (Müller-Wodarg et al. 2000) and subsequently its host planet - Saturn (Müller-Wodarg

et al. 2006). Smith and Aylward (2008) modified the Saturn model further by removing a dimension. This allowed Smith and Aylward (2008) to more easily investigate the effect of M-I coupling on the Kronian thermosphere. The same authors later modified their Kronian model in order to carry out similar investigations at Jupiter (Smith and Aylward 2009). It is essentially this Jovian model with some modifications which we use in the studies herein.

3.1.1 Thermospheric model details

The thermosphere model described below solves the non-linear Navier-Stokes equations for momentum, energy and continuity, using finite difference and explicit time integration[1] (Müller-Wodarg et al. 2006). The model has fixed spherical coordinates measured in co-latitude[2] θ and east longitude ϕ. The third coordinate is pressure p (instead of altitude z). Although the thermosphere model has three coordinates it assumes azimuthal symmetry and, as such, there are vanishing derivatives in the ϕ direction. For this reason we shall treat the thermosphere as a two-dimensional system with pressure (altitude) and co-latitude (latitude) coordinates. The resolution of the model grid is $0.2\,^\circ$ in latitude, and 0.4 pressure scale heights in the vertical direction. The axisymmetric assumption does not greatly influence the basic physics underlying the conclusions of this study (see also Smith and Aylward (2009)).

The Jovian homopause and mesopause lie practically at the same altitude; the mesopause is thus selected as the lower boundary of the thermosphere model used herein. The lower boundary is chosen to be a fixed pressure and altitude surface where temperature is constant and the velocity of the neutrals in the corotating frame is equal to zero (Smith 2006). Below the mesopause/homopause, hydrocarbons are abundant and their radiative cooling is efficient enough to keep local temperatures relatively stable. The negligible neutral wind speed is also somewhat expected as eddy viscosity is thought to be a dominant process around the mesopause. In accordance with the Achilleos et al. (1998) (JIM) and Grodent et al. (2001) (see section 3.2) models, the lower boundary pressure and temperature are $2\,\mu$bar (0.2 Pa; 300 km above the 1 bar level) and 260 K respectively. The upper boundary surface has a pressure of 0.02 nbar.

[1] A forward Euler time-stepping method is used to carry out the numerical time integration (Smith 2006).

[2] Starting from the North pole.

3.1.2 Pressure coordinates and the continuity equation

We use a vertical pressure coordinate system in place of an altitude system for two reasons: i) the assumption that the thermosphere lies in hydrostatic equilibrium[3] and ii) the continuity equation (see below) is considerably simplified in a pressure coordinate system compared to an altitude system.

The thermosphere model has n constant pressure surfaces determined by pressure scale heights. The pressure at each $n = 1, 2, 3...$ surface is given by $p(n)$,

$$p(n) = p_m exp\left(-\gamma(n-1)\right) \tag{3.1}$$

where p_m is the pressure at the mesopause (lower boundary of model) and γ is a dimensionless quantity representing the gap between the pressure levels (dependent on the local scale height):

$$\gamma = \frac{z_n - z_{n-1}}{H}. \tag{3.2}$$

Integrating Eq. (2.20) gives the altitude at specific pressures. However, this reveals a problem with using pressure coordinates. A constant pressure surface is not truly horizontal. Different regions of the atmosphere will have different thermal structures and this can lead to a slightly tilted pressure surface. In practice, pressure levels are only slightly tilted with respect to the horizontal, making the Cartesian pressure coordinate system, (x, y, p), approximately orthogonal.

Below we describe some necessary steps in converting from Cartesian-altitude coordinates to Cartesian-pressure coordinates (Fuller-Rowell 1981; Smith 2006)[4]. The gravitational potential Φ is defined (in Cartesian coordinates) as:

[3]The model thermosphere is actually in a state of quasi hydrostatic equilibrium, meaning that there are no strong vertical winds and small vertical winds are treated as perturbations of the equilibrium state (Smith 2006).

[4]A derivation for converting between altitude and pressure coordinates can be found in Appendix E of Smith (2006) or in Jacobson (2005).

$$d\Phi = gdz. \tag{3.3}$$

If we combine Eqs. (3.3 and 2.20), the gravitational potential can be used to define the equation for hydrostatic equilibrium such that

$$\frac{d\Phi}{dp} = -\frac{1}{\rho}. \tag{3.4}$$

Let us now define some scalar a for which its partial derivative with respect to x, whilst keeping z fixed can be given by

$$\left.\frac{\partial a}{\partial x}\right|_z = \left.\frac{\partial a}{\partial x}\right|_p + \rho\frac{\partial a}{\partial p}\left.\frac{\partial \Phi}{\partial x}\right|_p. \tag{3.5}$$

The left hand side is merely the horizontal spatial derivative of a but the right hand side shows that the spatial derivative at constant altitude z has two components in the pressure coordinate system. The first representing movement along the slightly tilted constant pressure surface and the second compensating for the change in altitude along the pressure surface. If we carry out similar operations with respect to y and t and use a vector $\mathbf{a}$, we obtain the horizontal divergence for both surfaces of fixed altitude ∇_z and pressure ∇_p.

$$\nabla_z \cdot \mathbf{a} = \nabla_p \cdot \mathbf{a} + \rho\frac{\partial \mathbf{a}}{\partial p} \cdot \nabla_p \Phi. \tag{3.6}$$

The above transformations allow us to convert from vertical velocity in altitude coordinates u_z to vertical velocity in pressure coordinates w. Given that

$$w = \frac{Dp}{Dt} \tag{3.7}$$

where D/Dt is the *total (material)* derivative. u_z is defined as:

$$u_z = \left.\frac{\partial z}{\partial t}\right|_p + \mathbf{u} \cdot \nabla_p z - \frac{w}{\rho g}. \tag{3.8}$$

Eq. (3.8) consists of three parts, from left to right, these terms represent: i) vertical velocity caused by the vertical motion of the pressure surface; ii) vertical velocity associated with flow along the fixed pressure surface and iii) vertical flow relative to the fixed pressure surface.

The continuity equation describing the flow of mass in a hydrodynamic system, assuming that there are no sources and sinks, is given by

$$\frac{\partial \rho}{\partial t} + \nabla \cdot (\rho \mathbf{u}) = 0. \tag{3.9}$$

Converting Eq. (3.9) into pressure coordinates by using Eqs. (3.6 and 3.8) gives the continuity equation in pressure coordinates:

$$\nabla_p \cdot \mathbf{u} + \frac{\partial w}{\partial p} = 0. \tag{3.10}$$

This equation indicates that the divergence of horizontal velocity (on the constant pressure surfaces) is balanced by the divergence (with respect to pressure) of the vertical velocity w. This equation can be used to calculate w from $\mathbf{u}$, if we assume that there is no mass outflow from the top level of the model i.e. $w = 0$. Mass outflow and inflow at the bottom level must therefore be present in order for continuity to be conserved (Smith 2006).

In the following sections, we discuss the horizontal equation of motion and the energy equation employed in our thermosphere model.

3.1.3 Horizontal equation of motion

We begin this section by stating Newton's second law

$$\mathbf{F} = m\mathbf{a}, \tag{3.11}$$

where $\mathbf{F}$ is force, m is mass and $\mathbf{a}$ is acceleration. We can alter Eq. (3.11) in order obtain a force per unit mass $\mathbf{f}$ acting on a fluid:

$$\mathbf{f} = \frac{D\mathbf{u}}{Dt}, \tag{3.12}$$

where $\mathbf{u}$ is the horizontal velocity and the total time derivative is given by

$$\frac{D}{Dt} = \frac{\partial}{\partial t} + \mathbf{u} \cdot \nabla. \tag{3.13}$$

If we let $\mathbf{u} = u_i e_i$ where u_i and e_i are the components and respective unit vectors of $\mathbf{u}$, and the subscript i represents the index of dimensions of $\mathbf{u}$. By substituting $\mathbf{u}$ in Eq. (3.12) and using the chain rule to differentiate $u_i e_i$ gives

$$\mathbf{f} = \left[\frac{\partial u_i}{\partial t} + u_k \frac{\partial u_i}{\partial x_k}\right] e_i + u_i \left[\frac{\partial e_i}{\partial t} + u_k \frac{\partial e_i}{\partial x_k}\right], \tag{3.14}$$

where we now sum implicitly over k. $\partial e_i / \partial t = 0$ as unit vectors do not explicitly change with time. So Eq. (3.14) can be rearranged to

$$\frac{\partial u_i}{\partial t} e_i = \mathbf{f} - u_k \frac{\partial u_i}{\partial x_k} e_i - u_i u_k \frac{\partial e_i}{\partial x_k}. \tag{3.15}$$

This equation represents the partial time derivative of each component of velocity $\mathbf{u}$ in terms of: i) the sum of true forces acting on the gas (first term on the RHS); ii) the advection of velocity (second term on the RHS); and iii) fictitious forces resulting from the advection of the coordinate system (third term on the RHS). This derivative is used to calculate the change in velocity at a point fixed in space (Smith 2006).

True forces

The true horizontal forces per unit mass on the model gas are represented by

$$\mathbf{f} = \mathbf{f_P} + \mathbf{f}_\eta + \mathbf{f_D}, \tag{3.16}$$

where $\mathbf{f_P}$ is the pressure gradient force, $\mathbf{f}_\eta$ is the horizontal and vertical viscosity and $\mathbf{f_D}$ is the ion drag.

Pressure gradient $\mathbf{f_P}$

The force per unit mass due to the horizontal pressure gradient is

$$\mathbf{f_P} = \frac{-1}{\rho}\nabla_z p, \tag{3.17}$$

in the altitude coordinate system. To change to pressure coordinates we can use Eq. (3.6). This gives the pressure gradient force in the pressure coordinate system as:

$$\mathbf{f_P} = -\nabla_p \Phi = -g\nabla_p z. \tag{3.18}$$

$\mathbf{f_P}$ can be thus be thought of as the pressure gradient or the component of gravity acting along the tilted fixed pressure surface.

Viscous force $\mathbf{f}_\eta$

The viscous force term has already been described in section 2.2.2 but for an altitude coordinate system. As in Smith (2006) we divide the viscous force into two components (horizontal and vertical)

$$\mathbf{f}_\eta = \mathbf{f}_{\eta\mathbf{xy}} + \mathbf{f}_{\eta\mathbf{z}}. \tag{3.19}$$

Horizontal viscosity is expected to be relatively small compared to vertical viscosity and more importantly, any coupling between the two is expected to be negligible.

The total viscous force $\mathbf{f}_\eta$ is thus given by

$$\mathbf{f}_\eta = \frac{\eta}{\rho}\nabla_p^2\mathbf{u} + g^2\frac{\partial}{\partial p}\left(\eta\rho\frac{\partial \mathbf{u}}{\partial p}\right). \tag{3.20}$$

The first term on the RHS is the horizontal component and the second term is the vertical component (obtained by converting Eq. (2.29) from altitude to pressure coordinates). The horizontal component is approximated using a simple diffusion equation as it is not expected to vary significantly along fixed pressure surfaces (Smith 2006).

Ion drag force $\mathbf{f_D}$

The ion drag force was discussed in section 2.3.4. The ion drag force per unit mass $\mathbf{f_D}$ is:

$$\mathbf{f_D} = \frac{1}{\rho}\mathbf{j}\times\mathbf{B}, \tag{3.21}$$

where $\mathbf{j}$ is the ionospheric current density and $\mathbf{B}$ is the magnetic field.

Advection force

The advective portion of Eq. (3.15) for the altitude coordinate system needs to be converted to the pressure coordinates. This can be achieved by comparing the material derivative in the altitude coordinate system with that in the pressure system:

$$u_k\frac{\partial u_i}{\partial x_k}e_i = \mathbf{u}\cdot\nabla_p + w\frac{\partial}{\partial p}. \tag{3.22}$$

The RHS of this equation is the advective term in pressure coordinates. The total horizontal (θ and ϕ components) advection term in the equation of motion is:

$$-u_k\frac{\partial u_i}{\partial x_k}e_i = -e_\theta\left(\mathbf{u}\cdot\nabla_p u_\theta + w\frac{\partial u_\theta}{\partial p}\right) - e_\phi\left(\mathbf{u}\cdot\nabla_p u_\phi + w\frac{\partial u_\phi}{\partial p}\right). \tag{3.23}$$

The parts of the above terms dependent on ∇_p represents the advection of momentum by

horizontal wind parallel to the fixed pressure surfaces whilst the partial differential part (involving $\partial/\partial p$) represents the vertical advection of winds flowing across the pressure surfaces (Smith 2006).

Fictitious forces $\mathbf{f_C}$

The fictitious forces in the horizontal equation of motion are represented in the third term on the RHS of Eq. (3.15). These forces, Coriolis and curvature, respectively result from the use of a non-inertial frame as well as the use of non-Cartesian coordinates in our model. As they are fictitious, they do no work on the system. Complete derivations for these forces are described in Appendix D of Smith (2006). The summed θ and ϕ components of both these forces are are stated below:

$$f_{C\theta} = \frac{u_\phi^2 \cot\theta}{R_J} - \frac{u_r u_\theta}{R_J} - 2\Omega_J u_\phi \cos\theta, \tag{3.24}$$

$$f_{C\phi} = -\frac{u_\phi u_\theta \cot\theta}{R_J} - \frac{u_\phi u_r}{R_J} + 2\Omega_J u_\theta \cos\theta, \tag{3.25}$$

where u_r is the vertical neutral wind velocity. The first two terms in Eqs. (3.24 and 3.25) represent the curvature force and the the third term represents the Coriolis force. The total fictitious force is thus

$$\mathbf{f_C} = f_{C\theta}\,\hat{\theta} + f_{C\phi}\,\hat{\phi}. \tag{3.26}$$

3.1.4 Thermospheric energy equation

We now discuss the energy equation used in our thermospheric model. Let us consider a fluid parcel moving at some velocity v. This parcel possesses three types of energy per unit mass: i) the kinetic energy $E_K = \frac{1}{2}v^2$; ii) the internal energy[5] $U = c_p T$; and iii) the gravitational potential energy Φ.

The first law of thermodynamics (a form of the conservation of energy) states that the rate of change of energy in a system is equal to the sum of heating and work (sources and

[5]The heat capacity per unit mass at constant pressure c_p is used to calculate the internal energy as it includes the energy needed to increase the gravitational potential as the atmosphere expands (Smith 2006).

sinks). Applying this principle to our thermosphere gives

$$\frac{D\psi}{Dt} + \frac{D\Phi}{Dt} = q_g + q, \tag{3.27}$$

where $\psi = E_K + U$, q_g is the work done by gravity and q is the sum of other energy sources and sinks (discussed below). If we assume that the acceleration due to gravity g is constant over the height of the thermosphere[6], q_g is given by

$$q_g = u_z g = g\frac{Dz}{Dt} = \frac{D\Phi}{Dt}. \tag{3.28}$$

q_g cancels out with the total rate of change of the gravitational potential energy. Incorporating this in Eq. (3.27) and expanding the total derivative (as done in section 3.1.3) gives

$$\frac{\partial\psi}{\partial t} = q - \mathbf{u}.\nabla_p\psi - w\frac{\partial\psi}{\partial p}, \tag{3.29}$$

where the advective term (second and third) has already been converted into pressure coordinates. q is defined as:

$$q = q_P + q_D + q_J + q_\eta + q_\kappa + q_\nu, \tag{3.30}$$

where the individual components of q consist of the work done from: pressure gradients (q_P), ion drag (q_D) and viscosity (q_η); along with heating from: Joule heating (q_J), thermal conduction (q_κ) and solar radiation (q_ν). We now describe these individual heating terms in more detail.

Work done by pressure gradients q_P

As discussed above, the constant pressure surfaces are slightly tilted compared to the horizontal. This leads to the work done by pressure gradients being divided into vertical

[6] Appropriate when one thinks that the vertical extent of the thermosphere is only a few 1000 km compared to the radius of Jupiter (71492 km).

and horizontal components:

$$q_P = q_{Pz} + q_{Pxy}, \tag{3.31}$$

Work done (per unit time) is the scalar product of velocity and force. The component of velocity which flows vertically with respect to the constant pressure surface is $w/(\rho g)$ (last term on the RHS of Eq. (3.8)). Thus, the vertical work done is

$$q_{Pz} = -\frac{w}{\rho g}\frac{1}{\rho}\frac{dp}{dz} = \frac{w}{\rho}. \tag{3.32}$$

This vertical pressure component corresponds to adiabatic heating (positive w) or cooling (negative w) term.

The work done by the horizontal component of the pressure gradient is:

$$q_{Pxy} = -\mathbf{u}.\frac{1}{\rho}\nabla_z p = -\mathbf{u}.g\nabla_p z. \tag{3.33}$$

Both versions of q_{Pxy} are equivalent as long as we assume that the tilt angle of the pressure surface with respect to the horizontal is small[7]. The total work done by pressure gradients is thus:

$$q_P = -\mathbf{u}.g\nabla_p z + \frac{w}{\rho}. \tag{3.34}$$

Work done by ion drag q_D

The work done by ion drag has been described in section 2.3.4, it is just the scalar product of velocity $\mathbf{u}$ with $\mathbf{f_D}$:

$$q_D = \mathbf{u}.\frac{1}{\rho}\mathbf{j} \times \mathbf{B}. \tag{3.35}$$

[7]Such that $\sin\theta \approx \theta$.

Joule heating q_J

Joule heating has been described in section 2.3.4, and is:

$$q_J = \frac{1}{\rho}\mathbf{j}.\mathbf{E}^*, \tag{3.36}$$

where E^* is the rest-frame ionospheric electric field.

Work done by viscosity q_η

As discussed in section 2.2.2, the total work done by the viscous force is a combination of a change in kinetic energy and a viscous heating. Converting Eq. (2.30) into pressure coordinates and dividing by the mass density ρ gives the work done by the viscous force per unit mass:

$$q_\eta = g^2 \frac{\partial}{\partial p}\left(\eta\rho\mathbf{u}.\frac{\partial \mathbf{u}}{\partial p}\right). \tag{3.37}$$

Thermal conductivity q_κ

The heating caused by the thermospheric thermal conductivity can be obtained by taking the divergence of the thermal heating flux (Eq. (2.27)) and dividing by ρ. The total heating rate due to thermal conduction is

$$q_\kappa = \frac{\kappa}{\rho}\nabla_p^2 T + g^2 \frac{\partial}{\partial p}\left(\kappa\rho\frac{\partial T}{\partial p}\right), \tag{3.38}$$

where $\kappa = \kappa_m + \kappa_e$ (respectively the thermal conductivities for molecular and eddy conduction). The first term represents the horizontal heating and the second term corresponds to vertical heating.

Radiation q_ν

Radiation consists of two components: i) Absorption of solar radiation and ii) Radiative cooling by thermospheric species.

The absorption of solar radiation is a small energy source in this model (Smith 2006). Waite et al. (1983) calculated that the total energy deposited by solar EUV (assuming 50 % absorption efficiency) in the Jovian thermosphere amounted to ∼1.2 TW. This is considerably smaller than all the other energy sources discussed herein. We implement the absorption of solar radiation as described in the studies of Moore et al. (2004) and Müller-Wodarg et al. (2006), who use solar EUV fluxes from version 2.24 of the SOLAR 2000 model (Tobiska et al. 2000; Tobiska 2004). We employ solar minimum conditions for all simulations presented in Chapters 4 - 6. The solar minimum fluxes are averaged from September 14-17 1996, giving a F10.7 solar flux of 70 . This results in a total solar EUV heating rate of ∼0.15 TW which is approximately two orders of magnitude smaller than Joule heating. For more details regarding solar heating the reader is referred to the studies by Moore et al. (2004) and Müller-Wodarg et al. (2006).

Radiative cooling due to IR emission from H_3^+ is not included in the model at the present time. Ground-based observations of an auroral heating event (Stallard et al. 2001, 2002; Melin et al. 2006), showed that the magnitude of the H_3^+ cooling rate was ≤ 10 % of typical Joule heating rates. Melin et al. (2006) also found that H_3^+ cooling rates are at least an order of magnitude larger than cooling by downward conduction. Modelling by Tao et al. (2009) shows that it has a magnitude ≤ 10 % of the typical Joule heating rate and at least an order of magnitude less than downward conduction across most altitudes in the thermosphere. A future modification of our coupled model will included H_3^+ emission in order to simulate a more physically realistic system.

Advection

The advective term can be calculated in much the same way as for the momentum equation in section 3.1.3.

$$u_k \frac{\partial \psi}{\partial x_k} = \mathbf{u} \cdot \nabla_p \psi + w \frac{\partial \psi}{\partial p}. \tag{3.39}$$

It represents the transport of energy (internal and kinetic) by horizontal winds flowing along the fixed pressure surfaces and by vertical winds flowing across the pressure surfaces.

3.2 Ionosphere model

This coupled model was created as a tool to investigate how the magnetosphere influences thermospheric dynamics, particularly in the magnetodisc region. A full ionospheric description, such as JIM (Achilleos et al. 1998), would considerably increase the model runtime and complexity. Smith (2006) concluded that in order to more simply represent the effect of the ionosphere on the pure thermospheric dynamics, a simplified auroral conductivity model could be coupled to the thermosphere model (section 3.1). This conductivity model consists of both horizontal (Nichols and Cowley 2004) and vertical (Grodent et al. 2001) components which we shall briefly summarise in sections 3.2.1 and 3.2.2. For a more detailed description of the conductivity model employed, the reader is referred to the following studies: Nichols and Cowley (2004); Grodent et al. (2001).

3.2.1 Horizontal conductivity model

Nichols and Cowley (2004) created an analytical model for the height-integrated Pedersen conductance Σ_P using modelling carried out by Millward et al. (2002). This model allows for the enhancement of Σ_P by FACs[8] and is thus a function of FAC density and consequently ionospheric latitude. The enhancement of Σ_P is considered only for upward (positive) FACs in the inner and middle magnetosphere regions. The latitudinal profile for Σ_P is obtained using (Nichols and Cowley 2004):

$$\Sigma_P(j_{||i}) = \Sigma_{PO} + \Sigma_{Pj}(j_{||i}), \tag{3.40}$$

where

$$\Sigma_{Pj}(j_{||i}) = 0.16 j_{||i} + \left\{ 2.45 \left[\frac{(j_{||i}/0.075)^2}{1 + (j_{||i}/0.075)^2} \right] \times \frac{1}{[1 + exp(-(j_{||i} - 0.22)/0.12)]} \right\}. \tag{3.41}$$

$\Sigma_{PO} = 0.0275$ mho is the background conductivity due to solar photoionisation (Hill 1980), and $\Sigma_{Pj}(j_{||i})$ in mho is an auroral enhancement due to the FAC density $j_{||i}$ in μA m^{-2}.

[8] Enhancements result from a higher flux of precipitating auroral electrons which increases the production rate of ionospheric plasma.

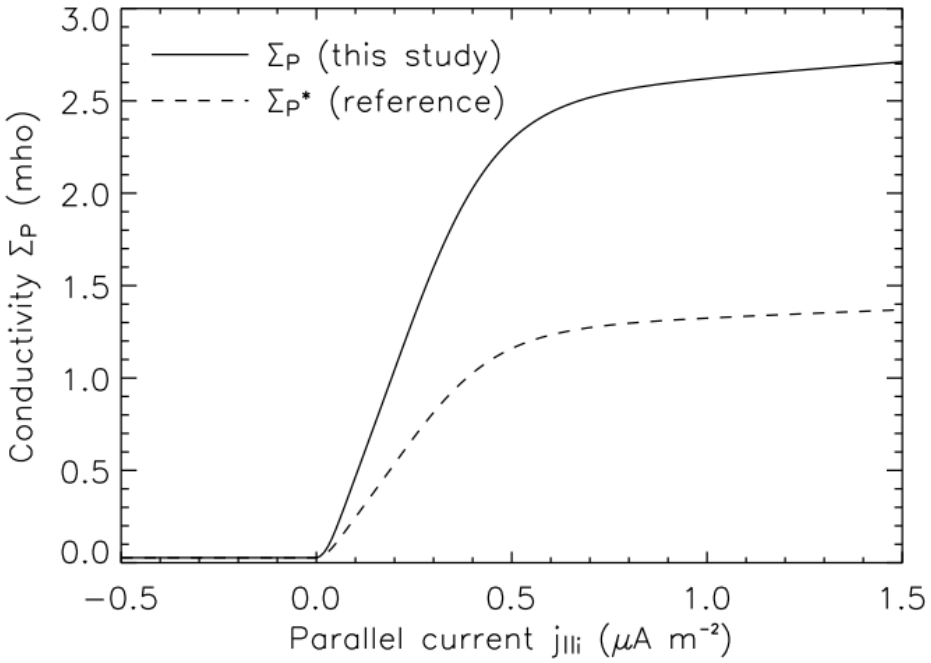

Figure 3.1. Height-integrated Pedersen conductance as a function of FAC densities. The solid line represents the true height-integrated Pedersen conductance (used in this model) whilst the dashed line represents the 'effective' conductance (used in Nichols and Cowley (2004)). This Figure is from Smith and Aylward (2009).

The dependence of the Hall conductance Σ_H on $j_{||i}$ is also calculated using similar formulae (e.g. Luhmann (1995 p.201)). The total conductivity in the ionisation region is dominated by Σ_P due to the small values of Σ_H (see Fig. 3.2).

The solid line in Fig. 3.1 (Smith and Aylward 2009) shows Σ_P as a function of FAC density in the present study. It also shows the final profile used by Nichols and Cowley (2004) (dashed line). The difference between the two profiles results from our use of the true height-integrated Pedersen conductance whilst Nichols and Cowley (2004) use an 'effective' conductance $\Sigma_P^* = (1 - K)\Sigma_P$. Nichols and Cowley (2004) use a value of $K = 0.5$ in attempting to include the 'slippage' of the thermosphere. However, subsequent work by Smith and Aylward (2009); Yates et al. (2012) found this approximation to be inadequate (see section 4.2.1). We calculate the thermospheric angular velocity using the GCM described in section 3.1.

In the outer magnetosphere and polar cap regions, conductivity enhancement is likely

Table 3.1. Steady state Pedersen conductances in our model thermosphere. General regions of the thermosphere are indicated in the left column whilst their respective ionospheric latitude is indicated in the middle column. The right column shows the value/profile of the height-integrated Pedersen conductance assumed in each respective region.

Location	Ionospheric latitude / °	Σ_P / mho
Equatorial	< 60	0.0275
Auroral	$60 \leq \theta \leq 74$	as given by Eq. (3.40)
Polar regions	> 74	0.2

Table 3.2. Transient state Pedersen conductances in our model thermosphere. General regions of the thermosphere are indicated in the left column whilst their respective ionospheric latitude is indicated in the middle column. The right column shows the value/profile of the height-integrated Pedersen conductance assumed in each respective region.

Location	Ionospheric latitude / °	Σ_P / mho
Equatorial	< 60	0.0275
Auroral	$60 \leq \theta \leq 74$	0.5
Polar regions	> 74	0.2

to be present since UV and IR auroral emissions are detected. Cowley et al. (2005) set Σ_P^*=0.2 mho in these regions in accordance with the theory of Isbell et al. (1984). To allow for comparison, we employ the same fixed conductivity value in these regions but assigned to the true Pedersen conductance Σ_P.

The enhanced conductivity component of the ionosphere model (given by Eq. (3.40)) is only used in the steady state work described in Chapter 4. For clarity, the steady-state Pedersen conductances used in different regions of the thermosphere are summarised in Table 3.1. Conductivity enhancements by FACs are not included in the transient work described in Chapters 5 and 6 in order to simplify the response of the thermosphere (see section 3.5.2). A constant Pedersen conductance ($\Sigma_P = 0.5$ mho in the inner and middle magnetosphere) is used instead. Conductivities in the equatorial regions (Σ_{PO}) and outer magnetosphere along with the polar cap regions remain unchanged throughout all the studies presented here. Transient Pedersen conductances in the thermosphere are summarised in Table 3.2.

3.2.2 Vertical dependence of conductivity

The Jovian one-dimensional auroral ionosphere model developed by Grodent et al. (2001) is used to establish the pressure (vertical) dependence of ionospheric conductivity. The auroral model uses a two-stream electron transport code to calculate auroral electron and ion densities. There are two versions of this model, i.e. 'diffuse' and 'discrete' but for our studies, both versions produce similar results at altitudes relevant to our thermosphere model. We employ the diffuse version as it covers a greater region of the main auroral oval and polar cap.

The Grodent et al. (2001) model outputs Pedersen and Hall conductivity profiles for a fixed thermal structure. However our thermosphere model has a variable thermal structure which is a function of latitude. In order to maintain realistic height-integrated conductivities in the model, at each pressure level we calculate the conductivity per unit mass as follows (Smith and Aylward 2009)

$$s_i = \frac{\sigma_i}{\rho}, \tag{3.42}$$

where i=P or H representing Pedersen or Hall, σ is the conductivity and ρ is the neutral mass density obtained from the thermosphere model. Conductivities and their 'per unit mass' counterparts are shown in Fig. 3.2 as functions of thermospheric pressure (obtained from Smith and Aylward (2009)). This Figure shows that Pedersen conductivities dominate over Hall conductivities at almost all pressure levels (altitude). By calculating σ_P and σ_H from the Grodent et al. (2001) thermal structure model we can obtain values of s_i. The s_i vertical profiles are constant throughout our thermosphere; thus height-integrated Pedersen (Σ_P) and Hall (Σ_H) conductances depend solely on s_i and not thermal structure, as shown below:

$$\Sigma_i = g \int_{p_1}^{p_0} s_i dp, \tag{3.43}$$

Once vertical s_i profiles are calculated, their magnitudes are scaled in order to match the value of Σ_i calculated as a function of latitude (see section 3.2.1). We define the

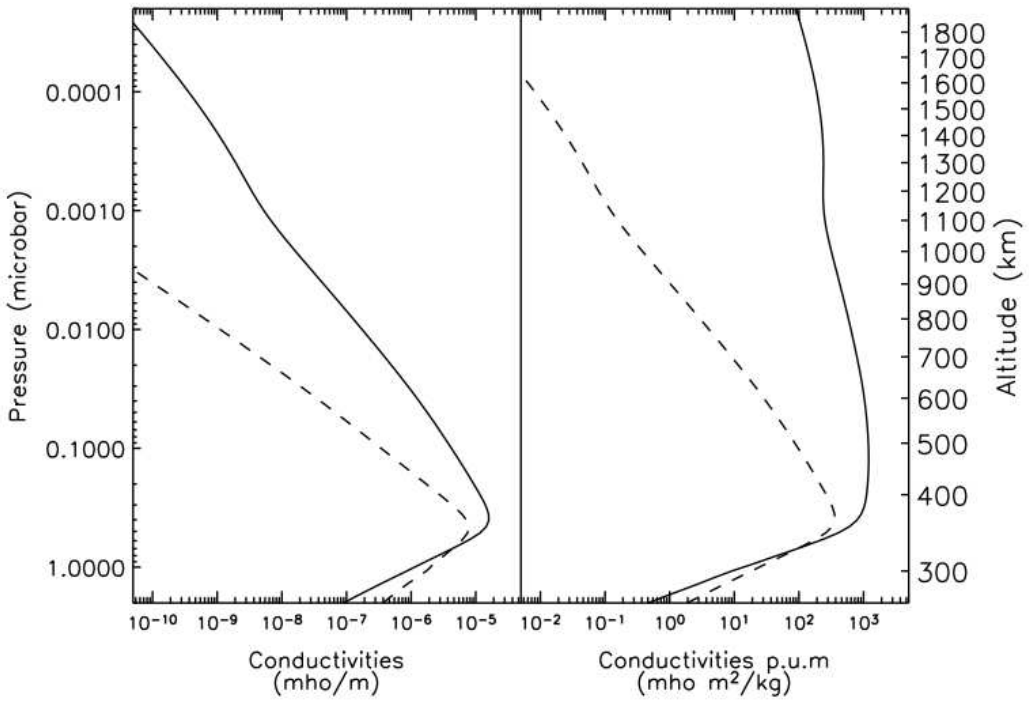

Figure 3.2. Vertical profile for Pedersen and Hall conductivities (left plot) and the conductivities per unit mass (right plot). Pedersen conductivity is represented by the solid lines whilst Hall conductivity is represented by the dashed lines. This Figure is from Smith and Aylward (2009).

Pedersen conducting layer as the region with conductivity greater than 10 % of the Pedersen conductivity at the auroral ionisation peak, located at pressures of $\sim 0.8 - 0.04\,\mu$bar or at altitudes of $\sim 350 - 600$ km above the 1 bar level.

3.3 Magnetosphere model

The magnetosphere model component used in this thesis is essentially the same as that used by Smith and Aylward (2009), based on the Cowley et al. (2005) axisymmetric model for the entire magnetosphere and the more advanced middle magnetosphere model proposed by Nichols and Cowley (2004). The difference between the Smith and Aylward (2009) model and the one used in this study is that we also use the formalism from Cowley et al. (2007) to calculate equatorial magnetic profiles for compressed and expanded configurations of the magnetosphere. For modelling purposes we split the magnetosphere into two major parts, each compromising of two regions: i) the inner and middle magnetosphere (Nichols and Cowley 2004) and ii) the outer magnetosphere and the open field lines (Cowley et al. 2005). For brevity we label these four regions using Roman numerals I-IV. Region I represents the

Dungey-type interaction of the polar, open field lines with the solar wind. The closed field lines of the outer magnetosphere are involved in Dungey and Vasyliunas cycles (associated with mass loss from the disc) are represented by region II. Regions III (shaded region in subsequent figures) and IV represent the middle magnetosphere (magnetodisc) and the corotating inner magnetosphere respectively (see Fig. 3.4).

3.3.1 Middle magnetosphere model

Our middle magnetosphere model uses equatorial profiles of magnetic field strength, along with the corresponding flux function (the flux function is the magnetic flux per radian of azimuth integrated from the given location to infinity). For the axisymmetric, poloidal field models which we employ, surfaces of constant flux function define a shell of field lines with a common equatorial radial distance ρ_e and ionospheric co-latitude θ_i. This allows us to magnetically map the ionosphere to the equatorial plane using $F_i(\theta_i)=F_e(\rho_e)$ (Nichols and Cowley 2004). The ionospheric form of the flux function is given by

$$F_i(\theta_i) = B_J \rho_i^2 = B_J R_i^2 \sin^2\theta_i. \tag{3.44}$$

The equatorial magnetic field in the middle magnetosphere, B_{ze}, and corresponding flux function, F_e, in this region are given by the equations below (Nichols and Cowley 2004)

$$B_{ze}(\rho_e) = -B_o \left(\frac{R_J}{\rho_e}\right)^3 \exp\left[-\left(\frac{\rho_e}{\rho_{eo}}\right)^{5/2}\right] - A\left(\frac{R_J}{\rho_e}\right)^m, \tag{3.45}$$

$$F_e(\rho_e) = F_\infty + \frac{B_o R_J^3}{2.5\rho_{eo}}\Gamma\left[-\frac{2}{5}, \left(\frac{\rho_e}{\rho_{eo}}\right)^{5/2}\right] + \frac{AR_J^2}{m-2}\left(\frac{R_J}{\rho_e}\right)^{m-2}, \tag{3.46}$$

where B_o=3.335 $\times 10^5$ nT, ρ_{eo}=14.501 R_J, A=5.4 $\times 10^4$ nT, m=2.71 , $F_\infty \approx$2.841 $\times 10^4$ nT R_J^2, and $\Gamma(a,z)=\int_z^\infty t^{a-1}e^{-t}dt$ is the incomplete gamma function. These parameters represent an analytical fit to spacecraft magnetometer data (Connerney et al. 1981; Khurana and Kivelson 1993). The magnetic field model has a grid resolution of 0.01 R_J which, when magnetically mapped to the ionosphere, produces footprints of the field lines separated by angles equal to or smaller than the thermospheric model's latitudinal grid spacing. This is a sufficient condition to sample realistic FAC profiles and thermospheric flow patterns

within the ionospheric part of the model.

Using Eqs. (3.45 - 3.46) as a starting point we are able to calculate model magnetic fields and flux functions corresponding to states of differing magnetospheric size. These models are valid within the range of $\sim$5 R_J to near the magnetopause, however in this study we employ a middle magnetosphere with maximum radial distance of 85 R_J. Cowley et al. (2007) assume that Jupiter's magnetosphere consists of two components; the middle and the outer regions. They take the equatorial magnetic field strength in the outer magnetosphere (beyond 65 R_J for their 'baseline' case) to be constant between $\sim$5 and $\sim$15 nT. Using Eqs. (3.45-3.46), valid only within the middle magnetosphere, we apply their method of compressing and expanding this region's magnetic field configuration. We then use our middle magnetosphere field model to obtain solutions for plasma angular velocity Ω_M in this region (section 3.4.1). For the outer magnetosphere we shall use constant, assumed values of Ω_M (see section 3.3.2).

The magnetosphere model described above was implemented by Smith and Aylward (2009). The additions to this magnetosphere model implemented by me, as part of this PhD thesis, involve allowing the model to calculate different magnetic field profiles depending on the size of the magnetodisc. This is described below for the middle magnetosphere. Different magnetospheric configurations will possess different plasma angular velocities in the outer magnetosphere region; we also implement such changes as part of my thesis work (see section 3.3.2 for further details).

Using the principles of magnetic flux conservation described by Cowley et al. (2007), we were able to calculate equatorial field profiles for Jupiter's magnetosphere for different values of solar wind dynamic pressure. To compress (resp. expand) a magnetodisc (middle magnetosphere) from an initial radius R_{MMO}, a uniform southward (resp. northward) perturbation field, ΔB_z, is applied to our initial magnetospheric model (described by equations Eqs. (3.45-3.46)). The formalism in Cowley et al. (2007) enables us to calculate ΔB_z as a function of magnetodisc radius R_{MM}. At a given R_{MM} ('final' disc radius), the flux conservation condition is

Table 3.3. Three different steady state magnetospheric configurations used in Chapter 4. The radii of the magnetodisc R_{MM} and magnetopause R_{MP} are shown along with the values of the perturbation field. Note R_{MP} is calculated as in Cowley et al. (2007). Solar wind dynamic pressure (P_{SW}) is also shown for both Joy et al. (2002) and Huddleston et al. (1998) magnetopause models (J or H respectively).

Case	A	B	C
R_{MM}/ R_J	45	65	85
R_{MP}/ R_J	68	85	101
ΔB_z/ nT	−1.16	0.0	0.19
P_{SWJ}/ nPa	0.213	0.063	0.021
P_{SWH}/ nPa	0.052	0.019	0.009

$$-\pi R_{MM}^2 \Delta B_z = 2\pi \left(F_O\left(R_{MM}\right) - F_O\left(R_{MMO}\right)\right), \tag{3.47}$$

where F_O is the initial profile of the flux function (given by Eq. (3.46)). Rearranging to solve for ΔB_z

$$\Delta B_z = \frac{-2\Delta F}{R_{MM}^2}, \tag{3.48}$$

where ΔB_z<0 for a southward field perturbation, and

$$\Delta F = F_O\left(R_{MM}\right) - F_O\left(R_{MMO}\right). \tag{3.49}$$

Using Eqs. (3.45-3.49) we calculated equatorial magnetic field and flux function profiles for three different magnetospheric configurations, namely a compressed system, case A with R_{MM}=45 R_J, a baseline system, case B with R_{MM}=65 R_J and case C, an expanded system with R_{MM}=85 R_J. We choose R_{MM0}=65 R_J (as used by Cowley et al. (2007)). These configurations are listed in Table 3.3 and the respective profiles are shown in Fig. 3.3.

Fig. 3.3a shows how the magnetic field strength varies with equatorial distance in the magnetodisc for the three cases. The red and green lines show compressed (case A) and expanded (case C) magnetic field profiles respectively. Case A with a disc radius of

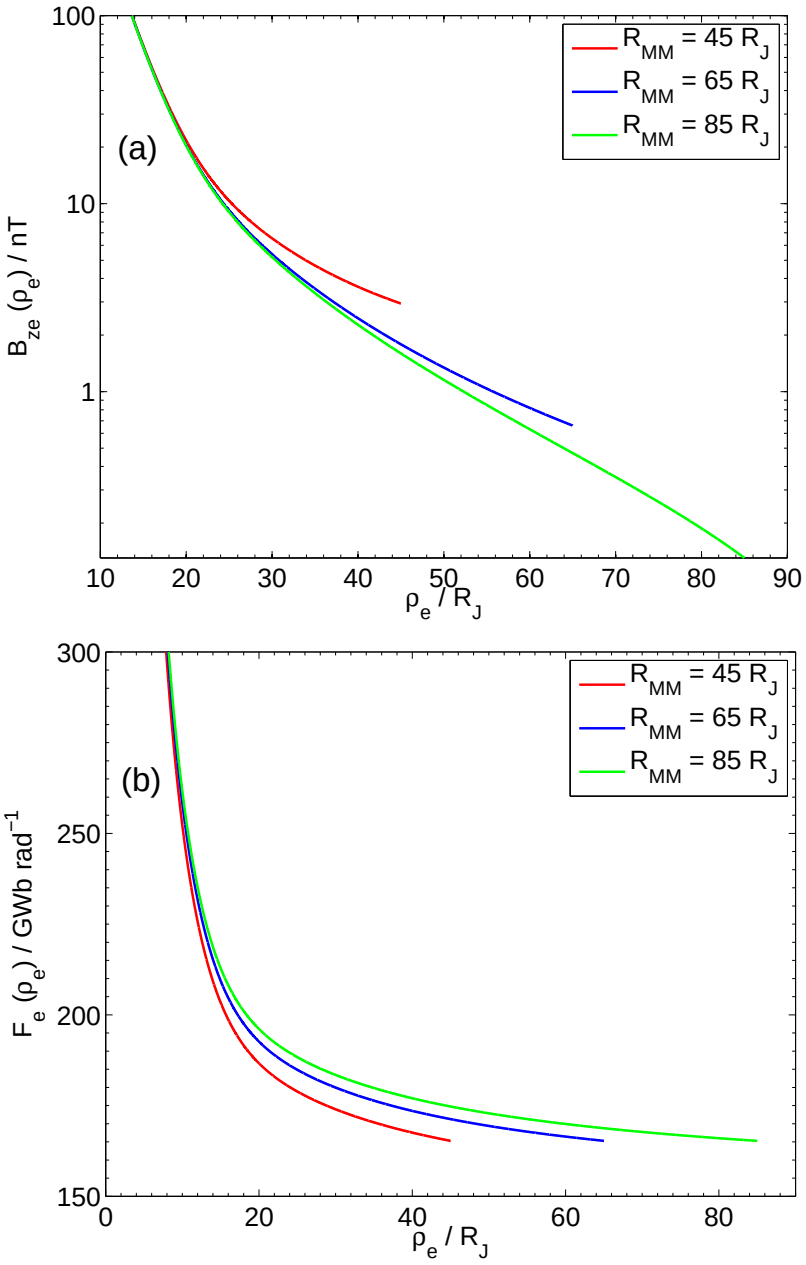

Figure 3.3. (a) Variation of the magnetic field strength (log scale) with equatorial radial distance within the magnetodisc for the three configurations used. Case A is represented by the red solid line, whilst cases B and C are represented by the blue and green solid lines respectively. (b) The corresponding flux functions for the three magnetospheric cases are plotted against equatorial radial distance using the same colour code.

R_{MM}=45 R_J corresponds to a relatively high solar wind pressure and a strong equatorial magnetic field. Case C, representing a relatively low solar wind pressure has a magnetodisc radius of R_{MM}=85 R_J and a comparatively weak magnetic field. Fig. 3.3b shows how the corresponding flux functions vary with equatorial distance. By definition the value of the flux function at ρ_e=R_{MM} has the same value for all cases.

3.3.2 Outer magnetosphere model

The outer magnetosphere is still a poorly constrained region of the magnetosphere. So when it comes to modelling such a region, various assumptions must be made. We model the outer magnetosphere (region II [9]) and polar cap (region I) regions by employing almost the same method as Cowley et al. (2005). The only difference is that, in the outer magnetosphere, we use a value for the plasma angular velocity that is dependent on the size of the magnetodisc[10] (whereas Cowley et al. (2005) use two fixed angular velocities depending on whether the magnetosphere is compressed (0.5 Ω_J) or expanded (0.25 Ω_J)). As described in section 2.1.4, the outer magnetosphere represents a region of the magnetosphere that possesses depleted flux tubes and is thought to be involved in Dungey and Vasyliunas type interactions. The polar cap region represents the open field lines connected directly to the solar wind.

The plasma angular velocity profile (as a function of ionospheric co-latitude) in the outer magnetosphere and polar cap (open field lines) is given by (Cowley et al. 2005)

$$\Omega_M(\theta) = \omega_I + \frac{1}{2}\left[1 + \tanh\left(\frac{\theta - \theta_{OCB}}{\Delta\theta_{OCB}}\right)\right](\omega_{II} - \omega_I). \tag{3.50}$$

where $\theta_{OCB} = 10.25\,^\circ$ is the ionospheric co-latitude of the mapped open-closed field line boundary (Cowley et al. 2005), $\omega_I = 0.0909\,\Omega_J$ in accordance with theory of Isbell et al. (1984) and ω_{II} is determined using the assumptions described above.

3.4 The steady-state model

[9] See section 3.4.1 for full description of magnetospheric regions.

[10] We assume plasma angular momentum conservation and use a plasma angular velocity value of 0.5 Ω_J for a compressed magnetosphere (case C) (Kane et al. 1995).

Smith and Aylward (2009) describe the method of coupling the magnetosphere, thermosphere and ionosphere models. We employ essentially the same method, with a few minor changes (R_J=71492 km is used for both our flux function calculations and atmospheric modelling). The coupled model in Smith and Aylward (2009) ran for 200 Jovian rotations to reach steady-state. Comparisons of height, temperature and azimuthal velocity in the inertial frame data for case B were made for run-times of 200 and 50 rotations. Calculations show that between both run-times there was a maximum relative difference of ∼0.4 %, ∼0.8 % and ∼1.2 % for height, temperature and azimuthal velocity respectively. This difference causes no significant change in any other parameters obtained from the model and running the model for 50 rotations saves considerable CPU time. Thus for the purposes of this study, running the model for 50 rotations was considered sufficient to reach steady state.

3.4.1 Solving the coupled equations of thermospheric and magnetospheric momentum

Studies such as Hill (1979) and Pontius (1997) have shown that for the middle magnetosphere to be in a steady state, the radial gradient of the outward angular momentum flux of iogenic plasma must be equal in magnitude to the torque per unit radial distance on that plasma. The plasma model that describes the middle magnetosphere is based on four equations

$$\frac{1}{\rho_e}\frac{d}{d\rho_e}\left(\rho_e^2\Omega_M\right) = \frac{8\pi\Sigma_P F_e|B_{ze}|}{\dot{M}}\left(\Omega_T - \Omega_M\right), \tag{3.51}$$

$$j_{||i} = \frac{4B_J}{\rho_e|B_{ze}|}\frac{d}{d\rho_e}\left[\Sigma_P F_e\left(\Omega_T - \Omega_M\right)\right], \tag{3.52}$$

$$\Sigma_P = \Sigma_P(j_{||i}), \tag{3.53}$$

$$\Omega_T = \Omega_T(\Omega_M, \Sigma_P), \tag{3.54}$$

where $\dot{M}$=1000 kg s^{-1} is the assumed mass outflow rate from the Io torus.

These equations describe the inter-dependence of magnetospheric angular momentum per unit mass ($\rho_e^2\Omega_M$), FAC density ($j_{||i}$) and Pedersen conductance (Σ_P). Eq. (3.54) represents the output from the thermospheric model component, which is forced by magneto-

spheric inputs of $\Omega_M(\rho_e)$. Eq. (3.51) is the Hill-Pontius equation (Hill 1979; Pontius 1997) with a modification by Smith and Aylward (2009) to include effects of neutral thermosphere flow, represented by Ω_T. This equation balances torques caused by the outward diffusion of the disc plasma and the $\boldsymbol{J}\times\boldsymbol{B}$ force associated with the magnetosphere-ionosphere coupling currents. Eq. (2.65) is used to calculate the FAC in the ionosphere. An increase in field-aligned current should have an effect on angular velocities $\Omega_M(\rho_e)$, through enhancement of the ionospheric conductivities. We account for this in Eq. (3.53), representing Eqs. (3.40 and 3.41), which describe how enhancements in $j_{||i}$ also affect the Pedersen conductance Σ_P.

Our method for solving these equations is the same as that in Smith and Aylward (2009) and Nichols and Cowley (2004). This is essentially a shooting method which varies the value of Ω_M at the outer edge of the disc until the solution, integrated inwards from this location, smoothly joins an appropriate 'inner disc' analytical solution at 12 R_J. We set the azimuthally integrated radial current at the outer edge of the disc to a value of 100 MA as our outer boundary condition (following Nichols and Cowley (2004)), whilst we have near-rigid corotation of plasma as an inner boundary condition. The resultant angular velocity profiles are shown below in Fig. 3.4. The corresponding Pedersen conductance solutions for our steady state runs are presented and discussed in section 4.2.1.

Fig. 3.4 shows how the thermospheric (solid lines) and magnetospheric (dashed lines) angular velocities vary in Jupiter's high latitude region for our three steady state cases. We also show the region boundaries used in our model and the magnetically mapped location of Io in the ionosphere. As stated in section 2.3.2, Ω_T is a weighted average of the effective angular velocity throughout the thermosphere-ionosphere, computed over all altitudes at each co-latitude θ_i. Ω_M in region I has a constant value of $\sim$0.1 Ω_J (Isbell et al. 1984). Region II also has a fixed value of Ω_M that depends on magnetospheric size, in accordance with observations (Cowley et al. 2007). The profiles of Ω_M in regions I, II and III are joined smoothly across their boundaries with the use of hyperbolic tangent functions. Case B, our 'baseline' is shown in blue. At low latitudes, rigid corotation with Jupiter's deep atmosphere is maintained. At the higher latitudes ($> 60\,^\circ$) the magnetosphere (represented by Ω_M) sub-corotates to a greater degree than the thermosphere (expressed by Ω_T). The shape of these Ω_M and Ω_T profiles are similar to those obtained in the studies of Smith

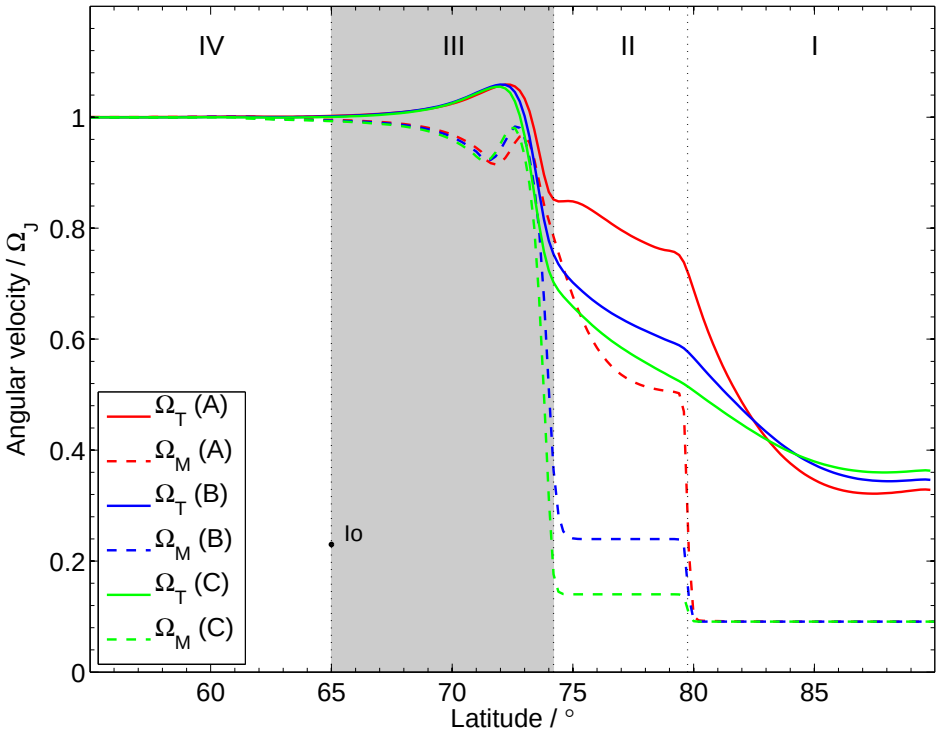

Figure 3.4. Thermospheric and magnetospheric angular velocities for cases A-C in the high latitude region and are represented by solid and dashed lines respectively. Red lines represent case A, blue case B and green case C. The black dot labelled 'Io' indicates the magnetically mapped position of the moon Io's orbit in the ionosphere. The magnetospheric regions (region III is shaded) considered in this study are labelled and separated by the dotted black lines.

and Aylward (2009). Ω_M and Ω_T profiles for case C, our expanded case, are represented by green lines. These profiles resemble those of case B but they possess slightly smaller angular velocities in region II. For case A, Ω_M and Ω_T are shown by the red lines. Both Ω_M and Ω_T indicate sub-corotation to a lesser extent than the respective profiles from cases B and C, in agreement with the study of Cowley et al. (2007) who modelled Ω_M, assuming simplified profiles for Ω_T (where K=0.5). We thus show that the thermosphere and magnetosphere for compressed configurations corotate to a greater degree than in the case of expanded configurations. Our plotted profiles quantify this result for both Ω_M and Ω_T.

3.4.2 Limitations to our steady state approach

We need to ensure that the height-integrated Pedersen conductivities at the poleward ionospheric boundary of the magnetodisc field line region, Σ_P(disc), and at the equatorward

boundary of the outer magnetosphere region, Σ_P(outer), join smoothly together in order to avoid discontinuities at this interface. This is particularly important for large compressions such as that of case A. We thus applied a Gaussian function to extrapolate Σ_P from the magnetodisc into the outer magnetosphere region for compressed magnetospheres. We ensured the Gaussian function would terminate with a polar value equal to the chosen background Σ_P in the outer magnetosphere, and that this transition would occur with a small latitudinal scale (0.2 °). The amplitude and centre of the Gaussian function were calculated using the gradient of $d\Sigma_P/d\theta$ at the poleward edge of the disc region. We further discuss the resulting profiles of Σ_P in section 4.2.1.

3.5 The transient-state model

In Chapters 5 and 6 we investigate the response of the Jovian thermosphere to changes in solar wind dynamic pressure (magnetodisc size) on small timescales ($\leq$3 hours). The model discussed above cannot be considered to be in steady-state under such circumstances. As such, certain necessary changes to the middle magnetosphere model are discussed in the following section. Other than the changes discussed in sections 3.5.1 and 3.5.2, the coupled model remains essentially unchanged from that described above. The changes described below and the incorporation of a 'transient regime' to the coupled model represent the main portion of my PhD thesis.

3.5.1 Obtaining the transient plasma angular velocity

We now discuss the calculation of plasma angular velocity once the model has entered the transient regime i.e. once our initial, steady-state system begins to undergo a transient compression/expansion of the magnetosphere. Our method of calculating transient plasma angular velocities follows that of Cowley et al. (2007). Prior to the rapid compression or expansion, the system exists in a steady state, with plasma angular velocity $\Omega_M(\theta_i, t{=}0)$ as a function of co-latitude θ_i and time t. Using the magnetic mapping method discussed in section 3.3.1, the equatorial radial distance $\rho_e(\theta_i, t{=}0)$ of the local field line can be found. The arrival of the solar wind pulse or rarefaction (via CIRs/CMEs discussed in section 2.1.3) causes the magnetosphere to compress or expand by several tens of R_J (typical choice for the simulations) and the model enters the transient (time-dependent) regime. Thus, a given co-latitude θ_i now maps to a new radial distance $\rho_e(\theta_i, t)$. If, as discussed in

section 1.4, the solar wind pulse causes perturbations that occur on sufficiently small time scales (∼2−3 hours), we can assume that plasma angular momentum is approximately conserved. The plasma angular velocity profile throughout the 'pulse' in solar wind pressure is then given by:

$$\Omega_M(\theta_i, t) = \Omega_M(\theta_i, t{=}0) \left(\frac{\rho_e(\theta_i, t{=}0)}{\rho_e(\theta_i, t)} \right)^2, \tag{3.55}$$

where the notation $t{=}0$ and t denote the initial (steady-state) and transient (at each time-step throughout the event) states respectively.

For this study, the time evolution of solar wind dynamic pressure, and thus magnetodisc size, is represented by a Gaussian function. $R_{MM}(t)$ represents the magnetodisc radius as a function of time and is given by

$$R_{MM}(t) = A \exp\left(-\frac{(t - t_o)^2}{2\Delta t^2} \right) + R_{MMO}, \tag{3.56}$$

where $A{=}R_{MM}(t_o) - R_{MMO}$ and is the amplitude of the corresponding curve, $R_{MM}(t_o)$ is the maximum or minimum radius, t_o is the time at which $R_{MM}(t){=}R_{MM}(t_o)$ (90 minutes after pulse start time t_s), and Δt controls the width of the 'bell' (obtained using $(2/3)(t_o - t_s) = 2\sqrt{2\ln 2}\ \Delta t$). After achieving steady-state, we run the model for a single Jovian day, transient mode is then initialised 3 hours prior to the end of the Jovian day (and model runtime). Profiles of $R_{MM}(t)$ for compressions and expansions are shown in Fig. 3.5.

As indicated in Fig. 3.5, the simulated pulse lasts for a total of three hours, after which the magnetodisc returns to its initial size. This is represented by the red (compression) and blue (expansion) lines. The grey dashed line indicates the point of maximum compression/expansion (at $t{=}t_o$) where we take a 'snapshot' of model outputs in order to investigate the thermospheric response midway through the transient pulse (henceforth, this phase of the event is referred to as 'half-pulse'). The magnetospheric reconfigurations modelled in our transient scenarios (compressions and expansions) are indicated in Table 3.4. The starting configuration (steady-state) for the compression event is referred to as 'case CS'

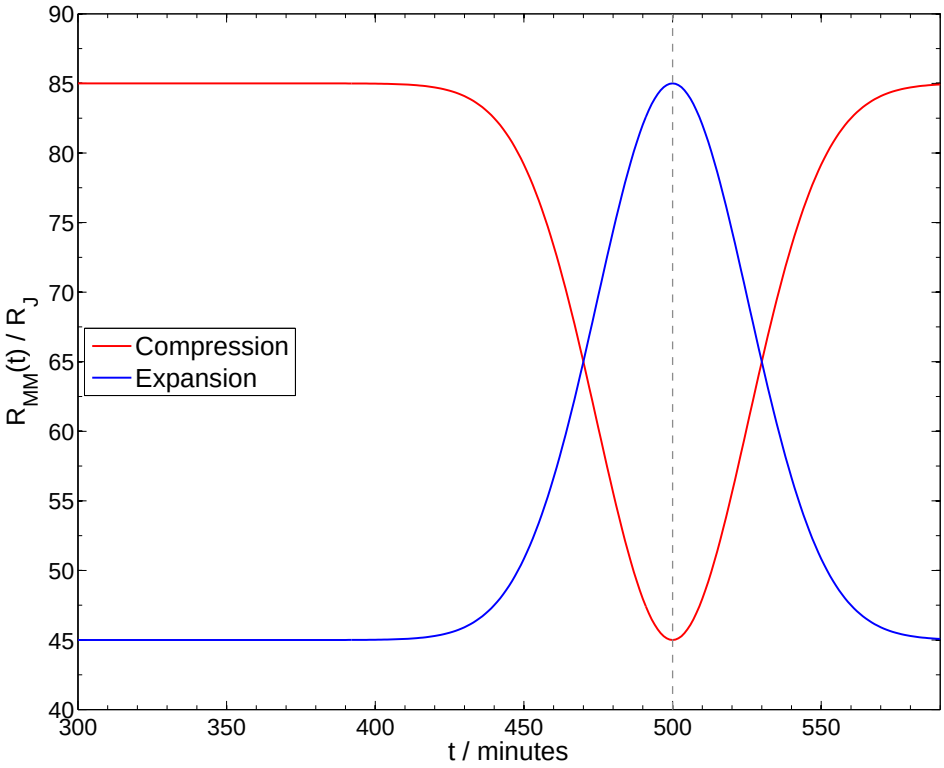

Figure 3.5. The variation of magnetodisc radius $R_{MM}(t)$ with time during a pulse in the solar wind. The red and blue lines represent a compression and expansion respectively throughout the entire pulse. The grey dashed line indicates the point of maximum variation.

(pre-Compression Steady-state). The state where the magnetodisc radius is at a minimum (halfway through the pulse) is referred to as case CH (Compression Half-pulse). Case CF (Compression Full-pulse) represents the state of the system after the pulse subsides. The expansion event nomenclature follows from the compression event but we replace 'C' with 'E' (for expansion) giving cases ES, EH and EF.

As described in section 3.3, we divided the magnetosphere into four regions: region I, representing open field lines of the polar cap; region II containing the closed field lines of the outer magnetosphere; region III (shaded in figures) is the middle magnetosphere (magnetodisc) where we assume the Hill-Pontius equation is valid for steady-state conditions. Region IV is the inner magnetosphere (which is assumed to be fully corotating in steady state). Region III is our main region of interest throughout this study since it plays a central role in determining the morphology of auroral currents.

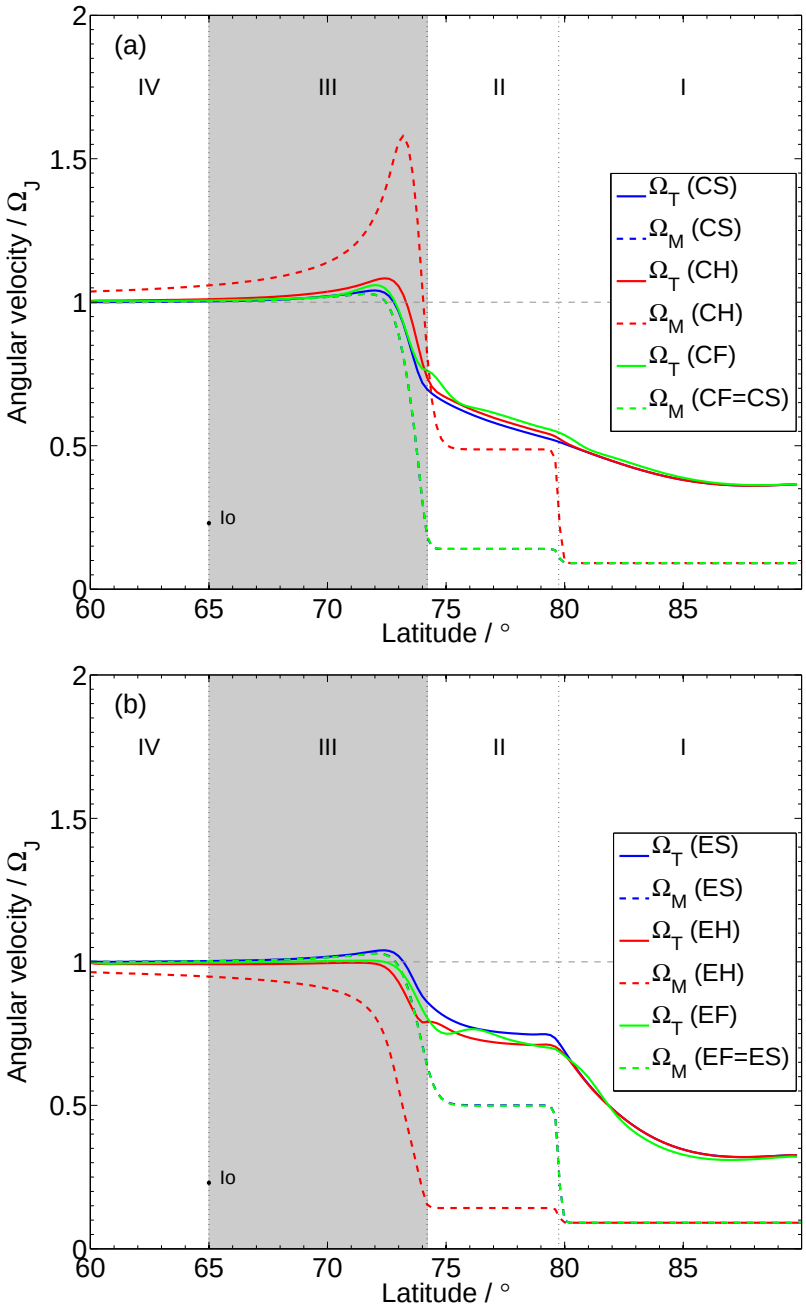

Figure 3.6. (a) Thermospheric and plasma angular velocity profiles for the transient compression cases as a function of ionospheric latitude. Solid lines represent thermospheric profiles whilst dashed lines represent plasma profiles. The black lines represent case CS (steady state before compression) whilst the red and blue lines indicate cases CH (system at minimum disc radius) and CF (system just returned to initial disc radius) respectively. The magnetospheric regions (region III shaded) are labelled and separated by the black dotted lines. The magnetically mapped location of Io on the ionosphere is marked and labelled. (b) Thermosphere and plasma angular velocity profiles for the transient expansion cases as a function of ionospheric latitude. The line styles are the same as (a) but the cases are now ES, EH and EF respectively, where 'E' denotes expansion, and the 'S', 'H' and 'F' symbols represent the same phases of the event as for Fig. 3.6a.

Table 3.4. The three different stages of the transient magnetospheric reconfiguration events (compression and expansion) used in Chapters 5 and 6. The radii of the magnetodisc R_{MM}, magnetopause R_{MP} and solar wind pressure P_{SW} (Joy et al. 2002) are shown.

Case	CS	CH	CF	ES	EH	EF
R_{MM}/ R_J	85	45	85	45	85	45
R_{MP}/ R_J	101	68	101	68	101	68
P_{SW}/ nPa	0.021	0.213	0.021	0.213	0.021	0.213

Plasma velocities are shown in Fig. 3.6 (dashed lines) along with their corresponding thermospheric angular velocities (solid lines). Fig. 3.6a shows angular velocity profiles pertaining to the transient compression scenario. Case CS is indicated by black lines, case CH by red lines and case CF by the blue lines. In Fig. 3.6a, we see an average of ∼3 % increase in peak Ω_T in response to the transient compression event. This is small compared to the factor of two increase in peak Ω_M (for case CH). The significant difference in response between the thermosphere and magnetosphere is due to the larger mass of the neutral thermosphere and thus, its greater resistance to change (inertia). There is significant super-corotation of the magnetodisc plasma throughout most of regions IV and III, midway through the compression. Plasma rotating faster than both the thermosphere and deep planet creates a reversal of currents and angular momentum transfer between the ionosphere and magnetosphere (Cowley et al. 2007). Thus angular momentum is transported from the magnetosphere to the thermosphere, where rotation rate increases from its initial state. After the subsidence of the pulse, the magnetosphere returns to its initial size and thus, the Ω_M profile for case CF is equal to that of CS at all latitudes. The same cannot be said for the thermospheric angular velocities; the CF thermosphere rotates slightly faster (∼2 % at maximum Ω_T) for parts of regions III and I and all of region II. This comparison highlights the difference in response between the thermosphere and magnetosphere to the prescribed changes in solar wind pressure.

Fig. 3.6b shows angular velocity profiles corresponding to transient expansion scenario. Like in the compression scenario, we have cases ES, EH and EF indicated by black, red and blue lines respectively. The behaviour is very different from the compression: midway through the event (case EH), the magnetodisc plasma sub-corotates to an even greater degree in regions IV and III compared to the initial steady-state case, ES. The thermosphere also sub-corotates to a greater degree, but remains at higher angular velocity than

the disc plasma, meaning that current reversal does not occur. Thermospheric angular velocities for cases ES and EF differ slightly, as in the compression scenario i.e due to the greater lag in the thermospheric response time. Fig. 3.6 theoretically demonstrates the effect that transient increases and rarefactions in the solar wind dynamic pressure have on both plasma and thermospheric angular velocities.

Steady state (case CS and ES) plasma angular velocity profiles in Fig. 3.6 show that the magnetodisc plasma super-corotates in region III. This is unexpected when considering Ω_M profiles from previous studies (e.g. Cowley et al. (2007), Smith and Aylward (2009) and steady-state work based on Fig. 3.4), which show only corotating and sub-corotating steady-state plasma velocities. We attribute the visible steady-state super-corotation to arise from two reasons: i) the high conductivity (Hall and Pedersen) in latitudes between 60° and 70° in our model, and ii) the super-corotation of the thermosphere. The combination our high conductances and thermospheric super-corotation are capable of increasing Ω_M until it super-corotates. The reason why steady-state plasma super-corotation is not seen in Fig. 3.4 or Smith and Aylward (2009) is that the conductance in this region ($60 - 70^\circ$ latitude) is small compared to the constant high conductance present in the transient model. So even though the super-corotating thermosphere acts to accelerate the magnetodisc plasma, the low conductances inhibit how efficiently the plasma is accelerated. It is worth noting that despite the fact that in the transient model, both the neutral thermosphere and magnetodisc plasma super-corotate compared to the deep atmosphere, as long as the plasma sub-corotates compared to the thermosphere, angular momentum and energy will be transferred from the upper atmosphere to the magnetosphere as is expected in steady state.

3.5.2 Limitations to our transient approach

Our approach for obtaining transient solutions for plasma angular velocity is only valid within the middle magnetosphere region, which we take to lie between $4\,\mathrm{R_J}$ and R_{MM}. The 'outer magnetosphere' in our transient model remains unchanged from that described in section 3.3.2. We do note however, that transient effects on thermospheric velocities are transmitted throughout the higher/polar latitudes ($>74^\circ$) of the model Jovian thermosphere.

The main limitation to our transient model is the use of a fixed conductivity model (see section 3.2). Whilst not ideal, we feel it is a suitable first step to developing a fully self-consistent, time-dependent model of the Jovian magnetosphere-ionosphere-thermosphere system. The constant Pedersen conductance essentially decouples Ω_M and Σ_P meaning that we no longer require an outer boundary condition for the radial current at the middle-outer magnetosphere boundary. Use of an enhanced conductivity model would concentrate all but background levels of conductance just equatorward of the main auroral oval location ($\sim$74 °) (see Chapter 4 or Smith and Aylward (2009)); effectively increasing the coupling between the atmosphere and magnetosphere in this region. We would thus expect the magnitude of current densities to increase in the region near the main oval (region III/II boundary in our model), along with an increase in the Joule heating rate. The high conductivity at latitudes between 60 ° and 70 ° in the transient model are also in part responsible for the super-corotation of magnetodisc plasma as discussed above. We currently plan to incorporate enhancements in Pedersen conductance due to auroral precipitation of electrons in a future study.

Other limitations to this model include:

i) Assumption of axial symmetry: Discussions in Smith and Aylward (2009) conclude that the assumption of axial symmetry with respect to the planets rotation axis does not significantly alter the thermospheric outputs of our model. They find that axial symmetry leads to modelling errors on the order of $\sim$20 % which are less than, or at least comparable to, errors derived from the various other assumptions and simplifications made in this coupled model. This limitation applies to both steady-state and transient-state studies presented in the following chapters.

ii) No development of field-aligned potentials: Our model does not currently include the development of field-aligned potentials, which accelerate electrons from the high latitude magnetosphere into the ionosphere. We simply apply the linear approximation to the Knight relation (see section 2.3.5) to obtain precipitating electron energy fluxes. Ray et al. (2009) show that significant field-aligned potentials develop at high-latitudes to supply the necessary FACs, and hence angular momentum, demanded by the magnetospheric plasma. By applying the linear approximation to the Knight relation, we assume that the top of the acceleration region is far enough from the planet such that the ratio of

the energy gained by a particle traveling through the potential drop to its thermal energy is significantly less than the mirror ratio between top and bottom of the acceleration region. Consequently, possible current saturation effects are ignored, with the field-aligned current density increasing to values beyond those that would result from the entire electron distribution accelerated into the loss cone. The M-I coupling modelling by Ray et al. (2010) also showed that including field-aligned potentials in a self-consistently treatment of the auroral current system alters the electric field mapping between the ionosphere and the magnetosphere, decoupling the ionospheric and magnetospheric flows. Their model did not explicitly include thermospheric flows; however the presence of field-aligned potentials may also alter the thermospheric angular velocity.

iii) Fixed plasma angular velocity in the polar cap region (latitudes $>80\,^{\circ}$*)*: The plasma angular velocity in the polar cap region Ω_{Mpc} is fixed at a constant value of $\sim 0.1\,\Omega_{\mathrm{J}}$, in accordance with the formulations in Isbell et al. (1984) which depend in part to the solar wind velocity v_{sw}. A change in solar wind dynamic pressure p_{sw} would generally be accompanied by a corresponding change in v_{sw}, so when we change the magnetospheric configuration of our model, Ω_{Mpc} should also change depending on the new value of v_{sw}. If we assume that the solar wind density ρ_{sw} remains constant and that $p_{sw} \approx \rho_{sw} v_{sw}^2$, $\Omega_{Mpc}(CS) \approx 0.06\,\Omega_{\mathrm{J}}$ and $\Omega_{Mpc}(CH) \approx 0.17\,\Omega_{\mathrm{J}}$. We find the difference between the plasma angular velocities across the open-closed field line boundary with a constant or variable Ω_{Mpc} to be negligible for both compressed and expanded magnetospheres and thus does not meaningfully influence the results discussed above and in the following chapters.

Chapter 4

Influence of solar wind on steady-state thermospheric flows

Nature does not hurry, yet everything is accomplished.

Lao Tzu

4.1 Introduction

Work from recent theoretical and modelling studies (e.g. Southwood and Kivelson (2001); Cowley and Bunce (2003b); Cowley et al. (2005, 2007)) show that a compressed magnetosphere having higher plasma angular velocities would have a small flow shear ($\Omega_T - \Omega_M$) resulting in weaker M-I coupling currents and associated aurora compared to an expanded magnetosphere, whose magnetospheric plasma would be sub-corotating significantly compared to Ω_J and thus have a larger flow shear with the thermospheric neutrals. The above models assume either that the Jovian thermosphere corotates with Jupiter or that the neutral atmospheres departure from corotation can be obtained using a slippage parameter, $K = 0.5$ and Eq. (2.56). Smith and Aylward (2009) showed this to be incorrect as K can vary significantly with ionospheric latitude.

The aim of this study is to see how magnetospheric compressions and expansions due to changes in solar wind pressure affect steady-state thermospheric flows and temperatures, and the ensuing effect on predicted Jovian auroral activity. The differentiating aspect of this study compared to the ones mentioned above is that we include a realistic atmospheric GCM to represent our thermosphere implying a natural extension from the previously mentioned studies. Our basic approach is as follows. We start with a 'baseline' magnetodisc of equatorial radius, R_{MM}=65 R_J. We then produce compressed and expanded disc configurations (section 3.3). Using these magnetospheric models as input to the atmospheric model, we run for 50 Jovian rotations until steady-state is reached.

The theoretical background for our study is given in Chapter 2. In section 4.2 we show and discuss our results, in section 4.3 we show cases where our radial current boundary condition is changed, and we summarise the findings and conclude in section 7.1.

4.2 Results and Discussion

In this section we present the results obtained from our modelling. We firstly discuss results concerning conductivities and currents. Then we proceed to discuss the thermospheric flows and energies.

4.2.1 Conductivities and currents

Previous studies of the effect of solar wind-induced compressions and expansions of Jupiter's magnetosphere have shown that magnetospheric compressions reduce ionospheric and parallel currents (in the steady state). Expansions on the other hand, have the opposite effect due to the increased transport of angular momentum to the magnetosphere (Southwood and Kivelson 2001; Cowley and Bunce 2003b; Cowley et al. 2007). Our profiles in Fig. 3.4 confirm and quantify the expected angular velocity profiles of both the thermosphere and magnetospheric plasma in the steady state, when the rate of addition of angular momentum to the plasma (at a given radial distance), due to the magnetosphere-ionosphere currents, exactly balances the rate of removal due to the radial plasma outflow. We consider the solutions for Ω_M and Ω_T in more detail in section 3.4.1. The weaker average magnetic field for the expanded cases, combined with the finite ionospheric conductivity, leads to lower Ω_M values, despite increased rates of angular momentum transport in the system. In

this section we present our quantitative findings regarding ionospheric conductivities and currents for the different magnetospheric configurations of our coupled system.

The variation of height-integrated true Pedersen conductivity Σ_P for our three magnetospheric cases is shown in Fig. 4.1a, where cases A-C are represented by red, blue and green lines respectively. The magnetically mapped location of Io in the ionosphere is shown by the black dot and the magnetospheric regions used in this study are marked and separated by black dotted lines. All three cases have peaks just equatorward of the region III / II boundary — characteristic features of the Ω_M solutions (Eqs. (3.51-3.54)) — and then fall to the assumed conductivity value in regions II and I. Cases B and C have similar profiles and peak values close to those calculated in Smith and Aylward (2009), whilst case A has a peak that is significantly higher than both of these cases. The profile for case A resembles that from Nichols and Cowley (2004) for the near-rigid corotation approximation where $(1 - \Omega_M/\Omega_J) << 1$, which are conditions met by case A in regions IV and III. Another feature that distinguishes case A is that the peak conductivity is shifted poleward slightly compared to cases B and C. This is partly due to the model method which connects the Pedersen conductivity in region III with the fixed value in region II for case A (see section 3.4.2). The poleward shift is also due to the higher Σ_P required in case A in order to achieve the prescribed value of radial current at the outer edge of the magnetodisc (poleward boundary of region III) (see section 3.4.1).

Fig. 4.1b shows how the slippage parameter K varies with latitude for our three magnetospheric cases. The profiles for K indicate the ratio between thermospheric and magnetospheric angular velocities with respect to Jupiter's planetary rotation velocity (K=$(\Omega_J - \Omega_T) \,/\, (\Omega_J - \Omega_M)$). Positive values for K represent situations when both the thermosphere and magnetosphere are sub-corotating or super-corotating with respect to the planet, as seen in region IV, II and I. Negative K values represent situations where the thermosphere and magnetosphere are undergoing opposing motions i.e one is super-corotating whilst the other is sub-corotating. This is seen just equatorward of Io's magnetic footprint on the ionosphere and for the latitudinal majority of region III. This distinction is important because the last half degree of latitude in region III maps to the largest part of the equatorial magnetosphere.

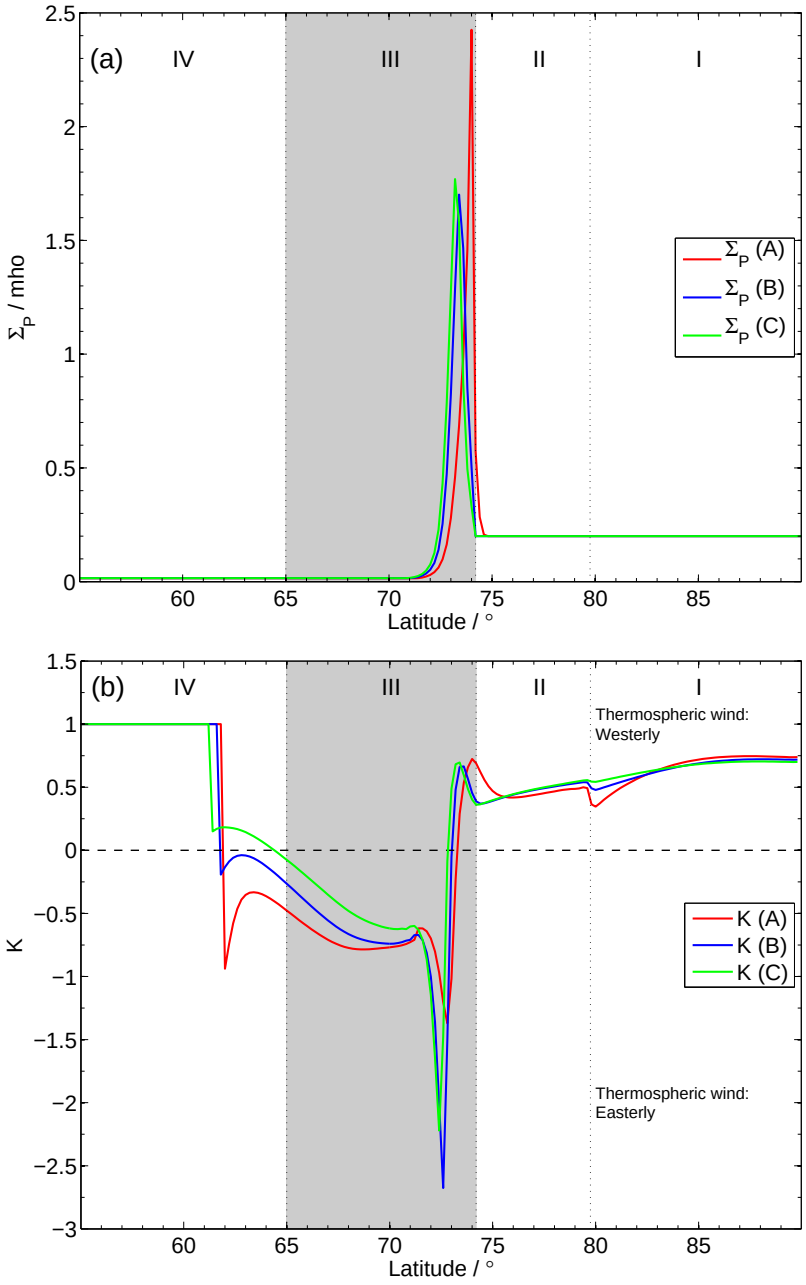

Figure 4.1. (a) Height-integrated Pedersen conductivities for cases A-C plotted versus latitude. Cases A-C are represented by red, blue and green solid lines respectively. The magnetically mapped location of Io in the ionosphere is labelled and marked by the black dot. Magnetospheric regions (region III is shaded) are labelled and separated by dotted black lines. (b) 'Slippage' parameter K plotted versus latitude for cases A-C. The colour code for cases A-C remains the same as (a).

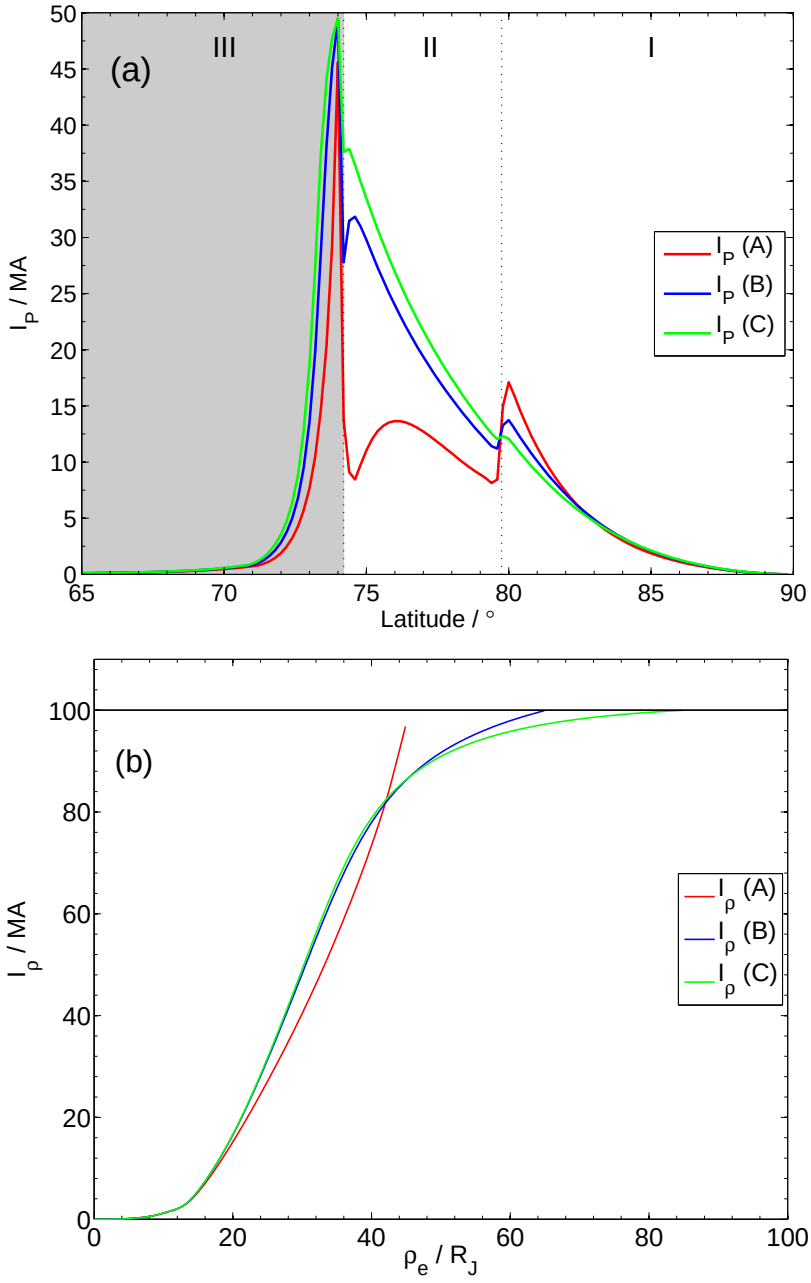

Figure 4.2. (a) Azimuthally-integrated Pedersen current shown as a function of latitude for cases A-C. Case A is represented by the solid red line, case B by the blue line and case C by the green line. The magnetospheric regions (region III is shaded) are also marked and separated by the dotted black lines. (b) Azimuthally-integrated radial current plotted against equatorial radial distance from Jupiter for cases A-C. The colour code is the same as in (a).

Fig. 4.2a shows the corresponding variation of azimuthally-integrated Pedersen current with latitude. The colour code is the same as that in Fig. 3.4. Profiles for cases B and C follow a similar trend to the steady-state Pedersen current profiles in Cowley et al. (2007), whilst the profile for case A is different within regions III and II, due to conditions comparatively nearer to corotation.

Fig. 4.2b shows the azimuthally integrated radial currents through the magnetospheric equator for all three cases in regions IV and III and how they vary with radial distance. The radial currents for cases B and C show a 's-curve' structure which is consistent with previous studies such as Smith and Aylward (2009). Case A however, shows a more linear relation between the equatorial radial distance and azimuthally integrated radial current which is not seen in the more expanded case of Smith and Aylward (2009) but is consistent with the near-rigid corotation approximation conditions presented in Nichols and Cowley (2004). As previously noted, this near-rigid corotation condition applies to case A throughout regions IV and III. We also note that, as mentioned in section 3.4.1, our outer boundary condition is that the radial current value at the region III / II boundary is 100 MA. The case A curve in Fig. 4.2b does not quite reach this value due to the joining of the Pedersen conductivity across regions III and II (see section 3.4.2). A hyperbolic tangent function is used to smoothly join the Perdesen conductivity across regions II and III, using information from a few points either side of this boundary. This leads to a smoothing of the disc solution near its outer edge, leading to a slightly different value of the azimuthally integrated radial current at this location. This curve does demonstrate however, that I_P and I_ρ in case A have to increase very rapidly in the outer magnetodisc in order to satisfy the boundary condition. Since there is no a priori reason why $I_{\rho\infty}$ should be independent of magnetosphere size, we will also investigate, later, the effect of varying the boundary condition upon the resulting profiles of current and angular velocity (section 4.3).

FAC densities are plotted against latitude in Fig. 4.3. For all three cases, FAC densities have three positive peaks, the first two lying on either side of the region III / II boundary and the third lying on the region II / I boundary. Positive peaks correspond to upward directed FACs that produce aurorae. At the boundary between region III and II, the negative peaks indicate strong downward-directed FACs whose magnitude is dependent on the equatorial radius of region III (R_{MM}). The main auroral oval is located at $\sim 73^\circ$

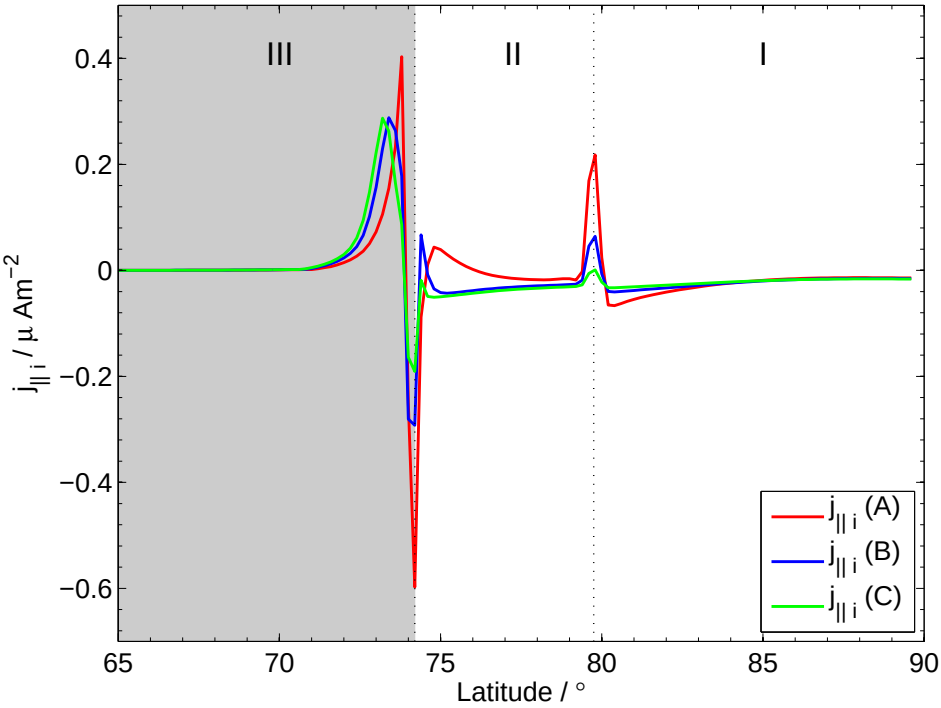

Figure 4.3. FAC densities in the high latitude region for cases A-C. Red solid lines represent FACs for case A whilst blue and green solid lines represent FACs for cases B and C respectively. The magnetospheric regions (region III is shaded) are labelled and separated by black dotted lines.

latitude where upward FACs peak, indicating a maximum in the precipitating electron flux. Our model suggests that there may also be weaker more distributed aurora poleward of the main oval, represented by upwards FAC peaks at ∼80 °. A relatively dark region would arise from the downward FACs minimum at ∼74 ° latitude, creating 'dark rings'. The latter feature is also obtained in previous studies by Cowley et al. (2005, 2007) but at present, we lack the observations required to constrain the value of $j_{||i}$ downward. The strong downward FACs at ∼74 ° are due to the significant changes in Pedersen current on crossing the boundary between regions II and III, which in turn is due to the changes in magnetospheric and thermospheric angular velocities. The Pedersen conductivity in the model also changes significantly across this boundary, which also contributes to a large magnitude for $j_{||i}$. The strongest downward FACs in our calculations are even less constrained by observations, but they also occur in the modelling of Tao et al. (2009) who also used a coupled magnetosphere-thermosphere approach.

Our calculations shown in Figs. 3.4-4.2 all support the expected trends described in

Southwood and Kivelson (2001). The angular velocity profiles (Fig. 3.4) for both the thermosphere and magnetodisc show that there is a greater degree of sub-corotation for more expanded magnetospheres, corresponding to lower solar wind dynamic pressures. This is due to the thermosphere being able to transfer momentum to a compressed magnetosphere (stronger field) with greater efficiency than a larger, expanded one. The Pedersen conductivities (Fig. 4.1a), FAC densities (Fig. 4.3) and azimuthally-integrated Pedersen and radial currents (Figs. 4.2a-b) all show an increase in region III (shaded) for expanded magnetospheres. In this region, the integrated auroral FAC for case A is $\sim$50$-$60 % of that cases B and C suggesting that auroral emission would be greater for an expanded magnetosphere than a compressed one. Our currents naturally have similar values to those obtained in Smith and Aylward (2009). They also show similar trends and profiles to studies such as those of Cowley et al. (2005, 2007) and Tao et al. (2009). Our study is an extension of these works in the sense that we use an atmospheric circulation model coupled to three distinct magnetospheric configurations.

4.2.2 Thermospheric flows and energies

Fig. 4.4 shows momentum balances for our compressed and expanded configurations in both the low and high altitude regions. Figs. 4.5-4.6 shows the thermospheric flows, temperature distributions and power dissipated per unit area for all three model configurations. Results for each case are displayed in the columns of the figure.

Thermospheric flows

According to Smith and Aylward (2009), meridional advection is the main process by which angular momentum is transferred to the high latitude thermosphere. Advection (combination of the horizontal and vertical advection of momentum by winds blowing along and across fixed pressure surfaces) is just one of the means by which momentum is changed at a fixed location within the thermosphere. In Fig. 4.4 we present force balance diagrams at low (a-b) and high (c-d) altitudes for cases A and C. The force colour codes are in the figure caption. Considering the high altitude region first, advection and other zonal force components (ion drag and Coriolis) are small. Thus, the pressure gradient is balanced almost perfectly by the Coriolis force. This force balance creates a sub-corotational flow with a small equatorward component. We now consider low altitudes near the Pedersen conductivity peak, where the ion drag term $\boldsymbol{J}\times\boldsymbol{B}$ is strong. Coriolis, pressure gradient

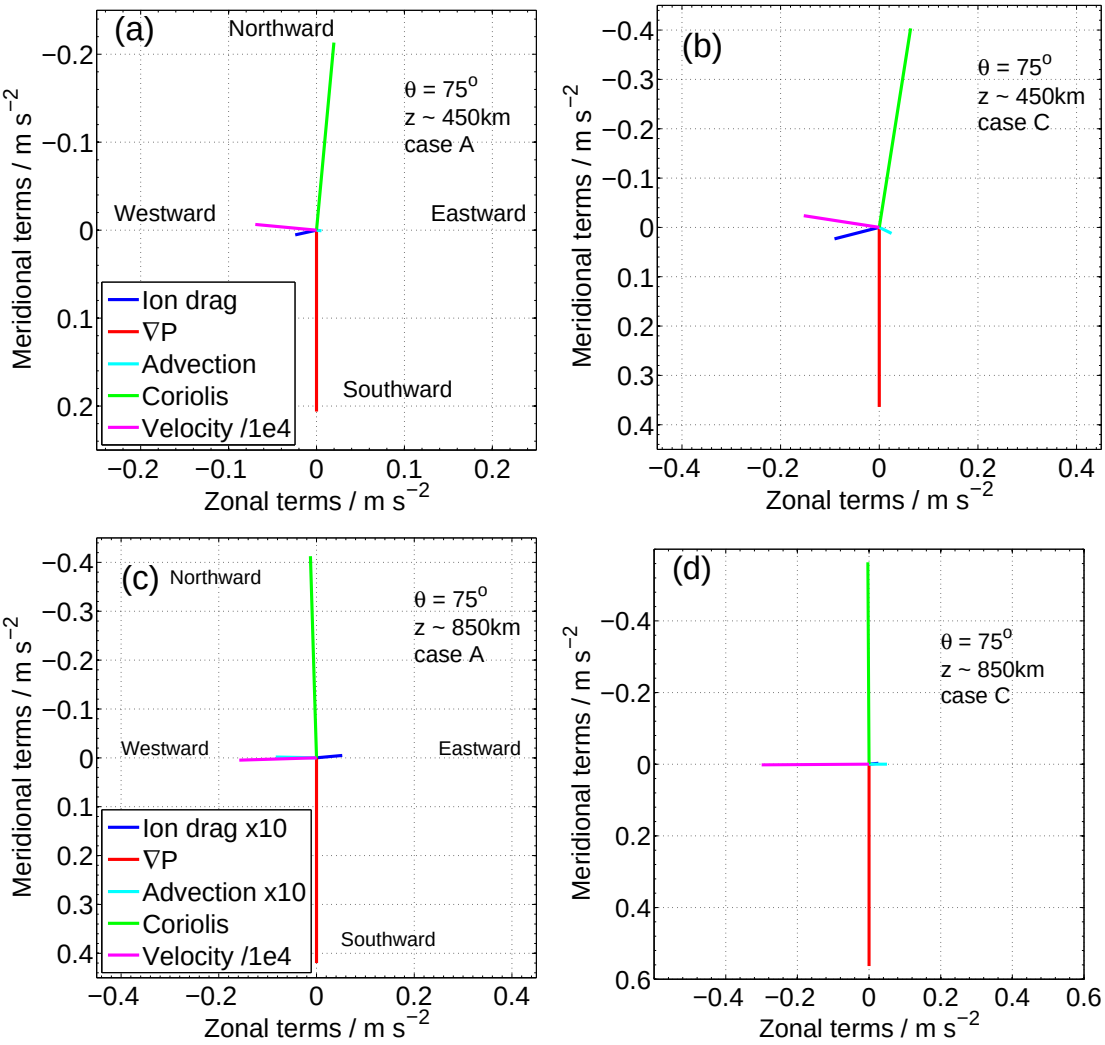

Figure 4.4. Force balance diagrams for cases A (left column) and C (right column) at ionospheric co-latitude of 75 °. (a)-(b) show meridional and zonal force balance in the low altitude region whilst (c)-(d) show meridional and zonal force balance in the high altitude region. Ion drag forces are represented by blue lines, fictitious (Coriolis) forces by green lines, pressure gradient by red and advection by the cyan line. The velocity vector is also plotted and is represented by the magenta lines. Note that the magnitude of velocity components have been divided by a factor of 1×10^4 to fit the plotted scale and that in (c)-(d) the components of ion drag and advection have been multiplied by a factor of 10 to increase visibility.

and ion drag forces are not balanced. Thus, a significant advection term arises to restore equilibrium, resulting in a region of strong poleward acceleration (see Figs. 4.5b, d and f). The resulting meridional flow at low altitudes is thus polewards and transports heat to the polar region.

Figs. 4.5a, c and e show how the thermospheric azimuthal velocity in the corotating reference frame varies within the high latitude region for the different cases. Positive (resp. negative) values of neutral azimuthal velocity indicate super (resp. sub) -corotating regions. Arrows indicate the direction of meridional flow, and the white line the locus of rigid corotation. The magnetospheric region boundaries are plotted with the dotted black lines. We can see a broad azimuthal jet (blue area) in regions I and II that sub-corotates to a greater degree with an increase in magnetospheric size. Also present is a super-corotational jet (dark red region) just equatorward of the region III / II boundary, visible in Fig. 3.4. Ion drag (see Fig. 4.4) gives rise to the sub-corotational azimuthal flows seen in regions I, II and III. As the magnetosphere expands, the $\boldsymbol{J}\times\boldsymbol{B}$ term increases and azimuthal flows sub-corotate to an even greater degree. Advection forces arise due to the lack of equilibrium at low altitudes, causing an accelerated poleward flow whose velocity increases by $\sim$90 % from case A to C. The effect of advection can be seen in Figs. 4.5b, d and f, which show meridional flows in the high latitude region. This accelerated flow transports energy from Joule heating, depositing it at higher latitudes and forming a polar 'hot spot' (Smith et al. 2007). Super-corotation occurs at latitudes where zonal ion drag and advection forces are negligible compared to the Coriolis force, which can then accelerate the flow beyond corotation. At high altitudes, forces are essentially balanced. Thus high altitude zonal flows now have an equatorward component. Therefore, meridional flows show a poleward low-altitude flow and an equatorward high-altitude flow consistent with the previous studies of Smith et al. (2007) and Smith and Aylward (2009).

Figs. 4.6a, c and e show thermospheric temperature distributions. The temperature scale is shown on the colour bar. Magenta and solid grey contours enclose areas where Joule heating and ion drag energy inputs exceed 20 $\mathrm{W\,kg^{-1}}$ and dashed grey contours highlight regions where ion drag decreases kinetic energy at a rate greater than 20 $\mathrm{W\,kg^{-1}}$. A uniform rate of 20 $\mathrm{W\,kg^{-1}}$ gives an integrated energy input rate of the order of 100 $\mathrm{mW\,m^{-2}}$ (1 $\mathrm{ergs\,cm^{-2}\,s^{-1}}$ =1 $\mathrm{mW\,m^{-2}}$) within the Pedersen conducting layer. This

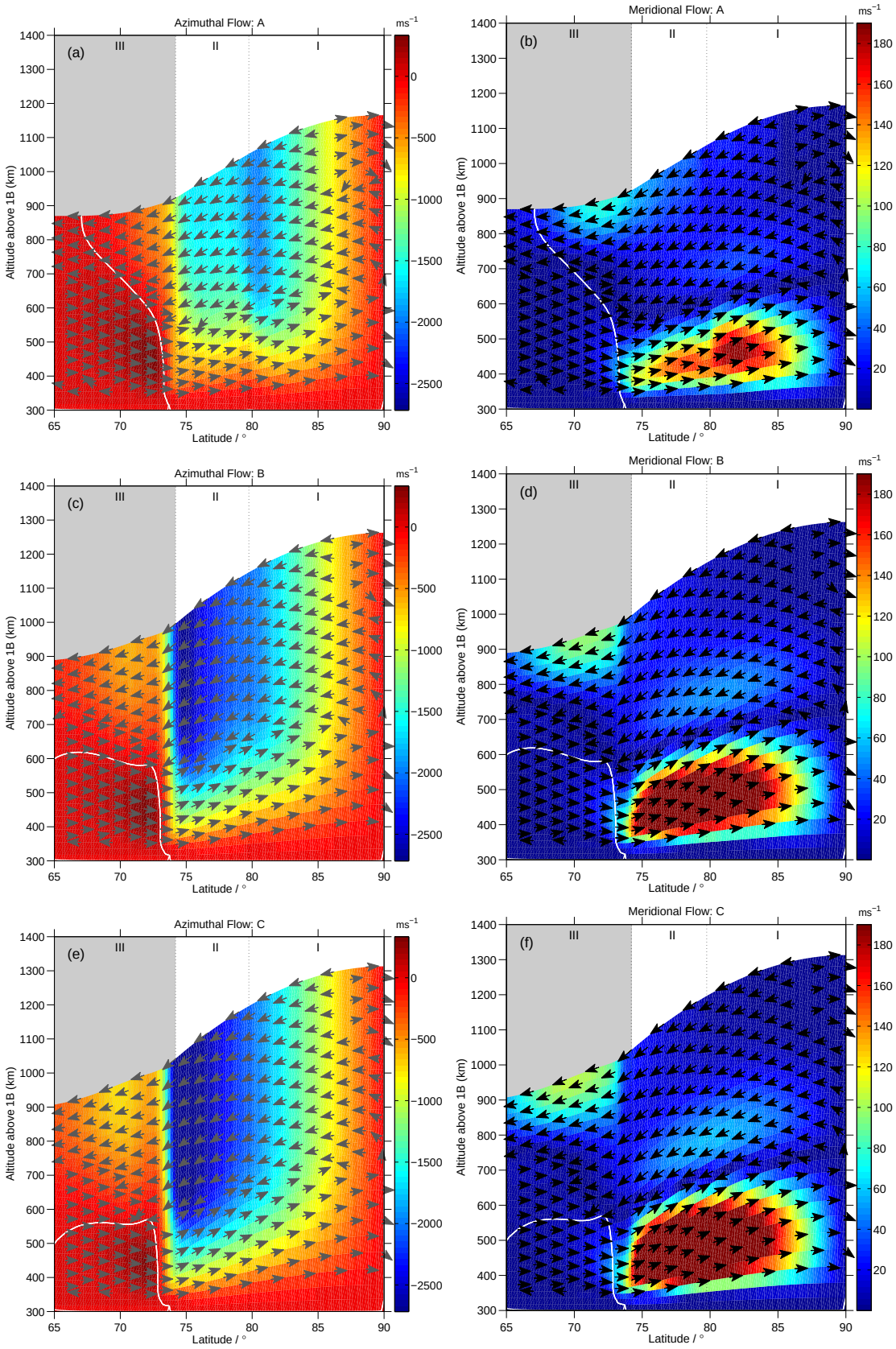

Figure 4.5. Figures a, c and e show the variation of thermospheric azimuthal velocity (colour scale) in the corotating reference frame for cases A-C respectively. Positive values (dark red) represent super-corotation, whilst negative values (light red to blue) represent sub-corotation. The direction of meridional flow is indicated by the arrows and the white line represents the locus of rigid corotation. Magnetospheric regions (region III is shaded) are labelled and separated by black dotted lines. Figures b, d and f show the meridional velocity in the thermosphere for cases A-C. The colour scale indicates the speed of flows. Other labels and lines are as for (a).

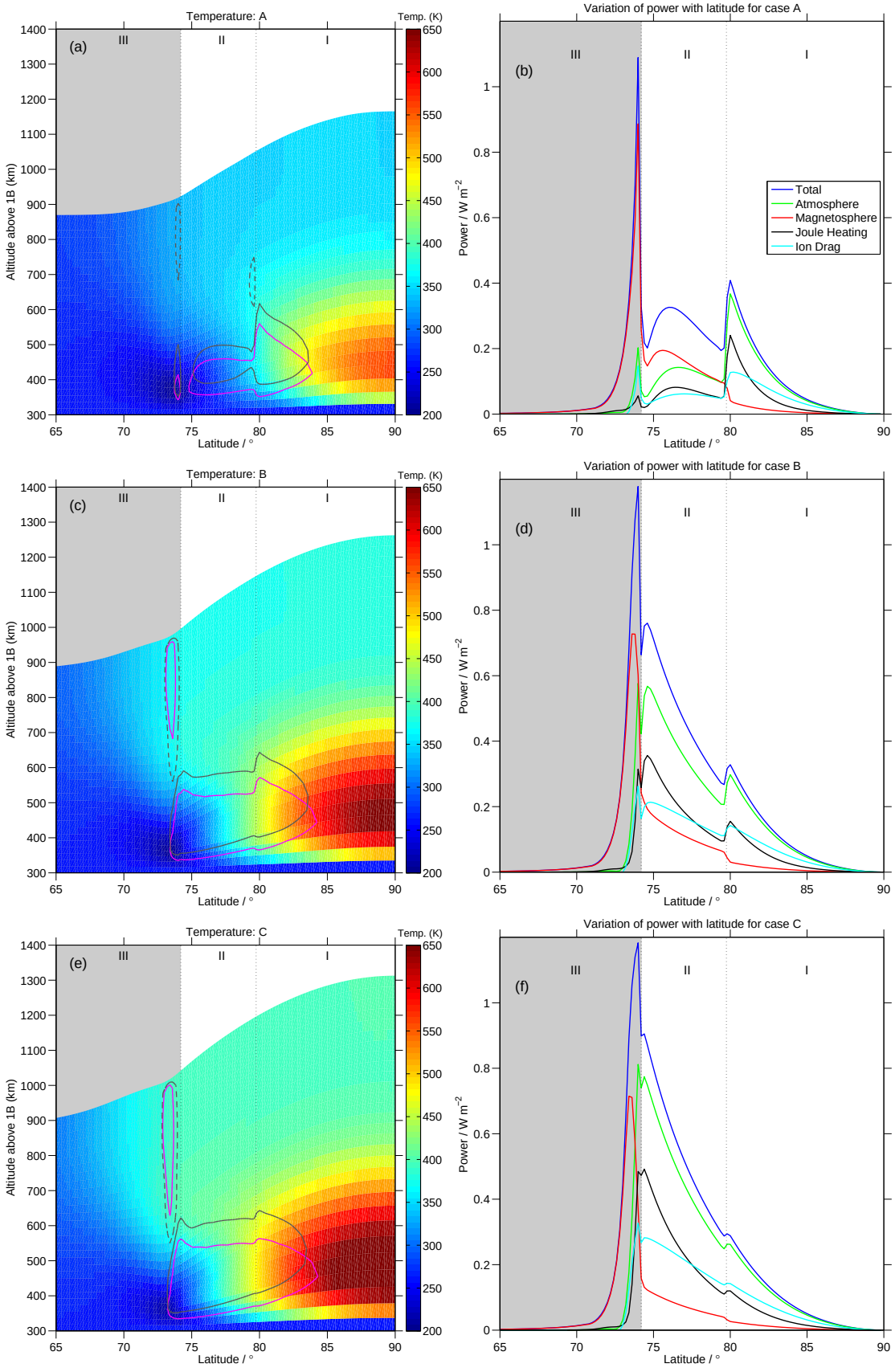

Figure 4.6. Figures a, c and e show thermospheric temperature distributions for cases A-C respectively. Magenta contours enclose regions where Joule heating exceeds 20 W kg^{-1}, solid grey contours enclose regions where ion drag increases the kinetic energy at rates exceeding 20 W kg^{-1} and dashed grey contours enclose regions where ion drag decreases the kinetic energy at rates greater than 20 W kg^{-1}. Figures b, d and f show respective power per unit area. The blue line represents total power which is the sum of magnetospheric power (red line) and atmospheric power (green line); atmospheric power is the sum of Joule heating (black solid line) and ion drag (cyan solid line). Other labels are as for Fig. 4.5.

integrated rate is of a similar order of magnitude to the estimated total IR auroral emission ($200\,\mathrm{ergs\,cm^{-2}\,s^{-1}}$ from Drossart et al. (1993)). We see significant energy input from Joule heating and ion drag at low altitudes and between $73\,^\circ - 85\,^\circ$ latitude due to their dependence on the strength of the current density $\boldsymbol{j}$. $\boldsymbol{j}$ is proportional to the difference between local thermospheric and plasma angular velocity, and to the Pedersen conductivity σ_P which peaks at low altitudes. There lies a narrow region of high altitude Joule heating just equatorward of the region III / II boundary in expanded cases due to the large shear between Ω_T and Ω_M. The decrease in kinetic energy (grey dashed lines) occurs as the ion drag force now acts to accelerate thermospheric flows towards corotation (see Figs. 4.4c-d where ion drag is eastwards). The remaining feature of prominence is the large 'hot spot' at low altitudes in region I as discussed above. The peak temperature of the 'hot spots' increase from $\sim$560 K in case A to $\sim$695 K in C, which is similar to the 125 K increase in thermospheric temperature observed by Stallard et al. (2002) during an auroral heating event.

To date, there are two vertical temperature profiles of the Jovian upper atmosphere. The first, obtained in-situ from the Galileo probe at equatorial latitudes is presented in Seiff et al. (1998); whilst the second was derived from ground-based telescope observations of Jupiter's polar region presented in Lystrup et al. (2008). Profiles show that thermospheric temperatures increase with altitude from: i) $\sim 200 - 900\,\mathrm{K}$ in the equatorial region and ii) $\sim 800 - 1400\,\mathrm{K}$ in the polar region. Fig. 4.7 shows the vertical temperature profiles for case B at the equator ($0\,^\circ$), auroral region ($74\,^\circ$) and near the pole ($86\,^\circ$) respectively represented by the green, blue and red lines. For comparison, the temperature profile obtained by Seiff et al. (1998) is indicated by the black solid line. Vertical temperature profiles in region III (blue line), obtained using the temperature distributions in Figs. 4.6a, c and e, qualitatively resemble profiles obtained using the observations described above (Seiff et al. 1998; Lystrup et al. 2008) but with considerably smaller neutral temperatures ($\sim 220 - 400\,\mathrm{K}$). In region I, our model vertical temperature profiles (red line) initially show a large temperature increase from $\sim 260 - 650\,\mathrm{K}$ with altitudes up to $\sim 450\,\mathrm{km}$ before decreasing back to $\sim 400\,\mathrm{K}$ at our model's upper boundary. Equatorial temperature profiles (green line) only range from $\sim 260 - 280\,\mathrm{K}$ which is $\sim 30\,\%$ of the maximum measured in-situ temperature from the Galileo probe. These profiles are very different from observations in the polar and equatorial regions (Lystrup et al. 2008; Seiff et al. 1998) and demonstrate

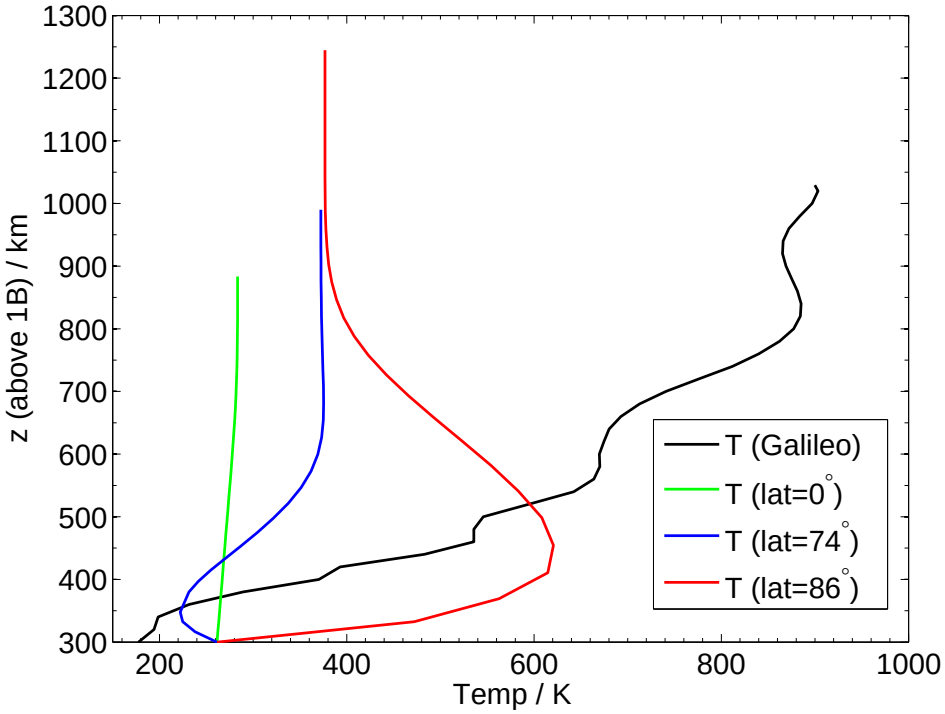

Figure 4.7. Vertical temperature profiles for our case B thermosphere along with the Galileo probe profile (Seiff et al. 1998). We present three model profiles from the equatorial, auroral and polar regions represented by green, blue and red lines respectively. We also include the Galileo probe vertical profile from Seiff et al. (1998) indicated by the black line.

some limitations of our current model; namely it's inability to: i) heat an initially cool thermosphere to the observed temperatures and ii) effectively transport heat equatorwards.

If we were to assume an initially hot thermosphere, as is observed, the neutrals in the thermosphere would have higher temperatures and consequently higher kinetic energy than an initially cool thermosphere (as employed above). Consequently, we would expect the speed of thermospheric winds to increase. This is exactly what is seen in Bougher et al. (2005), who use a GCM (called JTGCM) to simulate the Jovian thermosphere for varying degrees of external heating (Joule heating, ion drag and auroral precipitation). Temperature profiles modelled by Grodent et al. (2001) are used in JTGCM and they find that higher atmospheric temperatures lead to faster thermospheric winds. These fast winds are in turn able to efficiently distribute heating from the auroral and polar thermosphere to equatorial latitudes. To demonstrate this we have completed an expanded magnetosphere simulation where we assume an initial neutral temperature structure as presented by Gro-

dent et al. (2001). We let the system reach steady-state and compared the temperature and meridional flows to that of case C. Fig. 4.8 shows the temperature difference between a hot thermosphere simulation and case C, along with the meridional wind direction (black arrows) in the new hot thermosphere simulation. The new hot thermosphere is found to cool systematically throughout the simulation, particularly in the equatorial regions where there is no heating source present. The polar region still cools but to a lesser degree as there is substantial Joule heating present. The mean neutral temperature across the entire model thermosphere has increased by $\sim 60\,\mathrm{K}$ and the maximum temperature has increased to $\sim 730\,\mathrm{K}$. Meridional winds essentially remain unchanged with small deviations ($\pm 15\,\mathrm{ms}^{-1}$) from case C whereas zonal wind speeds are generally increased (in both eastwards and westwards directions). Even with slightly faster winds, the equatorial regions still remain relatively cool compared to the poles because meridional winds are still directed polewards at locations where significant heating is present. Therefore, although the temperature distribution in the thermosphere may differ as a result of using a hot thermosphere, the overall atmospheric dynamics remain unchanged.

Atmospheric and magnetospheric energy 'budget'

Figs. 4.6b, d and f present the total, magnetospheric, atmospheric, ion drag and Joule heating power per unit area (see Eqs. (2.69-2.74)) for each magnetospheric configuration. The colour code indicates the form of energy dissipation (blue curve shows total power). Total power is the sum of the magnetospheric and atmospheric powers and atmospheric power is the sum of Joule heating and ion drag powers. Integrating the power per unit area over the model hemisphere gives us the global powers for each of these mechanisms, shown in Fig. 4.9.

Figs. 4.6b, d and f exhibit peaks in power per unit area just equatorward of the interface between regions III and II due to the large ionospheric current associated with the breakdown in corotation of the magnetodisc (region III). Most of the energy dissipated in region III accelerates the magnetospheric plasma towards corotation. This magnetospheric power dominance diminishes for the expanded magnetosphere, in which more power is dissipated in the atmosphere via Joule heating and ion drag. Region II is dominated by these atmospheric power terms in cases B and C whilst the same region in case A is still noticeably magnetospheric power-dominated. Atmospheric power is the major form of energy dissipa-

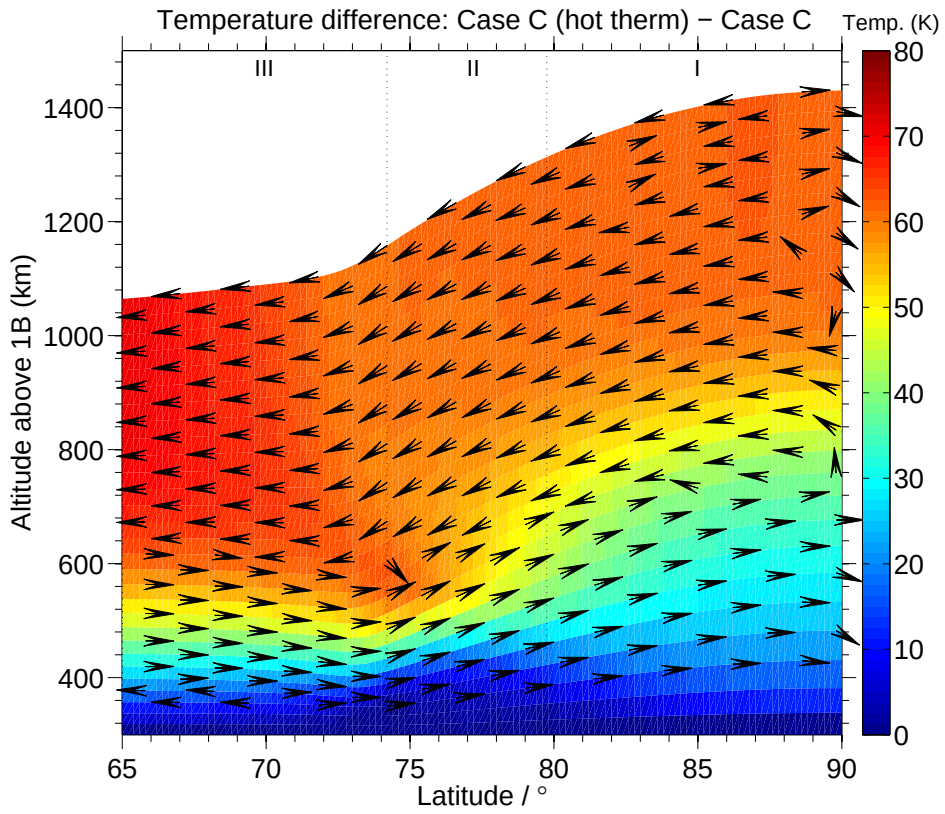

Figure 4.8. Shows the temperature difference between case C assuming an initially hot thermosphere and case C presented above (assuming an initially cold thermosphere). The black arrow indicate the direction of meridional flow in the hot thermosphere case C.

tion in region I. The atmospheric power dominance in regions II and I is mainly due to the low assumed values for magnetospheric angular velocity Ω_M (see Fig. 3.4). The difference $(\Omega_T - \Omega_M)$ is largest in these regions, which produces relatively large ionospheric Pedersen currents and atmospheric power. The low value of Ω_M produces a magnetospheric power that remains low compared to other regions. Note that relative amounts of energy provided to the atmosphere and magnetosphere on any flux shell depends on the difference $(\Omega_T - \Omega_M)$ through Eqs. (2.70-2.72). They are equal when Ω_M=0.5 Ω_J.

These figures suggest that as Jupiter's magnetosphere is compressed a higher proportion of the total power of planetary rotation (in the steady state) is transferred to the magnetosphere via the magnetic field, and by contrast, as the magnetosphere is expanded more heat is dissipated in the atmosphere.

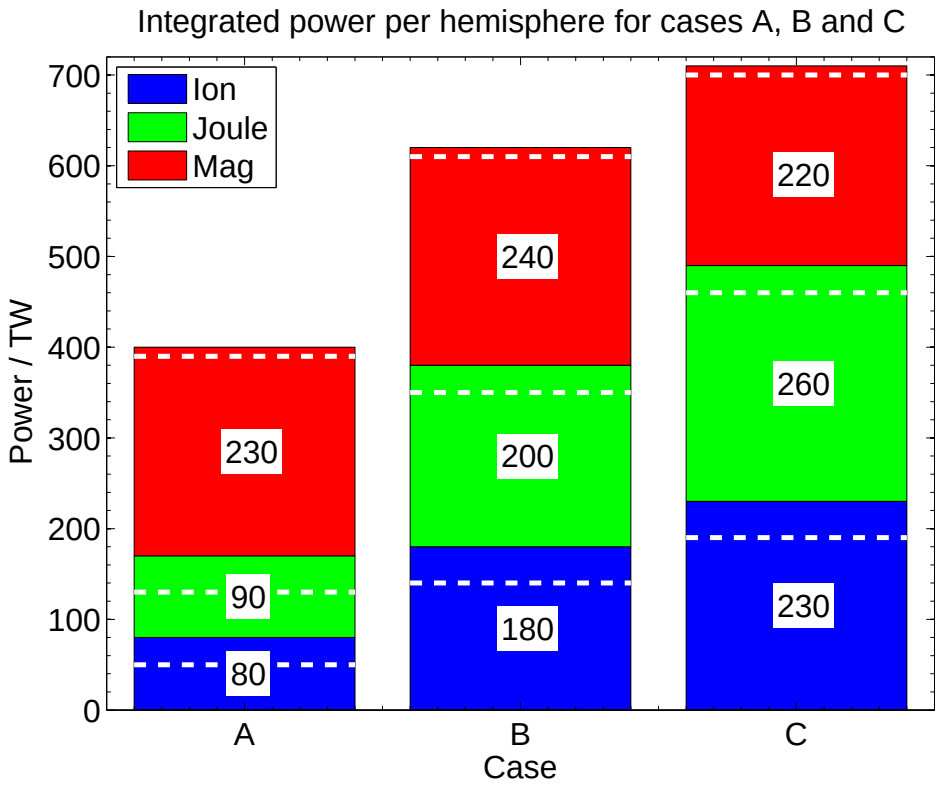

Figure 4.9. Integrated ionospheric powers per hemisphere for cases A-C are represented in this figure. Ion drag is represented by blue bars, Joule heating by green bars and magnetospheric power by red bars. The white dashed line shows the division in powers between closed and open field line regions. Powers in the closed field regions lie below the dashed white line whilst powers in the open field regions lie above it. Total power dissipated for each mechanism (in TW) is printed on its respective colour bar.

Fig. 4.9 shows the integrated ion drag (blue), Joule heating (green) and magnetospheric (red) power per hemisphere for each case and how these powers are distributed in the open and closed field line regions. Powers in the closed field regions lie below the dashed white line whilst powers in the open field regions lie above it. Integrated powers within region I remain essentially unchanged for both atmospheric (ion drag plus Joule heating) and magnetospheric mechanisms due to the assumed constant value of the magnetospheric angular velocity for all cases. Atmospheric power increases significantly with magnetospheric size, by a factor of ~ 3 from case A to C. Magnetospheric power shows a slight decrease between cases A and C and is a maximum in case B. Magnetospheric power is proportional to the torque, which increases with magnetospheric expansion, and the magnetospheric angular velocity which decreases with expansion. One would thus expect that, given a large enough range of magnetospheric sizes, the magnetospheric power would display a non-monotonic

profile that is 'modulated' by the difference between the angular velocity of the neutral thermosphere and plasmadisc.

We now compare our integrated powers per hemisphere with those calculated by Cowley et al. (2007) to take into account how using a two-dimensional model of Jupiter's thermosphere changes previous theoretical power estimates. We only compare cases A and B with the 'intermediate' and 'baseline' cases from Cowley et al. (2007) respectively, as they have comparable magnetodisc radii. The total integrated magnetospheric powers per hemisphere are comparable in magnitude; 'intermediate' and 'baseline' cases in Cowley et al. (2007) are ∼85 % those of our cases A and B. The difference between atmospheric powers is greater, since this study uses a detailed thermospheric model. In region I, cases A and B have atmospheric powers ∼35 % of Cowley et al. (2007)'s 'intermediate' and 'baseline' cases. In regions III and II (closed field) the atmospheric powers in Cowley et al. (2007) are ∼70−80 % those in cases A and B. Thus, within the closed field region of cases A and B, the inclusion of a detailed thermospheric flow model has led to more energy transferred from the thermosphere to the magnetosphere for accelerating the magnetospheric plasma and more heat dissipated within the thermosphere via Joule heating and ion drag.

Stallard et al. (2001, 2002) observed an auroral heating event between September 8 and 11, 1998, which led to a factor-of-two increase in the line-of-sight auroral electrojet velocity (ionospheric plasma velocity) and H_3^+ vibrational temperature from 940 K to 1065 K. They proposed that such an atmospheric response in could be due to an expansion of the Jovian middle magnetosphere due to a decrease in the solar wind dynamic pressure. Melin et al. (2006) subsequently analysed the above observations in order to determine heating and cooling rates in the thermosphere during this auroral heating event. Joule heating and ion drag were found to increase from 67 mW m^{-2} to 277 mW m^{-2} by the end of the event. This extra heat must was then assumed to be transported equatorward from the auroral regions by an increase in equatorward meridional winds (Waite et al. 1983). If we assume that their auroral region ranges from 65 ° to 85 ° latitude and that these heating rates are uniform across such a region, the total energy dissipated by Joule heating and ion drag (per hemisphere) increases from ∼193 TW to ∼800 TW. The total Joule heating and ion drag power in cases A and C show an increase of ∼300 %, smaller than the ∼400 % increase found in the auroral heating event (Melin et al. 2006). Cases A and C are assumed to lie in

steady state, therefore there is a large time difference between achieving steady state and the auroral heating event lasting only three days, meaning that such observations may not necessarily be compared to steady-state modelling. This demonstrates some limitations of steady state modelling, which we rectify in Chapters 5 and 6 and will revisit this interesting observation.

4.3 Effect of outer boundary conditions

The results for case A exhibit a relatively large peak for the Pedersen conductivity and FAC density just equatorward of the boundary between regions III and II (Fig. 4.3). Previous studies such as Southwood and Kivelson (2001) suggest that such peaks for compressed magnetospheres should be smaller in magnitude than those for more expanded magnetospheres. This is in contrast to what we observe in section 4.2. If the radial current at the region III / II boundary, $I_{\rho\infty}$ is larger than realistic values for a compressed magnetosphere, large FACs would develop in the poleward part of region III to satisfy the $I_{\rho\infty}$ boundary condition. In this section we present model outputs with smaller values of $I_{\rho\infty}$. We select illustrative $I_{\rho\infty}$ values for each case which minimise the variance in the current profiles throughout regions III and II. Decreasing $I_{\rho\infty}$ decreases current gradients in the well constrained Ω_M model for region III and allows for a smoother transition to region II, whose Ω_M profile is poorly constrained (due to paucity of observations).

4.3.1 Outer boundary conditions for a compressed magnetosphere

To commence this part of our study, we ran case A but with $I_{\rho\infty}$=45 MA, to see whether any significant changes would arise in the currents at the region III / II boundary. These results are shown in Figs. 4.10 and 4.11, where blue and red lines represent cases A_{100} and A_{45} respectively (subscript denotes the value of $I_{\rho\infty}$).

Comparison of angular velocities and currents for case A

In this section we compare angular velocities and current-related parameters for cases A_{45} and A_{100} (case A in section 4.2). The differences between these cases essentially lie within 72−78° latitude and so our subsequent discussions will focus on this range.

Fig. 4.10a shows the influence of $I_{\rho\infty}$ on the Ω_M and Ω_T values. Case A_{100} with the

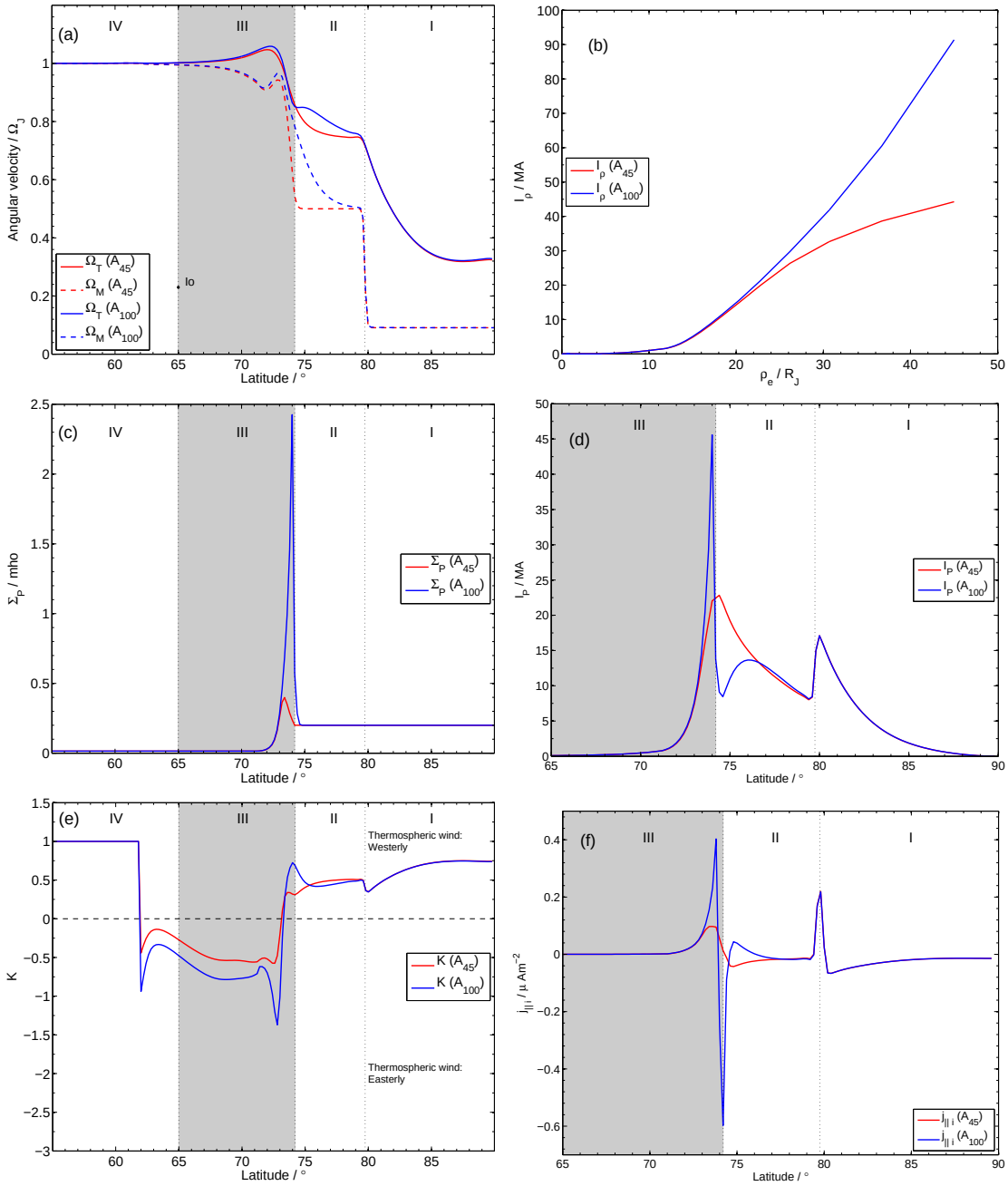

Figure 4.10. Figures a-f show thermospheric and magnetospheric angular velocities, azimuthally-integrated radial current, height-integrated Pedersen conductivity, azimuthally-integrated Pedersen current, 'slippage' parameter and FAC density respectively for case A with $I_{\rho\infty}$=45 MA (A_{45}) represented by red lines and case A with $I_{\rho\infty}$=100 MA (A_{100}) represented by blue lines. Note that case A_{100} is the same as case A in section 4.2. For (a) the solid lines represent the thermospheric angular velocity and the dashed lines represent the magnetospheric angular velocity. Magnetospheric regions (region III is shaded) are labelled and separated by dotted black lines.

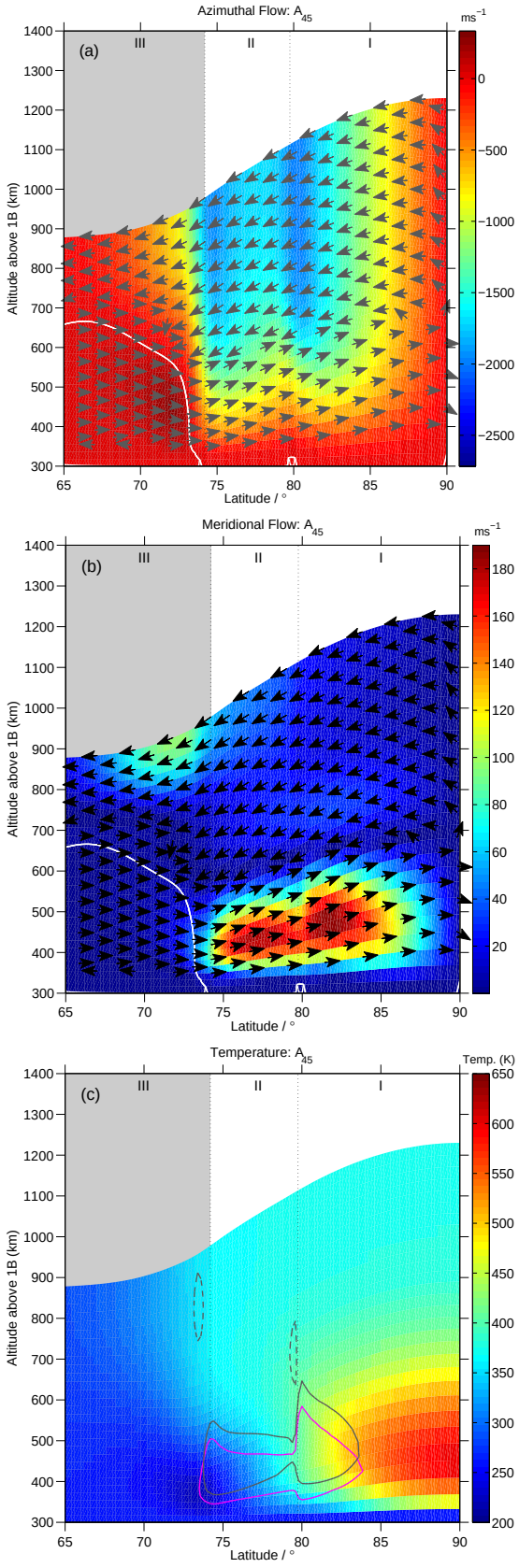

Figure 4.11. Figures a-c show thermospheric azimuthal velocity, meridional velocity and temperature distributions in the high latitude region for case A_{45}. Arrows, contours and colour bars are the same as in Figs. 4.5 and 4.6.

higher $I_{\rho\infty}$ value also has a higher torque on the disc plasma, which results in a smaller difference $\Omega_T - \Omega_M$ near the disc boundary (74−75 °). Equatorward of 74 °, the Ω_T and Ω_M profiles are very similar for both cases. The outer disc region 74−75 ° thus develops a strong FAC in case A_{100} in order to satisfy the higher $I_{\rho\infty}$ imposed.

Due to the smaller values of Ω_M and radial current for case A_{45}, Pedersen conductivity values (Fig. 4.10c) are significantly smaller near the region III / II boundary compared to case A_{100}. The different gradients in Ω_M and Ω_T for case A_{45} cause a slight equatorward shift in the conductivity peak compared to A_{100}. The 'slippage' parameter for A_{45} in Fig. 4.10e differs only slightly from that of case A_{100} due to its smaller $\Omega_T - \Omega_M$ differences.

The azimuthally-integrated radial, Pedersen and FACs for cases A_{45} (red line) and A_{100} (blue line) are shown in Figs. 4.10b, d and f respectively. The other labels are the same as in Fig. 4.2. For A_{100} the magnetosphere near-rigidly corotates with Ω_J throughout regions IV and most of III (Nichols and Cowley 2004). The A_{45} radial current profile resembles those for expanded cases, due to the magnetosphere sub-corotating to a greater degree (see Fig. 4.10a). The Pedersen current for case A_{45} has a smooth, almost linear transition across and through regions III and II as opposed to the abrupt cutoff at the region III / II boundary in A_{100}. The A_{45} profile quantitatively resembles Pedersen currents for expanded cases and those in Cowley et al. (2007). For A_{45}, FAC profiles are similar to those for A_{100} with the exception that the magnitude of the peaks just equatorward of the region III / II boundary and the trough are significantly smaller. For lower $I_{\rho\infty}$ values, then, the main auroral oval would be significantly dimmer, and possibly more similar to the putatively weak auroral signature at the region I / II boundary.

Thermospheric distributions for case A

Here we discuss the changes in azimuthal and meridional velocity as well as the temperature distribution, which arise from setting $I_{\rho\infty}$=45 MA for case A. All conventions and colours in Fig. 4.11 are the same as those in Figs. 4.5 and 4.6.

Figs. 4.11a-c show the distribution of azimuthal and meridional velocities across the high latitude region for case A_{45}. In A_{100} (Fig. 4.5a) there is a large sub-corotational jet in regions II and I with the strongest degree of sub-corotation just poleward of the region

II / I boundary. In A_{45}, the large sub-corotating jet now has two regions of strong sub-corotation, the new one being just poleward of the region III / II boundary. These two strong sub-corotational jets within the larger jet are evident in Fig. 4.10a at the region boundaries (dotted black lines), where there are large changes in magnetospheric angular velocity. Meridional velocities for case A_{45} follow the same trend as in A_{100} (Fig. 4.5b) where there is a poleward flow at low altitudes and an opposite flow at high altitudes. The main difference between the meridional flows is that localised accelerated flows (high altitude in region III and low altitude in regions II and I) have larger velocities in case A_{45} due to larger advection terms.

Fig. 4.10c shows the temperature distribution for case A_{45}. Comparing this with case A_{100} (Fig. 4.6a) indicates that energy input via Joule heating (magenta contours) and ion drag (solid grey contours) is greater in A_{45}. The larger energy input, predominantly in region II, is caused by larger shear between thermospheric and magnetospheric angular velocities. This leads to a slight increase in thermospheric temperature ($\sim$6 %) most evident in region I, the polar 'hotspot' into which auroral heat energy is transported by meridional winds.

4.3.2 Outer boundary conditions for the baseline magnetosphere

For our baseline case, case B, the smallest variance in current profiles occurred with $I_{\rho\infty}$=68 MA. We compare this case B_{68} with the original B_{100} case in Figs. 4.12 - 4.13.

Comparison of angular velocities and currents for case B

As for the compressed magnetosphere, we compare angular velocities and current-related parameters of the B_{68} and B_{100} models in the $72-75^\circ$ latitude range where significant differences arise. Fig. 4.12a compares the variation of magnetospheric and thermospheric angular velocities for cases B_{68} and B_{100}. In region III, both the magnetosphere and thermosphere for B_{68} are slightly sub-corotating compared to the B_{100}. The Pedersen conductivity and 'slippage' parameter for B_{68} also have similar profiles, but with smaller magnitudes in region III, to those for B_{100}. These minor differences are caused by smaller thermospheric and magnetospheric angular velocities in region III.

Fig. 4.12b and d show azimuthally-integrated radial and Pedersen currents. The corre-

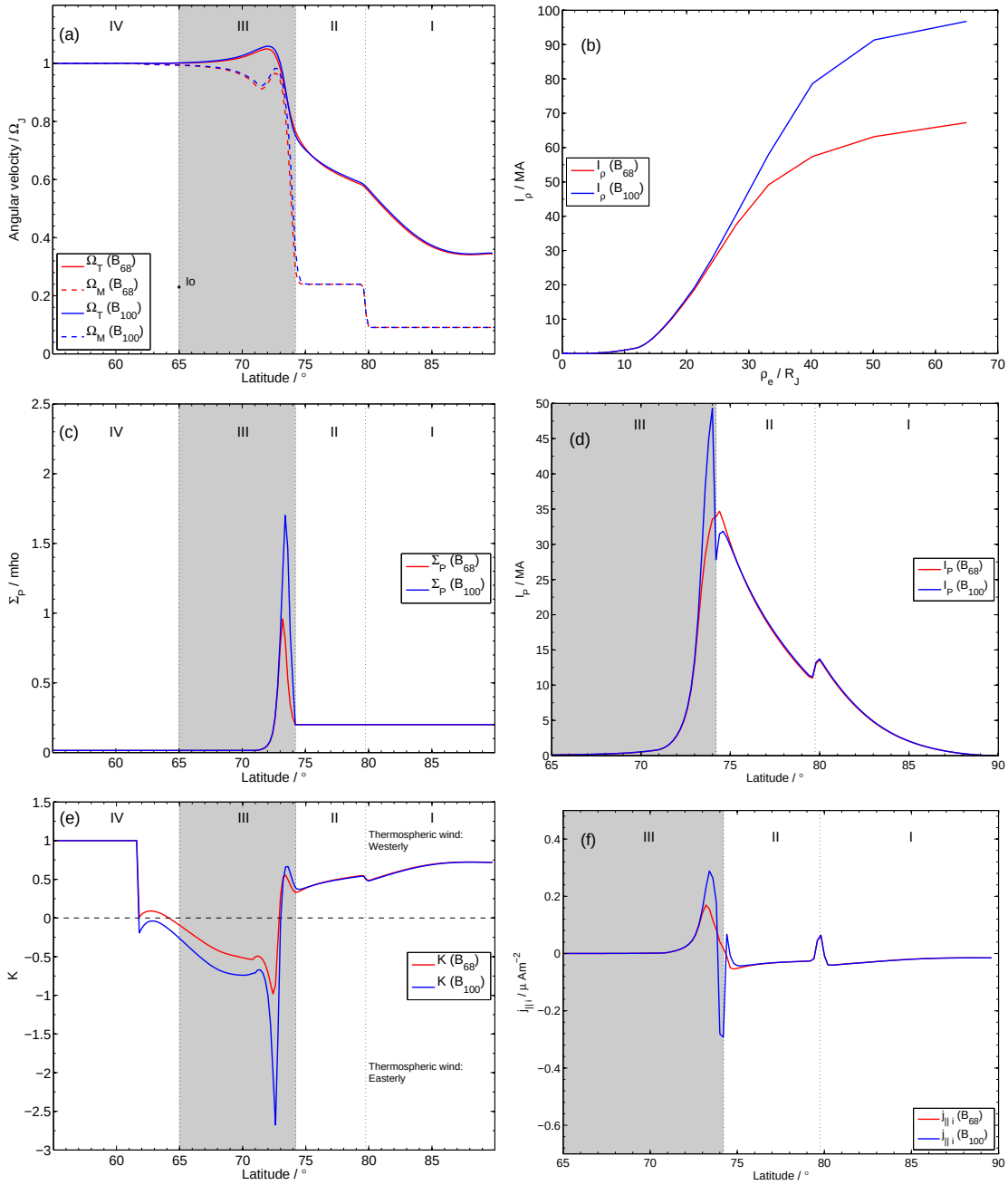

Figure 4.12. Figures a-f show thermospheric and magnetospheric angular velocities, azimuthally-integrated radial current, height-integrated Pedersen conductivity, azimuthally-integrated Pedersen current, 'slippage' parameter and FAC density respectively for case B with $I_{\rho\infty}$=68 MA (B_{68}) represented by red lines and case B with $I_{\rho\infty}$=100 MA (B_{100}) represented by blue lines. Note that case B_{100} is the same as case B in section 4.2. For (a) the solid lines represent the thermospheric angular velocity and the dashed lines represent the magnetospheric angular velocity. Magnetospheric regions (region III is shaded) are labelled and separated by dotted black lines.

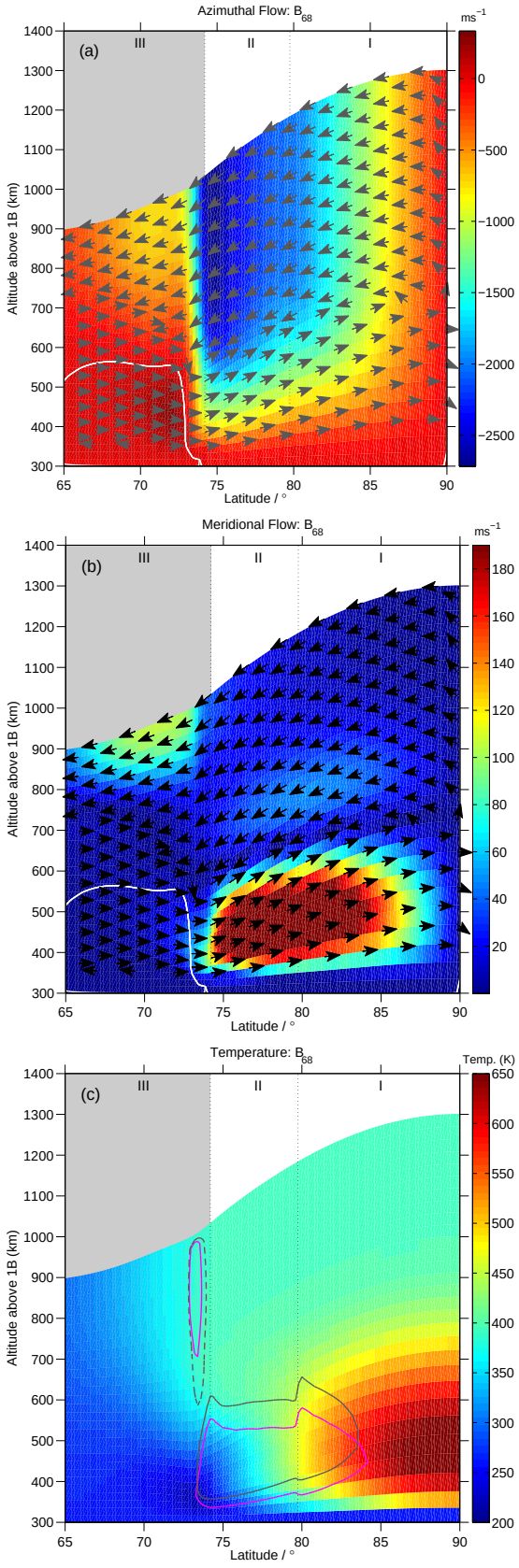

Figure 4.13. Figures a-f show this thermospheric azimuthal velocity, meridional velocity and temperature distribution in the high latitude region for case B_{68}. Arrows, contours and colour bars are the same as in Fig. 4.5 and 4.6.

sponding FAC density as a function of latitude is shown in Fig. 4.12f. The radial current profile is smaller in magnitude than that of B_{100}. The B_{68} Pedersen current has a single small peak at the region III / II boundary in contrast with the sharp peak in B_{100}. The FAC density has a smaller, slightly broader peak in region III, suggesting a low intensity auroral oval compared to the B_{100} case. The absence of strong downward FAC for B_{68} also suggests that the method used to join the region III currents with the region II currents could produce artefacts for relatively large values of $I_{\rho\infty}$.

As with case A, the fine structure around the boundary between the middle and outer magnetosphere in Fig. 4.12 has been removed by decreasing the value of $I_{\rho\infty}$ from 100 MA to 68 MA for our baseline case.

Thermospheric distributions for case B

Here we discuss the minor changes in Jupiter's thermospheric flows and temperature distribution made by changing the radial current boundary condition value for our baseline case. All conventions and colours are the same as those in Figs. 4.5 and 4.6.

The azimuthal velocity in the high latitude region is shown in Fig. 4.13a. We expect a slight increase in sub-corotation throughout region III (see Fig. 4.12a) compared to B_{100}. This is evident by comparing Fig. 4.13a with Fig. 4.5c where we can see that the region of super-corotation (dark red) has diminished for B_{68}. The meridional velocity distribution is shown in Fig. 4.13b. The high altitude localised accelerated flow in region III is slightly faster than in case B_{100} because the pressure gradient and advection terms are 27−40 % larger in this region of B_{68}. This would lead to a minimal temperature increase ∼3 %, most notably in regions II and I (see Fig. 4.13c).

4.3.3 Outer boundary conditions for an expanded magnetosphere

For our expanded configuration, we found that $I_{\rho\infty}$=80 MA gave a smooth profile (least variance in FAC density). This change in $I_{\rho\infty}$ produced corresponding changes in model outputs, which are far less significant than those from our compressed case. Both magnetospheric and thermospheric angular velocities in case C_{80} have slightly smaller magnitudes in the magnetodisc region when compared to C_{100}. The current profiles calculated by setting $I_{\rho\infty}$=80 MA produced currents strongly resembling those for case B_{68}. Peak values

for currents at the region III / II boundary are ∼70–80 % of those in case C_{100}. Thermospheric flows for C_{80} differ slightly from C_{100}, most significantly in the larger degree of sub-corotation in C_{80}. The 'hotspot' in the polar region is ∼2 % hotter than in case C_{100} because of faster poleward flows transporting heat more efficiently. These faster flows are due to stronger advection in case C_{80} producing stronger acceleration compared to C_{100}.

4.3.4 Effect of outer boundary conditions on ionospheric powers

In this section, we examine figures for ionospheric power per unit area and their respective integrated power per hemisphere for cases A_{45}, B_{68} and C_{80}.

The power per unit area for case A_{45} in the high latitude region is shown in Fig. 4.14a. Colour conventions and labels are the same as those in Figs. 4.6b, d and f. Powers per unit area (in Fig. 4.14a) are integrated over each hemisphere and are shown in Fig. 4.14b. The transition between region III and II is the most interesting for comparison; A_{100} has a large prominent peak in magnetospheric power whereas A_{45} has a significantly reduced peak due to smaller values of Ω_M. In region II $\Omega_M \sim 0.5\,\Omega_J$ (see Fig. 4.10a) implying that magnetospheric and atmospheric power in this region are equal. Joule heating and ion drag are thus increased in A_{45} compared to A_{100} to meet the above requirement. These results suggest that smaller $I_{\rho\infty}$ values will generally dissipate more heat in the atmosphere but less efficiently maintain corotation in the magnetosphere.

For cases B_{68} and C_{80} the power per unit area and integrated powers per hemisphere are shown in Figs. 4.14c-d and e-f respectively. In comparing these two cases with B_{100} and C_{100} we find only small differences in atmospheric powers (Joule heating and ion drag), predominantly at the region III / II boundary where there are two peaks with a small trough in between. The integrated atmospheric powers per hemisphere thus remain relatively uniform with the changes in $I_{\rho\infty}$ specified for all baseline (B_{68} and B_{100}) and expanded (C_{80} and C_{100}) cases. The magnetospheric power per unit area for B_{68} and C_{80} has significantly smaller magnitudes in region III compared to their $I_{\rho\infty}$=100 MA counterparts. Therefore, for these configurations of the magnetosphere, decreasing the value of $I_{\rho\infty}$ decreases the efficiency with which the atmosphere can accelerate the magnetosphere towards corotation, but has no significant effect on atmospheric powers.

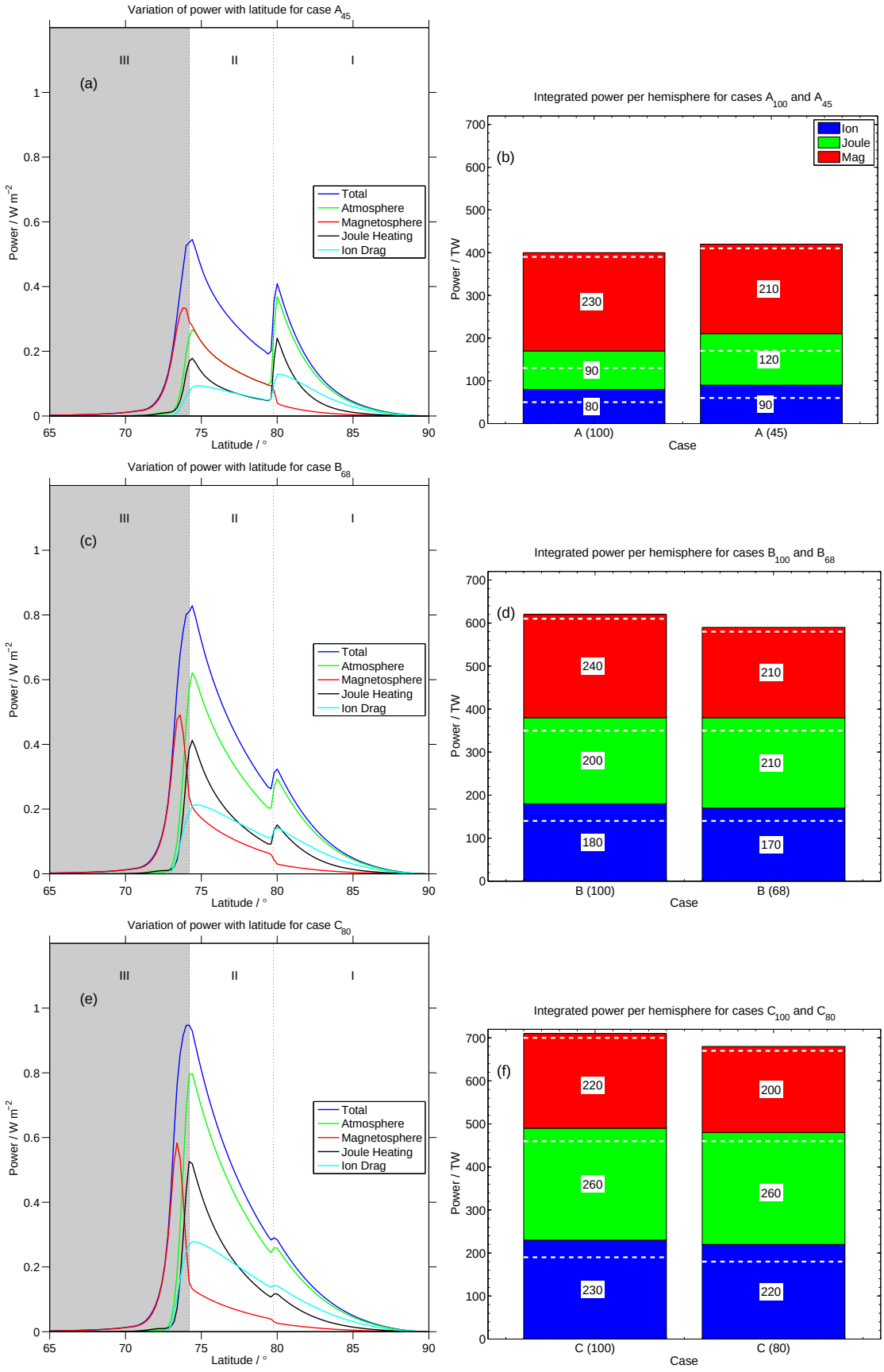

Figure 4.14. Figures a, c and e show ionospheric powers per unit area in the high latitude region for cases A_{45}, B_{68} and C_{80} respectively. All colours, styles and labels are as in Fig. 4.6b. Figures b, d and f show integrated powers per hemisphere for cases A_{45}, B_{68} and C_{80} respectively. All colours, styles and labels are as in Fig. 4.9.

4.4 Conclusions

The steady state work presented here in this chapter has confirmed many predictions and simulations such as those by Southwood and Kivelson (2001); Cowley and Bunce (2003b); Cowley et al. (2007). We find that angular velocities for both magnetodisc plasma and thermospheric neutrals increase with decreasing magnetospheric size. Whilst the reverse occurs for the M-I coupling currents and neutral thermospheric temperature. Like previous GCM studies (e.g. Smith and Aylward (2009)) our low-latitude thermosphere is significantly cooler than the polar regions due to strong poleward meridional winds transporting heat towards the pole. This is an issue with using GCM models without arbitrary heating sources in the equatorial regions. To try and solve this energy crisis issue at Jupiter, we now propose to move away from steady-state studies and look at how small time scale (less than a few hours) variation in solar wind dynamic pressure effects the Jovian thermosphere, particularly in regards to the variation of heating and momentum terms associated with M-I coupling. Time-dependent M-I coupling comprises the largest part of this thesis and will be presented in Chapters 5 and 6.

This page was intentionally left blank

Chapter 5

Response of thermospheric dynamics to transient solar wind pulses.

Adapt or perish, now as ever, is nature's inexorable imperative.

H. G. Wells

5.1 Introduction

In Chapter 4 we showed how the Jovian thermosphere and M-I coupling currents respond to variations in solar wind dynamic pressure on steady state time scales. Those results were in agreement with previous theoretical and modelling studies (e.g. Southwood and Kivelson (2001); Cowley et al. (2005)). One issue with thermospheric GCMs for rapidly rotating planets is that of the 'ion drag fridge' (Smith et al. 2007), where deposited energy is transported polewards effectively cooling the equatorial regions of the atmosphere. The flow systems creating the ion drag fridge are prevalent in steady state conditions but may change when time-dependent perturbations are applied to the coupled system. Cowley and Bunce (2003a); Cowley et al. (2007) investigated the response of M-I coupling currents and aurora to rapid magnetospheric reconfigurations (perturbations) which would either compress or expand the Jovian magnetosphere on time scales of $< 3\,hours$. They found that expansions led to significant sub-corotating plasma and as such an increase in coupling

currents and auroral emission. However, drastic compressions ($\sim 40\,\mathrm{R_J}$) could cause the magnetospheric plasma to super-corotate compared to both the planet and thermosphere resulting in a reversal in the direction of angular momentum transfer and coupling currents.

In this Chapter, we use 'JASMIN', to estimate the response of Jovian thermospheric dynamics to transient changes in the solar wind dynamic pressure and, consequently, magnetospheric size. By transient, we mean changes on time scales $\lesssim$3 hours, where the angular momentum of the magnetospheric plasma is approximately conserved (Cowley et al. 2007). The time scales required for changes in the M-I currents to affect Ω_M are much longer, $\sim$10$-$20 hours. We investigate the response of M-I coupling currents and thermospheric dynamics to our time-dependent profiles of plasma angular velocity in the magnetosphere. We employ different $\Omega_M(\rho_e, t)$ profiles (ρ_e represents equatorial radial distance; t denotes time) to represent compressions and expansions of the middle magnetosphere (see section 3.5.1). In the present study, we focus on the dynamic response of the thermosphere. This will be the first study to investigate how transient variations in solar wind pressure influence both magnetospheric and thermospheric properties of the Jovian system, and to use a realistic GCM to represent the thermosphere.

In Chapter 2 we summarise the scientific background needed for this study, details and limitations for our current model are presented in section 3.5. In sections 5.2 and 5.3 we present and discuss our findings for the transient compression and expansion scenarios respectively. We present our conclusions in section 7.2.

5.2 Magnetospheric Compressions

In this section we present findings for our transient magnetospheric compression scenario. We show initial, steady state profiles (case CS with R_{MM}=85 $\mathrm{R_J}$), 'half-pulse' profiles (case CH with R_{MM}=45 $\mathrm{R_J}$) and 'full-pulse' profiles (case CF with R_{MM}=85 $\mathrm{R_J}$). The transient event lasts for a total of three hours.

5.2.1 M-I coupling currents

Here we discuss how a transient compression event affects the M-I coupling currents. We compare initial steady-state currents with those calculated at 'half-' and 'full-' pulse inter-

vals; indicated by cases CS, CH and CF respectively.

In the model of Cowley et al. (2007) a transient compression of the magnetosphere causes significant super-corotation of the magnetodisc plasma, compared to both the thermospheric and planetary angular velocities. This leads to a current reversal throughout the middle magnetosphere (region III). Fig. 5.1a shows the variation of azimuthally integrated radial current with equatorial radial distance for cases CS, CH and CF. The blue line shows case CS, whilst the red and green lines show the respective half- and full-pulse cases (CH and CF). Comparing cases CS and CH we see very different profiles. The expected current reversal (negative I_ρ), for the compressed system, is caused by the super-corotation of the magnetosphere compared to the thermosphere (see Fig. 3.6a in section 3.5.1); thus, the shear $(\Omega_T - \Omega_M)$ is negative and creates disc currents which flow radially planetward (reversed), instead of outward (as in steady-state). The profile for case CF resembles that of CS but with larger radial current ($\sim$20 % on average) at all equatorial radii. The differences between these two cases are attributed to the response of the thermosphere to the transient pulse. At full-pulse, $\Omega_M(CF)$=$\Omega_M(CS)$ but $\Omega_T(CF)\neq\Omega_T(CS)$ as the thermosphere has not had sufficient time to settle back to a steady-state (due to its large inertia, as discussed in section 3.5.1). Although this is a subtle example of the atmospheric modulation of auroral currents, future simulations will aim at further exploring how this effect changes within the parameter space of the pulse duration and its change in solar wind pressure. Currently, preliminary work suggests a minimum thermospheric response time on-the-order of one hour; thus we would expect steady-state conditions to be reached within, at most, two Jovian rotations where any enhancements of coupling currents resulting purely from thermospheric modulations would cease. Further studies are currently beyond the scope of this work.

Fig. 5.1b shows the azimuthally integrated Pedersen current I_P in the high latitude ionosphere for cases CS, CH and CF. Conjugate magnetospheric regions are labelled and separated with dotted black lines. The line colour code is the same as Fig. 5.1a. I_P is half of the radial current I_ρ flowing through the magnetically conjugate location in the plasmadisc (continuity of current between disc and two planetary hemispheres). Thus, in region III, the trends in Fig. 5.1b reflect those in Fig. 5.1a. For example, in case CH, where I_P is negative (region III), the Pedersen current flows polewards instead of equatorwards,

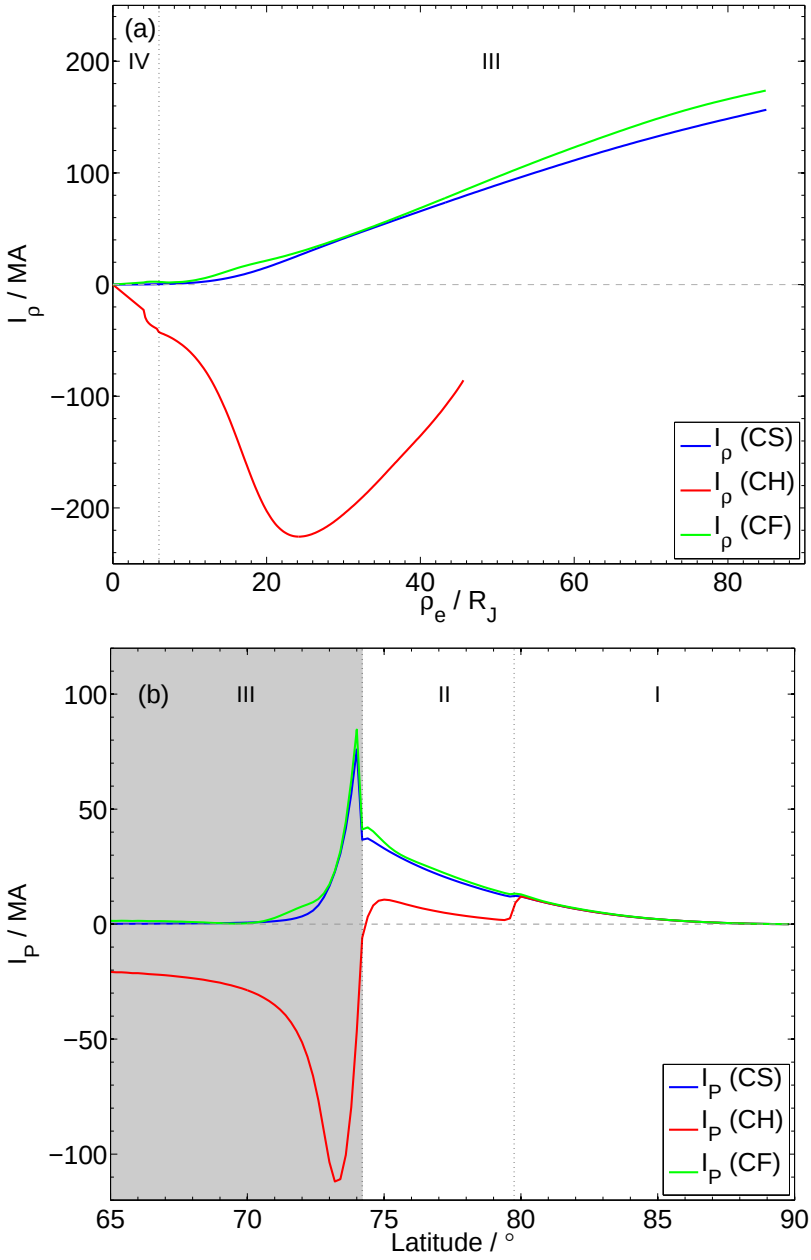

Figure 5.1. (a) Azimuthally integrated radial current as a function of equatorial radial distance from Jupiter. The blue line represents case CS, whilst the red and green lines indicate cases CH and CF, respectively. (b) Azimuthally integrated Pedersen current as a function of ionospheric latitude. The line colours are the same as in (a). The dotted black lines separate the magnetospheric regions considered in this study. Positive I_P indicates equatorward current.

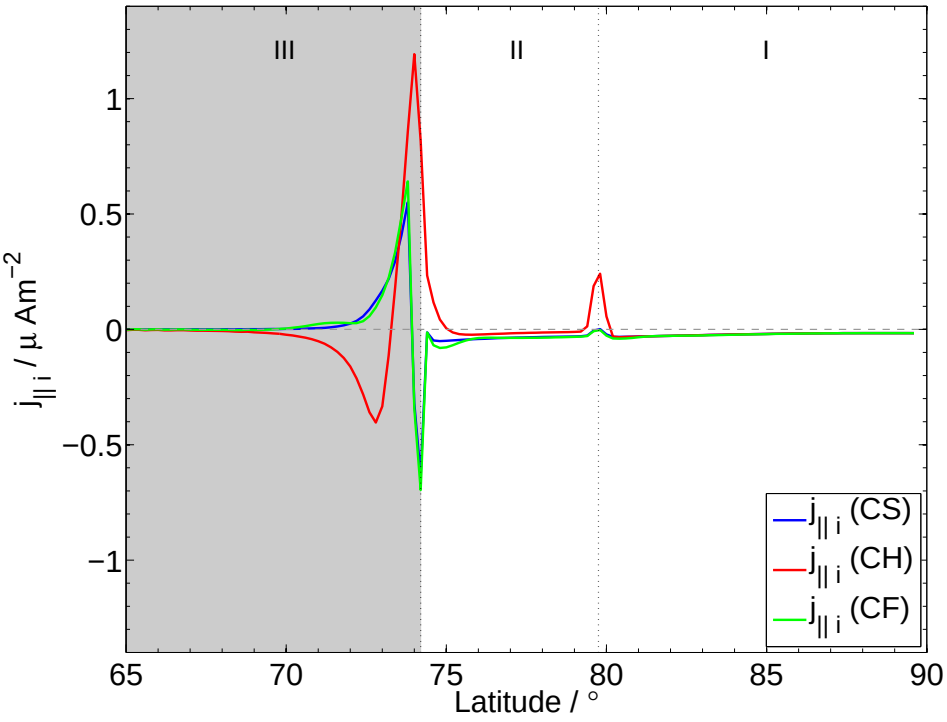

Figure 5.2. FAC densities in the high latitude ionospheric region for our transient compression cases. The black line represents case CS whilst the red and blue lines indicate cases CH and CF respectively. The conjugate magnetospheric regions (region III is shaded) are separated by dotted black lines and labelled.

as in steady-state. In region II, we have fixed Ω_M at a value depending on magnetodisc size (Cowley et al. 2005). This causes the difference in I_P between case CS and CH in region II. The analogous difference between cases CS and CF is, once again, due to the lag in thermospheric response as discussed above. In region I, we select a fixed value of $0.10\,\Omega_\mathrm{J}$, over all cases, for Ω_M in concordance with Isbell et al. (1984), resulting in minimal differences between the current profiles in this region.

Fig. 5.2 shows FAC density as a function of latitude (computed from the horizontal divergence of I_P) for cases CS, CH and CF. The line colour code is the same as for Fig. 5.1. Comparing cases CS and CF in region III, with increasing latitude (moving polewards), there is one region of upward-directed FAC density and one region of downward-directed FAC for each case. The peak in upward-directed current is located at $\sim 74\,^\circ$, corresponding to the 'main auroral oval'. The minimum downward-directed current, in both cases is located at the region III/II boundary. In regions II and I, FAC density profiles remain slightly negative (downward). Peaks in FAC arise from strong spatial gradients in Ω_M

(Ω_M decreases by $\sim$78 % across $\sim$2 °), and consequently, flow shears located at or near magnetospheric region boundaries. The troughs at the region III boundary are due to large spatial gradients in Ω_M and Σ_P encountered as we traverse this boundary (Yates et al. 2012).

Case CH, on the other hand, is more interesting, as it shows the largest deviation from steady state. The CH FAC density profile is initially directed downwards at latitudes up to $\sim$73 °. At this location, the FAC becomes positive (upwards) maximising at $\sim$74 °. FACs then decrease to roughly constant negative values throughout regions II and I, but with a large, $\sim 0.2\,\mu\,\mathrm{A\,m^{-2}}$ upward current at the region II/I boundary due to a corresponding change in Ω_M. In terms of auroral emissions, we would expect relatively dark regions where the FAC is negative. The factor of two increase in peak FAC (at $\sim$74 °) compared to cases CS and CF suggests a much brighter and somewhat narrower 'main auroral oval' for the most compressed configuration of the magnetosphere. Observations reported by Clarke et al. (2009) and Nichols et al. (2009) indicate that the UV auroral emission increases in brightness by factors of two, in response to rapid increases in solar wind dynamic pressure of the order of $\sim 0.01-0.3$ nPa. Our results also suggest the possibility of observable polar emission located at the open-closed field line boundary (region II/I). However, this conclusion is strongly dependent on the assumptions made for the outer magnetospheric plasma flow. The latitudinal location of the main peak has also shifted polewards by $\sim$0.2 ° in the CH profile, which has been seen in modelling by Yates et al. (2012). Observations by Nichols et al. (2009) have seen poleward shifts in main oval emission by up to $\sim$1 ° corresponding to the arrival of solar wind shocks.

We briefly compare FAC densities from case CH with transient results from Cowley et al. (2007) (compression from $85-45\,\mathrm{R_J}$). Despite a resemblance in FAC profiles, peak FACs in the magnetodisc (region III) are $\sim$2.5 times larger in case CH than the equivalent case (with a responsive thermosphere) in Cowley et al. (2007). The peak FACs in case CH, are actually closer to those in Cowley et al. (2007)'s non-responsive thermosphere compression case. This suggests that, the thermosphere (represented by a GCM) in our study lies somewhere in between a responsive and non-responsive thermosphere (although closer to the latter, for the pulse parameters assumed).

For completeness, we also calculated M-I coupling currents for the case of a non-responsive thermosphere (Gong 2005). To do this, we assume that Ω_T=$\Omega_T(CS)$ throughout the entire transient event. In this non-responsive thermosphere scenario, there is an average increase in M-I currents of ∼20 % midway through the pulse compared to case CH (obtained using GCM). At full-pulse, however, the non-responsive case has M-I currents that are on average ∼12 % smaller than currents in case CF. These differences between a non-responsive thermosphere and a responsive one (GCM), are related to the flow shear between thermosphere and magnetosphere; which, is maximal (resp. minimal) at half-pulse (resp. full-pulse) when using a non-responsive thermosphere.

In summary, the FAC densities in Fig. 5.2 suggest that a transient compression will cause a narrowing and poleward shift in the location of the main auroral oval (∼0.2 °), as well as an increase by a factor of ∼2 in peak brightness. These predictions are of similar order to HST observations carried out by Nichols et al. (2009) and Clarke et al. (2009).

5.2.2 Thermospheric dynamics

In this section, we discuss the thermospheric response to the simulated transient magnetospheric compressions. We present the variation of azimuthal and meridional thermospheric flows and temperature distribution. We then proceed to interpret the model outputs, in the context of the dominant acceleration terms contributing to the evolution of momentum.

Smith et al. (2007), Smith and Aylward (2009) and Yates et al. (2012) showed that in the Jovian auroral thermosphere, there are two main steady-state flow patterns:

i) Low-altitude (<600 km*)*: Here, ion drag acceleration becomes strong due to the Pedersen conductivity layer (maximum value of 0.1163 mho m^{-1} at ∼370 km). An imbalance is created between ion drag, Coriolis and pressure gradient terms; thus, giving rise to advection of momentum which, restores equilibrium in this low altitude region. This results in mostly sub-corotational, poleward flow as shown in Fig. 5.3a.

ii) High-altitude (>600 km*)*: Conditions are quite different at high-altitudes, meridional Coriolis and pressure gradient accelerations are essentially balanced, whilst terms such as ion drag, advection and zonal Coriolis are small and insignificant. This creates a 'jovistrophic' condition, whereby flow is directed very slightly equatorwards and is sub-corotational, as shown in Fig. 5.3b.

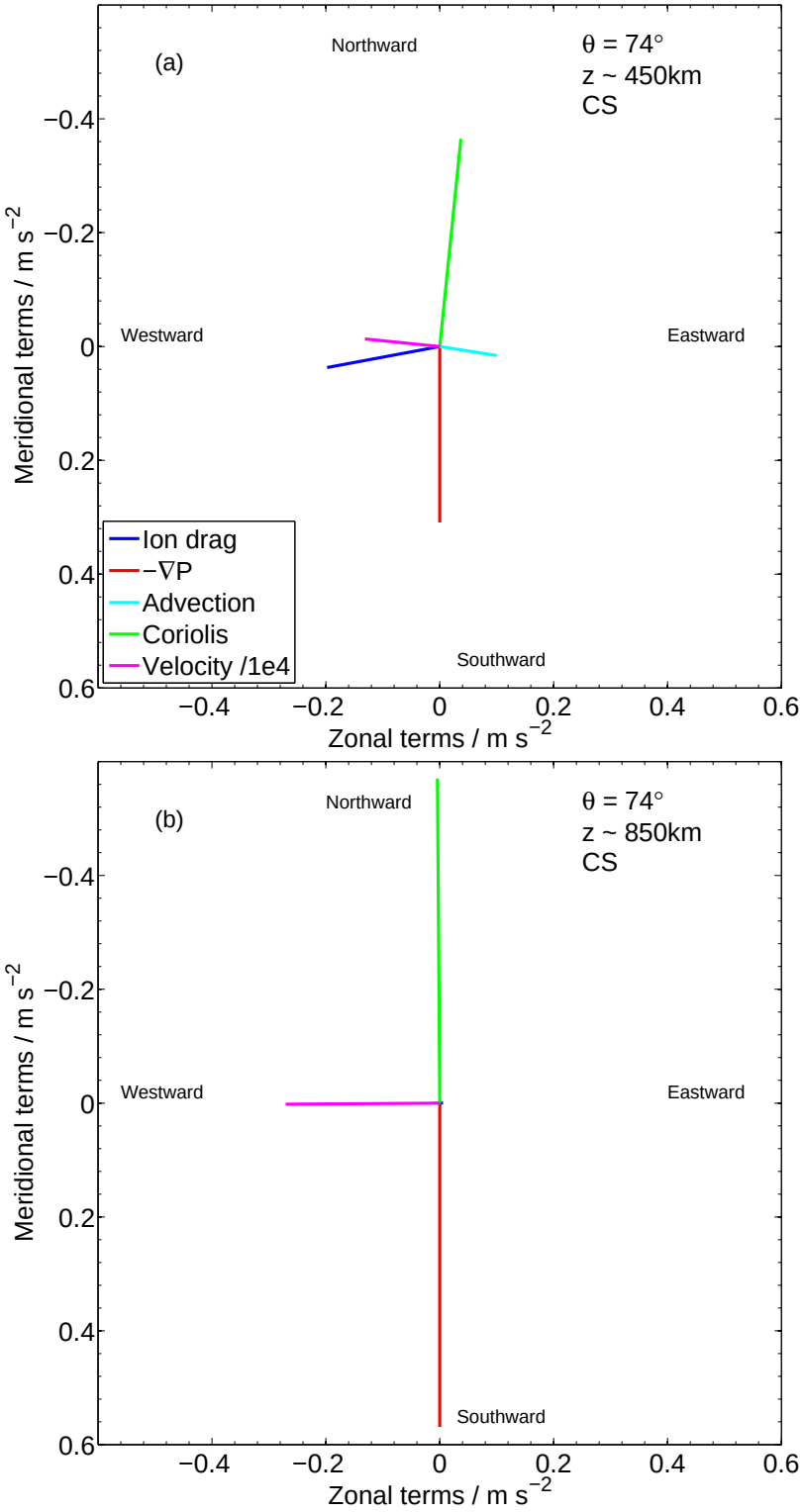

Figure 5.3. Meridional and zonal acceleration balance diagrams for case CS at an ionospheric latitude of 74 °. (a) Shows acceleration terms at low altitude whilst (b) shows the equivalent terms at high altitude. Ion drag terms are represented by blue lines, fictitious (Coriolis) by green lines, pressure gradient by red lines and advection by the cyan lines. The velocity vector (in the corotating reference frame) is represented by the magenta lines. Note that the magnitude of velocity components have been divided by a factor of 10, 000 to fit the plotted scale.

Fig. 5.4 shows the altitude and latitude variation of azimuthal and meridional thermospheric velocities for the transient compression cases. Fig. 5.5 shows corresponding thermospheric temperature distributions for the transient compression scenario. Fig. 5.6 shows zonal and meridional ion drag and advection momentum terms and is used to aid in the description of relevant thermospheric flows. For completeness Figs. B.1 - B.3, in Appendix B, show all momentum terms (including those in Fig. 5.6) in the thermosphere.

Figs. 5.4a, c and e shows the variation of thermospheric azimuthal velocity, in the corotating reference frame, in the high latitude thermosphere for cases CS-CF. Positive (resp. negative) values of azimuthal velocity indicate super (resp. sub)-corotating regions. The direction of meridional flow is indicated by the black arrows, the locus of rigid corotation is indicated by the white line, strong super-corotation is indicated by the black contour, strong sub-corotation is indicated by the dashed white contour, and the magnetospheric regions are labelled and separated by black dotted lines. Zonally, there are two prominent features in our transient compression cases: i) a low altitude small super-corotating jet (black contour), centred at $\sim 72^\circ$, and ii) a large sub-corotating jet , from region III - I (blue region in Figs. 5.4a, c and e;). Figs. 5.4b, d and f shows the variation of meridional flows in the high latitude thermosphere for our transient compression cases. Magnetospheric labels, locus of corotation and arrows are the same as in Figs. 5.4a. These figures, show the meridional flow pattern in the thermosphere, as well as, localised accelerated regions (red/brown hues).

As discussed in Smith and Aylward (2009) and Yates et al. (2012), the super-corotational jet in case CS (Fig. 5.4a) is created by a small excess in the zonal Coriolis and advection momentum terms compared to the ion drag term. At low altitude, Coriolis force is primarily directed eastwards corotational and unopposed can promote super-corotation in the neutrals. The large sub-corotational jet is caused by the drag of the sub-corotating magnetosphere on the thermosphere. Zonal flows are, for the most part, sub-corotational and momentum terms are balanced in case CS as it is in steady-state. Meridionally, momentum is balanced mainly between Coriolis and pressure gradient terms (see first column of Figs. B.2), except at low altitudes where ion drag is present (due to conductivity layer)

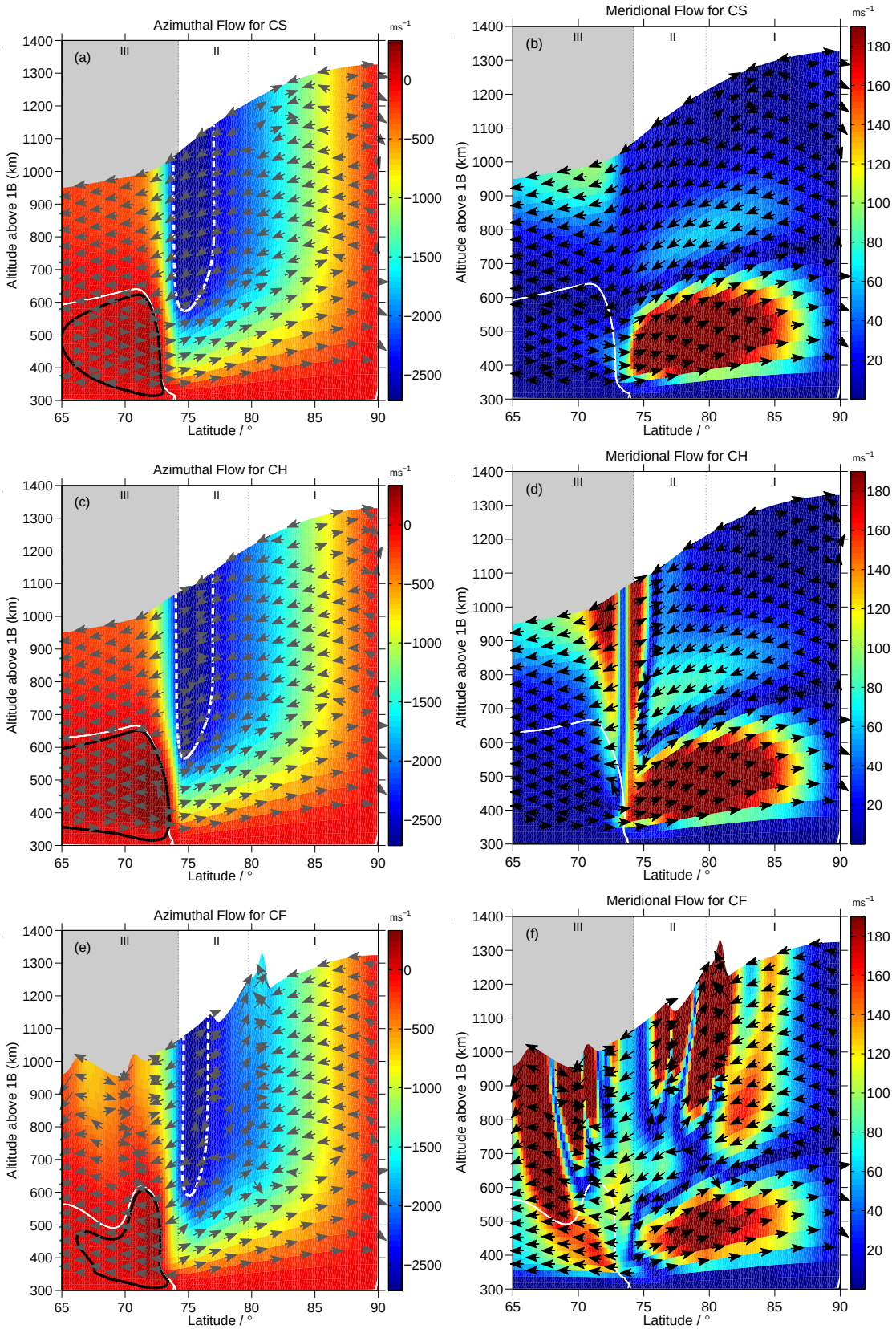

Figure 5.4. (a), (c) and (e) show the variation of thermospheric azimuthal velocity (colour scale) in the corotating reference frame for cases CS-CF respectively (left to right). Positive values (dark red) indicate super-corotation, whilst negative values (light red to blue) indicate sub-corotation. The arrows show the direction of meridional flow and the solid white line indicates the locus of rigid corotation. The solid black encloses regions of super-corotation ($> 25\,\mathrm{m\,s^{-1}}$) and the dashed white line encloses regions that are sub-corotating at a rate $> -2500\,\mathrm{m\,s^{-1}}$. The magnetospheric regions (region III is shaded) are separated by dotted black lines and labelled. (b), (d) and (f) show the meridional velocity in the thermosphere for cases CS-CF. The colour scale indicates the speed of flows. All other labels and are as for (a).

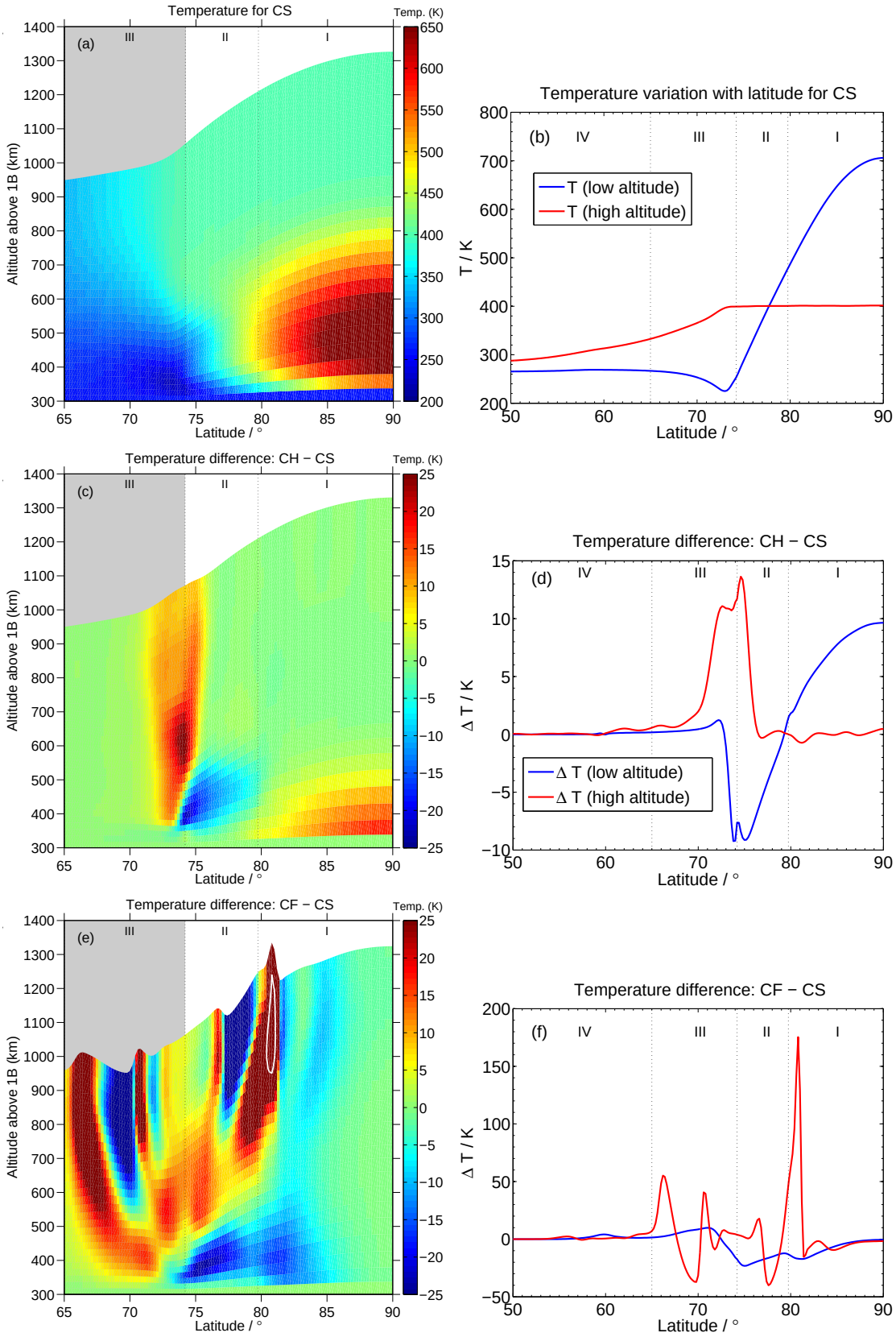

Figure 5.5. (a) shows the thermospheric temperature distribution for case CS whilst (c) and (e) show the temperature difference of cases CH and CF with case CS. The white contour encloses temperature differences $> 100\,\mathrm{K}$. The magnetospheric regions (region III is shaded) are separated by dotted black lines and labelled. (b) shows the latitudinal temperature profile for case CS and (d) and (f) show latitudinal temperature difference profiles at low (blue line) and high (red line) altitudes for CH and CS, and CF and CS. All other labels and are as for (a).

which leads to the advection of momentum and accelerated poleward flows as seen in Fig. 5.4d. These steady-state flow patterns are as shown in Fig. 5.3.

Zonal flows for case CH (see Fig. 5.4c), at first glance seem similar to those of case CS, but there is a factor of two increase in the zonal velocity within the region of super-corotation, as well as an increase in latitudinal size of the super-corotating jet. The large, sub-corotational jet remains roughly unchanged but the overall degree of sub-corotation has decreased i.e. the magnitude of azimuthal velocity has decreased by $\sim$4 %. Meridional flows in Fig. 5.4d, show two additional local acceleration regions either side of $\sim$73 ° latitude and from altitudes >500 km. The thermosphere has undergone significant changes in both zonal and meridional momentum terms. The most pronounced being with regards to ion drag, where these terms have changed sign. Fig. 5.6 shows the distribution of ion drag momentum with altitude and latitude for case CS (plot a) and CH (plot c). Blue and orange contours respectively show southward and northward acting ion drag whilst purple and cyan represent corotational (eastwards) and anti-corotational (westwards) ion drag respectively. It can clearly be seen that for case CH ion drag now acts in the opposite direction compared to steady-state, particularly in region III. This results from the current reversal discussed in section 5.2.1. The increase in super-corotation is mainly caused by eastwards ion drag, which is now larger than both Coriolis and advection terms in region III. Fig. 5.6d shows that the local acceleration regions (in Fig. 5.4e) primarily result from meridional advection of momentum (blue and orange lines) created to balance the non-equilibrium state of the thermosphere (at the half-pulse phase). The direction of flow (arrows) has also reversed in the lower altitude section of region III. This change is attributed to the reversal of meridional ion drag in this region, which now promotes equatorward flow. These changes in dynamics lead to temperature deviations from case CS of $\sim \pm 25$ K (see Fig. 5.5c).

The thermospheric flows of case CF are in the third row of Fig. 5.4, and the corresponding zonal and meridional momentum terms are shown in the third column of Figs. B.1 - B.3. The first thing we notice is that the thermosphere's altitudinal profile is highly unusual compared to cases CS and CH; there are peaks and troughs poleward of $\sim$65 ° latitude along the upper boundary of our thermosphere. These result from the large temperature deviations (-40 to $+175$ K) evident at high altitudes in Fig. 5.5e and in the red line of

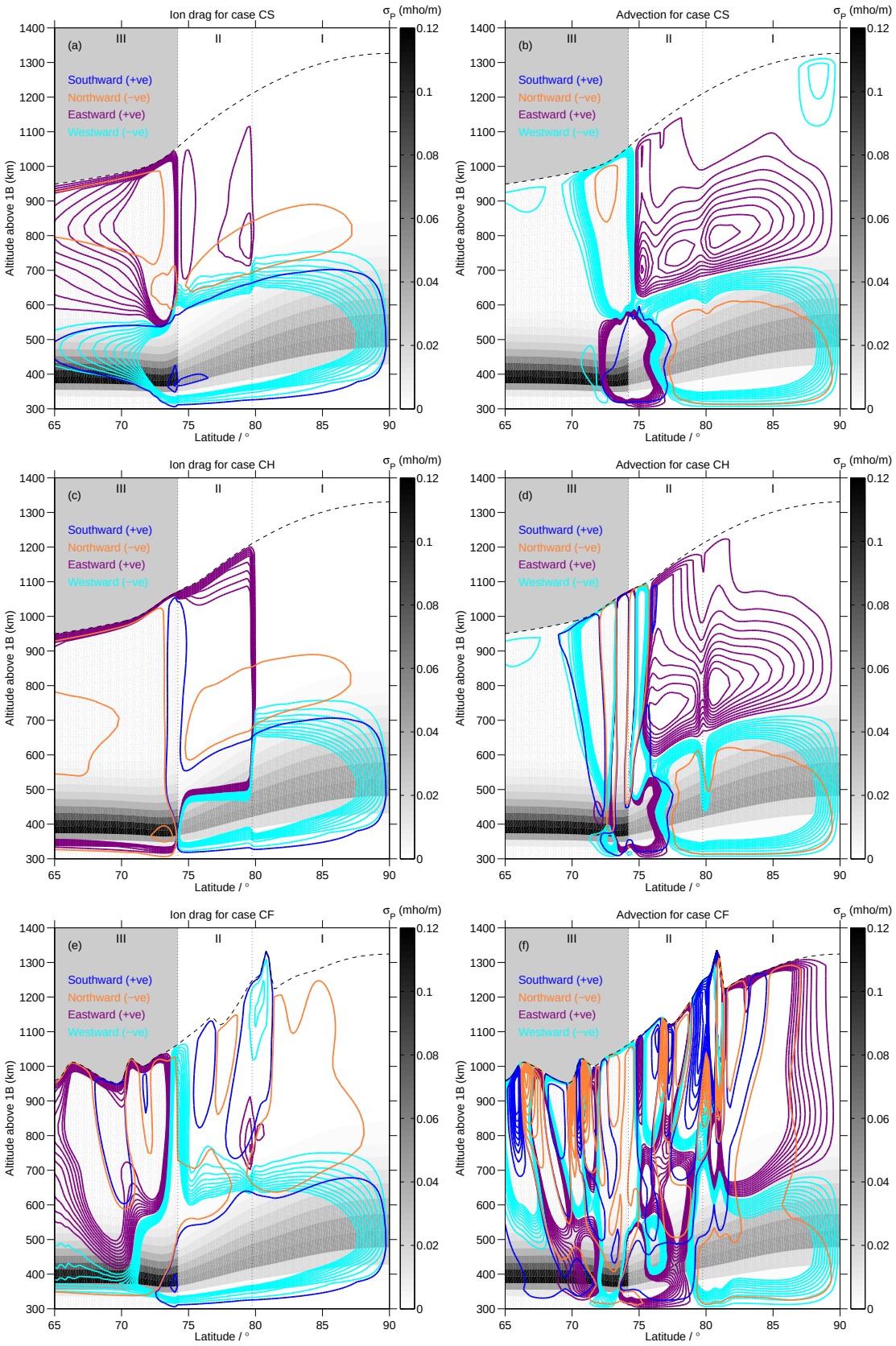

Figure 5.6. (a), (c) and (e) shows the variation of zonal and meridional ion drag momentum with altitude, latitude and Pedersen conductivity (colour bar) for cases CS-CF respectively. The meridional contours (blue and orange) range from $1 - 500\,\mathrm{mm\,s^{-2}}$ with an interval of $50\,\mathrm{mm\,s^{-2}}$ and with blue being positive (southward) and orange being negative (northward). The zonal contours (purple and cyan) range from $1 - 10\,\mathrm{mm\,s^{-2}}$ with an interval of $1\,\mathrm{mm\,s^{-2}}$ and with purple being positive (eastwards) and cyan being negative (westwards). The magnetospheric regions are separated and labelled. (b), (d) and (f) same as for (a), (c) and (e) but for advection of momentum.

Fig. 5.5f. The zonal flows in Fig. 5.4e, continue to exhibit the general features present in cases CS and CH: i) a large sub-corotational jet in regions II and I and, ii) a small super jet at low altitudes in region III. The zonal momentum terms (purple and cyan lines) in Fig. 5.6e-f (and third column of Fig. B.1), exhibit a somewhat complex nature - particularly in the advection terms (Figs. 5.6f). These show latitudinal and altitudinal fluctuations between positive and negative momentum terms. The zonal ion drag momentum distribution (Fig. 5.6e) is, however, starting to return to its initial state (case CS, Fig. 5.6a). This is not surprising as ion drag is directly linked to the magnetosphere (see Eq. (3.21)) and as such would respond more quickly to changes in magnetospheric conditions when compared to Coriolis, advection or viscous terms. Meridionally, in Fig. 5.4f, the number of local accelerated regions poleward of 65 ° latitude, have increased significantly. The direction of meridional flow (black arrows) is similar to that of case CH except for high altitudes in regions III and II, where flow directions change on relatively small spatial scales. This complex flow pattern is directly influenced by meridional ion drag (Figs. 5.6e), where (for example) negative ion drag contours map to equatorward flow whilst positive contours map to poleward flow (schematically shown in Fig. 5.3). On the other hand, the localised accelerations result from advective terms, which respond to the disequilibrium created by the transient event, and also attempt to re-establish hydrostatic equilibrium (see almost one-to-one mapping of advection contours in Figs. 5.6f (blue and orange contours) and 5.4f).

Figs. 5.4-5.6 represent the changes that occur in the thermosphere throughout a transient, magnetospheric compression event. We see that the zonal flow structure of the thermosphere does not change significantly with a transient compression event i.e a large sub-corotational jet and a small super-corotational jet. We note, however, that the degree of corotation is strongest when the magnetodisc radius is minimum. In the meridional direction, numerous local accelerated regions develop as the event progresses, as well as significant deviations from steady-state flow patterns. From Figs. 5.4 and 5.6, we see that thermospheric flows are mostly influenced by changes in ion drag and momentum advection terms.

5.3 Magnetospheric Expansions

This section presents our findings for a transient magnetospheric expansion event. The initial steady-state (magnetodisc radius of 45 R_J), is expanded to a maximum radius of 85 R_J, before subsequently returning to its initial size. The duration of this expansion event is the same as the compression event i.e. three hours.

5.3.1 M-I coupling currents

We investigate how a transient expansion (a rarefaction region in the solar wind) affects the M-I coupling currents. We compare initial compressed steady-state currents with those calculated at half- and full-pulse intervals; indicated by cases ES, EH and EF respectively.

Fig. 5.7a shows azimuthally integrated radial current as a function of equatorial radial distance from Jupiter. Case ES is represented by the black line, whilst cases EH and EF are represented by red and blue lines respectively. The dotted grey line merely emphasises zero radial current. Firstly, we compare case ES with EH. There is a factor of three increase in peak radial current from case ES to EH at the outward edge of the magnetodisc. This increase in I_ρ is caused by the large increase in flow shear between the thermosphere and magnetosphere as shown in Fig. 3.6b. The I_ρ profile for case EF decreased throughout the magnetodisc region to a peak value $\sim$75 % that of case ES. At radii $\lesssim$20 R_J there is a small amount of current reversal due to the lag of the thermosphere (see Fig. 3.6b). If allowed to progress, this reversal would lead to an increase in thermospheric angular velocity towards corotation.

The variation of azimuthally integrated Pedersen current with latitude is shown in Fig. 5.7b. In region III, the current profiles reflect those seen in Fig. 5.7a as I_P=0.5 I_ρ. The variation between ES and EH in region II is caused by the different values of Ω_M that we prescribe for this region. Differences between ES and EF are, as stated in section 5.2.1, due to the lag in the response time of the thermosphere to the transient changes in Ω_M.

FAC densities in the high latitude region are plotted for cases ES, EH and EF in Fig. 5.8. The line colour code is the same in Fig. 5.7b. Comparing cases ES with EH we see three main differences: i) EH has two upward FAC peaks in region III (of similar

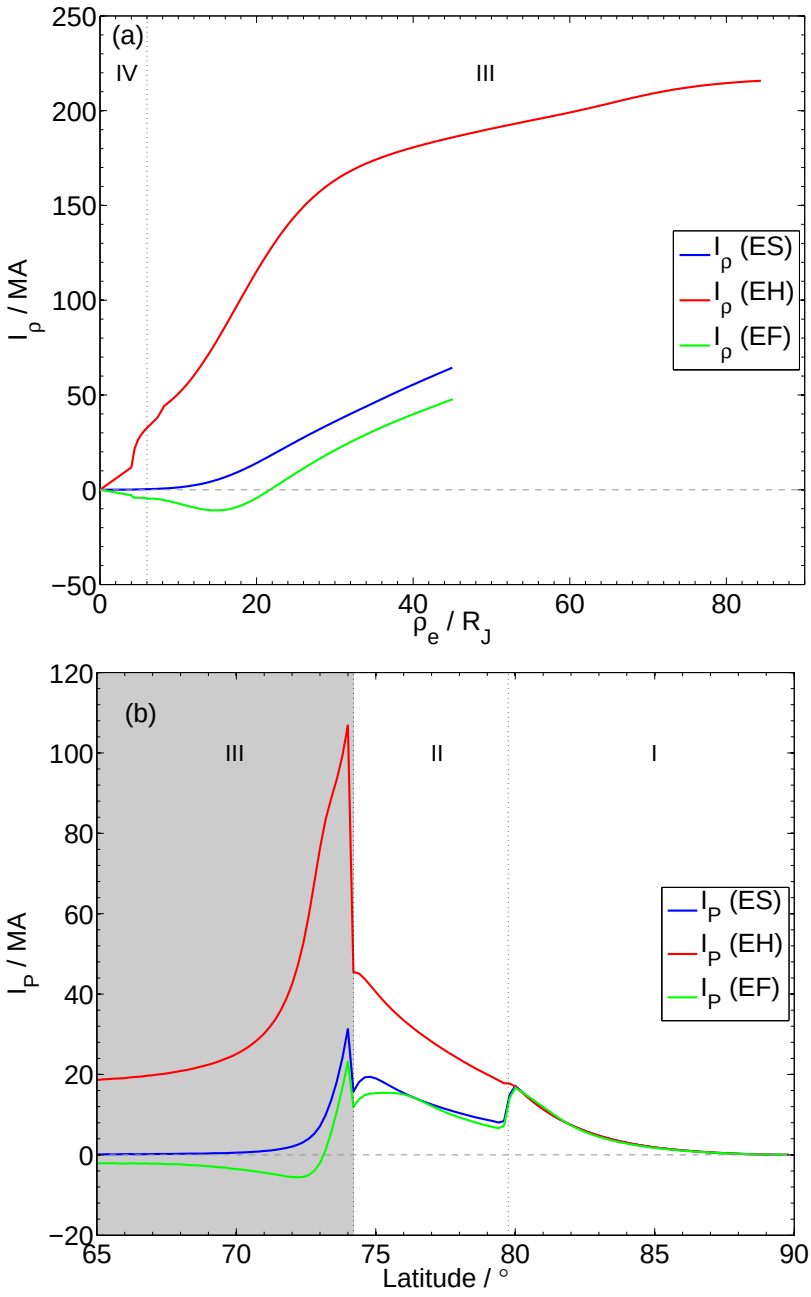

Figure 5.7. (a) Azimuthally integrated radial current as a function of equatorial radial distance from Jupiter. The black line represents case ES whilst the red and blue lines indicate cases EH and EF respectively. (b) Azimuthally integrated Pedersen current as a function of ionospheric latitude. The line colour code is the same as in (a) whilst the dotted black lines separate the magnetospheric regions considered in this study (region III is shaded).

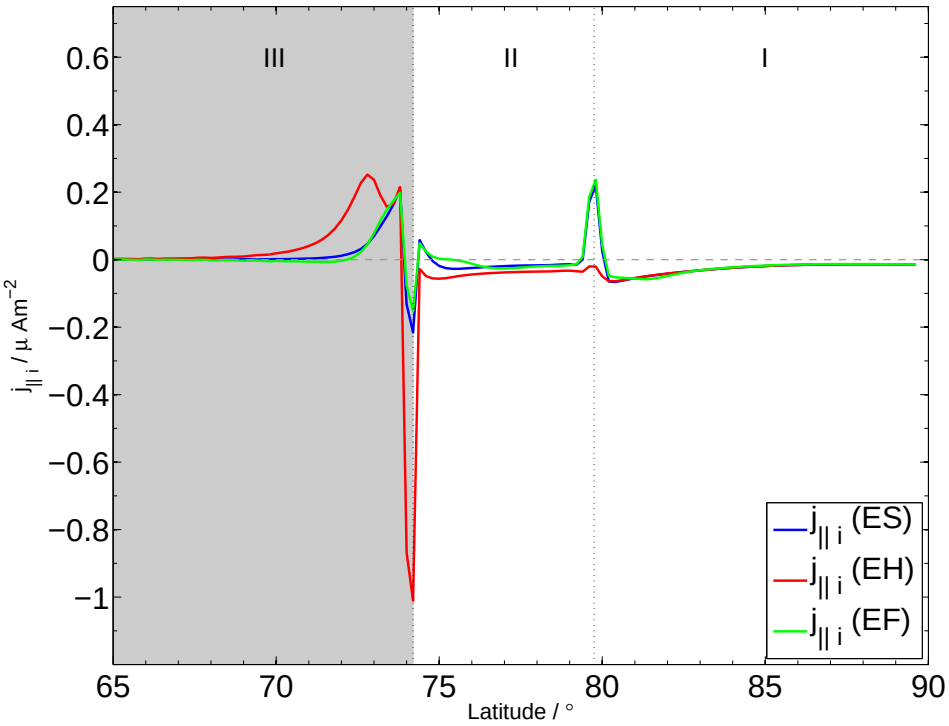

Figure 5.8. FAC densities in the high latitude region for our transient expansion cases. The black line represents case ES whilst the red and blue lines indicate cases EH and EF respectively. The magnetospheric regions (region III is shaded) are separated by dotted black lines and labelled.

magnitude to the peak in case ES) resulting in a large area of upward-directed FAC, ii) the magnitude of downward FAC near the region III boundary has increased by a factor of four (from ES to EH) and iii) FAC densities at the region II/I boundary are entirely downward-directed unlike case ES. As the magnetosphere expands, its magnetic field strength and plasma angular velocity decrease. This change in Ω_M (see Fig. 3.6b) increased the flow shear between the magnetosphere and thermosphere and thus increased the FAC in region III by ∼15 %. The strong downward FAC results from the large gradients in Ω_M and Σ_P through the poleward boundary of region III. The lack of any upwards currents at the region II/I boundary is due to the small change in Ω_M as the model traverses these two regions. Case EF shows only minor differences with case ES due to the lag in response time of the thermosphere to transient magnetospheric changes.

Comparing case EH FAC densities with the corresponding result from Cowley et al. (2007) (expansion from 45−85 R_J), we notice a few differences: i) the magnitude of peak upward FAC in case EH is ∼25 % larger than that in Cowley et al. (2007) and, ii) case

EF has no upward FAC at the region II/I boundary, contrary to results in Cowley et al. (2007). These differences emphasise the effect of using a time-dependent GCM for the thermospheric response. For example, the 'double-peak' structure in the Region III FACs is due to modulation of current by thermospheric flow.

As in section 5.2.1, we summarise the differences between the M-I coupling currents discussed above and those which arise if we assume a non-responsive thermosphere; such that Ω_T=$\Omega_T(ES)$ for the duration of the transient event (Gong 2005). We find that, for both half- and full-pulse datasets, there is, on average, a ∼20 % increase in the maximum magnitude of M-I currents in the non-responsive thermosphere scenario compared to cases EH and EF (using our GCM). These changes are, once again, linked to the flow shear between the magnetosphere and thermosphere. $\Omega_T(ES)$ is uniformly larger than Ω_T for cases EH and EF (see Fig. 3.6b). As such, the flow shear in the non-responsive scenario will always be greater than the flow shear obtained in the GCM thermosphere.

FAC densities in Fig. 5.8 suggest that transient expansions will cause a broadening of the main auroral oval, a ∼1 ° equatorward shift in peak emission along with a ∼15 % increase in peak FAC density. These results also suggest a possible darkening in the polar cap regions during the expansion. Observations by Clarke et al. (2009) have seen little, if any change in the brightness of auroral emission close to the arrival of solar wind rarefaction regions whilst changes in main oval location (∼1 °) have been observed by Nichols et al. (2009).

5.3.2 Thermospheric dynamics

We present thermospheric model outputs associated with transient magnetospheric expansions. We firstly present the variation of azimuthal and meridional thermospheric flows and temperature with altitude and latitude. Their associated momentum terms are then used to assist in the interpretation.

The altitude-latitude variation of azimuthal and meridional thermospheric velocities are shown in Fig. 5.9. Fig. 5.10 shows the corresponding thermospheric temperature distributions for the expansion scenario. We use Fig. 5.11 showing zonal and meridional ion drag and advection momentum terms to aid in the description of thermospheric flows. For

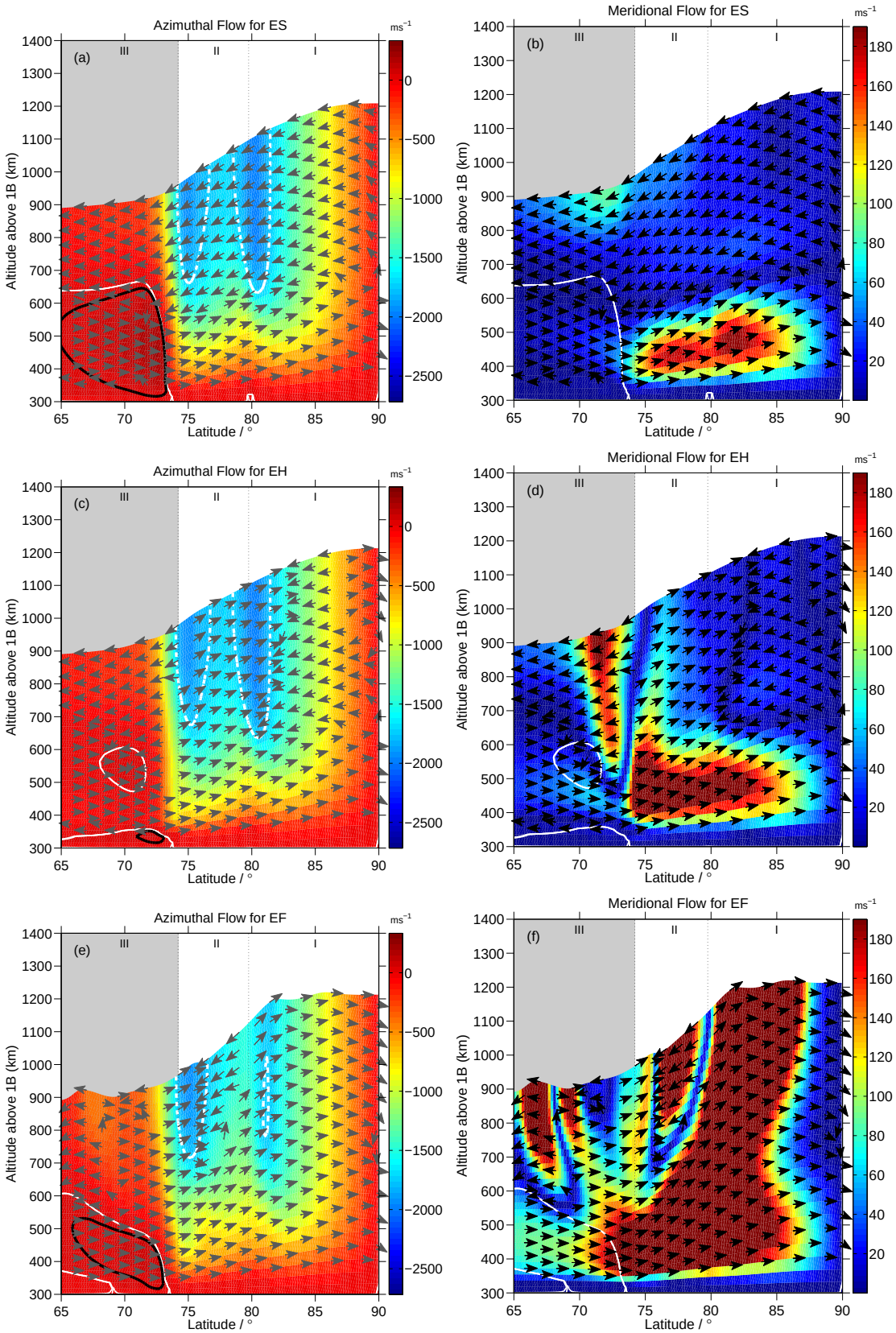

Figure 5.9. (a), (c) and (e) show the variation of thermospheric azimuthal velocity (colour scale) in the corotating reference frame for cases ES-EF respectively (left to right). Positive values (dark red) indicate super-corotation, whilst negative values (light red to blue) indicate sub-corotation. The arrows show the direction of meridional flow and the solid white line indicates the locus of rigid corotation. The solid black encloses regions of super-corotation ($> 25\,\mathrm{m\,s^{-1}}$) and the dashed white line encloses regions that are sub-corotating at a rate $> -1750\,\mathrm{m\,s^{-1}}$. The magnetospheric regions (region III is shaded) are separated by dotted black lines and labelled. (b), (d) and (f) show the meridional velocity in the thermosphere for cases ES-EF. The colour scale indicates the speed of flows. All other labels and are as for (a).

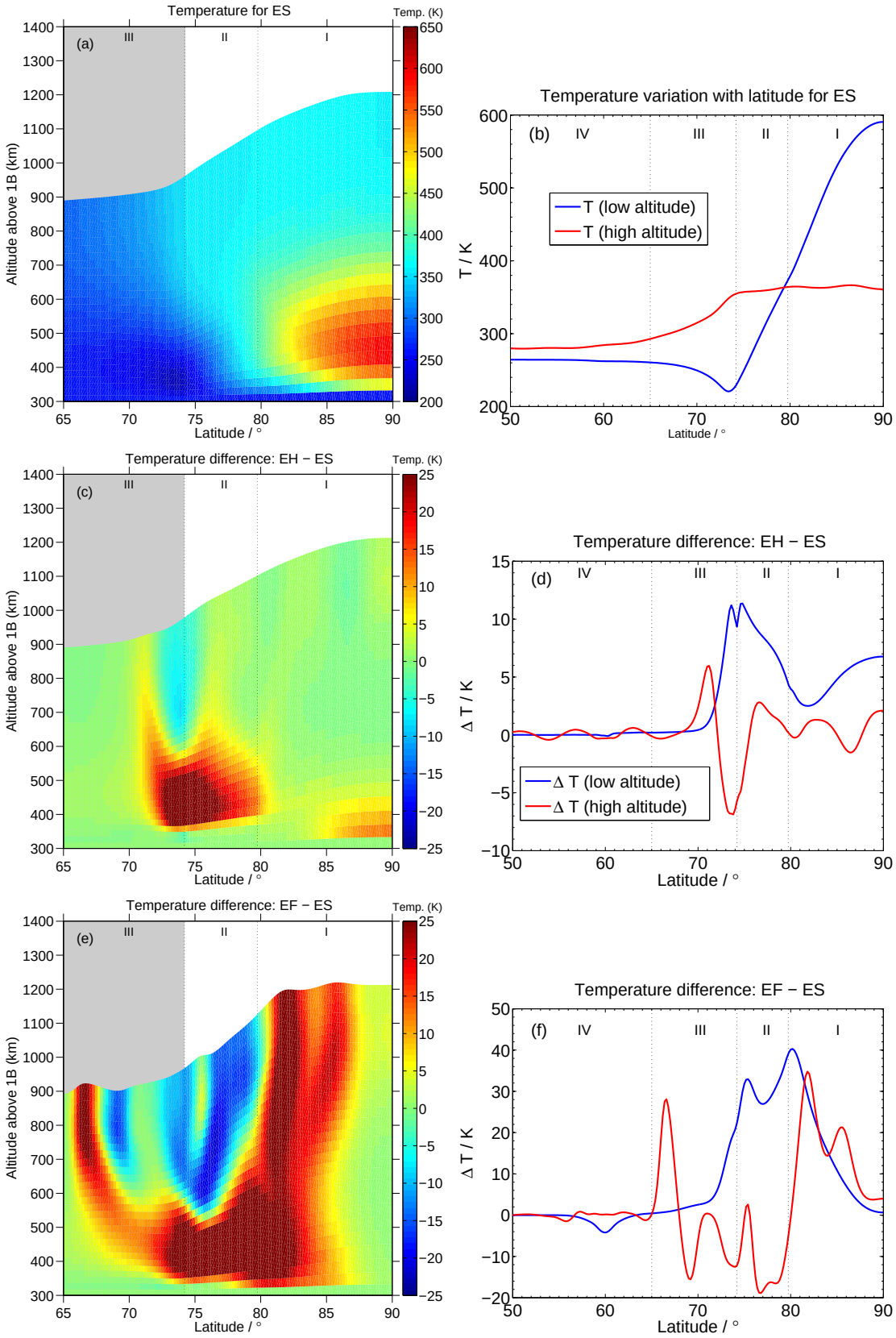

Figure 5.10. (a) shows the thermospheric temperature distribution for case ES whilst (c) and (e) show the temperature difference of cases EH and EF with case ES. The magnetospheric regions (region III is shaded) are separated by dotted black lines and labelled. (b) shows the latitudinal temperature profile for case ES and (d) and (f) show latitudinal temperature difference profiles at low (blue line) and high (red line) altitudes for EH and EF with ES. All other labels and are as for (a).

completeness Figs. B.4 - B.6, in Appendix B, shows all momentum terms (including those in Fig. 5.11) in the thermosphere.

For case ES, the zonal and meridional flows are very similar to those discussed in Yates et al. (2012) as the only difference between both steady-state compressed cases is that here we assume a constant height-integrated Pedersen conductivity whilst in Yates et al. (2012) the conductivity is enhanced by FACs. Zonally, there exists a small super-corotational jet at low altitudes in region III and a pair of large sub-corotational jets across regions II and I. The degree of sub-corotation is small compared with CS due to the highly compressed nature of the ES magnetosphere and the conservation of momentum. The meridional flows show a relatively large area of localised acceleration in regions II and I which, as explained above (section 5.2.2) and in Yates et al. (2012), is primarily due to the advection of momentum. Likewise, the direction of meridional flows is as discussed in section 5.2.2.

Thermospheric flows for case EH are slightly different from those of case ES. Zonally, there is a very small super-corotational jet ($\sim$25 % that of CS) and the degree of sub-corotation has increased over the entire thermosphere as shown in Fig. 5.9c. This is caused by the large decrease in magnetospheric corotation accompanying the expansion (Fig. 3.6b). Large negative ion drag (three times larger than case ES, see cyan contours in Fig. 5.11c) causes the thermosphere to lose a great amount of angular momentum (to magnetospheric plasma) which increases its degree of sub-corotation. In the meridional direction, Fig. 5.9d, the low altitude accelerated poleward flow in regions II and I have increased in size and velocity ($\sim$30 %) and there now exists another accelerated region of equatorward flow from mid to high altitudes centred at $\sim$73 °. Inspection of Fig. 5.11d (advection of momentum) shows areas of negative meridional advection (orange contours) at low altitudes of regions II and I which produce the poleward acceleration region. Positive meridional advection (blue contours) located in the middle of region III and at altitudes above $\sim$450 km, create the equatorward accelerated flow in this region. The direction of meridional flow indicated by the black arrows has also changed, mainly in region II, where flow at all altitudes is now directed poleward. Finally, in Fig. 5.10c-d, there is a significant increase in temperature ($\sim$50 K) in region III and I, near the Pedersen conductivity layer, resulting from these dynamical changes.

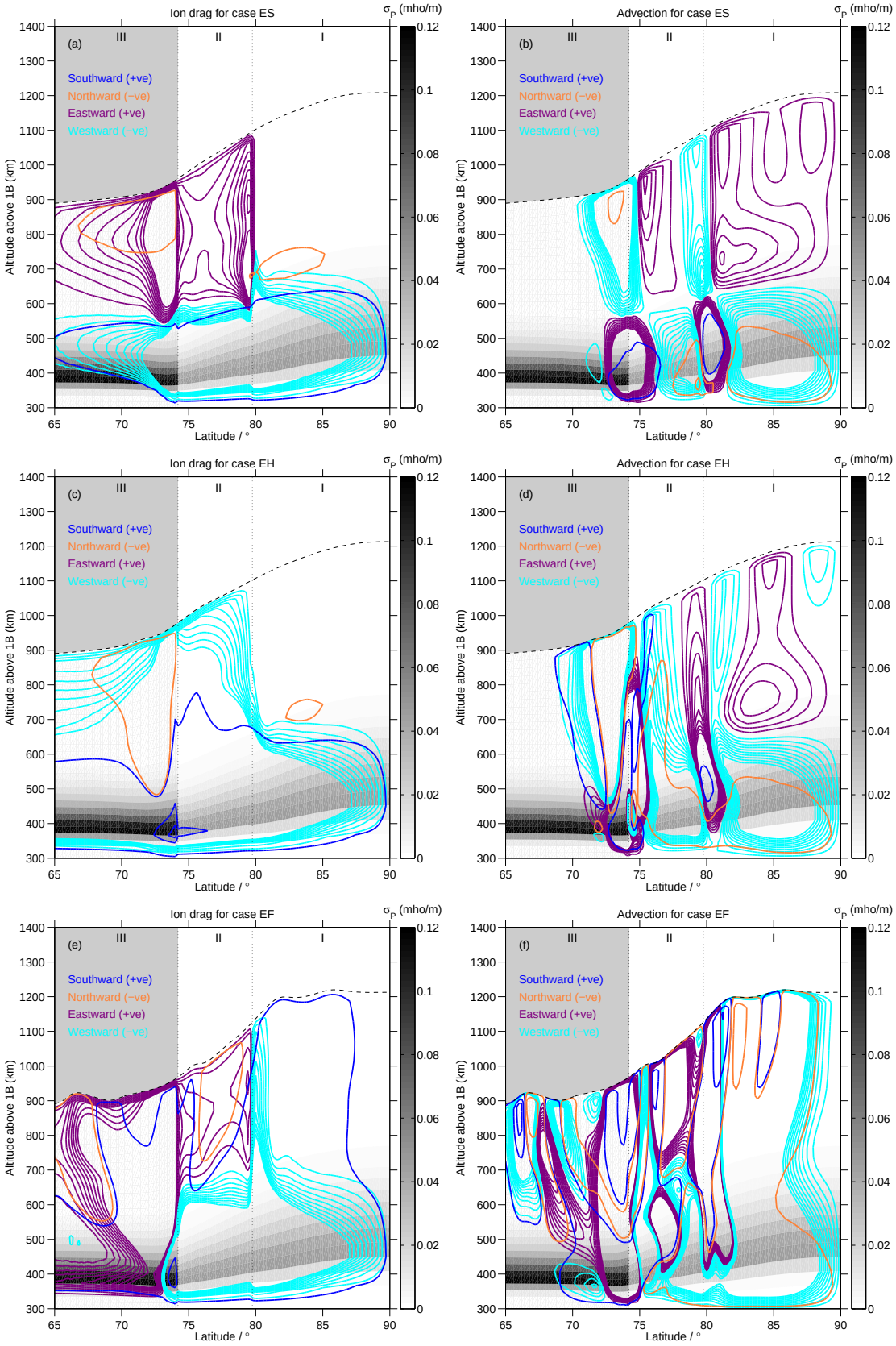

Figure 5.11. (a), (c) and (e) shows the variation of zonal and meridional ion drag momentum with altitude, latitude and Pedersen conductivity (colour bar) for cases ES-EF respectively. The meridional contours (blue and orange) range from $1 - 500\,\mathrm{mm\,s^{-2}}$ with an interval of $50\,\mathrm{mm\,s^{-2}}$ and with blue being positive (southward) and orange being negative (northward). The zonal contours (purple and cyan) range from $1 - 10\,\mathrm{mm\,s^{-2}}$ with an interval of $1\,\mathrm{mm\,s^{-2}}$ and with purple being positive (eastwards) and cyan being negative (westwards). The magnetospheric regions are separated and labelled. (b), (d) and (f) same as for (a), (c) and (e) but for advection of momentum.

The thermospheric quantities at the end of the transient expansion event are shown in the third row of Fig. 5.9 - 5.11. Considering Figs. 5.9e-f we see that the only change in zonal flow patterns is a slight increase in the zonal velocity. The meridional flows show a large poleward accelerated flow originating at low altitudes in region III and reaching the high altitudes of region I. Two smaller regions of accelerated equatorward flow arise in the upper altitudes of regions III and II. The temperature difference between cases EF and ES, Fig. 5.10e-f, show increases in temperature up to ∼50 K co-located with accelerated meridional flow along with decreases in temperature (∼20 K) between these accelerated regions. As the magnetosphere returns to its initial compressed configuration, it weakly super-corotates over most of region III; this transfers angular momentum to the sub-corotating thermosphere which can essentially 'spin up' the latter. This effect can be seen in the zonal momentum terms, particularly ion drag and advection in Fig. 5.11e-f showing that momentum in regions III and II is mainly eastwards (positive) and thus promoting corotation. Fig. 5.11f clearly shows that the large poleward accelerated region and temperature deviations result from the advection of meridional momentum (orange (negative) contour).

Compared to the transient compression case CF, the EF thermosphere seems fairly stable i.e. there are no sharp peaks and troughs in the upper boundary. Our interpretation is that for the compression scenario the magnetosphere transfers a large amount of angular momentum to the thermosphere due to its large degree of super-corotation. This surge in momentum and energy input to the thermosphere over a short time scale causes significant strain on the thermosphere and thus requires a drastic reconfiguration in order to attempt to re-establish equilibrium. On the other hand, in our expansion scenario the magnetosphere significantly sub-corotates for most of the event and only super-corotates compared to the planet and thermosphere slightly nearing the end of the event. So for the majority of the transient event the thermosphere is losing angular momentum to the magnetosphere. Thus, its dynamics and energy input are generally smaller than the transient compression scenario. This leads to a less 'drastic' reaction. The influence of these transient events on heating in Jupiter's thermosphere will be discussed in Chapter 6.

5.4 Discussion and conclusions

We now discuss the steady-state, 'half-pulse' and 'full-pulse' results found in this study. As discussed in section 3.5.1, if we assume that the transient event occurs on small time scales ($\sim$2$-$3 hours), plasma angular momentum is conserved. Therefore, the initial and final magnetospheric states will be identical (see Fig. 3.6).

5.4.1 Magnetospheric response

In the compression scenario we observe super-corotation of the middle magnetosphere with angular velocities up to $\sim$1.6 Ω_J. This changes the M-I current systems in the thermosphere and magnetosphere. Thermospheric angular velocities are positively correlated to what happens in the magnetosphere, so with magnetospheric super-corotation the thermosphere responds by increasing its angular velocity. The response is, however, not as strong as that of the magnetosphere due to the immense inertia of the thermosphere. Thus, its response lags behind the magnetospheric response in region III; regions II and I show a small response. With regards to the coupling currents, the initial and final states show little variability, depending mainly on contributions from the lagging thermosphere. Midway through the pulse, there is a current reversal (see Figs. 5.1 - 5.2) as modelled previously by Cowley and Bunce (2003b); Cowley et al. (2007). This reversal is caused by the super-corotation of the magnetosphere and indicates that angular momentum is now being transferred from magnetosphere to thermosphere, contrary to steady state momentum transfer. This deposits energy and 'spins up' the thermosphere and planet (Cowley et al. 2007).

Considering the transient expansion scenario, we find that the degree of corotation of plasma angular velocity significantly decreases midway through the expansion event (maximum expansion). This causes a reduction in thermospheric angular velocity. These combined changes result in a large flow shear between the thermosphere and magnetosphere which correspondingly increases the magnitude of M-I coupling currents (see Figs. 5.7-5.8). At the end of the event, the magnetosphere super-corotates compared to the thermosphere, indicating the lag in thermospheric response time resulting from its large inertia. This creates a small amount of current reversal which acts to 'spin up' the thermosphere and replenish some of the energy lost in accelerating the previously severely sub-corotating

magnetosphere.

5.4.2 Thermospheric response

The arrival of solar wind shocks or rarefactions, has for the most part, a similar effect on thermospheric flows. Our modelling shows a general increase (resp. decrease) in the degree of corotation with solar wind dynamic pressure increases (resp. decreases). Zonal flow patterns remain essentially unchanged with a large sub-corotational jet and a small super-corotational jet. Meridional flow cells however, respond to transient magnetospheric reconfigurations somewhat chaotically, with numerous poleward and equatorward accelerated flow regions developing (at altitudes $> 600\,\mathrm{km}$) with time spent in event. The overall low-altitude poleward flow remains fixed with solar wind rarefactions but reverses in response to a solar wind shock (see cases CH and CF in Figs. 5.4d and f). This flow becomes equatorwards due to a reversal in the acting direction of ion drag momentum in region III, as shown in Fig. 5.6c and e, resulting from the super-corotation of magnetospheric plasma.

Compared to the transient compression case CF, the EF thermosphere seems fairly stable i.e. there are no sharp peaks and troughs in the upper boundary. Our interpretation is that for the compression scenario the magnetosphere transfers a large amount of angular momentum to the thermosphere due to its large degree of super-corotation. This surge in momentum and energy input to the thermosphere over a short time scale causes significant strain on the thermosphere and thus requires a drastic reconfiguration in order to attempt to re-establish equilibrium. On the other hand, in our expansion scenario the magnetosphere significantly sub-corotates for most of the event and only super-corotates compared to the planet and thermosphere slightly nearing the end of the event. So for the majority of the expansion event the thermosphere is losing angular momentum to the magnetosphere. Thus, its dynamics and energy input are generally smaller than the transient compression scenario. This leads to a less 'drastic' reaction.

5.4.3 Concluding remarks

This work demonstrates the response of Jupiter's thermosphere and M-I coupling currents to rapid compressions and expansions of Jupiter's magnetosphere caused by variation in solar wind dynamic pressure. Many of the results regarding angular velocities and coupling currents, i.e. plasma super-corotation and current reversal, are in qualitative agreement

with those obtained in previous studies (e.g. Cowley and Bunce (2003b); Cowley et al. (2007)). The novel aspect of the work presented in this chapter is the inclusion of a thermosphere GCM in order to model the thermospheric response to such magnetospheric reconfigurations. We have showed that solar wind expansions lead to a less drastic thermospheric response compared to a solar wind compression. Both expansions and compressions lead to local thermospheric temperature variations ranging from approximately -40 to $+175\,\mathrm{K}$ but compressions also cause a significant increase in equatorwards meridional winds, which one would expect to transport the high temperature neutrals to equatorial latitudes as suggested by Waite et al. (1983); Melin et al. (2006). This Chapter has primarily been concerned with the dynamics of the thermosphere and coupling currents. We have made no mention of specific heating rates, energy balance or the auroral response to these magnetospheric reconfigurations but will be discussed at length in Chapter 6.

Chapter 6

Response of atmospheric heating to transient solar wind pulses.

Can you imagine the utility bill to heat something of this size? It's equivalent to 9,000 homes.

Bob Gough

6.1 Introduction

Cowley et al. (2007) displaced the Jovian magnetopause by $\sim$40 R_J over a period of three hours and predict differing auroral responses dependent on the nature of the reconfiguration event - compression or expansion. For compressions, electron energy flux ($\sim$10 % of which is used to produce ultraviolet (UV) aurora) at the open-closed field line boundary (polar emission) increases by two orders of magnitude, whilst the main emission is halved. In the expansion case, there is a 30-fold increase in main emission mapping to the middle magnetosphere, whilst polar emission decreases to $\sim$2 % of its steady-state value. Recent observations of auroral emission by Clarke et al. (2009) show a factor of two increase in total ultraviolet (UV) auroral power, near the arrival of a solar wind compression region, typically corresponding to an increase in solar wind dynamic pressure of $\sim 0.01-0.3$ nPa. Furthermore, Nichols et al. (2009) showed, using the same Hubble Space

Telescope (HST) images as Clarke et al. (2009), that this increase in auroral emission consists of approximately even contributions from the so-called 'main oval' and the high-latitude polar emission. This increase can clearly be seen in the shaded regions of Fig. 6.1a and b, showing the emitted UV power in the high latitude and main oval regions as a function of day-of-year. The corresponding HST auroral images showing the increase in UV emission are presented in Fig. 6.2 where the subplot labels are also shown on the top of Fig. 6.1. Nichols et al. (2009) also showed that the location of the 'main oval' shifted polewards by $\sim 1^\circ$ in response to solar wind pressure increase of an order of magnitude. For a rarefaction region in the solar wind corresponding to an order of magnitude decrease in solar wind pressure, Clarke et al. (2009) observed little, if any, change in auroral emission.

Melin et al. (2006) analysed infrared data from an auroral heating event observed by Stallard et al. (2001, 2002) (from September 8-11, 1998) and found that particle precipitation could not account for the observed increase in ionospheric temperature ($940-1065\,\mathrm{K}$). The combined estimate of ion drag and Joule heating rates increased from $67\,\mathrm{mW\,m^{-2}}$ (on September 8) to $277\,\mathrm{mW\,m^{-2}}$ (on September 11) resulting from a doubling of the ionospheric electric field (inferred from spectroscopic observations); this increase in heating was able to account for the observed rise in temperature. Cooling rates (by Hydrocarbons and H_3^+ emission) was also found to increase during the event but only by $\sim 20\,\%$ of the total inferred heating rate. Thus, a net increase in ionospheric temperature resulted. More detailed analysis showed that these cooling mechanisms would be unlikely to return the thermosphere to its initial temperature before the onset of subsequent heating events. Melin et al. (2006) thus concluded that the temperature increases could plausibly lead to an increase in equatorward winds, which transport thermal energy to lower latitudes (Waite et al. 1983).

Here, we use the same model as in Chapter 5 to simulate how the Jovian aurora and thermospheric heating responds to transient variation in magnetospheric size (via solar wind dynamic pressure). We employ the same methodology as described in Chapter 5 and section 3.5.1 but here, the response of thermospheric heating and aurora is investigated. Scientific background and model details have been already described in Chapters 2 and 3. In sections 6.3 and 6.4 we present and discuss our findings for the transient compression and expansion scenarios respectively. We conclude in section 7.3.

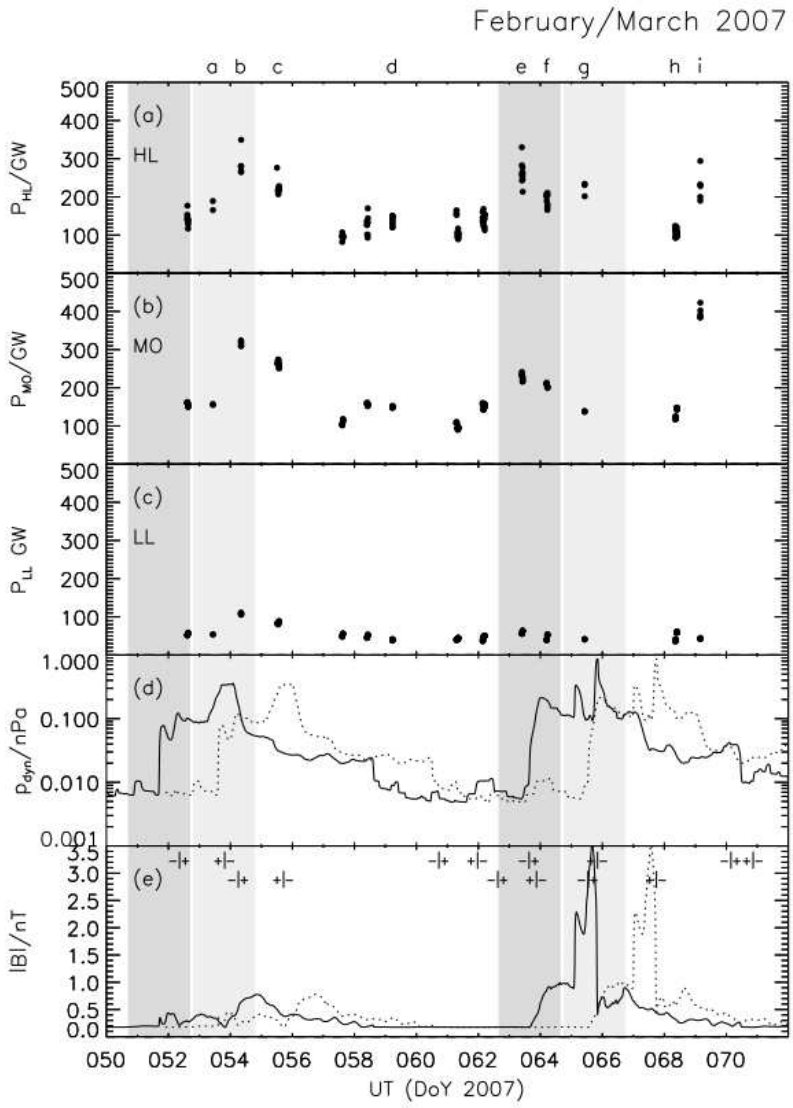

Figure 6.1. (a) - (c) respectively show the emitted UV power for the high latitude, main oval and low latitude regions of Jupiter's upper atmosphere. (d) - (e) shows corresponding solar wind dynamic pressures and Interplanetary Magnetic Field (IMF). All plots are functions of day of year in 2007. The solid lines in (d) - (e) are obtained from an MHD model (Clarke et al. 2009; Nichols et al. 2009) and its corresponding timings whilst the dashed lines are as the solid lines but with timings shifted by +2.1 days to match observations by the New Horizons spacecraft. Regions where shocks are predicted are shaded in dark grey for the original timings and in light grey for the new shifted timings. Note this plot is Fig. 3 in Nichols et al. (2009).

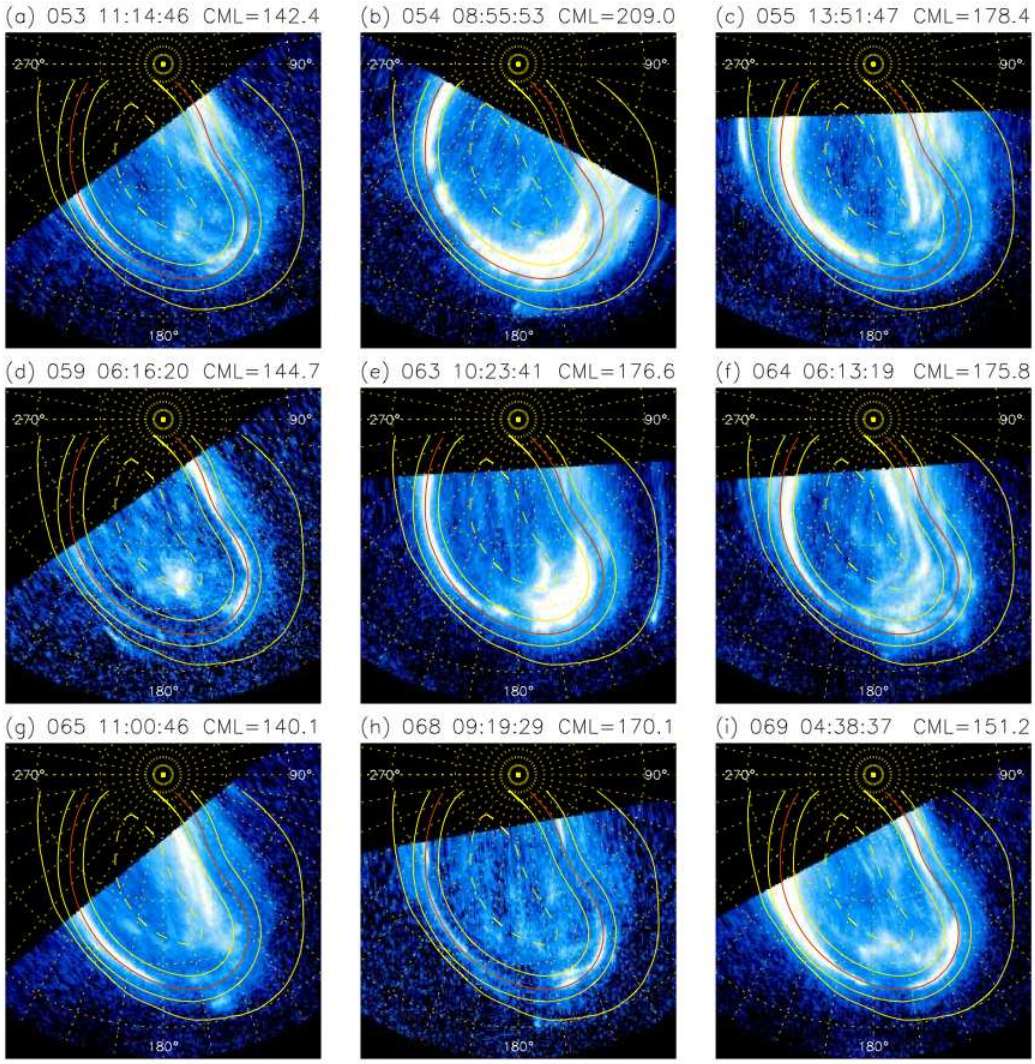

Figure 6.2. A collection HST images of Jupiter's aurora from above the north pole. The subplot labels correspond to the labels at the top of Fig. 6.1. The red lines indicates the location of the reference main oval whilst the solid yellow lines indicate the region boundaries. LL - low latitude, MO - main oval, HL - high latitude which is subdivided in inner (PI) and outer (PO) polar regions. The colour scale saturates at 500 kR. Note this plot is Fig. 4 in Nichols et al. (2009).

Table 6.1. Magnetospheric electron source parameters. This table is adapted from Table 1, Cowley et al. (2007). N represents the electron density, W_{th} the electron thermal energy, $j_{||i0}$ the unaccelerated current density and E_{f0} the unaccelerated energy flux.

Parameter	Open field lines	Outer magnetosphere	Middle magnetosphere
N / cm^{-3}	0.5	0.02	0.01
W_{th} / keV	0.05	0.25	2.5
$j_{\|\|i0}$ / μA m^{-2}	0.095	0.0085	0.013
E_{f0} / mW m^{-2}	0.0095	0.0042	0.067

6.2 Auroral energies

Once FAC densities have been calculated using Eq. (2.65), we can use the methods of Knight (1973) and Lundin and Sandahl (1978), as presented in Cowley et al. (2007) and in section 2.3.5, to calculate the enhanced precipitating electron energy flux E_f:

$$E_f = \frac{E_{f0}}{2}\left(\left(\frac{j_{||i}}{j_{||i0}}\right)^2 + 1\right), \tag{6.1}$$

where E_{f0} is the unaccelerated electron energy flux, $j_{||i0}$ is the unaccelerated FAC density (or the maximum current that can be carried by the electrons in the absence of field-aligned potential drops) and $j_{||i}$ is the upward (positive) FAC density. To enable a comparison with similar, earlier studies, we use the same electron population values described in Cowley et al. (2007), which are based on observations by Scudder et al. (1981) and Phillips et al. (1993a,b). These parameters are presented in Table 6.1. E_f can subsequently be used to calculate the brightness of the UV aurora assuming that 1 mW m^{-2} of precipitating energy flux creates ∼10 kR of UV output. Note that Eq. (6.1) and Table 6.1 are the same as Eq. (2.79) and Table 2.1 in section 2.3.5.

6.3 Magnetospheric Compressions

In this section we present auroral and thermospheric heating results for a transient magnetospheric compression event. We present results from three phases throughout the transient event: i) Steady state (case CS with R_{MM}=85 R$_J$), ii) 'half-pulse' (case CH with R_{MM}=45 R$_J$) and, iii) 'full-pulse' (case CF with R_{MM}=85 R$_J$).

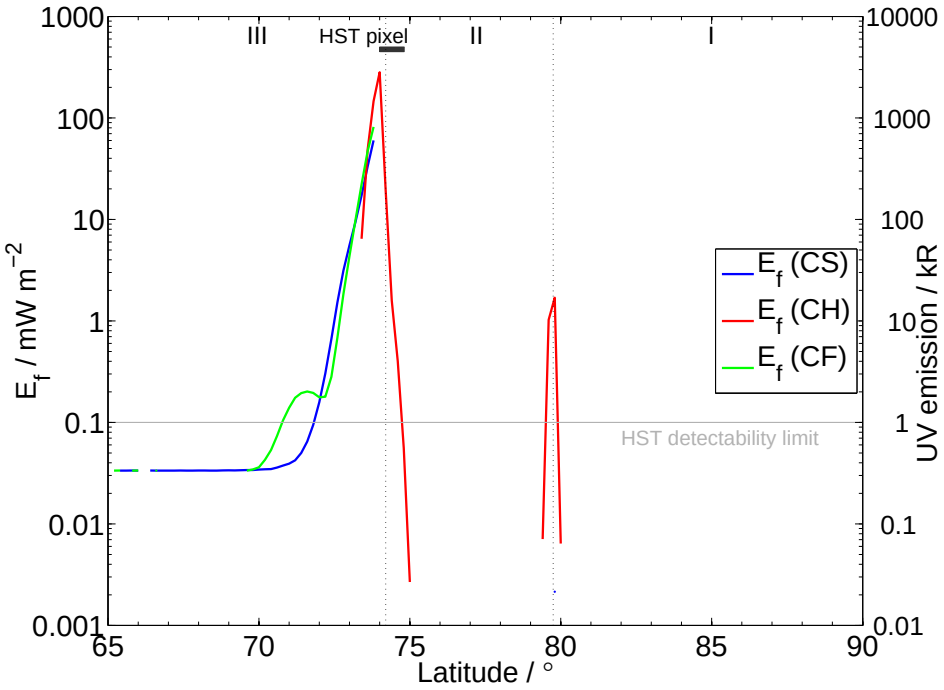

Figure 6.3. Shows the latitudinal variation of the precipitating electron flux(left axis) and corresponding UV emission (right axis) for the transient compression cases. The blue line represents case CS whilst the red and green lines indicate cases CH and CF respectively. The conjugate magnetospheric regions are separated by dotted black lines and labelled. The latitudinal size of an ACS-SBC HST pixel located near the main auroral emission is represented by the dark grey box (see Appendix A). The solid grey line indicates the limit of detectability of the HST (Cowley et al. 2007).

6.3.1 Auroral response

Here we discus how a transient magnetospheric compression affects the aurorae by looking at the energy flux carried by precipitating electrons. For the detailed response of global M-I coupling currents the reader is referred to Chapter 5.

We begin our discussion by briefly summarising the response of FAC densities (see Chapter 5 and Fig. 5.2). Between cases CS and CF there are only minor differences in FAC profiles emanating from the lag in response of the thermosphere to the transient pulse (due to its large inertia; see section 3.5.1). Comparing case CS with CH, CH has: i) substantial current reversal in region III, ii) maximum upward FAC about twice that of case CS, iii) increased FAC at the region II/I boundary (although this result is sensitive to our assumed choice of uniform angular velocity in region II). The current reversal over

$\sim 4^\circ$ of region III is a direct result of the super-corotation of Ω_M (see Fig. 3.6a) whilst the increases in upward FAC result from increases in the Pedersen current (see Chapter 5) caused by an increase in flow shear ($\Omega_T - \Omega_M$).

Precipitating electron energy fluxes as a function of latitude are shown in Fig. 6.3. The blue line represents case CS, the red line corresponds to case CH and the green line represents case CF. Magnetospheric regions are separated by black dotted lines, the latitudinal size of a Hubble Space Telescope (HST) ACS-SBC pixel (0.03x0.03 arc sec) is indicated by the dark grey rectangle (assuming that the magnetic axis of the Jovian dipole is perpendicular to the observer's line of sight. see Appendix A.) and the grey solid line indicates the limit of present detectability with HST instrumentation ($\sim$1 kR; Cowley et al. (2007)). These fluxes are obtained using Eq. (6.1) and Table 6.1, which uses only the upward (positive) FAC densities presented in Fig. 5.2. We initially compare electron energy fluxes for cases CS and CF. These profiles are identical poleward of $\sim 74^\circ$; equatorward of this location, case CF shows little deviation from CS, despite the thermospheric lag discussed in section 3.5.1. In region III, we find that the peak energy flux for case CF is $\sim$35 % larger than that in case CS and the location of these peaks coincides with the location of the main auroral oval ($\sim 74^\circ$). The slight increase in peak energy flux is due to a relative increase in flow shear as seen in Fig. 3.6a. Case CF would therefore produce main oval emission of approximately $\sim$200 kR brighter than that of CS (assuming that 1 mW m^{-2} of precipitation creates $\sim$10 kR of UV output (Cowley et al. 2007)). The main oval would also be $\sim 1.5^\circ$ broader for CF than for case CS.

The E_f profile for case CH is different from those of both cases CS and CF. There are three main changes in CH compared to CS: i) peak energy flux in region III is $\sim$280 mW m^{-2}, almost a factor of five larger, ii) location of peak energy flux has shifted polewards by $\sim 0.2^\circ$ and, iii) presence of a second peak with an energy flux of 1.7 mW m^{-2} at the region II/I boundary. The large increase in energy flux is caused by a substantial increase in flow shear between the thermosphere and magnetosphere, resulting from the super-corotation of the middle magnetosphere (see Fig. 3.6). The presence of a second peak at the region II/I boundary is also due to flow shear increase across the boundary, as the magnetosphere in region II corotates at a larger fraction of Ω_J compared to case CS. The result for this higher-latitude boundary should be regarded as preliminary, since it is

sensitive to the values of Ω_M we assume in the outer magnetospheric region and polar cap. Flow velocities in these regions are poorly constrained by observations (Stallard et al. 2003). In section 7.5 we discuss how values of Ω_M in these outer regions may change depending on the solar wind dynamic pressure using the formulations presented in Isbell et al. (1984).

Comparing the energy flux profile of case CH with the equivalent case in Cowley et al. (2007) (with a responsive thermosphere; they do not calculate energy fluxes for a non-responsive thermosphere), we see that in the closed field regions (III and II), peak energy fluxes are two orders of magnitude larger in case CH. This demonstrates the differences between using a GCM to represent the thermosphere or using a simple 'slippage' relation between thermospheric and magnetospheric angular velocities. At the open-closed field line boundary (II/I boundary) our peak flux is an order of magnitude smaller than that in Cowley et al. (2007); this difference arises from the different models used to represent the outer magnetosphere. The outer magnetosphere (region II) and open field line region (region I) in this study is modelled using Cowley et al. (2005).

The increase in E_f for case CH would lead to corresponding increases in auroral emission. As such, we would expect 'main oval' emission for case CH to shift polewards by $\sim$0.2 $^\circ$ and be $\sim$4.7 $\times$ larger than emission in case CS i.e. $\sim$2800 kR compared to $\sim$600 kR. By looking at the size of an HST pixel in the auroral region, as indicated by the grey box in Fig. 6.3, it seems unlikely that our predicted poleward shift of $\sim$0.2 $^\circ$ would be detectable above the usual signal contamination (e.g instrument noise, background signals etc) and small scale variation of the auroral oval (see Fig. 6.2 for example). Clarke et al. (2009) and Nichols et al. (2009) observed that the brightness of UV auroral emission increased by a factor of approximately two, in response to transient (almost instantaneous) increases in solar wind dynamic pressure ($\sim$0.01$-$0.3 nPa or equivalently $\sim$112$-$63 R_J) as shown on day-of-year 54 and 64 in Fig. 6.1a, b and d. Nichols et al. (2009) also observed poleward shifts in main oval emission on the order of $\sim$1 $^\circ$ corresponding to the arrival of solar wind shocks. Total emitted UV power may be used to quantity auroral activity, assuming that this quantity is $\sim$10 % of the integrated electron energy flux per hemisphere (Cowley et al. 2007). Case CH thus has a total UV power of $\sim$1.58 TW (compared to $\sim$420 GW for case CS), which is a factor of $1.5 - 3$ times larger than UV powers observed by both Clarke et al. (2009) and Nichols et al. (2009) shown in the top panel of Fig. 6.4. The electron

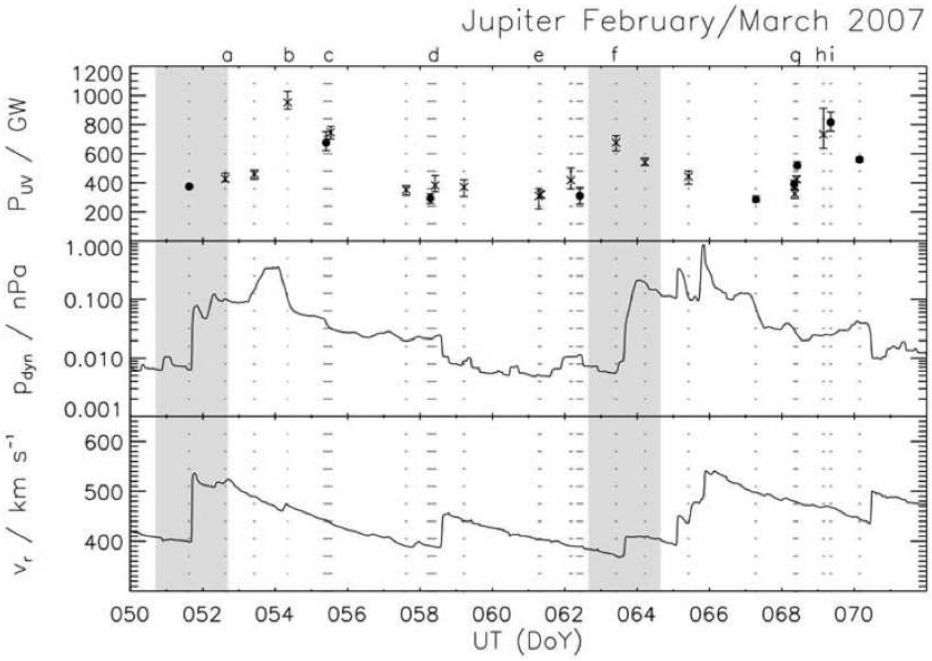

Figure 6.4. The top panel shows the total emitted UV power Jupiter's north (crosses) and south (filled circles) aurora. The middle and lower panels respectively show solar wind dynamic pressure and velocity propagated using MHD models. All plots are functions of day of year in 2007. As in Fig. 6.1 the arrival time of solar wind shocks were shifted by +2.1 days to match observations by the New Horizons spacecraft. Note this plot is Fig. 6 in Clarke et al. (2009).

energy flux profile of case CH also suggests the presence of polar emission at region II/I (open-closed) boundary. The brightness of such emission being 11 kR and thus strong enough to be observed by HST. This suggested emission is, however, sensitive to model assumptions in regions II and I but will be discussed in section 7.5.

6.3.2 Thermospheric heating

In this section, we present and discuss the response of thermospheric heating terms to our transient magnetospheric compression event. We presented azimuthal and meridional flows and temperature differences (from steady state) in Fig. 5.4 which have been discussed at length in Chapter 5. To aid in the description of thermospheric heating, we place (in this Chapter) a copy of Fig. 5.4 and refer to it as Fig. 6.5. We also summarise the major flow patterns associated with zonal (Figs. 6.5a, c and e) and meridional (Figs. 6.5b, d and f) flows. Thermospheric temperature distributions are presented in Figs. 6.6a, c and e and high and low altitude latitudinal temperature profiles are shown in Figs. 6.6b, d and f. Fig. 6.7 shows corresponding heating (left column) and cooling (right column)

rates for the transient compression cases. The colour bar indicates the thermospheric temperature whilst the contours enclose regions that are heated (resp. cooled) at rates exceeding $20\,\mathrm{W\,kg^{-1}}$. Fig. 6.8 shows powers per unit area (calculated using Eqs. (2.69 - eq:bg:iondrag)) for cases CS-CF. We use thermospheric heating and cooling terms and powers per unit area to aid in the following discussions. Cases CS, CH and CF are represented in rows 1−3 of Figs. 6.5 and 6.8 respectively.

Figs. 6.5a, c and e show thermospheric azimuthal velocity, in the corotating reference frame, as a function of altitude and latitude for cases CS, CH and CF. Positive velocities indicate super-corotation whilst negative velocities indicate sub-corotation. The white contour indicates the locus of rigid corotation, black contour indicates regions of strong super-corotation ($> 25\,\mathrm{m\,s^{-1}}$), the white dashed contour shows regions that are strongly ($> -2500\,\mathrm{m\,s^{-1}}$) sub-corotating and the black arrows indicate the direction of meridional flow. Magnetospheric regions are labelled and separated by black dotted lines. The zonal flow patterns include: i) a low-altitude ($\sim 400 - 500\,\mathrm{km}$) super-corotating jet (black contour), centred at $\sim 72\,^{\circ}$; and ii) a large sub-corotating jet, spanning region III - I (blue region in Figs. 6.5a, c and e). These general features are persistent throughout the transient compression event. Differences do arise in the speed of flows: where we see an increase in the degree of corotation (and super-corotation) in case CH (indicated by the area covered by the white-dashed contour having decreased and that covered by the black contour having increased). This is followed by a subsequent decrease in super-corotation in case CF. We do however note that in regions II, there is a slight increase in corotation in case CF. Figs. 6.5b, d and f show thermospheric meridional velocity as a function of altitude and latitude for cases CS-CF. The arrows indicate the direction of the steady-state meridional flow pattern (Fig. 6.5d), where we have low altitude ($<600\,\mathrm{km}$) poleward flows and high altitude ($>600\,\mathrm{km}$) equatorward flows, as predicted by Smith et al. (2007); Smith and Aylward (2009) and Yates et al. (2012). We also note the presence of localised accelerated regions (red/brown hues) which result from the advection of momentum (Yates et al. 2012). The response of the meridional flows can be seen in Figs. 6.5b, d and f where flow patterns evolve with time to become quite complex. The number of local regions with strongly accelerated flows increases significantly with time. The reader is referred to Chapter 5 for more detailed discussions on these flows and their causes.

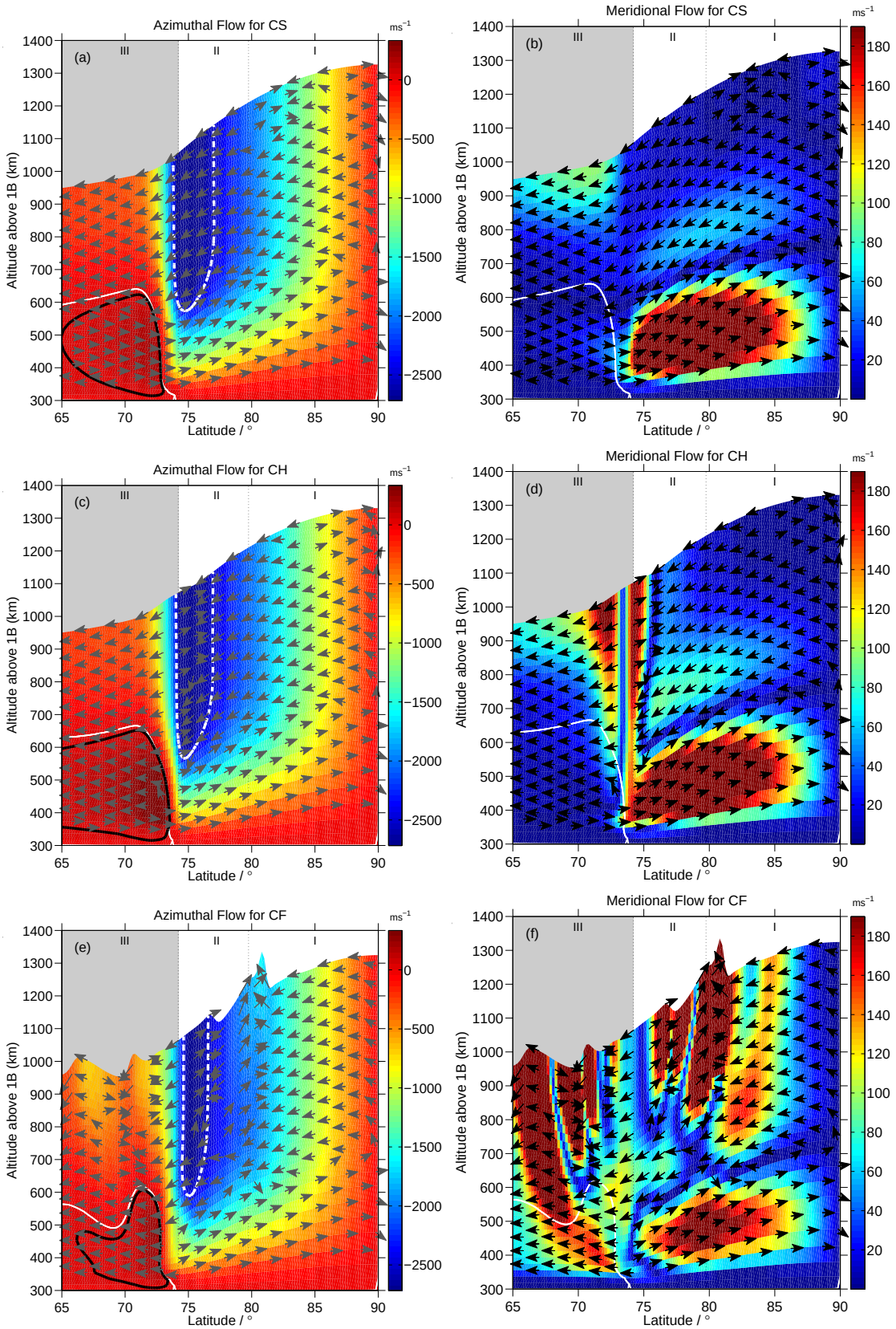

Figure 6.5. (a), (c) and (e) show the variation of thermospheric azimuthal velocity (colour scale) in the corotating reference frame for cases CS-CF respectively (left to right). Positive values (dark red) indicate super-corotation, whilst negative values (light red to blue) indicate sub-corotation. The arrows show the direction of meridional flow and the solid white line indicates the locus of rigid corotation. The solid black encloses regions of super-corotation ($> 25\,\mathrm{m\,s^{-1}}$) and the dashed white line encloses regions that are sub-corotating at a rate $> -2500\,\mathrm{m\,s^{-1}}$. The magnetospheric regions (region III is shaded) are separated by dotted black lines and labelled. (b), (d) and (f) show the meridional velocity in the thermosphere for cases CS-CF. The colour scale indicates the speed of flows. All other labels and are as for (a).

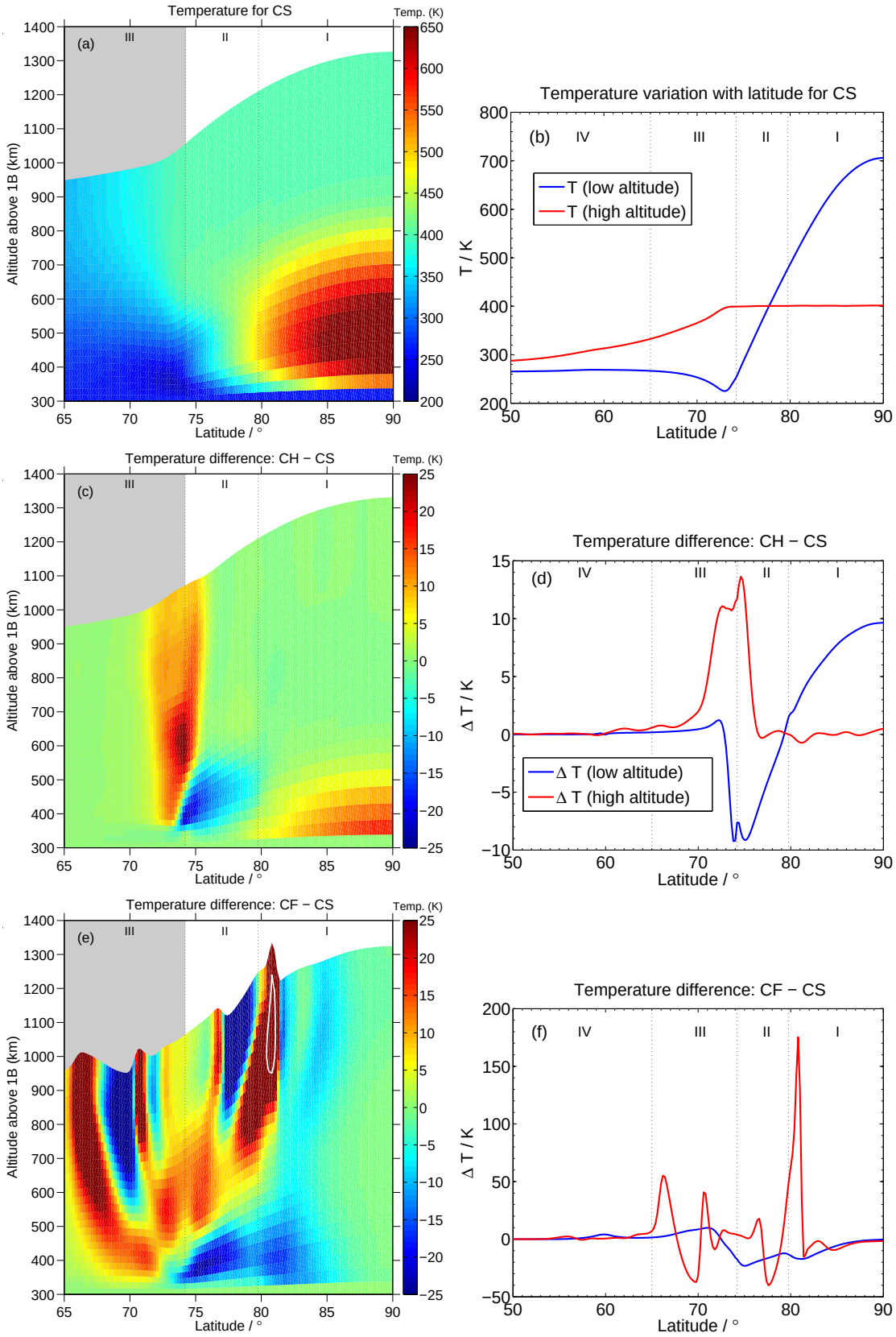

Figure 6.6. (a) shows the thermospheric temperature distribution for case CS whilst (c) and (e) show the temperature difference of cases CH and CF with case CS. The white contour encloses temperature differences $> 100\,\mathrm{K}$. The magnetospheric regions (region III is shaded) are separated by dotted black lines and labelled. (b) shows the latitudinal temperature profile for case CS and (d) and (f) show latitudinal temperature difference profiles at low (blue line) and high (red line) altitudes for CH and CS, and CF and CS. All other labels and are as for (a).

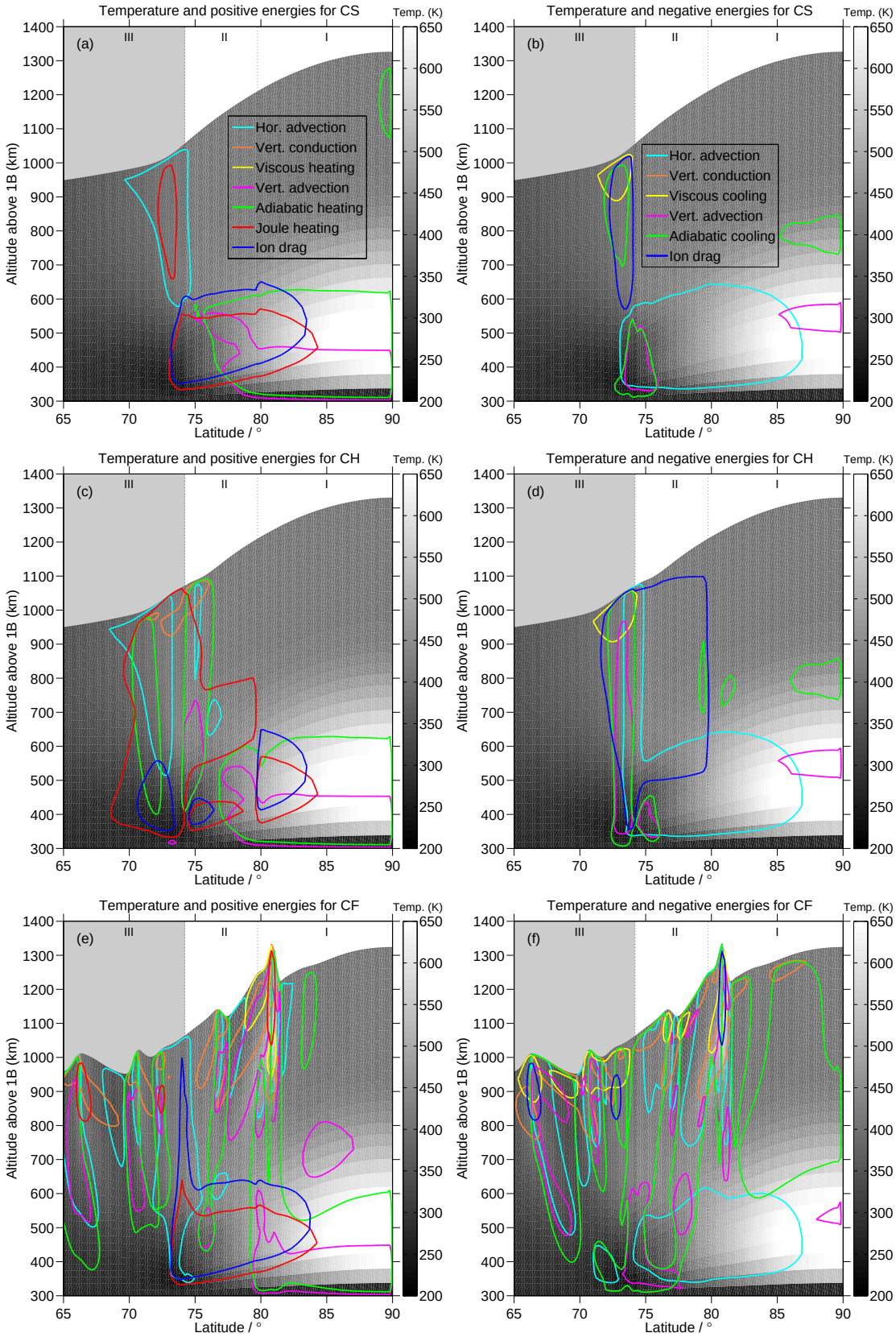

Figure 6.7. (a), (c) and (e) shows the variation of atmospheric heating terms with altitude, latitude and temperature (colour bar) for cases CS, CH and CF (top to bottom in first column). The contours enclose regions where heating/kinetic energy rates exceed $20\,\mathrm{W\,kg^{-1}}$. Ion drag, Joule heating, vertical and horizontal advection of energy, adiabatic heating/cooling, viscous heating and heat conduction (vertical and turbulent) are represented by blue, red, yellow and magenta, green, cyan and orange lines. The magnetospheric regions are separated and labelled. (b), (d) and (f) show the variation of atmospheric cooling terms where the contours enclose regions where heating/kinetic energy are decreasing (cooling) with rates exceeding $20\,\mathrm{W\,kg^{-1}}$. All colours and labels

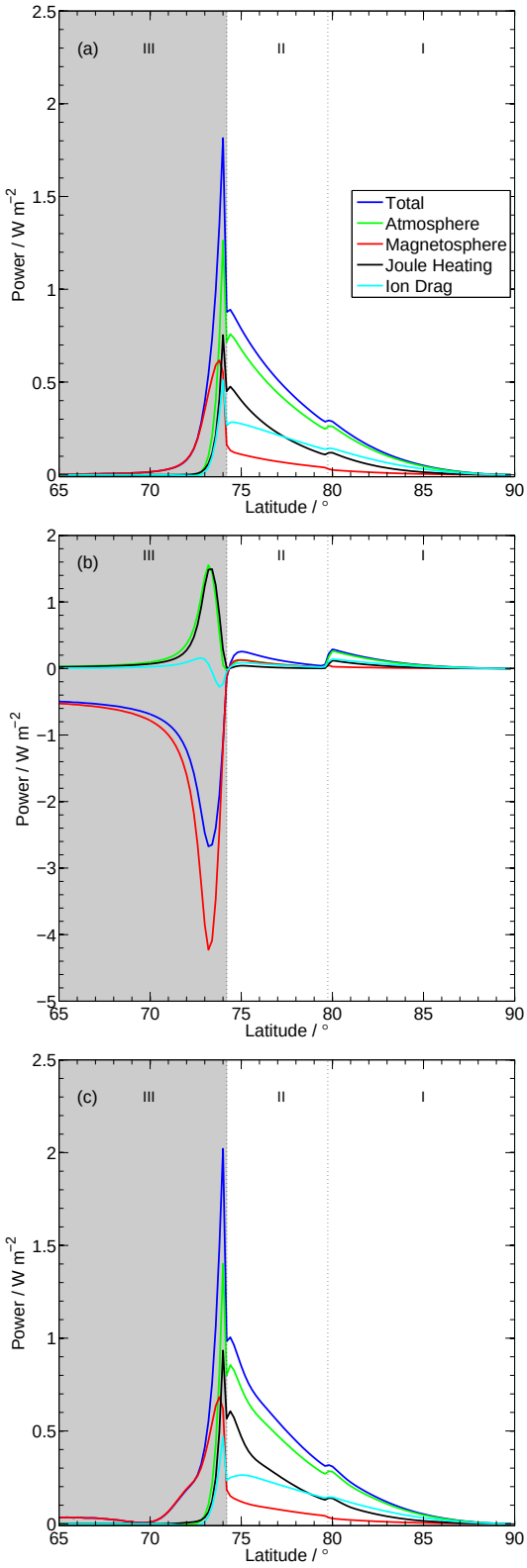

Figure 6.8. (a)-(c) show how the power per unit area varies for our transient compression cases. The blue line represents total power which is the sum of magnetospheric power (red line) and atmospheric power (green line); atmospheric power is the sum of both Joule heating (black solid line) and ion drag (cyan solid line). Magnetospheric regions and other labels are as for Fig. 6.7a.

Fig. 6.6a shows thermospheric temperature as a function of altitude and latitude for case CS. Figs. 6.6c and e show the difference in thermospheric temperature between cases CH and CS, and cases CF and CS. We will use Figs. 6.7a-f, showing contour plots for various thermospheric heating (Figs. 6.7a, c and e) and cooling (Figs. 6.7b, d and f) rates to interpret the temperature response.

In Fig. 6.6a we see a clear temperature difference between upper ($>75\,^{\circ}$) and lower ($<75\,^{\circ}$) latitudes; lower latitudes are cooled whilst upper latitudes are significantly heated (Smith et al. 2007; Smith and Aylward 2009). We see a 'hotspot' (in region I) with a peak temperature of $\sim$705 K. This arises from the poleward transport of Joule heating (from regions III and II) by the accelerated meridional flows shown in Fig. 6.5b (Smith and Aylward 2009; Yates et al. 2012).

Fig. 6.6c shows the temperature difference between cases CH and CS. There are three prominent features in Fig. 6.6c:

i) Temperature increase up to $\sim$26 K across the region III/II boundary ($z\geq$400 km) resulting from a large ($\times 2$) increase in Joule heating and the addition of other heat sources, such as adiabatic heating (see Fig. 6.7c). The large increase in Joule heating is caused by the increase in Pedersen currents and the rest-frame electric field (see Fig. 5.1b).

ii) Temperature decrease down to ~ -22 K, at low altitudes of region II. Fig. 6.7c shows that at low altitudes ($\leq$500 km) of region II there is, on average, a 20 % decrease in energy deposited by Joule heating and ion drag. This, coupled with the presence of energy lost by ion drag (Fig. 6.7d) in this region causes the significant decrease in temperature shown above. All the factors discussed above result from the reversal and decrease (in magnitude) of the flow shear between the magnetosphere and thermosphere in case CH.

iii) A maximum of $\sim$17 K increase at low altitudes in region I. The meridional velocity of case CH increases slightly ($\sim$2 %) in in this region and, as such, can transport heat from Joule heating and ion drag polewards more efficiently than in case CS.

Fig. 6.6e shows the temperature difference between cases CF and CS. Immediately, we can see that there are significant changes in the distribution of temperature in the upper thermosphere of case CF. There are four 'finger-like' regions with local temperature in-

creases up to a maximum of 175 K and three regions with temperature decreases ≤40 K as shown by Fig. 6.5f. These alternating temperature deviations increase with altitude and are collocated with accelerated meridional flow regions. Considering Figs. 6.7e and f, we see that the heating and cooling terms are now quite complex, with advective and adiabatic terms dominating (≥10 × Joule heating and ion drag terms). The CF thermosphere appears to be transporting heat (in 'waves'), both equatorward and poleward from the region III/II boundary (see Fig. 6.5f). Achilleos et al. (1998) also shows a similar phenomenon (see top left of Fig. 9 in Achilleos et al. (1998)), whereby 'wave-like' patterns of high temperature are being transported away from the auroral region. The energy deposited in the auroral regions heats the local thermosphere which increases local pressure gradients. Advection then attempts to redistribute this heat which momentarily cools the local area until enough heat is deposited again and the process restarts.

Figs. 6.8a-c show powers per unit area as functions of ionospheric latitude, calculated using Eqs. (2.69 - 2.74), for cases CS, CH and CF, respectively. Powers are indicated by legends on figures. In case CS, magnetospheric power (power used to accelerate magnetospheric plasma) is dominant up to ∼73 °, where atmospheric power (sum of Joule heating and ion drag) quickly dominates for all poleward latitudes (see Fig. 6.8a). This indicates that relatively expanded M-I systems (in steady-state) generally dissipate more heat in the atmosphere than in acceleration of outward-moving plasma (Yates et al. 2012). For case CH, Fig. 6.8b, we see the effects of plasma super-corotation in region III, where magnetospheric power reverses (now negative), heat dissipated as Joule heating doubles (as shown above), positive ion drag decreases by ∼70 % and negative ion drag increases by two orders of magnitude. Powers decrease in region II due to the decrease in flow shear (see Fig. 3.6a). In case CF, powers per unit area closely resemble those for case CS. There are small increases in peak magnetospheric power (∼10 %) and Joule heating (∼25 %) leading to an overall maximum increase in available power of ∼10 %. These findings are represented on a global scale in Fig. 6.14.

6.4 Magnetospheric Expansions

In this section we present auroral and thermospheric heating results for a transient expansion event. We present results from three periods throughout the transient event: i) Steady

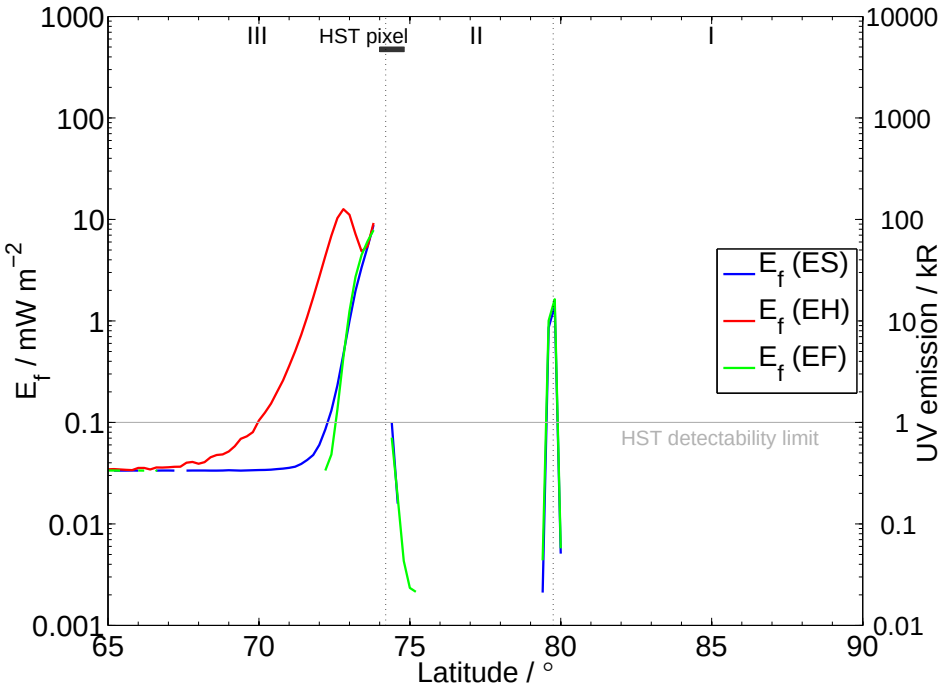

Figure 6.9. Shows the latitudinal variation of the precipitating electron flux(left axis) and corresponding UV emission (right axis) for the transient expansion cases. The blue line represents case ES whilst the red and green lines indicate cases EH and EF respectively. The magnetospheric regions are separated by dotted black lines and labelled. The latitudinal size of an ACS-SBC HST pixel located near the main auroral emission is represented by the dark grey box (see Appendix A). The solid grey line indicates the limit of detectability of the HST (Cowley et al. 2007).

state (case ES with R_{MM}=45 R_J), ii) 'half-pulse' (case EH with R_{MM}= 85 R_J) and, iii) 'full-pulse' (case EF with R_{MM}=45 R_J).

6.4.1 Auroral response

Here we discus how a transient magnetospheric expansion affects the aurorae by looking at the energy flux carried by precipitating electrons. For the detailed response of global M-I coupling currents the reader is referred to Chapter 5.

As for the case of our compression scenario, we summarise here the response of FAC densities (see Chapter 5 for detailed discussion). Fig. 5.8 shows the variation of FAC density with ionospheric latitude for cases ES (blue line), EH (red line) and EF (green line). Case EF exhibits only minor differences with case ES, which result from the lag in the

thermospheric response to transient magnetospheric changes. For case EH, the magnetospheric expansion causes the magnetic field strength (in the magnetodisc) and plasma angular velocity to decrease. Flow shear ($\Omega_T - \Omega_M$) thus increases and results in a broad region of upward FAC from ∼69 ° to ∼74 ° latitude. We also note a ∼15 % increase in FAC density in this broad upward region. At the region III/II boundary there is a small region of strong downward FAC produced by large gradients in Ω_M and Σ_P across this boundary. We also note that poleward of region III, only downward FACs exist due to the small imposed change in Ω_M in regions II and I.

Precipitating electron energy fluxes are shown in left hand axis of Fig. 6.9. Fluxes are plotted as functions of latitude and the blue line represents case ES, the red line corresponds to case EH and the green line represents case EF. On the right hand axis we indicate corresponding values of UV emission. Magnetospheric regions are separated by black dotted lines, the latitudinal size of a Hubble Space Telescope (HST) ACS-SBC pixel (0.03x0.03 arc sec) is indicated by the dark grey rectangle (see Appendix A) and the grey solid line indicates the limit of present detectability with HST instrumentation (∼1 kR; Cowley et al. (2007)). We begin by comparing cases ES and EF, which are almost identical except between ∼71 ° and ∼73 ° latitude. These differences are caused by the finite thermospheric response time. Both profiles peak at ∼74 ° latitude, equivalent to the location of the 'main auroral oval', and at ∼80 °, the boundary between open (region I) and closed field lines (region II). Therefore, we would expect a fairly bright auroral oval of ∼88 kR for case ES and ∼79 kR for case EF. The electron energy flux for case EF is ∼10 % smaller than case ES due to $\Omega_T(ES) > \Omega_T(EF)$ leading to a smaller flow shear. Our model also predicts the possibility of observable polar emission (region II/I boundary) of ∼15 kR for both cases ES and EF. However, this region is strongly dependent on the model used and poorly constrained by observations.

We now discuss the response of the energy flux E_f midway through our transient expansion event. The case EH profile, poleward of ∼74 ° latitude, lies entirely below the limit of detectability due to the downward (negative) FAC density in this region. In region III, there are now two peaks (corresponding to regions of upward FACs), separated by ∼1 °. The first peak, located at ∼73 ° is ∼37 % larger than the second one, at ∼74 °. These peaks result from the large degree of magnetospheric sub-corotation in region III (evident

in Fig. 3.6b). Comparing case EH with the equivalent expansion case in Cowley et al. (2007), case EH, in region III, has a maximum value of E_f that is twice that in Cowley et al. (2007). This study represents the thermosphere with a GCM which responds independently to Ω_M profiles. Our results indicate that this response is not as strong as that in Cowley et al. (2007), who use a simple 'slippage' relation to model the thermospheric angular velocity. At the open-closed field line (region II/I) boundary, Cowley et al. (2007) obtain large energy fluxes due to their large change in Ω_M across these regions; in our study, we obtain negligible changes in E_f due to our smaller change in imposed Ω_M across this boundary.

Considering the auroral response in case EH, we expect to see no polar emission (a darkening from case ES) at the region II/I boundary. In region III, we expect a $\sim 1\,^\circ$ equatorward shift along with a small increase ($\sim$40 kR) in peak main oval brightness compared to case ES. The size of the HST pixel (dark grey box) across this region is smaller than the separation of the two peaks in emission and thus suggests that it may be possible to observe both peaks in UV emission, creating a somewhat bifurcated main oval; with emission peaking at $\sim 73\,^\circ$ and $\sim 74\,^\circ$ latitude. The main oval would also be considerably broader ($\sim 2-3\,^\circ$) as a result of the large increase in the spatial region of magnetospheric sub-corotation. Clarke et al. (2009) observed little change in auroral brightness near the arrival of a solar wind rarefaction region, however Nichols et al. (2009) have seen changes in main oval location. The total UV power in case EH is $\sim$270 GW (compared to $\sim$78 GW in case ES). While this power is considerably smaller than that in case CH, it is comparable to UV powers calculated in Clarke et al. (2009) and Nichols et al. (2009), following solar wind rarefactions ($\sim 200 - 400$ GW).

6.4.2 Thermospheric heating

In this section, we present and discuss the response of thermospheric heating terms to our transient magnetospheric expansion event. We presented azimuthal and meridional flows and temperature differences (from steady state) in Fig. 5.9-5.10 which have been discussed at length in Chapter 5. To aid in the description of thermospheric heating, we place here, a copy of Fig. 5.9-5.10 and refer to them as Fig. 6.10-6.10. We also summarise the major flow patterns associated with zonal (Figs. 6.10a, c and e) and meridional (Figs. 6.10b, d and f) flows. Thermospheric heating and cooling rates, and powers per unit area are presented in

Fig. 6.12 and Fig. 6.13 and we use Fig. 6.11 to aid in their discussion. Cases ES, EH and EF are represented in respective rows 1−3 of Figs. 6.10 to 6.13.

Figs. 6.10a, c and e show the variation of thermospheric azimuthal velocity, in the corotating reference frame, with altitude and latitude for cases ES, EH and EF. Positive velocities represent super-corotation whilst negative velocities indicate sub-corotation. The white contour indicates the locus of rigid corotation and the black arrows indicate the direction of meridional flow. Magnetospheric regions are labelled and separated by black dotted lines. The zonal flow patterns are as in section 6.3.2 i.e a low altitude super-corotating jet in region III and a large sub-corotating jet spanning regions III-I. We note that the area experiencing strong super-corotation (black contour) is at a minimum in case EH and that the degree of sub-corotation decreases as the system responds to the event. Figs. 6.10b, d and f show thermospheric meridional velocity as a function of altitude and latitude for cases ES-EF. Labels, arrows and contours are the same as in Figs. 6.10a, c and e. The steady-state flow pattern, consisting of high-altitude equatorward flows and low-altitude poleward flows, is as in case CS (discussed in Smith et al. (2007); Smith and Aylward (2009); Yates et al. (2012) and Chapter 5). As the system progresses through the expansion event, the high altitude meridional flow reverses for parts of regions III and II and all of I. Large, localised acceleration regions also develop. For further details on thermospheric flows, the reader is referred to Chapter 5.

Fig. 6.11a shows temperature as a function of altitude and latitude for case ES. Figs. 6.11c and e show the difference in thermospheric temperature between cases EH and ES, and cases EF and ES, as functions of altitude and latitude. Magnetospheric regions are labelled and separated by black dotted lines and temperatures are indicated by the colour bar. We interpret the response of thermospheric temperature with the aid of Figs. 6.12a-f, showing contour plots for various thermospheric heating (Figs. 6.12a, c and e) and cooling (Figs. 6.12b, d and f) terms (see plot legends for details).

Fig. 6.11a shows similar results to those described in section 6.3.2. The main difference is related to the polar 'hotspot' which is considerably cooler (maximum temperature of ∼590 K) than that for case CS (maximum temperature of ∼705 K). As previously discussed, the 'hotspot' results from the meridional transport, via poleward accelerated flows,

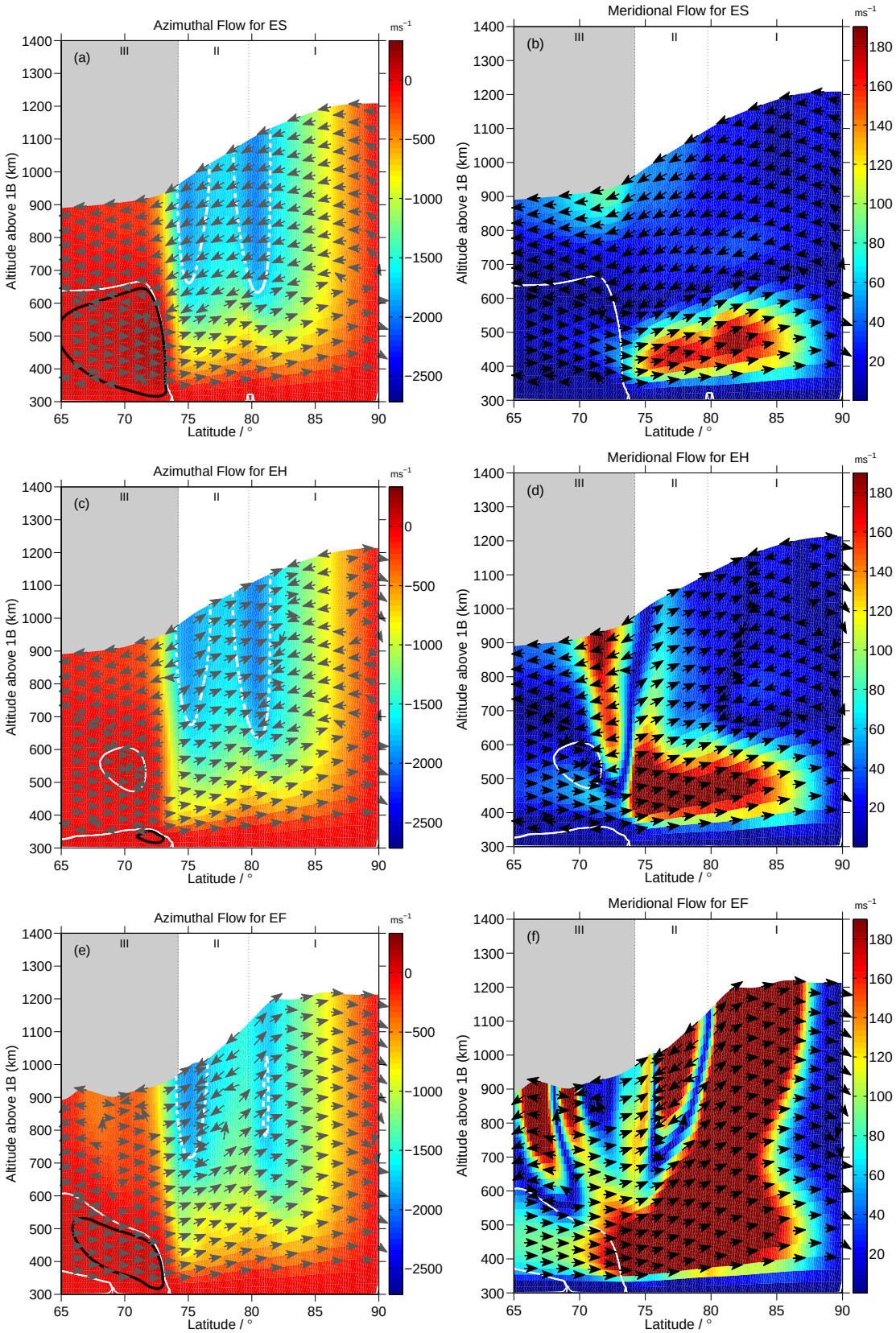

Figure 6.10. (a), (c) and (e) show the variation of thermospheric azimuthal velocity (colour scale) in the corotating reference frame for cases ES-EF respectively (left to right). Positive values (dark red) indicate super-corotation, whilst negative values (light red to blue) indicate sub-corotation. The arrows show the direction of meridional flow and the solid white line indicates the locus of rigid corotation. The solid black encloses regions of super-corotation ($> 25\,\mathrm{m\,s^{-1}}$) and the dashed white line encloses regions that are sub-corotating at a rate $> -1750\,\mathrm{m\,s^{-1}}$. The magnetospheric regions (region III is shaded) are separated by dotted black lines and labelled. (b), (d) and (f) show the meridional velocity in the thermosphere for cases ES-EF. The colour scale indicates the speed of flows. All other labels and are as for (a).

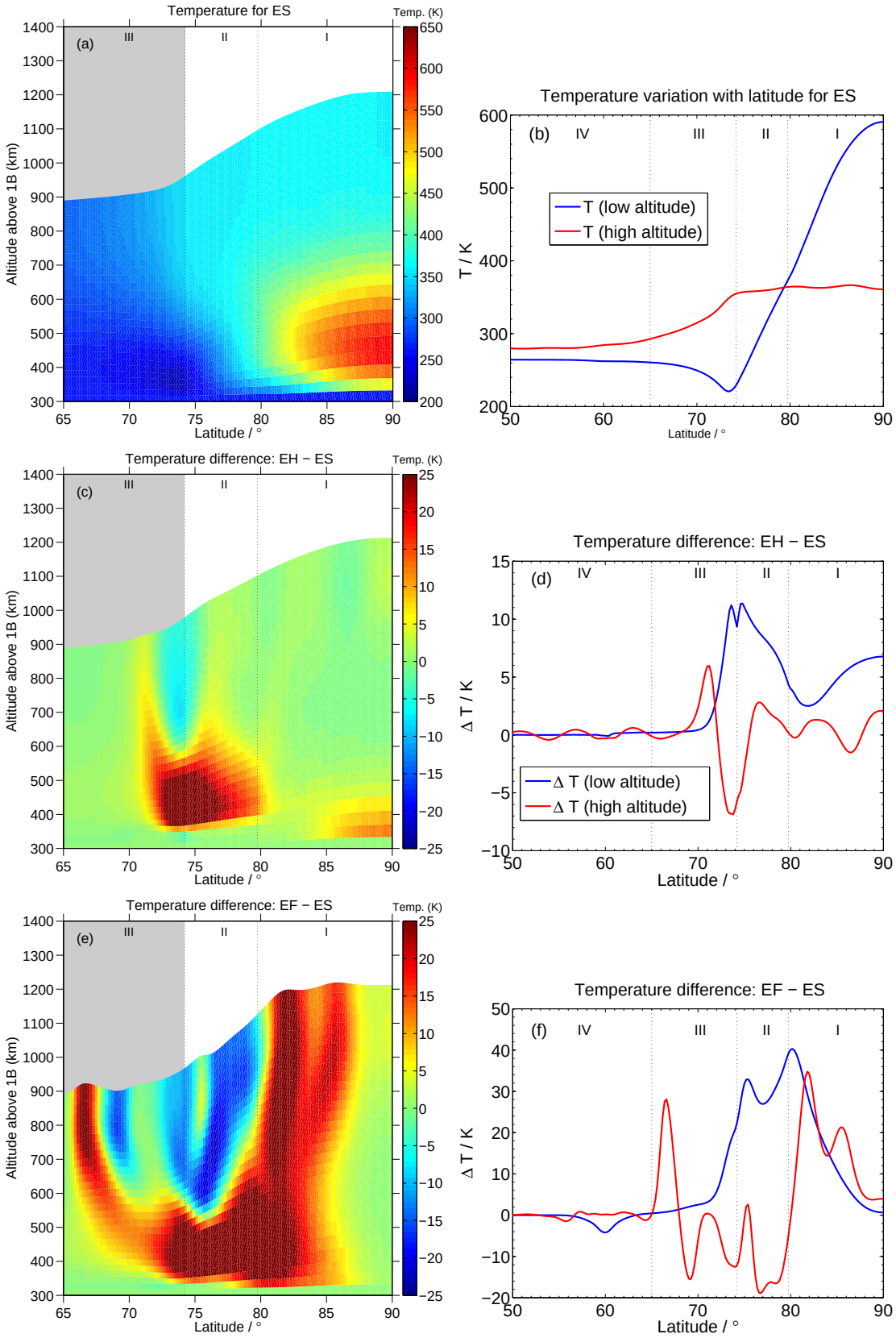

Figure 6.11. (a) shows the thermospheric temperature distribution for case ES whilst (c) and (e) show the temperature difference of cases EH and EF with case ES. The magnetospheric regions (region III is shaded) are separated by dotted black lines and labelled. (b) shows the latitudinal temperature profile for case ES and (d) and (f) show latitudinal temperature difference profiles at low (blue line) and high (red line) altitudes for EH and EF with ES. All other labels and are as for (a).

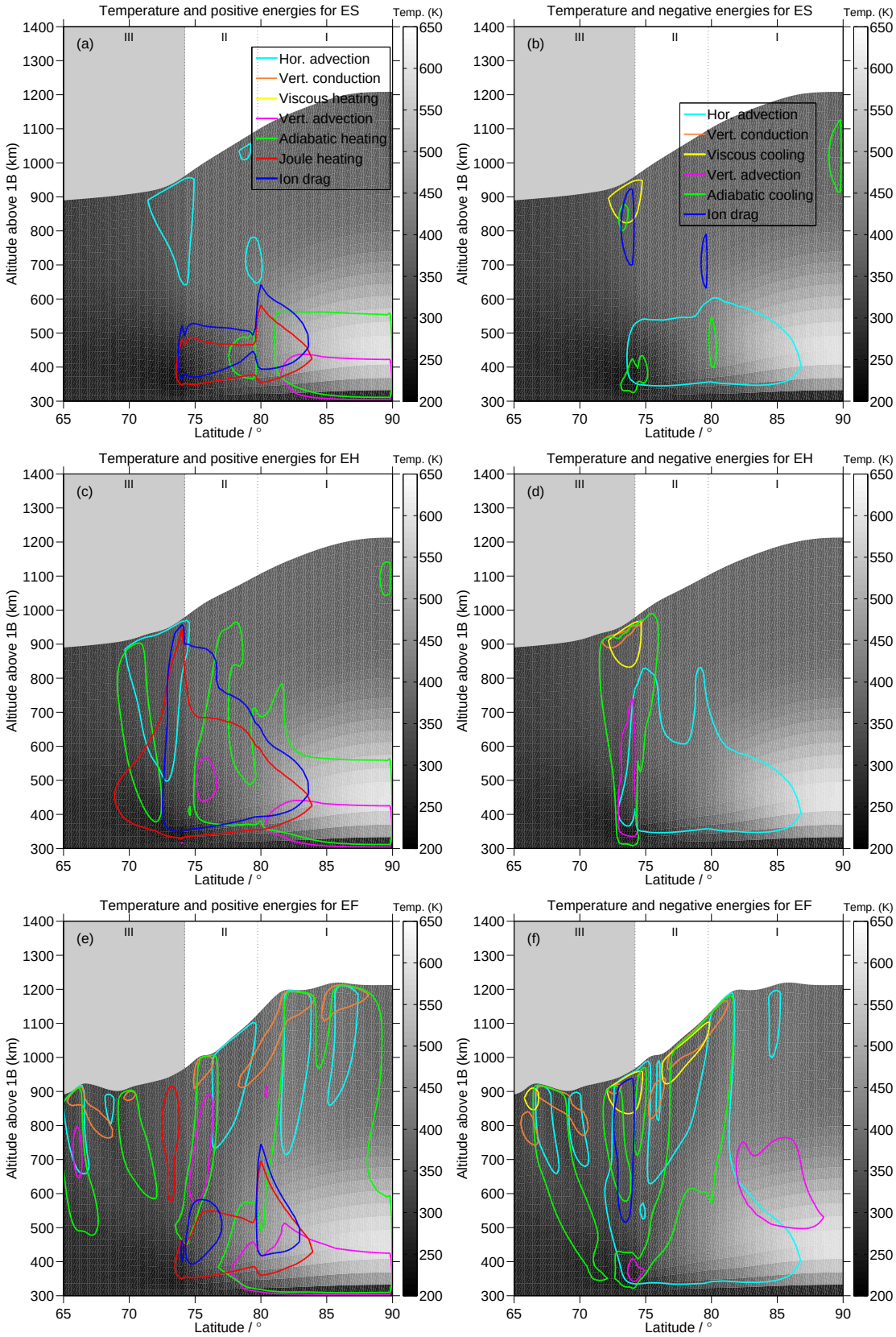

Figure 6.12. (a), (c) and (e) show the variation of atmospheric heating terms with altitude, latitude and temperature (colour bar) for cases ES, EH and EF (left to right). The contours enclose regions where heating/kinetic energy rates exceed $20\,\mathrm{W\,kg^{-1}}$. Ion drag, Joule heating, vertical and horizontal advection of energy, adiabatic heating/cooling, viscous heating and heat conduction (vertical and turbulent) are represented by blue, red, yellow and magenta, green, cyan and orange lines. The magnetospheric regions are separated and labelled. (b), (d) and (f) show the variation of atmospheric cooling terms where the contours enclose regions where heating/kinetic energy are decreasing (cooling) with rates exceeding $20\,\mathrm{W\,kg^{-1}}$. All colours and labels are as in (a).

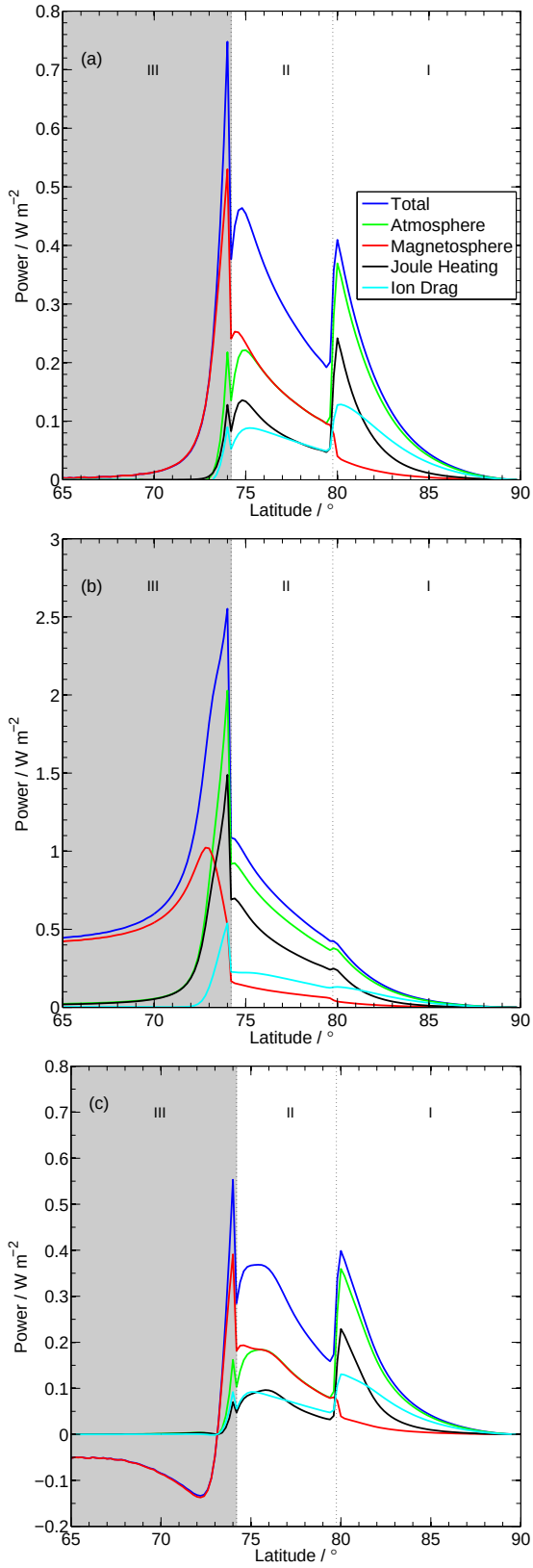

Figure 6.13. (a)-(c) show how the power per unit area varies for our transient compression cases. The blue line represents total power which is the sum of magnetospheric power (red line) and atmospheric power (green line); atmospheric power is the sum of both Joule heating (black solid line) and ion drag (cyan solid line). Other labels are as for Fig. 6.12a.

of Joule heating from lower latitudes (∼73−84 °; see Figs. 6.12a and b) (Smith and Aylward 2009; Yates et al. 2012).

Fig. 6.11c and d exhibits the temperature difference between cases EH and ES. The figure shows a ∼50 K local temperature increase at low altitudes (<700 km) in regions III and II. This is caused by a ≥4× increase in Joule heating and ion drag power in this region (see Figs. 6.12c and d). Also evident are two more minor temperature variations: i) ∼10 K decrease at high altitude, centred on the region III/II boundary and, ii) ∼10 K increase in the polar 'hotspot' region. We interpret that this local 'cold spot' arises mainly from the appearance of meridional accelerated flows, which efficiently transport heat away (equatorward and poleward) from the region III/II boundary, and the factor of three increase in adiabatic cooling. We attribute the small increase in temperature at the polar 'hotspot' to the 35 % increase in low altitude meridional velocity (itself due to poleward acceleration - more detail in Chapter 5).

Fig. 6.11e and f shows the temperature difference between cases EF and ES. The temperature profile has changed significantly from that in Fig. 6.11c. There are two regions where temperatures increase by up to ∼50 K: i) extending from ∼73−85 ° latitude and low altitudes in regions III and II, and all altitudes in region I (these map to the large poleward-accelerated region in Fig. 6.10f); and ii) high-altitude (>600 km) region, centred at ∼66 ° latitude. These regions are primarily heated by horizontal advection (high-altitude only) and adiabatic terms (all altitudes) as shown in Fig. 6.12e; these terms have increased from case ES by, at most, 800 % and 500 % respectively. The final feature of note in Fig. 6.11e is the region cooled by up to ∼−22 K, lying between the two heated regions at altitudes >550 km. This cooling is caused by a combination of local increases in horizontal advection and adiabatic cooling, by factors of three and greater. Similar to case CF, case EF's meridional flows seem to be transporting heat equatorward and poleward, although the majority of these flows act to transport thermal energy poleward.

Figs. 6.13a-c show powers per unit area as functions of ionospheric latitude for cases ES-EF respectively. Power sources are indicated by the legends on the figures. Fig. 6.13a shows the energy balance in the thermosphere for case ES. As discussed in Yates et al. (2012), most of the energy in region III is expended in accelerating magnetospheric plasma;

in region II we have a situation where magnetospheric power and atmospheric power (the sum of Joule heating and ion drag) are equal, due to Ω_M=0.5 Ω_J. Atmospheric power is dominant in region I. For case EH (Fig. 6.13b), the magnetospheric power is dominant up to ∼73 ° latitude; atmospheric power, primarily Joule heating, then dominates at all poleward latitudes. This results from the large increase in flow shear ($\Omega_T - \Omega_M$). The magnetosphere of case EF super-corotates, compared to the thermosphere, at latitudes ≤73 °. This causes a reversal in energy transfer, which now flows from magnetosphere to atmosphere (see Fig. 6.13c). Polewards of 73 °, the energy balance is similar to that of case ES.

6.5 Discussion and conclusions

6.5.1 Global thermospheric response

We now discuss the thermospheric response in terms of global energy balances by calculating the integrated power per hemisphere for Joule heating, ion drag and magnetospheric power (used to accelerate the sub-corotating magnetospheric plasma). These powers are calculated by integrating powers per unit area obtained using Eqs. (2.69 - 2.74) and presented in Figs. 6.8 and 6.8 over each hemisphere. Figs. 6.14 and 6.15 respectively show these integrated powers for our transient compression and expansion scenarios. The blue bars represent ion drag, green bars indicated Joule heating whilst red bars represent magnetospheric power. The total (sum) power is indicated by the orange bars.

Midway through our transient compression scenario, magnetospheric plasma is super-corotating, which leads to energy being transferred from the magnetosphere to the thermosphere. This leads to an increase in Joule heating and a decrease in ion drag as the ionospheric plasma is now losing kinetic energy through collisions with the 'relatively' sub-corotating neutrals. Our results indicate that ∼2000 TW of total power (magnetospheric and atmospheric) is gained by the coupled system as a result of plasma super-corotation (see Fig. 6.14). This energy transfer from the magnetosphere would act to, essentially 'spin up' the planet (Cowley et al. 2007) and increase the thermospheric temperature. Note that this is considerably larger than the ∼325 TW (closed and open field regions) calculated in Cowley et al. (2007) for a responsive thermosphere scenario. The differences between the total powers obtained with the simulations presented herein and those in

the study of Cowley et al. (2007) arise mainly from our use of a thermospheric GCM to self-consistently calculate the thermospheric angular velocity whilst Cowley et al. (2007) assumed that Eq. (2.56) were true with a constant slippage parameter of $K = 0.5$. Recent work by Smith and Aylward (2009); Yates et al. (2012) showed that the value of K varies considerably with latitude. Another difference lies in the prescribed values of the height-integrated Pedersen conductance, we assign $\Sigma_P = 0.5\,\mathrm{mho}$ in regions mapping to the middle magnetosphere whilst in Cowley et al. (2007) $\Sigma_P = 0.4\,\mathrm{mho}$. In case CF, plasma is not super-corotating; thus the picture is fairly similar to case CS. The main difference is that there is a $\sim$20 % increase in total power dissipated in the atmosphere and in acceleration of the magnetosphere. This arises from increases in flow shear due to the 'lagging' thermosphere (see Fig. 3.6) and inevitably leads to the local temperature increases seen in Fig. 6.6e and discussed above. The finite time required for thermospheric response results in the described 'residual' perturbations to the initial system (CS) even after the pulse has subsided (CF).

A transient magnetospheric expansion creates a significant increase in both power dissipated in the atmosphere due to Joule heating ($\sim$6$\times$ that of ES) and ion drag ($\sim$3$\times$ that of ES). Moreover, the power used to accelerate the magnetosphere towards corotation is $\sim$7$\times$ that of ES, and is shown in Fig. 6.15. These increases lead to a total power per hemisphere of $\sim$2600 TW which is three times larger than the responsive thermosphere case in Cowley et al. (2007). These changes in heating and cooling create the local temperature increases discussed above, but only by $\lesssim$7 K (compared to case ES). For case EF, where we now have the magnetosphere rotating faster than the thermosphere, there is a $\sim$75 % decrease in the magnitude of 'magnetospheric' power. The magnetosphere is thus transferring power to the thermosphere in this case, albeit a relatively small amount. This effectively 'pulls' the thermosphere along, increasing its angular velocity in order to return to the steady-state situation where $\Omega_T > \Omega_M$. We note that energy dissipated via Joule heating also decreases slightly due to the small decrease in flow shear. Overall, the total power per hemisphere in case EF is only 30 % that of case ES.

The magnetospheric reconfigurations discussed above have been shown to have a significant impact on the dynamics and energy balance of the thermosphere. Results for cases CH and EH shows large (approximately three orders of magnitude larger than solar

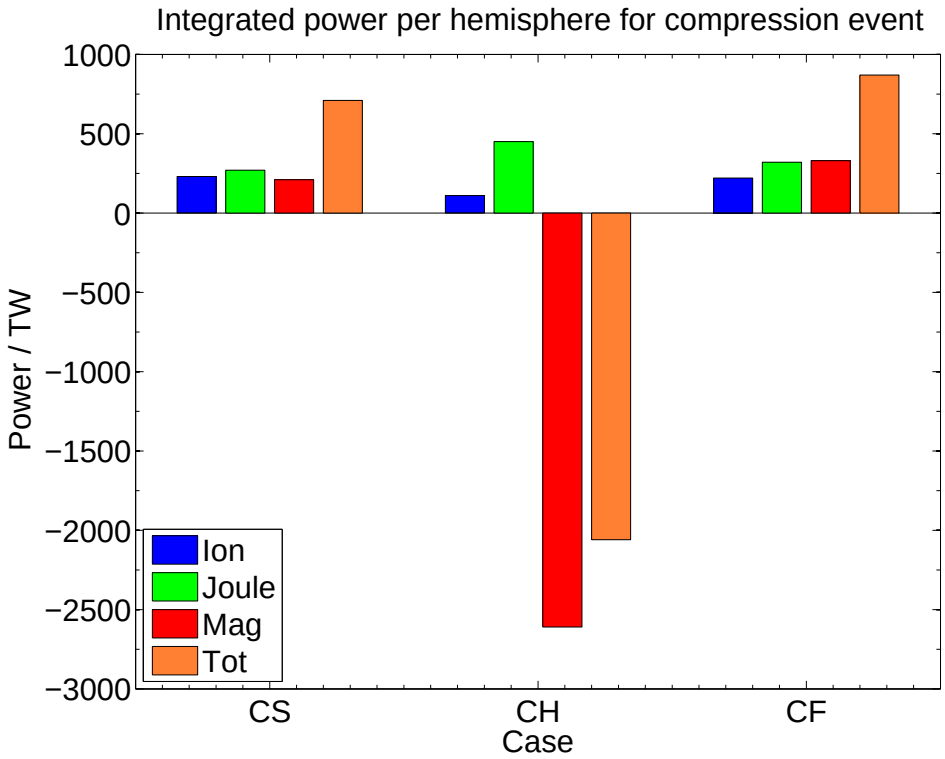

Figure 6.14. Integrated ionospheric powers per hemisphere for cases CS-CF are represented in this figure. Ion drag is represented by blue bars, Joule heating by green bars, magnetospheric power by red bars and total (sum of all above) is represented by orange bars. See text for further detail.

heating) increases in energy either being deposited or dissipated in the thermosphere. Let us now compare our simulated results with those of an auroral heating event observed by Stallard et al. (2001, 2002) and analysed by Melin et al. (2006). As discussed in section 1.1.2 and 4.2.2, Melin et al. (2006) found that the combined ion drag and Joule heating rates increased from 67 mW m^{-2} to 277 mW m^{-2} over three days. The heating event was deemed to have been caused by a decrease in solar wind dynamic pressure. Similarly to assumptions and calculations discussed in section 4.2.2, we calculate that the total energy dissipated by Joule heating and ion drag increases from ∼193 TW to ∼800 TW during the observed auroral heating event. These values are comparable to the increase of Joule heating and ion drag in our expansion scenario, ∼201 TW for case ES and ∼942 TW case EH. Increases in Joule heating and ion drag from case CS to CH is more modest (∼499 TW to ∼555 TW) due to the reversal of kinetic energy exchange between atmospheric neutrals and ions, and despite of an increase in Joule heating. Our modelling supports the work of Melin et al. (2006) in terms of i) the magnitude of energy dissipated in the thermosphere

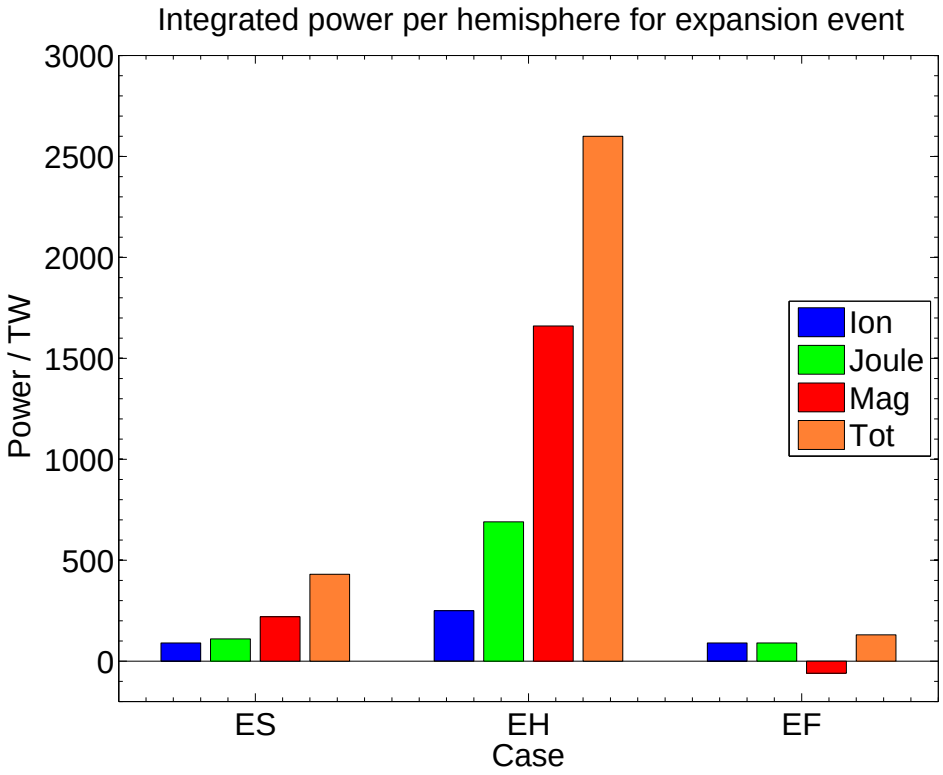

Figure 6.15. Integrated ionospheric powers per hemisphere for cases ES-EF are represented in this figure. Ion drag is represented by blue bars, Joule heating by green bars, magnetospheric power by red bars and total (sum of all above) is represented by orange bars.

and ii) the type of magnetospheric reconfiguration required (transient expansion). Melin et al. (2006) also suggest that a significant increase in equatorward flows would arise in order to redistribute the extra heating; our expansion scenario however, does not show any significant increases in equatorwards winds. Nevertheless, we note that our compression scenario does indeed show a large change in meridional flow patterns with a large portion of the thermosphere now possessing equatorward flows. The timescales of our simulations and the observations also differ significantly; our simulations all occur within a three hour period (approximately one-third of a Jovian rotation) where the observations occurred over three days (roughly six Jovian rotations). This suggests that although our transient simulations are able to qualitatively and somewhat quantitatively reproduce certain thermospheric observations further constraints and improvements need to be included, some of which will be discussed in section 7.5.

6.5.2 Concluding remarks

The transient work presented in this chapter has successfully demonstrated that the arrival of solar wind compression regions at Jupiter have a significant effect on the Jovian aurora and thermospheric energy balance. We see increases in auroral emission for solar wind shocks and to a lesser extent for solar wind rarefactions. Both magnetospheric compressions and expansions lead to an increase in high-latitude Joule heating and an increase in equatorward transport of energy; however, for our transient compression scenario, there is a significant increase in equatorward meridional winds which transports most Joule heating towards the equator. The extra heating results in local thermospheric temperature increases but unfortunately not enough to explain the observed high thermospheric temperatures at Jupiter.

The next chapter will present all the major conclusions from this thesis as well as their implications for the Jovian energy crisis and potential future improvements to the work and model presented herein.

Chapter 7

Conclusion

Satisfaction lies in the effort, not in the attainment, full effort is full victory.

Mahatma Gandhi

In this Chapter we conclude on the work and analyses presented in this thesis. We present conclusions for: i) our steady-state modelling of the Jovian thermosphere and M-I coupling currents (Chapter 4) in section 7.1; ii) the effect of rapid magnetospheric reconfigurations on Jupiter's thermospheric dynamics and coupling currents (Chapter 5) in section 7.2; and how these rapid reconfigurations affect the thermospheric energy balance and aurora (Chapter 6) in section 7.3. We then briefly discuss the implications of our results for the 'energy crisis' in section 7.4. Finally, we suggest potential future studies - carried out using the current (or improved) JASMIN model in section 7.5.

7.1 Conclusions to Chapter 4

In this study, we have expanded on the model of Smith and Aylward (2009) and described the effects of different solar wind dynamic pressures on the coupled ionosphere-magnetosphere system at Jupiter. We constructed three typical magnetospheric profiles (see Table 3.3), compressed, baseline (average) and expanded. These were then coupled to our global two-dimensional thermospheric model (Smith and Aylward 2008) and a global conductivity model of the ionosphere (Grodent et al. 2001). This allowed for a comparison

with results from Smith and Aylward (2009), but also provided a first quantitative investigation of how ionospheric, thermospheric and magnetospheric parameters were affected by differing solar wind conditions.

Our results confirm many results from previous studies such as those of Southwood and Kivelson (2001); Cowley and Bunce (2003b) and Cowley et al. (2007). We see an increase (resp. decrease) in thermospheric and magnetospheric angular velocities for compressed (resp. expanded) magnetospheres relative to our baseline. The thermosphere super-corotates just equatorward of the middle / outer magnetosphere boundary similarly to Smith and Aylward (2009). We solve for Ω_M self-consistently in the magnetodisc in all cases using the equations of disc dynamics. The Ω_M value in the outer magnetosphere is a constant, dependent on disc radius i.e solar wind pressure (Cowley et al. 2005). Magnetospheric angular velocities in the polar cap, are also fixed at a set fraction ($\sim$10 %) of rigid corotation (Ω_J) (Isbell et al. 1984). We also found that the coupling currents showed an increase ($\sim$20 %) in intensity when going from an average to a more expanded magnetosphere and a decrease ($\sim$40 %) when going from average to compressed.

Our thermospheric model was used to simulate azimuthal and meridional neutral velocities. We see super-corotation in the azimuthal flows equatorward of the edge of the magnetodisc flux shells. There lies a strong sub-corotational jet at mid to upper altitudes in the mapped ionospheric locations of the outer magnetosphere and polar cap. The spatial size of the strong sub-corotation region increases with increased magnetospheric size due to the weaker magnetic field strength in expanded magnetospheres; thus the transfer of angular momentum is less effective at maintaining corotation as system size increases. Angular momentum is transferred from the thermosphere to the magnetosphere, in order to accelerate the latter towards corotation. If the thermosphere itself is significantly sub-corotating, then there is a lower 'reservoir' of available angular momentum that can be transferred. This results in a decreased plasma angular velocity in these outer regions of the magnetosphere.

We see a meridional flow directed polewards at low altitudes and equatorwards at high altitudes. From the poleward edge of the magnetodisc to the centre of the polar cap, a region of accelerated poleward flow exists whose velocity magnitude increases from a com-

pressed to an expanded magnetosphere. This occurs because there is a force imbalance in this region that increases advection of momentum in expanded magnetospheres. Increased advection restores balance, which is equivalent to the acceleration discussed above. This accelerated flow produces a 'hotspot' in the polar cap, with a maximum temperature increase of ∼130 K from compressed to expanded magnetosphere. The size of the 'hotspot' also increases with an expanding magnetosphere. We find that the outer magnetosphere and polar cap are most strongly heated by Joule heating and ion drag. This heat is then distributed across the polar region via advection rather than viscous transport, whilst more equatorial regions are significantly cooled. This aspect of thermospheric flow is consistent with those presented in Smith and Aylward (2009), however these results are the first to quantify the effects of magnetospheric reconfiguration on the steady-state flow of the thermosphere. These results also suggest that accurate measurements of ionospheric temperature in the polar region could potentially be used as a sensitive diagnostic of not only atmospheric, but also magnetospheric conditions, as has been done in numerous studies e.g. Stallard et al. (2001, 2002); Melin et al. (2006).

We also showed that the power dissipated in the upper atmosphere (consisting of both Joule heating and ion drag) increases with an expanded magnetospheric configuration. The power used to accelerate the magnetospheric plasma initially increases as we expand the magnetosphere from compressed to average configurations, but then decreases with further expansion ('average' to 'expanded'). This behaviour suggests that the power used to accelerate the magnetosphere has a 'local' maximum for a magnetosphere size somewhere between our compressed and expanded configurations. The total power extracted from planetary rotation is the net sum of the atmospheric and magnetospheric powers, and is positively correlated with magnetosphere size. Comparing our compressed and average magnetospheres with the 'intermediate' and 'baseline' cases in Cowley et al. (2007), we showed that the use of a two-dimensional thermosphere model results in the transfer of ∼20 % more energy from the thermosphere to the magnetosphere in order to accelerate the plasma in the magnetodisc. Using our more realistic model of thermospheric flow also produced increased dissipation of energy in the thermosphere via Joule heating and ion drag, compared to the cases presented in Cowley et al. (2007).

We have shown that our original compressed case has some unusual current density

features due to a relatively high value for the radial current at the outer disc boundary. In order to confirm the behaviour of these features, we decreased the boundary value of $I_{\rho\infty}$ for each case in order to produce alternative models with minimum spatial variance in their FAC profiles. This led to the selection of $I_{\rho\infty}$ of 45 MA, 68 MA and 80 MA for the compressed, average and expanded cases, respectively.

Decreasing the radial current $I_{\rho\infty}$ at the boundary between the middle and outer magnetospheres resulted in all magnetosphere-ionosphere coupling currents being reduced in accordance with the new value of $I_{\rho\infty}$. This is expected under the assumption of current continuity. The main differences between cases with large and reduced radial currents lies mainly within the magnetodisc. For the FAC density, changes related to $I_{\rho\infty}$ were also significant throughout the outer magnetosphere. Thermospheric and magnetospheric angular velocities changed only slightly for the baseline and expanded case but much more substantially for our compressed case. For azimuthal flows we found that decreasing $I_{\rho\infty}$ also generally increased the level of sub-corotation throughout high latitudes. For meridional flows we found slight increases in localised regions of accelerated flow, most evident in the alternate compressed case. We also found that the polar region becomes slightly warmer with a decrease in $I_{\rho\infty}$ (mainly due to the corresponding change in the $\mathbf{J} \times \mathbf{B}$ force and the effect this has on the force balance); peak polar temperatures for the alternative configurations were increased relative to their $I_{\rho\infty}$=100 MA counterparts. The total integrated powers increased with decreasing $I_{\rho\infty}$ for our compressed case, but decreased for our baseline and expanded cases. The integrated magnetospheric power for all cases decreased along with $I_{\rho\infty}$, whilst atmospheric power increased by $\sim$20 % for the alternate compressed case, but remained almost equal for our baseline and expanded cases. Thus, it seems that decreasing the boundary radial current $I_{\rho\infty}$ (and thus limiting the total FAC which may flow) effectively decreases the 'ability' of the thermosphere to transfer angular momentum to the magnetosphere. This behaviour of the simulated Jovian system has been quantified for the first time in this thesis work and, as expected, decreases the intensity of auroral emissions and produces a slightly warmer polar region.

Our calculations suggest that main oval auroral emissions and brightness for an expanded magnetosphere would generally be greater than that of a compressed one. The detailed structure of the FAC density profile in the magnetodisc is most sensitive to the

value of $I_{\rho\infty}$ for the compressed case. Compressed magnetospheres in the steady state have larger field strength than expanded ones and are more efficient at maintaining the co-rotating magnetodisc plasma out to larger radial distances. This leads to a smaller shear in angular velocity between the magnetosphere and thermosphere and, consequently, smaller thermospheric temperatures. As a result, auroral emission is brightest for the most expanded magnetospheric systems. We also saw that auroral emissions would increase at the boundary between the outer magnetosphere and the polar region with magnetospheric compression due to the large change in plasma angular velocity at this boundary. Better observational constraints of Ω_M and polar auroral emissions (in particular, which class of these auroral features, if any, correspond to Jupiter's polar cap boundary) are required to confirm this prediction.

This aspect warrants further investigation, since we have not attempted to model the change in polar cap angular velocity with solar wind dynamic pressure (we note that Isbell et al. (1984) developed a formalism for deriving polar cap rotation as a function of upstream solar wind velocity). Furthermore, the caveat with our predictions is that the system is in a steady-state (where there is no explicit time dependence of the model outputs). We thus view this study as an initial step towards developing a model to study the transient effects of rapid changes in the solar wind dynamic pressure. Results of such studies could provide further insights to the 'energy crisis' at Jupiter (Smith and Aylward 2009), and the physical origin of transient auroral features.

Finally, the results presented in this study contribute to a larger set of theoretical investigations which have provided useful quantitative predictions of how the Jovian aurorae would respond to changes in solar wind dynamic pressure. Such results are useful for interpreting auroral observations, and for making more extensive use of such data as remote diagnostics of the physical state of the Jovian magnetosphere.

7.2 Conclusions to Chapter 5

We have investigated the effect of transient variations in solar wind dynamic pressure on the M-I coupling currents and thermospheric flows of the Jovian system. In this paper, we concentrated mainly on the response of thermospheric dynamics to these transient vari-

ations in the solar wind. We considered two scenarios: i) a transient compression event, and ii) a transient expansion event. Both of these were imposed over a time scale of three hours. A transient compression event consists of an initially expanded, steady-state magnetospheric configuration. The model Jovian magnetosphere then encounters a shock in the solar wind, which compresses the system. As the conceptual shock propagates past the magnetosphere, a rarefaction region follows and the magnetosphere subsequently expands back to its initial state. The opposite occurs for our expansion event. In sections 5.2 and 5.3 we presented the modelled response of M-I coupling currents and thermospheric flows to these events.

To summarise, the response of the magnetosphere to transient variations in solar wind dynamic pressure is similar to predictions and modelling by Cowley and Bunce (2003a,b) and Cowley et al. (2007). Transient compressions cause the magnetosphere to super-corotate compared to both planet and thermosphere. This results in the reversal of coupling currents and angular momentum transfer which 'spin up' the planet and deposit energy in the thermosphere. The main auroral oval is shifted polewards ($\sim$0.2 °) and its brightness is doubled; our modelling also suggests increases in auroral emission in the outer magnetosphere and polar cap. Transient expansions, on the other hand, cause a significant increase in the degree of sub-corotation which increases the flow shear between the magnetosphere and thermosphere and leads to increases in coupling currents. There is an increase in angular momentum transfer from the thermosphere to magnetosphere, which acts to accelerate the magnetospheric plasma towards corotation. Thus, the thermosphere loses energy and angular momentum. We predict a $\sim$2 ° broadening of the main oval and an equatorward shift of $\sim$1 ° in peak emission, as well as a reduction in polar emission. The modelled auroral responses are similar to those observed by Nichols et al. (2009) and Clarke et al. (2009).

To our knowledge, this is the first study that considers the response of the Jovian thermosphere to variations in solar wind pressure on relatively short time scales. The most significant changes to the thermosphere occurred at the end of the transient event. We found a positive correlation between the thermospheric and magnetospheric angular velocities. However, the thermospheric response lags behind that of the magnetosphere due to its large inertia. Dynamically, the most pronounced changes in the thermosphere occurred in ion drag and advection terms. The latter created large accelerated meridional flows

which subsequently increased and decreased the thermospheric temperature, particularly in regions mapping to the middle and outer magnetosphere. Previous studies, which treat the ionospheric electric field as a free parameter, have found that the thermosphere reacts more immediately (∼30 minutes) to magnetospheric changes (Millward et al. 2005) or have assumed no reaction at all (Gong 2005). Overall, we find that our model's thermospheric response lies, in a sense, between these limits. More specifically, the thermosphere does respond to the imposed magnetospheric changes, but with a considerable 'lag' in time, comparable to or longer than the timescale (∼3 hours) of our imposed change. Our results, when considered alongside those from the literature, suggest that the thermospheric response timescale is influenced not only by the magnitude of the imposed change in magnetospheric angular velocity, but also its detailed 'history' (i.e. how it changes as a function of time).

7.3 Conclusions to Chapter 6

This study models the effects of transient changes in solar wind dynamic pressure on Jovian auroral parameters and the thermospheric energy budget. The transient changes simulated are two types: i) a transient compression event, and ii) a transient expansion event. Both events are assumed to last for three hours, and we have presented and compared pre-event, midway (maximum compression or expansion) and post-event results in sections 6.3 and 6.4.

Simulations of the auroral response to a transient compression and the subsequent return to the initial magnetospheric configuration showed significant variation in auroral size, location and brightness. Midway through the compression event we find that auroral brightness, estimated from the precipitating electron energy flux, increases from ∼600 kR (in steady state) to ∼2800 kR. The location of the main auroral oval also shifts poleward by ∼0.2 ° latitude and its width shrinks slightly compared to the steady-state. Observations by Clarke et al. (2009) and Nichols et al. (2009) find factor-of-two increases in auroral brightness as well as poleward shifts of up to ∼1 ° (Nichols et al. 2009) due to the arrival of solar wind shocks (which represent increases of $0.01 - 0.3$ nPa in solar wind dynamic pressure). The total UV power can also be used to examine the auroral response, and we find that UV powers are approximately a factor of two or three larger than those observed

by Clarke et al. (2009) and Nichols et al. (2009). This is an interesting comparison, as their observed compressions (magnetopause change of $\sim$40 R_J) are larger than our modelled one (magnetopause change of $\sim$33 R_J). Immediately after the transient compression event, we find that the aurora differs slightly from the initial steady-state, and then only in regions mapping to the middle magnetosphere. There is an increase in auroral emission of $\sim$200 kR ($\sim$35 %) and a $\sim$1.5 ° broadening of the main oval.

The super-corotation of magnetospheric plasma midway through the compression event caused various changes in thermospheric heating and cooling terms. Joule heating increases by a factor of two and negative ion drag (decreases kinetic energy of the system) increases by a factor of seven, whilst positive ion drag (increase kinetic energy of the system) is halved. Overall, the magnetospheric super-corotation results in $\sim$2000 TW resultant power being dissipated in the thermosphere. This leads to local temperature changes of $\sim$25 K. After the transient event subsides, adiabatic and horizontal advective terms dominate over Joule heating and ion drag by an order of magnitude. This results in high-altitude thermospheric temperature increases of $\geq$40 K.

Our transient expansion simulations show less auroral variation than the compression simulations. At maximum expansion, peak auroral brightness increases from $\sim$88 kR to $\sim$126 kR and shifts equatorwards by $\sim$1 ° latitude. We do note, however, the presence of a slightly smaller auroral peak, approximately 1 ° poleward, creating a slight bifurcation of the main oval. The latitudinal width of the main oval also increased by $\sim$2$-$3 °. We would thus expect to observe a broad, slightly 'bifurcated' main oval and no significant polar emission midway through the expansion event. Observations of the auroral response near solar wind rarefaction regions by Clarke et al. (2009) have shown that there is little, if any, corresponding change in auroral brightness. As the expansion event subsides, we see only a small difference between the initial auroral profile and the final one. This difference is a small 10 % decrease in peak auroral emission, caused by the 'lagging' thermospheric response.

The transient magnetospheric expansion, similar to the compression, increased the total energy available to the thermosphere-magnetosphere system. The expansion lead to a factor-of-four increase in ion drag power and Joule heating rate (in the region mapped to

the middle magnetosphere), which resulted in local temperature increases $\lesssim$50 K. Globally, the large degree of magnetospheric sub-corotation increased the power expended in accelerating the magnetospheric plasma by a factor of seven. This aspect, coupled with the changes in Joule heating, produced a ∼2170 TW increase in the total power dissipated and used by the thermosphere. At the end of the expansion event, horizontal advection and adiabatic heating terms dominate, and are on average 650 % larger than in steady-state. This creates large areas of temperature variation $\lesssim$50 K. Globally, due to the magnetosphere rotating slightly faster than the thermosphere, the total power dissipated in the coupled system decreases significantly to ∼125 TW (∼30 % of the total in steady-state).

In summary, by examining our model's meridional flows and temperature distributions, we find that, by the end of the imposed transient changes, heat (thermal energy) has started to be transported both poleward and equatorward, particularly at high altitudes, in accordance with studies by Waite et al. (1983) and Melin et al. (2006). At present, though promising, these results are unable to explain the high thermospheric temperatures observed at low latitudes in Jupiter (∼900 K; Seiff et al. (1998)). The analysis which has been done, however, suggests that it may be informative, for future studies, to simulate the response of the thermospheric temperature to 'chains' of such compressions or expansions in the solar wind dynamic pressure. The prolonged exposure to such external perturbations may enhance the pole-to-equator transport of heat energy across the model planet.

7.4 Implications for the energy crisis

In short - we have not solved the energy crisis at Jupiter. What we have done, however, is made an initial step into investigating how time-dependent phenomena affect the Jovian system, in particular thermospheric heating, cooling and the aurora. We found that, in steady state, the more expanded the magnetosphere, the hotter Jupiter's thermosphere is likely to be. The caveat to this is that only the polar (high-altitude) region of the thermosphere (due to the poleward meridional winds) approaches the observable temperatures of $\sim$ 900 K (Seiff et al. 1998; Yelle and Miller 2004). The lower latitudes are still relatively cool with temperatures of $\sim 200-300$ K, compared to polar temperatures of up to $\sim$ 700 K. On the other hand, when we consider rapid magnetospheric reconfigurations, the situation is quite different. We see a change in the direction of meridional winds as well as a large (at

least a factor of two) increase in Joule heating. These winds redistribute the extra heat, essentially sending 'waves' of high-temperature gas (higher than ambient surroundings) towards both the polar and equatorial regions (Waite et al. 1983; Achilleos et al. 1998; Melin et al. 2006). Such temperature 'waves' may be observationally detectable through infrared spectroscopic techniques but are currently close to the noise level (T. Stallard, private communication 2012). The present results are not enough to increase the temperature of the equatorial thermosphere to its observed values but we stress that all the results presented in Chapters 5 and 6 occur within a period of three hours (approximately 1/3 of a Jovian day). This leads to the potential of future, more realistic, time-dependent studies, as discussed in the following section.

7.5 Future work

We set out to try and shed light on various solar wind and time-dependent aspects of the Jovian system. We modelled how the solar wind affects the Jovian thermosphere, aurora and M-I current systems in steady state. We then proceeded to model how these steady-state systems are perturbed if the magnetosphere is rapidly compressed or expanded by changes in the solar wind dynamic pressure. The work presented here is, to our knowledge, the first to successfully model rapid time-dependent changes in the Jovian thermosphere by using a coupled magnetosphere-ionosphere-thermosphere model.

The next logical step for future work would be to vary the duration of these transient events and to experiment with 'chains' of such events in order to model the dynamic response of the Jovian thermosphere over more extended periods of external perturbation. A more realistic solar wind dynamic pressure profile would maintain a compression/rarefaction region for a few days, thus allowing the Jovian system to reach at least a quasi-steady state. Currently our coupled model can run in either transient state where we assume that plasma angular momentum is conserved or steady state where we can solve the Hill-Pontius equation (Eq. (3.51)). The work in Chapters 5 - 6 shows that our model is capable of transitioning from a steady to transient state as long as the transient regime lasts less than three hours. Transitioning from a transient to steady state would however pose a few issues: i) we would no longer be able to assume that plasma angular momentum is conserved and ii) we would not be able to use the Hill-Pontius equation to

solve for plasma angular velocity as the system is not in steady state (where the equation is valid). Therefore for either multiple solar wind shocks or a rapid shock followed by extended periods of high/low dynamic pressure, we would require a new method to obtain magnetospheric plasma angular velocity profiles. This currently presents considerable difficulties and would require some time-dependent form of the Hill-Pontius equation. We note that it would be very useful for the development of a fully time-dependent coupled model.

Another interesting addition to the model would be to add a time-variable mass loading profile (for the Iogenic source) and simulate how this affects the Jovian system. Studies by Bagenal and Delamere (2011) have shown that Io ejects between 600 and 2600 $\mathrm{kg\,s^{-1}}$ of sulphur dioxide, half of which is ionised at or near Io. Work has already been undertaken on how different mass loading rates effect the Jovian system (e.g. Nichols and Cowley (2004)). They found that an increase in mass loading rate would lead to a corresponding increase in plasma sub-corotation as the more mass the magnetosphere contains the more angular momentum would need to be transferred by the thermosphere to keep it corotating. The opposite would occur in the case of a decrease in mass loading rate. More recently work by authors such as Yoneda et al. (2009, 2010) have shown that volcanic activity at Io, as observed using sodium D line emission, has a variable rate and these authors calculated that an increase in sodium brightness and scale height indicated increases in flux tube content. In the first instance, one could use an arbitrary time-dependent sodium brightness profile to assume similar increases in sulphur dioxide and use such profiles to see how the Jovian system responds to such a varying mass loading rate. Employing both variable solar wind pressure and mass loading could then form a subsequent exploration of the 'configuration space' of the system.

In reality, there are a large number of additions/improvements that can be made to the present coupled model e.g. make it three-dimensional, add H_3^+ cooling, add enhanced Pedersen conductivities. Work is currently underway to incorporate field-aligned potentials to the model, which seem to strongly control the intensity of auroral currents (ongoing work by L. C. Ray).

Other interesting avenues would be to simulate the transient phenomena modelled here,

but for the Kronian system by modifying the Smith and Aylward (2008) Saturn model. Modelling the M-I coupling at the Ice Giants would also be interesting, but this would present challenges, due to the intrinsic nature of the icy systems. It would not be possible, for example, to model the Ice Giants using axisymmtetric methods as the orientation of their magnetospheres are highly tilted with respect to their rotation axis. Nevertheless, this would be a scientifically important venture, especially with the recent interest in missions to the Ice Giants, such as the 'Uranus Pathfinder' concept.

Appendix A

HST pixel calculation

In this section we set out to calculate the latitudinal size of a single HST ACS-SBC pixel on the Jovian thermosphere. We begin by tracing out a schematic of the system (not to scale) as shown in Fig. A.1. The HST lies a distance $D(= 4.2\,\mathrm{AU})$ from Jupiter and an ACS-SBC pixel has an angular size δ of 0.03x0.03 arc sec equivalent to a physical size p of 25x25 μm. We assume that the magnetic axis of the Jovian dipole is perpendicular to the observer's line of sight.

Before we can proceed, it is necessary to calculate the magnification m of Jupiter is an image was taken using the HST:

$$m = \frac{f}{f - D}, \tag{A.1}$$

where $f(= 57.6\,\mathrm{m})$ is HST's focal length. It is now possible to calculate the physical size s (in km) on Jupiter that a single pixel represents:

$$s = \frac{p}{m}. \tag{A.2}$$

Using the values for D, f and p given above; $s \approx 273\,\mathrm{km}$. Fig. A.1 shows that:

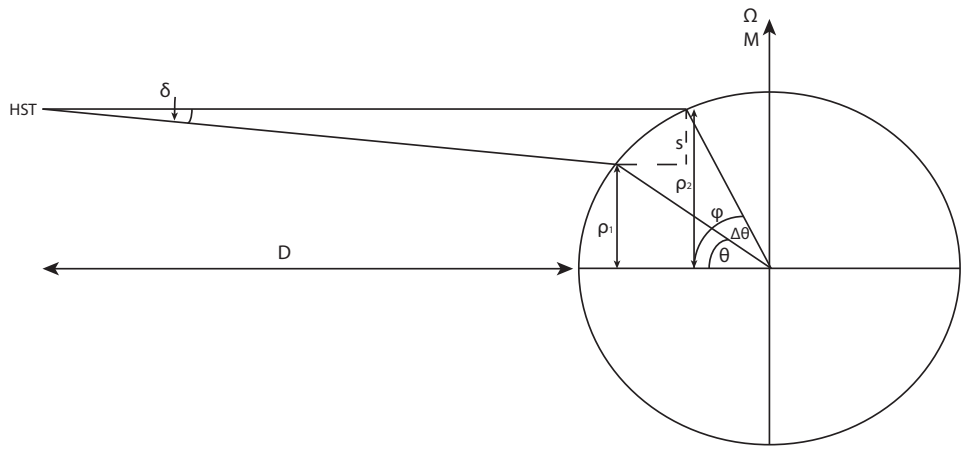

Figure A.1. Schematic to show calculation of latitudinal HST ACS-SBC pixel size on Jupiter's thermosphere.

$$\rho_2 = \rho_1 + s, \tag{A.3}$$

where as stated in Chapter 2, $\rho_i = R_i \sin\theta_i$. For simplicity we will assume that $R_i = R_J$. Substituting ρ_i in Eq. (A.3) and solving for ϕ gives

$$\phi = \arcsin\left(\frac{R_J \sin\theta + s}{R_J}\right). \tag{A.4}$$

We can now work out the latitudinal size representing a single pixel by noting that the difference between ρ_1 and ρ_2 is proportional to $\Delta\theta$, the difference between ϕ and θ (see Fig. A.1).

$$\Delta\theta = \arcsin\left(\frac{R_J \sin\theta + s}{R_J}\right) - \theta. \tag{A.5}$$

$\Delta\theta$ as a function of thermospheric (ionospheric) latitude (obtained using Eq. (A.5)) is plotted in Fig. A.2. Setting $\theta = 74\,^\circ$ (the location of the main auroral oval) gives the latitudinal size of a HST pixel as $\Delta\theta = 0.8\,^\circ$. This is the value used in Chapters 5 and 6.

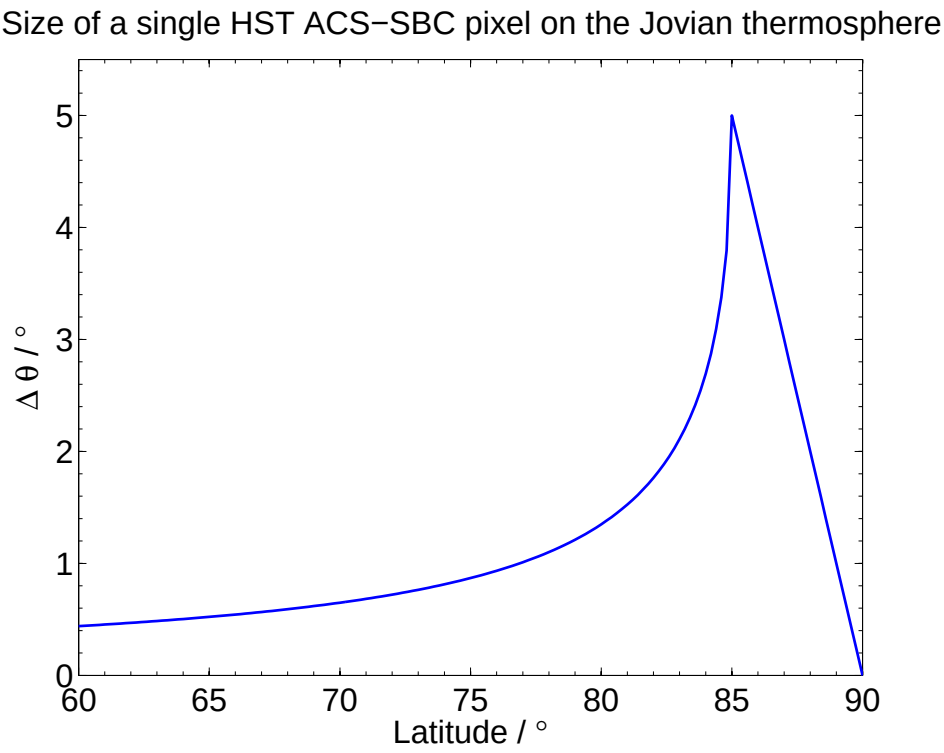

Figure A.2. Plot showing the latitudinal size of a single HST ACS-SBC pixel as a function of ionospheric latitude.

This page was intentionally left blank

Appendix B

Thermospheric dynamics: Acceleration terms

Here, we place the zonal and meridional acceleration terms used to aid the discussions in Chapter 5. Figs. B.1 - B.3 present acceleration terms for the transient compression scenario whilst Figs. B.4 - B.6 present the same terms for the expansion scenario.

Fig. B.1 shows the latitude-altitude distribution of Pedersen conductivity (magnitude indicated by the colour bar). Plotted on this conductivity distribution are contours (values described in Figure caption) of various zonal acceleration terms such as ion drag (first row), Coriolis (second row), advection of momentum (third row) and viscosity (fourth row). The columns, from left to right, represent cases CS, CH and CF respectively. The blue contours indicate positive (or eastward) accelerations whilst the red contours represent negative (or westwards) accelerations.

Figs. B.2 and B.3 shows the same Pedersen conductivity distribution as Fig. B.1 but the acceleration terms are now in the meridional direction. Blue contours now indicate positive (or southward) accelerations whilst the red contours represent negative (or northward) accelerations. The first row presents ion drag accelerations, the second Coriolis, the third pressure gradients and the fourth advection of momentum terms. Fig. B.3 shows the meridional viscous acceleration terms. The columns for both Figs. B.2 and B.3 are as in Fig. B.1.

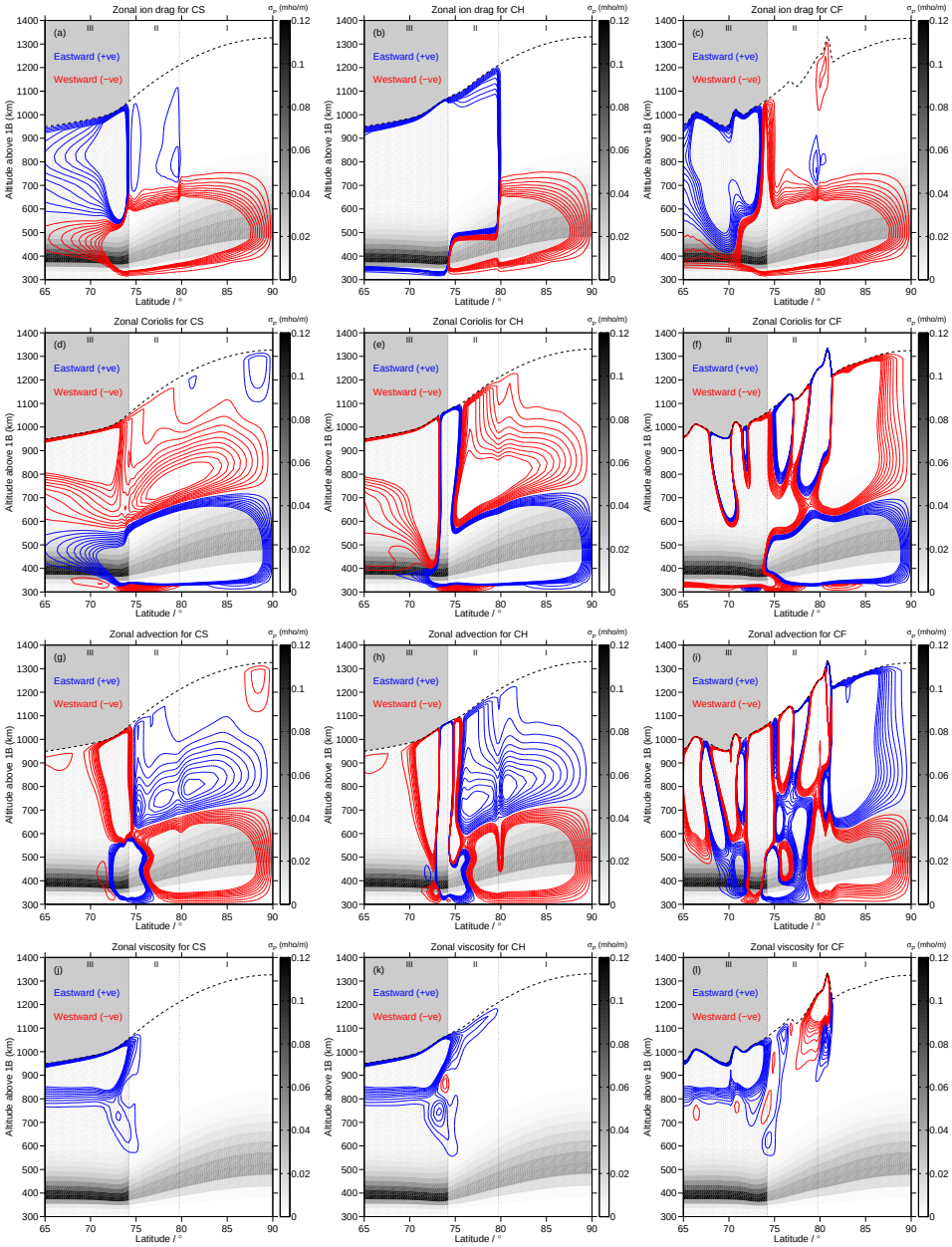

Figure B.1. (a)-(c) shows the variation of zonal ion drag momentum with altitude, latitude and Pedersen conductance (colour bar) for cases CS, CH and CF (left to right). The contours range from $1 - 10\,\mathrm{mm\,s^{-2}}$ with an interval of $1\,\mathrm{mm\,s^{-2}}$ but with blue being positive and red negative. The magnetospheric regions are separated and labelled. (d)-(l) represent zonal momentum terms related to Coriolis, advection and viscosity respectively. All colours and labels are as in (a)-(c).

Fig. B.4 is as Fig. B.1 but with each column, from left to right, representing cases ES, EH and EF respectively. Figs. B.5 and B.6 are as Figs. B.2 and B.3 with the cases ES, EH and EF being respectively represented in columns left to right.

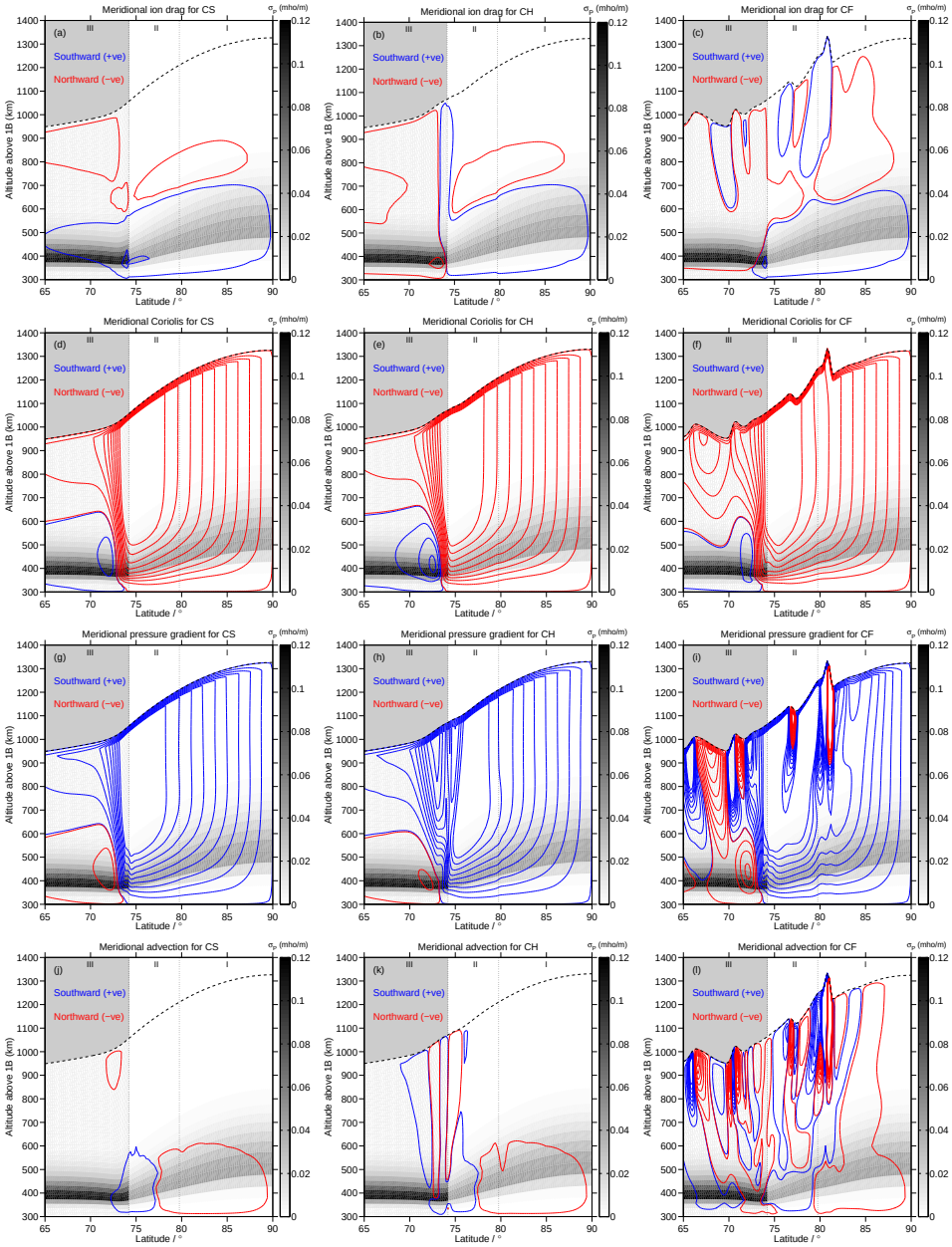

Figure B.2. (a)-(c) shows the variation of meridional ion drag momentum with altitude, latitude and Pedersen conductance (colour bar) for cases CS, CH and CF (left to right). The contours range from $1 - 500\,\mathrm{mm\,s^{-2}}$ with an interval of $50\,\mathrm{mm\,s^{-2}}$ but with blue being positive and red negative. The magnetospheric regions are separated and labelled. (d)-(l) represent meridional momentum terms related to Coriolis, pressure gradients and advection respectively. All colours and labels are as in (a)-(c).

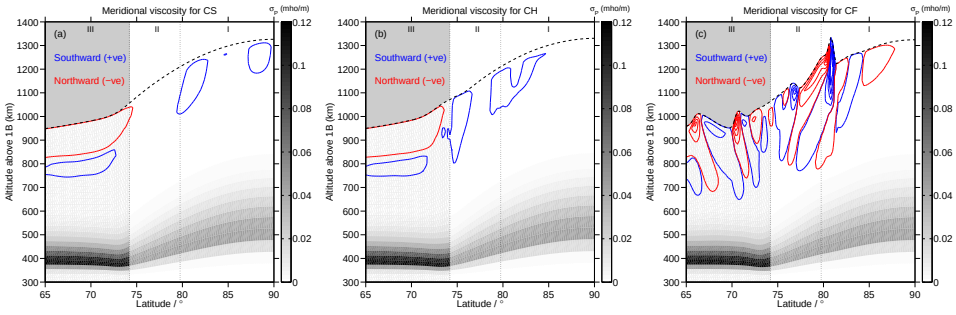

Figure B.3. (a)-(c) shows the variation of meridional viscosity with altitude, latitude and Pedersen conductance (colour bar) for cases CS, CH and CF (left to right). The contours range from $1 - 500\,\mathrm{mm\,s^{-2}}$ with an interval of $50\,\mathrm{mm\,s^{-2}}$ but with blue being positive and red negative. The magnetospheric regions are separated and labelled.

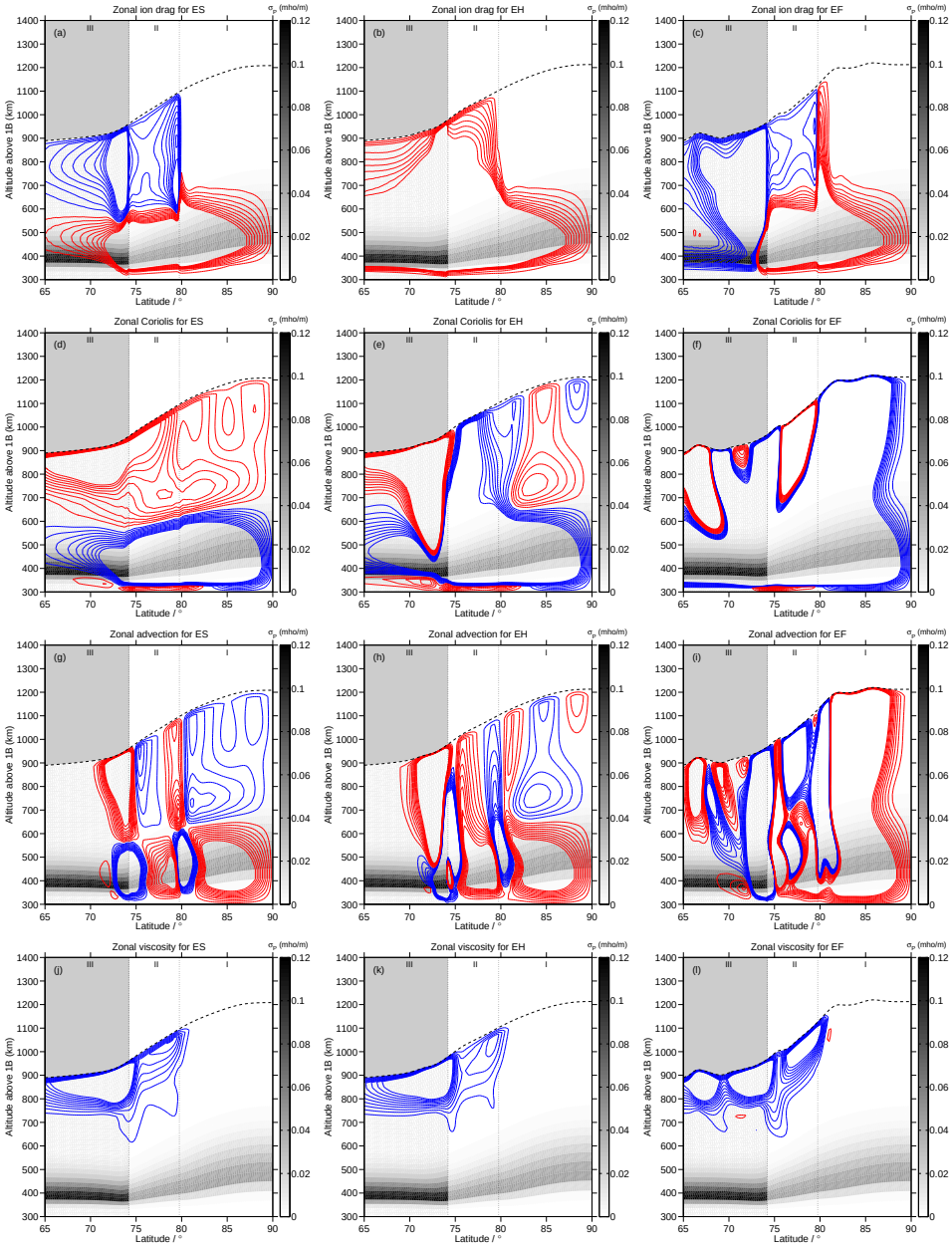

Figure B.4. (a)-(c) shows the variation of zonal ion drag momentum with altitude, latitude and Pedersen conductance (colour bar) for cases ES, EH and EF (left to right). The contours range from $1 - 10\,\mathrm{mm\,s^{-2}}$ with an interval of $1\,\mathrm{mm\,s^{-2}}$ but with blue being positive and red negative. The magnetospheric regions are separated and labelled. (d)-(l) represent zonal momentum terms related to Coriolis, advection and viscosity respectively. All colours and labels are as in (a)-(c).

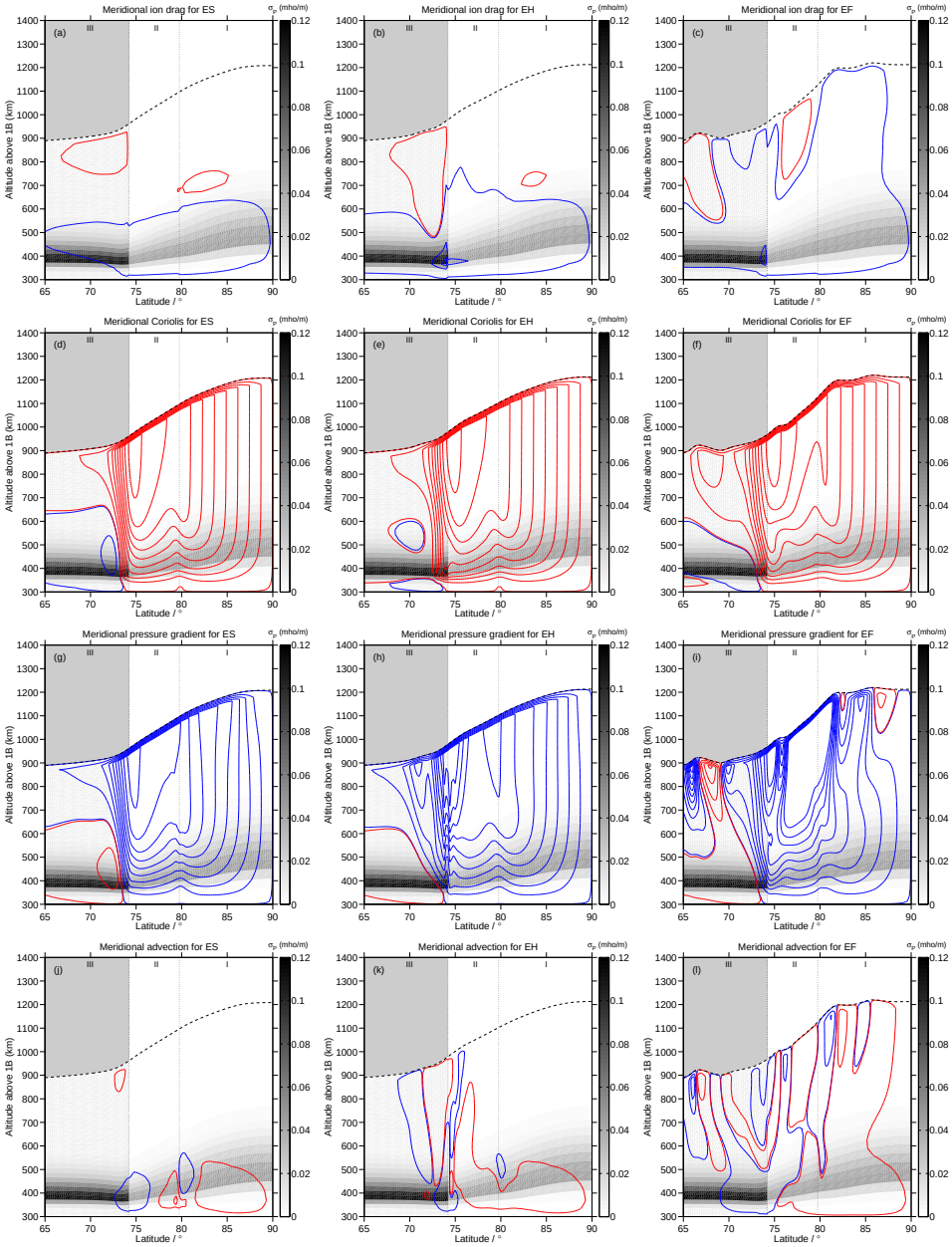

Figure B.5. (a)-(c) shows the variation of meridional ion drag momentum with altitude, latitude and Pedersen conductance (colour bar) for cases ES, EH and EF (left to right). The contours range from $1 - 500\,\mathrm{mm\,s^{-2}}$ with an interval of $50\,\mathrm{mm\,s^{-2}}$ but with blue being positive and red negative. The magnetospheric regions are separated and labelled. (d)-(l) represent meridional momentum terms related to Coriolis, pressure gradients and advection respectively. All colours and labels are as in (a)-(c).

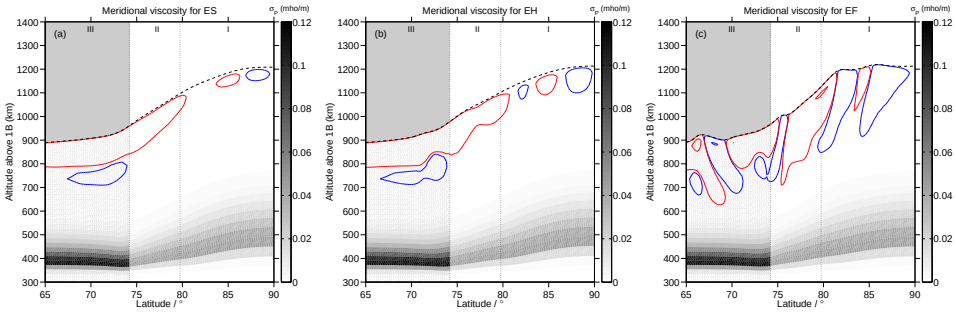

Figure B.6. (a)-(c) shows the variation of meridional viscosity with altitude, latitude and Pedersen conductance (colour bar) for cases ES, EH and EF (left to right). The contours range from $1 - 500\,\mathrm{mm\,s^{-2}}$ with an interval of $50\,\mathrm{mm\,s^{-2}}$ but with blue being positive and red negative. The magnetospheric regions are separated and labelled.

Bibliography

Achilleos, N., Miller, S., Prangé, R., Millward, G., Dougherty, M. K., Apr. 2001. A dynamical model of Jupiter's auroral electrojet. New Journal of Physics 3, 3. 1.2.1, 1.2.1

Achilleos, N., Miller, S., Tennyson, J., Aylward, A. D., Mueller-Wodarg, I., Rees, D., 1998. JIM: A time-dependent, three-dimensional model of Jupiter's thermosphere and ionosphere. J. Geophys. Res. 103, 20089–20112. 1.2.1, 1.2.1, 1.2.2, 2.2.2, 9, 3.1, 3.1.1, 3.2, 6.3.2, 7.4

Alfvén, H., 1956. The sun's general magnetic field. Tellus A 8 (1).
URL http://www.tellusa.net/index.php/tellusa/article/view/8946 2.1.2

Atreya, S. K., Aug. 1982. Eddy mixing coefficient on Saturn. Planet. Space Sci.30, 849–854. 2.2.2

Atreya, S. K., Donahue, T. M., Sandel, B. R., Broadfoot, A. L., Smith, G. R., Oct. 1979. Jovian upper atmospheric temperature measurement by the Voyager 1 UV spectrometer. Geophys. Res. Lett.6, 795–798. 1.1.1

Atreya, S. K., Mahaffy, P. R., Niemann, H. B., Wong, M. H., Owen, T. C., Feb. 2003. Composition and origin of the atmosphere of Jupiter-an update, and implications for the extrasolar giant planets. Planet. Space Sci.51, 105–112. 2.2.5

Badman, S. V., Cowley, S. W. H., May 2007. Significance of Dungey-cycle flows in Jupiter's and Saturn's magnetospheres, and their identification on closed equatorial field lines. Annales Geophysicae 25, 941–951. 2.1.4

Bagenal, F., Delamere, P. A., May 2011. Flow of mass and energy in the magnetospheres of Jupiter and Saturn. Journal of Geophysical Research (Space Physics) 116, 5209. 7.5

Bagenal, F., Sullivan, J. D., 1981. Direct plasma measurements in the Io torus and inner magnetosphere of Jupiter. J. Geophys. Res. 86, 8447–8466. 1.2, 2.1.4

Baron, R., Joseph, R. D., Owen, T., Tennyson, J., Miller, S., Ballester, G. E., Oct. 1991. Imaging Jupiter's aurorae from H3(+) emissions in the 3-4 micron band. Nature353, 539–542. 1.1.1

Bonfond, B., Grodent, D., Gérard, J.-C., Stallard, T., Clarke, J. T., Yoneda, M., Radioti, A., Gustin, J., Jan. 2012. Auroral evidence of Io's control over the magnetosphere of Jupiter. Geophys. Res. Lett.39, 1105. 1.3

Bougher, S. W., Waite, J. H., Majeed, T., Gladstone, G. R., Apr. 2005. Jupiter Thermospheric General Circulation Model (JTGCM): Global structure and dynamics driven by auroral and Joule heating. Journal of Geophysical Research (Planets) 110, 4008. 1.2.1, 1.2.1, 4.2.2

Broadfoot, A. L., Belton, M. J., Takacs, P. Z., Sandel, B. R., Shemansky, D. E., Holberg, J. B., Ajello, J. M., Moos, H. W., Atreya, S. K., Donahue, T. M., Bertaux, J. L., Blamont, J. E., Strobel, D. F., McConnell, J. C., Goody, R., Dalgarno, A., McElroy, M. B., Jun. 1979. Extreme ultraviolet observations from Voyager 1 encounter with Jupiter. Science 204, 979–982. 1.3

Clarke, J. T., Ben Jaffel, L., Gérard, J., 1998. Hubble Space Telescope imaging of Jupiter's UV aurora during the Galileo orbiter mission. J. Geophys. Res. 103, 20217–20236. 2.1.4

Clarke, J. T., Grodent, D., Cowley, S. W. H., Bunce, E. J., Zarka, P., Connerney, J. E. P., Satoh, T., 2004. Jupiter's aurora. Jupiter. The Planet, Satellites and Magnetosphere. pp. 639–670. 1.3, 2.1.4

Clarke, J. T., Moos, H. W., Atreya, S. K., Lane, A. L., Nov. 1980. Observations from earth orbit and variability of the polar aurora on Jupiter. ApJ241, L179–L182. 1.3

Clarke, J. T., Nichols, J., Gérard, J.-C., Grodent, D., Hansen, K. C., Kurth, W., Gladstone, G. R., Duval, J., Wannawichian, S., Bunce, E., Cowley, S. W. H., Crary, F., Dougherty, M., Lamy, L., Mitchell, D., Pryor, W., Retherford, K., Stallard, T., Zieger, B., Zarka, P., Cecconi, B., May 2009. Response of Jupiter's and Saturn's auroral activity to the solar wind. Journal of Geophysical Research (Space Physics) 114, 5210. (document), 1.3, 5.2.1, 5.3.1, 6.1, 6.1, 6.3.1, 6.4, 6.4.1, 7.2, 7.3

Connerney, J. E. P., Oct. 1993. Magnetic fields of the outer planets. J. Geophys. Res.98, 18659. 1.3

Connerney, J. E. P., Acuña, M. H., Ness, N. F., Satoh, T., 1998. New models of Jupiter's magnetic field constrained by the Io flux tube footprint. J. Geophys. Res. 103, 11929–11940. 2.3.3

Connerney, J. E. P., Acuna, M. H., Ness, N. F., 1981. Modeling the Jovian current sheet and inner magnetosphere. J. Geophys. Res. 86, 8370–8384. 3.3.1

Connerney, J. E. P., Baron, R., Satoh, T., Owen, T., Nov. 1993. Images of Excited H_3ˆ+ at the Foot of the Io Flux Tube in Jupiter's Atmosphere. Science 262, 1035–1038. 1.1.1

Cowley, S. W. H., Alexeev, I. I., Belenkaya, E. S., Bunce, E. J., Cottis, C. E., Kalegaev, V. V., Nichols, J. D., Prangé, R., Wilson, F. J., 2005. A simple axisymmetric model of magnetosphere-ionosphere coupling currents in Jupiter's polar ionosphere. J. Geophys. Res. 110, 11209–11226. 1.2.1, 1.2.1, 1.5, 2.3.5, 2.3.5, 3.2.1, 3.3, 3.3.2, 3.3.2, 4.1, 4.2.1, 5.1, 5.2.1, 6.3.1, 7.1

Cowley, S. W. H., Bunce, E. J., 2001. Origin of the main auroral oval in Jupiter's coupled magnetosphere-ionosphere system. Planet. Space Sci. 49, 1067–1088. 1.2.1, 1.3, 2.1, 2.1.4

Cowley, S. W. H., Bunce, E. J., 2003a. Modulation of Jovian middle magnetosphere currents and auroral precipitation by solar wind-induced compressions and expansions of the magnetosphere: initial response and steady state. Planet. Space Sci. 51, 31–56. 1.2.1, 1.2.2, 1.3, 1.4, 1.4, 5.1, 7.2

Cowley, S. W. H., Bunce, E. J., 2003b. Modulation of Jupiter's main auroral oval emissions by solar wind induced expansions and compressions of the magnetosphere. Planet. Space Sci. 51, 57–79. 1.2.1, 1.2.2, 1.3, 1.4, 4.1, 4.2.1, 4.4, 5.4.1, 5.4.3, 7.1, 7.2

Cowley, S. W. H., Bunce, E. J., Stallard, T. S., Miller, S., Mar. 2003. Jupiter's polar ionospheric flows: Theoretical interpretation. Geophys. Res. Lett.30 (5), 050000–1. 2.1.4, 2.1.4, 2.9

Cowley, S. W. H., Nichols, J. D., Andrews, D. J., 2007. Modulation of Jupiter's plasma flow, polar currents, and auroral precipitation by solar wind-induced compressions and

expansions of the magnetosphere: a simple theoretical model. Ann. Geophys. 25, 1433–1463. 1, 1.2.1, 1.2.2, 1.3, 1.4, 1.4, 2.1.4, 2.3.3, 2.3.3, 2.3.5, 2.3.5, 2.3.5, 2.1, 3.3, 3.3.1, 3.3, 3.3.1, 3.4.1, 3.5.1, 3.5.1, 4.1, 4.2.1, 4.2.1, 4.2.1, 4.2.2, 4.3.1, 4.4, 5.1, 5.2.1, 5.2.1, 5.3.1, 5.4.1, 5.4.3, 6.1, 6.1, 6.2, 6.2, 6.3, 6.3.1, 6.9, 6.4.1, 6.5.1, 6.5.1, 7.1, 7.2

Drossart, P., Bezard, B., Atreya, S. K., Bishop, J., Waite, Jr., J. H., Boice, D., 1993. Thermal profiles in the auroral regions of Jupiter. J. Geophys. Res. 98, 18803–18811. 4.2.2

Drossart, P., Maillard, J.-P., Caldwell, J., Kim, S. J., Watson, J. K. G., Majewski, W. A., Tennyson, J., Miller, S., Atreya, S. K., Clarke, J. T., Waite, J. H., Wagener, R., Aug. 1989. Detection of H3(+) on Jupiter. Nature340, 539–541. 1.1.1, 1.3

Dungey, J. W., Jan. 1961. Interplanetary Magnetic Field and the Auroral Zones. Physical Review Letters 6, 47–48. 2.1.4

Eviatar, A., Barbosa, D. D., Sep. 1984. Jovian magnetospheric neutral wind and auroral precipitation flux. J. Geophys. Res.89, 7393–7398. 1.1.2, 1.1.2

Festou, M. C., Atreya, S. K., Donahue, T. M., Sandel, B. R., Shemansky, D. E., Broadfoot, A. L., Jul. 1981. Composition and thermal profiles of the Jovian upper atmosphere determined by the Voyager ultraviolet stellar occultation experiment. J. Geophys. Res.86, 5715–5725. 1.1.1

French, R. G., Gierasch, P. J., Sep. 1974. Waves in the Jovian Upper Atmosphere. Journal of Atmospheric Sciences 31, 1707–1712. 1.1.2

Fuller-Rowell, T. J., 1981. A three-dimensional, time-dependent global model of the thermosphere. Ph.D. thesis, University College London. 3.1, 3.1.2

Fuller-Rowell, T. J., Rees, D., Quegan, S., Moffett, R. J., Codrescu, M. V., Millward, G. H., 1996. A coupled thermosphere-ionosphere model (ctim). pp. 217–238. 3.1

Gong, B., 2005. Variations of Jovian aurora induced by changes in solar wind dynamic pressure. Ph.D. thesis, Rice University. 1.4, 5.2.1, 5.3.1, 7.2

Grodent, D., Clarke, J. T., Kim, J., Waite, J. H., Cowley, S. W. H., 2003a. Jupiter's main auroral oval observed with HST-STIS. J. Geophys. Res. 108, 1389–1404. 1.3, 2.1.4

Grodent, D., Clarke, J. T., Waite, J. H., Cowley, S. W. H., Gérard, J.-C., Kim, J., Oct. 2003b. Jupiter's polar auroral emissions. Journal of Geophysical Research (Space Physics) 108, 1366. 1.3

Grodent, D., Waite, J. H., Gérard, J., 2001. A self-consistent model of the Jovian auroral thermal structure. J. Geophys. Res. 106, 12933–12952. 1.1.2, 1.2.1, 1.3, 1.5, 3.1.1, 3.2, 3.2.2, 3.2.2, 4.2.2, 7.1

Gross, S. H., Rasool, S. I., Nov. 1964. The Upper Atmosphere of Jupiter. Icarus 3, 311. 1.1.1

Hickey, M. P., Walterscheid, R. L., Schubert, G., Nov. 2000. Gravity Wave Heating and Cooling in Jupiter's Thermosphere. Icarus 148, 266–281. 1.1.2

Hill, T. W., 1979. Inertial limit on corotation. J. Geophys. Res. 84, 6554–6558. 1.1.1, 1.2, 1.2.1, 2.1.4, 3.4.1, 3.4.1

Hill, T. W., Jan. 1980. Corotation lag in Jupiter's magnetosphere - Comparison of observation and theory. Science 207, 301. 3.2.1

Hill, T. W., 2001. The Jovian auroral oval. J. Geophys. Res. 106, 8101–8108. 1.2.1, 2.1.4, 2.3.4

Hill, T. W., Dessler, A. J., Goertz, C. K., 1983. Magnetospheric models. Physics of the Jovian Magnetosphere. pp. 353–394. 1.2, 2.1.4

Houghton, J. T., 1986. The physics of atmospheres. 2.2.1

Huang, T. S., Hill, T. W., 1989. Corotation lag of the Jovian atmosphere, ionosphere, and magnetosphere. J. Geophys. Res. 94, 3761–3765. 1.2.1, 2.3.2

Hubbard, W., Nather, R. E., Evans, D. S., Tull, R. G., Wells, D. C., van Citters, G. W., Warner, B., vanden Bout, P., Feb. 1972. The Occultation of Beta Scorpii by Jupiter and Io. I. Jupiter. AJ77, 41. 1.1.1

Huddleston, D. E., Russell, C. T., Kivelson, M. G., Khurana, K. K., Bennett, L., 1998. Location and shape of the Jovian magnetopause and bow shock. J. Geophys. Res. 103, 20075–20082. 1.4, 3.3

Isbell, J., Dessler, A. J., Waite, Jr., J. H., 1984. Magnetospheric energization by interaction between planetary spin and the solar wind. J. Geophys. Res. 89, 10716–10722. 2.1.4, 3.2.1, 3.3.2, 3.4.1, 3.5.2, 5.2.1, 6.3.1, 7.1

Jackman, C. M., Arridge, C. S., Dec. 2011. Solar Cycle Effects on the Dynamics of Jupiter's and Saturn's Magnetospheres. Sol. Phys.274, 481–502. 2.4

Jackman, C. M., Arridge, C. S., Krupp, N., Bunce, E. J., Mitchell, D. G., McAndrews, H. J., Dougherty, M. K., Russell, C. T., Achilleos, N., Jones, G. H., Coates, A. J., Nov. 2008. A multi-instrument view of tail reconnection at Saturn. Journal of Geophysical Research (Space Physics) 113, 11213. 2.1.4

Jackman, C. M., Russell, C. T., Southwood, D. J., Arridge, C. S., Achilleos, N., Dougherty, M. K., Jun. 2007. Strong rapid dipolarizations in Saturn's magnetotail: In situ evidence of reconnection. Geophys. Res. Lett.34, 11203. 2.1.4

Jacobson, M. Z., Jun. 2005. Fundamentals of Atmospheric Modeling. 2.2.2, 4

Joy, S. P., Kivelson, M. G., Walker, R. J., Khurana, K. K., Russell, C. T., Ogino, T., 2002. Probabilistic models of the Jovian magnetopause and bow shock locations. J. Geophys. Res. 107, 1309–1325. 1.2.1, 2.1.4, 3.3, 3.4

Kane, M., Mauk, B. H., Keath, E. P., Krimigis, S. M., 1995. Hot ions in Jupiter's magnetodisc: A model for Voyager 2 low-energy charged particle measurements. J. Geophys. Res. 100, 19473–19486. 10

Kennel, C. F., Coroniti, F. V., 1977. Jupiter's magnetosphere. ARA&A15, 389–436. 1.2

Khurana, K. K., 2001. Influence of solar wind on Jupiter's magnetosphere deduced from currents in the equatorial plane. J. Geophys. Res. 106, 25999–26016. 1.2.1, 1.5, 1.2.1, 2.1.4

Khurana, K. K., Kivelson, M. G., 1993. Inference of the angular velocity of plasma in the Jovian magnetosphere from the sweepback of magnetic field. J. Geophys. Res. 98, 67–79. 3.3.1

Kim, S. J., Drossart, P., Caldwell, J., Maillard, J.-P., Herbst, T., Shure, M., Oct. 1991. Images of aurorae on Jupiter from H3(+) emission at 4 microns. Nature353, 536–539. 1.1.1

Kivelson, M. G., Bagenal, F., Kurth, W. S., Neubauer, F. M., Paranicas, C., Saur, J., 2004. Magnetospheric interactions with satellites. Jupiter. The Planet, Satellites and Magnetosphere. pp. 513–536. 2.1.4

Knight, S., May 1973. Parallel electric fields. Planet. Space Sci.21, 741–750. 2.3.5, 2.3.5, 6.2

Kronberg, E. A., Woch, J., Krupp, N., Lagg, A., Khurana, K. K., Glassmeier, K.-H., Mar. 2005. Mass release at Jupiter: Substorm-like processes in the Jovian magnetotail. Journal of Geophysical Research (Space Physics) 110, 3211. 2.1.4

Kunow, H., Nov. 2000. Solar Wind: Corotating Interaction Regions. 2.1.3, 2.1.3, 2.5

Lam, H. A., Achilleos, N., Miller, S., Tennyson, J., Trafton, L. M., Geballe, T. R., Ballester, G. E., Jun. 1997. A Baseline Spectroscopic Study of the Infrared Auroras of Jupiter. Icarus 127, 379–393. 1.1.1, 1.3

Lebreton, J.-P., Witasse, O., Sollazzo, C., Blancquaert, T., Couzin, P., Schipper, A.-M., Jones, J. B., Matson, D. L., Gurvits, L. I., Atkinson, D. H., Kazeminejad, B., Pérez-Ayúcar, M., Dec. 2005. An overview of the descent and landing of the Huygens probe on Titan. Nature438, 758–764. 1

Low, B., Nov. 2000. Solar Coronal Mass Ejection: Theory. 2.1.3

Luhmann, J. G., 1995. Introduction to Space Physics. Ch. Ionospheres, pp. 183–202. 2.2.3, 3.2.1

Lundin, R., Sandahl, I., Jun. 1978. Some characteristics of the parallel electric field acceleration of electrons over discrete auroral arcs as observed from two rocket flights. In: Halvorsen, T., Battrick, B. (Eds.), European Sounding Rocket, Balloon and Related Research, with Emphasis on Experiments at High Latitudes. Vol. 135 of ESA Special Publication. pp. 125–136. 2.3.5, 6.2

Lystrup, M. B., Miller, S., Dello Russo, N., Vervack, Jr., R. J., Stallard, T., Apr. 2008. First Vertical Ion Density Profile in Jupiter's Auroral Atmosphere: Direct Observations using the Keck II Telescope. ApJ677, 790–797. 4.2.2

Maillard, J.-P., Drossart, P., Watson, J. K. G., Kim, S. J., Caldwell, J., Nov. 1990. H3(+)

fundamental band in Jupiter's auroral zones at high resolution from 2400 to 2900 inverse centimeters. ApJ363, L37–L41. 1.1.1

Majeed, T., Waite, J. H., Bougher, S. W., Gladstone, G. R., Jul. 2009. Processes of auroral thermal structure at Jupiter: Analysis of multispectral temperature observations with the Jupiter Thermosphere General Circulation Model. Journal of Geophysical Research (Planets) 114, 7005. 1.2.1

Marten, A., de Bergh, C., Owen, T., Gautier, D., Maillard, J. P., Drossart, P., Lutz, B. L., Orton, G. S., May 1994. Four micron high-resolution spectra of Jupiter in the North Equatorial Belt: H3(+) emissions and the C-12/C-13 ratio. Planet. Space Sci.42, 391–399. 1.1.1

Matcheva, K. I., Strobel, D. F., Aug. 1999. Heating of Jupiter's Thermosphere by Dissipation of Gravity Waves Due to Molecular Viscosity and Heat Conduction. Icarus 140, 328–340. 1.1.2

McGovern, W. E., Burk, S. D., 1972. Upper atmospheric thermal structure of Jupiter with convective heat transfer. Journal of Atmospheric Sciences 29, 179–189. 1.1.1

McNutt, Jr., R. L., Belcher, J. W., Sullivan, J. D., Bagenal, F., Bridge, H. S., 1979. Departure from rigid co-rotation of plasma in Jupiter's dayside magnetosphere. Nature 280, 803–803. 1.2, 2.1.4

Melin, H., Miller, S., Stallard, T., Smith, C., Grodent, D., Mar. 2006. Estimated energy balance in the jovian upper atmosphere during an auroral heating event. Icarus 181, 256–265. 1.1.2, 3.1.4, 4.2.2, 5.4.3, 6.1, 6.5.1, 7.1, 7.3, 7.4

Miller, S., Achilleos, N., Ballester, G. E., Geballe, T. R., Joseph, R. D., Prangé, R., Rego, D., Stallard, T., Tennyson, J., Trafton, L. M., Waite, Jr., J. H., 2000. The role of H^+_3 in planetary atmospheres. In: Astronomy, physics and chemistry of H^+_3. Vol. 358 of Royal Society of London Philosophical Transactions Series A. p. 2485. 1, 1.1.2

Miller, S., Achilleos, N., Ballester, G. E., Lam, H. A., Tennyson, J., Geballe, T. R., Trafton, L. M., Nov. 1997. Mid-to-Low Latitude H^+_3 Emission from Jupiter. Icarus 130, 57–67. 1.1.1, 1.3

Miller, S., Joseph, R. D., Tennyson, J., Sep. 1990. Infrared emissions of H3(+) in the atmosphere of Jupiter in the 2.1 and 4.0 micron region. ApJ360, L55–L58. 1.1.1

Millward, G., Miller, S., Stallard, T., Achilleos, N., Aylward, A. D., Jan. 2005. On the dynamics of the jovian ionosphere and thermosphere. Icarus 173, 200–211. (document), 1.1.2, 1.2.1, 1.2.1, 1.2.2, 1.10, 1.4, 3.1, 7.2

Millward, G., Miller, S., Stallard, T., Aylward, A. D., Achilleos, N., Nov. 2002. On the Dynamics of the Jovian Ionosphere and ThermosphereIII. The Modelling of Auroral Conductivity. Icarus 160, 95–107. 1.2.1, 1.4, 1.2.1, 3.2.1

Millward, G. H., Moffett, R. J., Quegan, S., Fuller-Rowell, T. J., 1996. A coupled thermosphere-ionosphere-plasmasphere model (ctip). pp. 239–279. 3.1

Moore, L. E., Mendillo, M., Müller-Wodarg, I. C. F., Murr, D. L., Dec. 2004. Modeling of global variations and ring shadowing in Saturn's ionosphere. Icarus 172, 503–520. 3.1.4

Moses, J. I., Fouchet, T., Bézard, B., Gladstone, G. R., Lellouch, E., Feuchtgruber, H., Aug. 2005. Photochemistry and diffusion in Jupiter's stratosphere: Constraints from ISO observations and comparisons with other giant planets. Journal of Geophysical Research (Planets) 110, 8001. 2.2.2

Müller-Wodarg, I. C. F., Mendillo, M., Yelle, R. V., Aylward, A. D., Jan. 2006. A global circulation model of Saturn's thermosphere. Planet. Space Sci.180, 147–160. 3.1, 3.1.1, 3.1.4

Müller-Wodarg, I. C. F., Yelle, R. V., Mendillo, M., Young, L. A., Aylward, A. D., 2000. The thermosphere of Titan simulated by a global three-dimensional time-dependent model. J. Geophys. Res.105, 20833–20856. 3.1

Nichols, J., Cowley, S., 2004. Magnetosphere-ionosphere coupling currents in Jupiter's middle magnetosphere: effect of precipitation-induced enhancement of the ionospheric Pedersen conductivity. Ann. Geophys. 22, 1799–1827. (document), 1.2.1, 1.4, 1.5, 1.2.1, 1.2.1, 1.5, 2.3.3, 3.2, 3.2.1, 3.1, 3.2.1, 3.3, 3.3.1, 3.3.1, 3.4.1, 4.2.1, 4.2.1, 4.3.1, 7.5

Nichols, J. D., Bunce, E. J., Clarke, J. T., Cowley, S. W. H., Gérard, J.-C., Grodent, D., Pryor, W. R., Feb. 2007. Response of Jupiter's UV auroras to interplanetary conditions as observed by the Hubble Space Telescope during the Cassini flyby campaign. Journal of Geophysical Research (Space Physics) 112, 2203. 1.3

Nichols, J. D., Clarke, J. T., Gérard, J. C., Grodent, D., Hansen, K. C., Jun. 2009. Variation of different components of Jupiter's auroral emission. Journal of Geophysical

Research (Space Physics) 114, 6210. (document), 1.3, 5.2.1, 5.3.1, 6.1, 6.1, 6.2, 6.3.1, 6.4.1, 7.2, 7.3

Nichols, J. D., Cowley, S. W. H., Mar. 2005. Magnetosphere-ionosphere coupling currents in Jupiter's middle magnetosphere: effect of magnetosphere-ionosphere decoupling by field-aligned auroral voltages. Annales Geophysicae 23, 799–808. 1.2.1

Niemann, H. B., Atreya, S. K., Bauer, S. J., Carignan, G. R., Demick, J. E., Frost, R. L., Gautier, D., Haberman, J. A., Harpold, D. N., Hunten, D. M., Israel, G., Lunine, J. I., Kasprzak, W. T., Owen, T. C., Paulkovich, M., Raulin, F., Raaen, E., Way, S. H., Dec. 2005. The abundances of constituents of Titan's atmosphere from the GCMS instrument on the Huygens probe. Nature438, 779–784. 1

Niemann, H. B., Atreya, S. K., Carignan, G. R., Donahue, T. M., Haberman, J. A., Harpold, D. N., Hartle, R. E., Hunten, D. M., Kasprzak, W. T., Mahaffy, P. R., Owen, T. C., Spencer, N. W., Way, S. H., May 1996. The Galileo Probe Mass Spectrometer: Composition of Jupiter's Atmosphere. Science 272, 846–849. 1

Niemann, H. B., Atreya, S. K., Carignan, G. R., Donahue, T. M., Haberman, J. A., Harpold, D. N., Hartle, R. E., Hunten, D. M., Kasprzak, W. T., Mahaffy, P. R., Owen, T. C., Way, S. H., Sep. 1998. The composition of the Jovian atmosphere as determined by the Galileo probe mass spectrometer. J. Geophys. Res.103, 22831–22846. 1

Nishida, A., Watanabe, Y., Nov. 1981. Joule heating of the Jovian ionosphere by corotation enforcement currents. J. Geophys. Res.86, 9945–9952. 1, 1.1.2, 1.1.2, 1.4

Oka, T., Geballe, T. R., Mar. 1990. Observations of the 4 micron fundamental band of H3(+) in Jupiter. ApJ351, L53–L56. 1.1.1

Pallier, L., Prangé, R., 2001. More about the structure of the high latitude Jovian aurorae. Planet. Space Sci. 49, 1159–1173. 2.1.4

Parker, E. N., Nov. 1958. Dynamics of the Interplanetary Gas and Magnetic Fields. ApJ128, 664. 2.1.3

Phillips, J. L., Bame, S. J., Barraclough, B. L., McComas, D. J., Forsyth, R. J., Canu, P., Kellogg, P. J., Nov. 1993a. Ulysses plasma electron observations in the Jovian magnetosphere. Planet. Space Sci.41, 877–892. 2.3.5, 6.2

Phillips, J. L., Bame, S. J., Thomsen, M. F., Goldstein, B. E., Smith, E. J., Dec. 1993b. ULYSSES plasma observations in the Jovian magnetosheath. J. Geophys. Res.98, 21189. 2.3.5, 6.2

Pontius, D. H., 1995. Implications of variable mass loading in the Io torus: The Jovian flywheel. J. Geophys. Res. 100, 19531–19540. 1.2.1

Pontius, D. H., 1997. Radial mass transport and rotational dynamics. J. Geophys. Res. 102, 7137–7150. 1.2, 1.2.1, 2.1.4, 3.4.1, 3.4.1

Prangé, R., Rego, D., Pallier, L., Connerney, J., Zarka, P., Queinnec, J., 1998. Detailed study of FUV Jovian auroral features with the post-COSTAR HST faint object camera. J. Geophys. Res. 103, 20195–20216. 2.1.4

Ratcliffe, J. A., 1972. An introduction to the ionosphere and magnetosphere. 2.2.3, 2.3.1, 2.3.4

Ray, L. C., Ergun, R. E., Delamere, P. A., Bagenal, F., Sep. 2010. Magnetosphere-ionosphere coupling at Jupiter: Effect of field-aligned potentials on angular momentum transport. Journal of Geophysical Research (Space Physics) 115, 9211. 1.2.1, 2.3.5, 3.5.2

Ray, L. C., Ergun, R. E., Delamere, P. A., Bagenal, F., Jan. 2012. Magnetosphere-ionosphere coupling at Jupiter: A parameter space study. Journal of Geophysical Research (Space Physics) 117, 1205. 1.2.1, 2.3.5

Ray, L. C., Su, Y.-J., Ergun, R. E., Delamere, P. A., Bagenal, F., Apr. 2009. Current-voltage relation of a centrifugally confined plasma. Journal of Geophysical Research (Space Physics) 114, 4214. 2.3.5, 3.5.2

Russell, C. T., 2000. Reconnection in Planetary Magnetospheres. Advances in Space Research 26, 393–404. 2.7, 2.8

Sagan, C., Veverka, J., Wasserman, L., Elliot, J., Liller, W., May 1974. Jovian Atmosphere: Structure and Composition between the Turbopause and the Mesopause. Science 184, 901–903. 1.1.2

Sanchez-Lavega, A., 2010. An Introduction to Planetary Atmospheres. Taylor & Francis. 2.2.5

Sandel, B. R., Shemansky, D. E., Broadfoot, A. L., Bertaux, J. L., Blamont, J. E., Belton, M. J. S., Ajello, J. M., Holberg, J. B., Atreya, S. K., Donahue, T. M., Nov. 1979. Extreme ultraviolet observations from Voyager 2 encounter with Jupiter. Science 206, 962–966. 1.3

Satoh, T., Connerney, J. E. P., Oct. 1999. Jupiter's H^+_3 Emissions Viewed in Corrected Jovimagnetic Coordinates. Icarus 141, 236–252. (document), 1.1.1, 1.2

Satoh, T., Connerney, J. E. P., Baron, R. L., 1996. Emission Source Model of Jupiter's H3+ Aurorae: A Generalized Inverse Analysis of Images. Icarus 122, 1–23. 1.1.1, 2.1.4

Scudder, J. D., Sittler, E. C., Bridge, H. S., Sep. 1981. A survey of the plasma electron environment of Jupiter - A view from Voyager. J. Geophys. Res.86, 8157–8179. 2.3.5, 6.2

Seiff, A., Kirk, D. B., Knight, T. C. D., Mihalov, J. D., Blanchard, R. C., Young, R. E., Schubert, G., von Zahn, U., Lehmacher, G., Milos, F. S., Wang, J., May 1996. Structure of the Atmosphere of Jupiter: Galileo Probe Measurements. Science 272, 844–845. 1

Seiff, A., Kirk, D. B., Knight, T. C. D., Young, R. E., Mihalov, J. D., Young, L. A., Milos, F. S., Schubert, G., Blanchard, R. C., Atkinson, D., 1998. Thermal structure of Jupiter's atmosphere near the edge of a 5-μm hot spot in the north equatorial belt. J. Geophys. Res. 103, 22857–22890. 1, 1.1.2, 2.2.5, 2.11, 2.2.5, 4.2.2, 4.7, 7.3, 7.4

Shimizu, M., Apr. 1971. The Upper Atmosphere of Jupiter. Icarus 14, 273. 1.1.1

Siscoe, G. L., Summers, D., Sep. 1981. Centrifugally driven diffusion of Iogenic plasma. J. Geophys. Res.86, 8471–8479. 2.1.4

Smith, C. G. A., 2006. Modelling the Thermosphere of the Giant Planets. Ph.D. thesis, University College London. (document), 1.7, 2.1.4, 2.2.2, 2.2.2, 5, 2.2.2, 2.2.4, 2.10, 3.1.1, 1, 3.1.2, 3, 4, 3.1.2, 3.1.3, 3.1.3, 3.1.3, 3.1.3, 3.1.3, 5, 3.1.4, 3.2

Smith, C. G. A., Aylward, A. D., 2008. Coupled rotational dynamics of Saturn's thermosphere and magnetosphere: a thermospheric modelling study. Ann. Geophys. 26, 1007–1027. (document), 1.6, 2.3.2, 3.1, 7.1, 7.5

Smith, C. G. A., Aylward, A. D., 2009. Coupled rotational dynamics of Jupiter's thermosphere and magnetosphere. Ann. Geophys. 27, 199–230. 1.2.1, 1.5, 1.2.1, 1.2.1, 1.2.1, 1.2.2, 1.5, 2.3.2, 2.3.3, 2.3.3, 3.1, 3.1.1, 3.1, 3.2.1, 3.2.2, 3.2.2, 3.2, 3.3, 3.3.1, 3.4, 3.4.1,

3.4.1, 3.5.1, 3.5.2, 4.1, 4.2.1, 4.2.1, 4.2.1, 4.2.2, 4.4, 5.2.2, 5.2.2, 6.3.2, 6.3.2, 6.4.2, 6.4.2, 6.5.1, 7.1

Smith, C. G. A., Aylward, A. D., Millward, G. H., Miller, S., Moore, L. E., 2007. An unexpected cooling effect in Saturn's upper atmosphere. Nature 445, 399–401. (document), 1.2.1, 1.8, 4.2.2, 5.1, 5.2.2, 6.3.2, 6.3.2, 6.4.2

Smith, C. G. A., Miller, S., Aylward, A. D., 2005. Magnetospheric energy inputs into the upper atmospheres of the giant planets. Ann. Geophys. 23, 1943–1947. 1.1.2, 2.3.4

Southwood, D. J., Kivelson, M. G., 2001. A new perspective concerning the influence of the solar wind on the Jovian magnetosphere. J. Geophys. Res. 106, 6123–6130. 1.2.1, 1.2.2, 1.3, 2.1.4, 4.1, 4.2.1, 4.2.1, 4.3, 4.4, 5.1, 7.1

Stallard, T., Miller, S., Millward, G., Joseph, R. D., Dec. 2001. On the Dynamics of the Jovian Ionosphere and Thermosphere. I. The Measurement of Ion Winds. Icarus 154, 475–491. 1.1.1, 1.1.2, 2.1.4, 3.1.4, 4.2.2, 6.1, 6.5.1, 7.1

Stallard, T., Miller, S., Millward, G., Joseph, R. D., Apr. 2002. On the Dynamics of the Jovian Ionosphere and Thermosphere. II. The Measurement of H_3^+ Vibrational Temperature, Column Density, and Total Emission. Icarus 156, 498–514. (document), 1.1.1, 1.1, 1.1.1, 1.1.2, 2.1.4, 3.1.4, 4.2.2, 4.2.2, 6.1, 6.5.1, 7.1

Stallard, T. S., Miller, S., Cowley, S. W. H., Bunce, E. J., Mar. 2003. Jupiter's polar ionospheric flows: Measured intensity and velocity variations poleward of the main auroral oval. Geophys. Res. Lett.30 (5), 050000–1. 6.3.1

Strobel, D. F., Atreya, S. K., 1983. Ionosphere. pp. 51–67. 2.2.3

Strobel, D. F., Smith, G. R., 1973. On the temperature of the Jovian thermosphere. Journal of Atmospheric Sciences 30, 718–725. 1.1.1, 1.1.1, 2.2.5

Tao, C., Badman, S. V., Fujimoto, M., Jun. 2011. UV and IR auroral emission model for the outer planets: Jupiter and Saturn comparison. Icarus 213, 581–592. 1.3

Tao, C., Fujiwara, H., Kasaba, Y., 2009. Neutral wind control of the Jovian magnetosphere-ionosphere current system. J. Geophys. Res. 114, 8307–8323. (document), 1.2.1, 1.2.1, 1.9, 1.2.2, 3.1.4, 4.2.1

Tobiska, W. K., Jan. 2004. SOLAR2000 irradiances for climate change research, aeronomy and space system engineering. Advances in Space Research 34, 1736–1746. 3.1.4

Tobiska, W. K., Woods, T., Eparvier, F., Viereck, R., Floyd, L., Bouwer, D., Rottman, G., White, O. R., Sep. 2000. The SOLAR2000 empirical solar irradiance model and forecast tool. Journal of Atmospheric and Solar-Terrestrial Physics 62, 1233–1250. 3.1.4

Tomasko, M. G., Archinal, B., Becker, T., Bézard, B., Bushroe, M., Combes, M., Cook, D., Coustenis, A., de Bergh, C., Dafoe, L. E., Doose, L., Douté, S., Eibl, A., Engel, S., Gliem, F., Grieger, B., Holso, K., Howington-Kraus, E., Karkoschka, E., Keller, H. U., Kirk, R., Kramm, R., Küppers, M., Lanagan, P., Lellouch, E., Lemmon, M., Lunine, J., McFarlane, E., Moores, J., Prout, G. M., Rizk, B., Rosiek, M., Rueffer, P., Schröder, S. E., Schmitt, B., See, C., Smith, P., Soderblom, L., Thomas, N., West, R., Dec. 2005. Rain, winds and haze during the Huygens probe's descent to Titan's surface. Nature438, 765–778. 1

Trafton, L., Lester, D. F., Thompson, K. L., Aug. 1989. Unidentified emission lines in Jupiter's northern and southern 2 micron aurorae. ApJ343, L73–L76. 1.1.1

Vasavada, A. R., Bouchez, A. H., Ingersoll, A. P., Little, B., Anger, C. D., the Galileo SSI Team, 1999. Jupiter's visible aurora and Io footprint. J. Geophys. Res. 104, 27133–27142. 2.1.4

Vasyliūnas, V. M., Song, P., Feb. 2005. Meaning of ionospheric Joule heating. Journal of Geophysical Research (Space Physics) 110, 2301. 2.3.4

Vasyliunas, V. M., 1983. Plasma distribution and flow. Physics of the Jovian Magnetosphere. pp. 395–453. 1.2, 2.1.4, 2.1.4

Vasyliunas, V. M., Mar. 1994. Role of the plasma acceleration time in the dynamics of the Jovian magnetosphere. Geophys. Res. Lett.21, 401–404. 1.4

Vogt, M. F., Kivelson, M. G., Khurana, K. K., Joy, S. P., Walker, R. J., Jun. 2010. Reconnection and flows in the Jovian magnetotail as inferred from magnetometer observations. Journal of Geophysical Research (Space Physics) 115, 6219. 2.1.4

Waite, J. H., Cravens, T. E., Kozyra, J., Nagy, A. F., Atreya, S. K., Chen, R. H., Aug. 1983. Electron precipitation and related aeronomy of the Jovian thermosphere and

ionosphere. J. Geophys. Res.88, 6143–6163. 1, 1.1.2, 1.1.2, 1.1.2, 3.1.4, 4.2.2, 5.4.3, 6.1, 7.3, 7.4

Watanabe, Y., Nishida, A., Oct. 1982. Field line distortion and Joule heating by the corotation enforcement current in the Jovian magneto-ionosphere. J. Geophys. Res.87, 8111–8117. 1.4, 1.4

Yates, J., Achilleos, N., Guio, P., 2012. Influence of upstream solar wind on thermospheric flows at jupiter. Planetary and Space Science 61 (1), 15 – 31, surfaces, atmospheres and magnetospheres of the outer planets and their satellites and ring systems: Part VII. 1, 1.2.1, 1.2.2, 3.2.1, 5.2.1, 5.2.2, 5.2.2, 5.3.2, 6.3.2, 6.3.2, 6.4.2, 6.4.2, 6.5.1

Yelle, R. V., Miller, S., 2004. Jupiter's thermosphere and ionosphere. pp. 185–218. 1.1.1, 1.3, 1.1.1, 1.1.2, 2.2.5, 7.4

Yelle, R. V., Young, L. A., Vervack, R. J., Young, R., Pfister, L., Sandel, B. R., 1996. Structure of Jupiter's upper atmosphere: Predictions for Galileo. J. Geophys. Res.101, 2149–2162. 1.1.2

Yoneda, M., Kagitani, M., Okano, S., Dec. 2009. Short-term variability of Jupiter's extended sodium nebula. Icarus 204, 589–596. 7.5

Yoneda, M., Nozawa, H., Misawa, H., Kagitani, M., Okano, S., Jun. 2010. Jupiter's magnetospheric change by Io's volcanoes. Geophys. Res. Lett.37, 11202. 7.5

Young, L. A., Yelle, R. V., Young, R., Seiff, A., Kirk, D. B., Apr. 1997. Gravity waves in Jupiter's thermosphere. Science 276, 108–111. 1, 1.1.2, 1.1.2